Using Novel Techniques in Fluorescent Microscopy to Investigate the Energy Consumption of HCM-Related Proteins in Striated Muscles

Matvey Pilagov

Thesis submitted to the Division of Natural Sciences for the degree of Doctor of Philosophy in Biochemistry

University of Kent, June 2025

I declare that no part of this thesis has been submitted for another degree or qualification. This statement applies to both the University of Kent and other educational establishments.

Table of Contents

TABLE OF CONTENTS 3

DISCLAIMERS 8

COVID-19 Disclaimer 8

Dyslexia Disclaimer 8

Hyperlinks and Cross-Referencing 9

LIST OF ABBREVIATIONS 10

TABLE OF FIGURES 12

LIST OF TABLES 16

ACKNOWLEDGEMENTS 17

ABSTRACT 18

CHAPTER 1 – INTRODUCTION 20

1.1. Muscle Structure and Function 20

1.1.1. Muscle Tissue Types and Their Organisation 20

1.1.2. Sarcomere Structure 22

1.1.3. Sliding Filament Theory 24

1.1.4. Thin Filament Proteins 25

1.1.4.a. Actin 25
1.1.4.b. Troponin – Tropomyosin complex 28
1.1.5. Thick Filament Structure 35
1.1.5.a. Myosin 35
1.1.5.b. Myosin Binding Protein C 42
1.1.6. Titin 46

1.2. Muscle contraction 48

1.2.1. Cross-Bridge Cycle 48
1.2.2. Dual-filament regulation 50
1.2.2.a. Regulation of Muscle Contractions by the Thin Filament 50
1.2.2.b. Myosin Cooperativity and Mechanosensing 53
1.2.2.c. Disordered States of Myosin Heads (SRX, DRX) and Interactive Head Motif (IHM) 53
1.2.3. Post-Translational Modifications of Regulatory Proteins 58
1.2.3.a. MyBP-C 58
1.2.3.b. RLC 59

1.3. Diseases Associated with Mutations in Sarcomeric Proteins 61

1.3.1. Cardiomyopathy 61
1.3.2. Pharmacology 62
1.3.2.a. Mavacamten (MAVA) 63
1.3.2.b. Aficamten (AFI) 63
1.3.2.c. 2'-deoxy-ATP (dATP) 63

1.4. Aims of this Thesis 64

CHAPTER 2 – MATERIALS AND METHODS 65

2.1. Buffers and Solutions 65

2.1.1. Rabbit Psoas (Skeletal) 65
2.1.2. Porcine Cardiac 66
2.1.3. Cy3-ATP Ensemble Experiments 67

2.2. Muscle Preparation ____ 68

2.2.1. Cardiac tissue preparation from full heart ____ 68

2.2.2. Chemical Skinning ____ 68

2.2.2.a. Rabbit Skeletal ____ 68

2.2.2.b. Porcine Cardiac ____ 69

2.2.3. Myofibril Preparation ____ 69

2.3. Myofibril Imaging ____ 71

2.3.1. Flow Chamber Preparation ____ 71

2.3.1.a. Rabbit Skeletal ____ 72

2.3.1.b. Porcine Cardiac ____ 73

2.3.2. Microscope Experimental Setup ____ 74

2.3.3. Image Acquisition ____ 74

2.3.3.a. Single-Molecule Imaging ____ 74

2.3.4. Image Processing ____ 74

2.3.4.a. Skeletal Study ____ 74

2.3.4.b. Cardiac Study ____ 79

2.3.4.c. Z-disc Tilt Correction Control Simulation ____ 80

2.3.4.d. Statistical Analys ____ 81

2.4. Gel-Based phosphorylation assays ____ 83

2.4.1. Rabbit Skeletal ____ 83

2.4.2. Porcine Cardiac ____ 83

2.4.3. Relative Gel-Based Phosphorylation Levels ____ 84

CHAPTER 3 – USING A NOVEL SINGLE-MOLECULE APPROACH TO MAP ATPASE ACTIVITY IN PSOAS RABBIT MYOFIBRILS ____ 84

3.1. Introduction ____ 84

3.1.1. Skeletal MyBP-C Splicing is Tissue-Dependent ____ 85

3.2. Results ____ 87

3.2.1. Tracking Cy3-ATP Events On the Sub-sarcomeric Level 87
3.2.2. Mapped Cy3-ATP Events Reveal Three Lifetimes 91
3.2.3. Altering myosin ATPase using PKA and MAVA 94
3.2.3.a. Mavacamten decreases ATPase in Skeletal Muscles 96
3.2.3.b. PKA Increases ATPase Activity of Skeletal Myofibrils 98
3.2.4. Visualising the Effects of PKA Using Pro-Q Dimond Phosphoprotein Gel Stain 100
3.2.5. Imaging Technique and Photobleaching Rate Derivation 101
3.2.5.a. Stroboscopic Imaging 102
3.2.5.b. Defining Photobleaching Rate of the System 103
3.2.6. Regenerating Cy3-ATP Using PK/PEP Regeneration System 105

3.3. Discussion 108

3.3.1. MAVA cannot fully repress myosin heads 109
3.3.2. PKA activity is localised to the C-zone of the Thick Filament 110

3.4. Conclusion 112

CHAPTER 4 – EXPLORING THE EFFECTS OF POST-TRANSLATIONAL MODIFICATIONS ON B-MYOSIN USING SINGLE-MOLECULE MICROSCOPY 113

4.1. Introduction 113

4.1.1. The Effects of β-adrenergic Response on Cardiac Tissue 113

4.2. Results 117

4.2.1. Imaging Porcine Cardiac Myosin ATPase in Relaxed Conditions 117
4.2.2. PKA Treatment of Porcine Left Ventricle Reveals a Zonal Compensatory Mechanism 122
4.2.3. Targeting the RLC on Porcine Left Ventricle Using MLCK 127

4.3. Discussion 131

4.3.1. PKA Represses Myosins in the D-zone, While Activating Them in the C-zone 131
4.3.2. Hierarchical Nature of Post-Translational Modifications in the Thick Filament 132

4.4. Conclusions 135

CHAPTER 5 – USING A NOVEL ENSEMBLE APPROACH TO INVESTIGATE THE EFFECTS OF MAVACAMTEN AND 2'-DEOXY-ATP ON BETA CARDIAC MYOFIBRILS 136

5.1. Introduction 136

5.1.1. Drug Development and Treatments for Hypertrophic Cardiomyopathy (HCM) 136

5.2. Results 137

5.2.1. Ensemble Sample Preparation 138

5.2.2. Ensemble Flow Chamber Assembly 139

5.2.3. Ensemble Imaging Technique 145

5.2.4. Determining the Accuracy of Stage Repositioning 146

5.2.5. Using Adjacent ROIs to Calculate Measurement Errors 149

5.2.6. Pulse-Chase Optimisation 150

5.2.7. Step-Resolution Optimisation 152

5.2.8. The Effects of Known Myosin Modulators on Porcine β-cardiac Myofibrils 152

5.2.9. Determining the Photobleaching Rate of Ensemble Experiments 155

5.3. Discussion 159

5.3.1. Addressing the Pulse-Chase Controversy 160

5.3.2. Small Molecule Perturbation Shows the Viability of the Novel Ensemble Imaging 161

5.4. Conclusions 164

CHAPTER 6 – FINAL WORDS AND CONCLUSIONS 166

6.1. Conclusions 166

REFERENCES 170

Disclaimers

COVID-19 Disclaimer

The COVID-19 pandemic had a significant impact on the progression of this PhD project. Public health measures, including nationwide lockdowns, led to a complete suspension of laboratory access, halting experimental work until the university reopened. Upon reopening following the initial lockdown, access to laboratory facilities remained restricted due to health and safety protocols. Our research group operated on a rotation and booking system to comply with occupancy limits, which severely limited the pace and scope of experimental work for several months. Similar restrictions were reintroduced in early 2021 due to a resurgence of cases. As a result of these disruptions, some aspects of the planned research could not be completed within the timeframe of this thesis.

Dyslexia Disclaimer

The author of this thesis is a diagnosed moderate-severe dyslexic. I can assure examiners that a lot of work went into multiple spelling revisions from this candidate and others, but some errors are natural to occur in such a large piece of written work. This candidate would like for examiners to consider being more understanding of inevitable spelling errors.

Hyperlinks and Cross-Referencing

This work relies on the use of in-text hyperlinks and cross-references for the ease of navigation. Each comment, normally indicated via (see …), should be linked via a cross-link to the relevant section of this thesis. The reader should be able to navigate through cross-referencing using CTRL + Left Click on the selected word to navigate to the relevant section. To return to the place of the hyperlink press Alt+Left Arrow Key (←). The linking includes all Headings of this thesis Figures, and Tables.

List Of Abbreviations

MyBP-C – Myosin Binding Protein C

MyBP-H – Myosin Binding Protein H

cryo-EM – Cryogenic electron microscopy

MyHC – Myosin Heavy Chains

IQ – isoleucine-glutamine

CaM – calmodulin

LMM – Light Meromyosin

HMM – Heavy Meromyosin

S1 – Subfragment 1

RLC – Regulatory Light Chain

CM – Cardiomyopathy loop

ELC – Essential Light Chain

Fn3 – fibronectin II

PKA – Protein Kinase A

SRX – Super Relaxed State

DRX – Disordered Relaxed state

IHM – Interactive Head Motif

MyBP-HL – Myosin-Binding Protein H-like

cAMP – Cyclic Adenosine Monophosphate

MLCK – Myosin Light Chain Kinase

HCM – Hypertrophic Cardiomyopathy

DCM – Dilated Cardiomyopathy

ACM – Arrhythmogenic Cardiomyopathy

TTS – Takotsubo Cardiomyopathy

SCD – Sudden Cardiac Death

MAVA – Mavacamten

AFI – Aficamten

dATP – 2’-deoxy-ATP

OAF – Oblique Angle Fluorescent Microscope

Table Of Figures

Figure 1. Figure showing three types of muscle tissues. 21

Figure 2. Different levels of structure for skeletal muscle. 23

Figure 3. A schematic representation of a sarcomere with an additional details of the structure for both thick and thin filaments. 24

Figure 4. A structural diagram to show the changes in filament positions before and after contraction. 25

Figure 5. The process of actin treadmilling. 27

Figure 6. Diagram showing the effects Ca^{2+} binding to TnC. 30

Figure 7. Reconstructed images of the thin filament in Ca^{2+}-free (A) and Ca^{2+}-bound (B) conformations. 32

Figure 8. A reconstruction of the core region of troponin complex in calcium bound and free states. 33

Figure 9. A reconstruction of tropomyosin positions during calcium free, bound and myosin + calcium bound states. 34

Figure 10. Side (A) and top-down (B) view of myosin molecules assembled in myosin crowns imaged and reconstructed using Cryo-EM. 37

Figure 11. A schematic breakdown of myosin II molecule. 39

Figure 12. Structural reconstruction of β-cardiac myosin S1 fragment. 41

Figure 13.Domain schematics for three isoforms of Myosin Binding Protein C (MyBP-C). 43

Figure 14. The position and structure of MyBP-C. 44

Figure 15. A structural representation of a ½ sarcomere. 47

Figure 16. Structural representation of cross-bridge cycle of myosin head. 49

Figure 17. Conformational changes of troponin complex in a Ca^{2+} bound (a, c) and free (b, d) states. 52

Figure 18. Figure to show regions interacting between MyBP-C and myosin crowns as described by a recent cryo-EM study. 56

Figure 19. A schematic diagram showing the structure of a flow chamber (cell). 72

Figure 20. A visual representation of a tracking process using TrackMate plugin for ImageJ. 76

Figure 21. A visual explanation of a step-by-step process of superposition and tilt-correction employed in the analysis of skeletal myofibrils. 77

Figure 22. A representation of a data simulation workflow and the following analysis. 81

Figure 23. A graphical representation of a myofibril that was analysed by fitting a survival frequency graph. 88

Figure 24. A bar chart of myosin states distribution throughout all measured myofibrils. 91

Figure 25. A cumulative frequency histogram to show the distribution of Cy3-ATP events through the zones of the thick filament. 92

Figure 26. Bar chart showing the relative percentage of each myosin state in each zone of the A-band. 93

Figure 27. A bar chart showing difference in Cy3-ATPase attachment lengths in untreated and perturbed skeletal myofibrils. 95

Figure 28. Bar charts showing the effects of MAVA on skeletal myofibrils. 97

Figure 29. Bar charts showing the effects of PKA on skeletal myofibrils. 99

Figure 30. SDS-PAGE gels showing both protein concentration and phosphorylation levels using Coomassie and ProQ-Dimond stains. 101

Figure 31. A diagram explaining the concept of stroboscopic illumination. 103

Figure 32. A schematic/mathematical representation of photobleaching process. . 104

Figure 33. Graphs to present the results of photobleaching experiments. 105

Figure 34. Cy3-ATP binding curves prior and following the regeneration. 107

Figure 35. Figure illustrating the activation and inhibition pathways for adenylyl cyclase enzyme..... 114

Figure 36. Residue maps for all isoforms of MYBPC gene showing the reported positions of phosphorylation sites (blue circles). 116

Figure 37. Figure showing a cartoon and a coloured video images of sarcomeres with Cy3-ATP attached. 118

Figure 38. Graphs showing the distribution of sarcomere lengths in all experimental conditions. 120

Figure 39. Graph and a chart showing the breakdown of the analysis process, resulting in an estimation of percentage myosin heads in SRX/DRX..... 121

Figure 40. Image showing an SDS-PAGE gel for observing the effects of PKA, with a subsequent analysis. 123

Figure 41. Figure showing the percentage of myosin heads in SRX across all conditions. 124

Figure 42. Bar chart to show the difference between the effects of PKA on porcine cardiac and rabbit skeletal muscles. 126

Figure 43. SDS PAGE gels showing the levels of phosphorylation of MLCK-treated myofibrils. 129

Figure 44. SDS PAGE gels to show the phosphorylation levels of RLC after MLCK and CIAP treatments. 130

Figure 45. A schematic representing flow chamber setup used in Ensemble experiments. 141

Figure 46. A schematic of an automated stage. 143

Figure 47. A circuit schematic showing the wiring of the Arduino board to the unipolar stepper motor. 144

Figure 48. A typical cardiomyocyte as seen during imaging with 20 ROIs overlayed during the analysis. 146

Figure 49. The image representing the pipeline of user-defined image alignment using Template Matchmaking plugin. 147

Figure 50. Figure showing the maximum displacement of myofibril during the stage movement for ensemble experiments to show the stage movement error. 148

Figure 51. A typical cardiomyocyte showing the pipeline of analysis of three adjacent ROIs. 150

Figure 52. Figure showing distribution of myofibrils on the surface of the flow chamber. 151

Figure 53. Bar charts reflecting the percentage of DRX and SRX. 153

Figure 54. A bar chart showing the changes of average DRX and SRX percentage in each treatment group. 155

Figure 55. Figure representing a control experiment to calculate the photobleaching rate of the ensemble experiments. 158

List Of Tables

Table 1. Table showing distribution of relative % myosin states for all zones of the A-band. 93

Table 2. Table, showing the distribution of SRX/DRX ration for each zone of the thick filament..... 95

Table 3. Tables mirroring the results obtained in Figure 30. 98

Table 4. Tables mirroring the results obtained in Figure 31. 100

Table 5. Table quantifying the percentage of myosin heads in SRX for each condition. 124

Table 6. Table showing the differences in SRX percentage for skeletal psoas and porcine cardiac tissues following PKA treatment. 127

Table 7. Table summarising the percentage change for each condition for both: zones separately and all zones together. 130

Table 8. Table showing the distribution of DRX and SRX across perturbed and unperturbed conditions for ensemble imaging. 163

Acknowledgements

Let me begin by thanking my wonderful supervisor, Prof. Neil Kad, who has accepted me as part of his lab during my master's and then PhD. He has always been an understanding and fair supervisor and without his guidance I doubt that I would have had the will or the capability to finish this monumental work. Most importantly, I would like to thank him for always knowing when to push me that extra mile, so that I could publish a couple of articles ahead of my thesis examination. Furthermore, I would like to thank my secondary supervisor Prof. Michael Geeves for his insightful and fruitful discussions that helped me broaden my knowledge of the field.

Next, I would like to thank my lab mates: Dr Arya Gupta, Dr Alex Moores and Dr James Leech for discussions. James was always patient with me, and I would like to dedicate a special "thank you" to him for that. Furthermore, I would like to thank: Dr Robert Charman, Dr. Lorenzo Bernacchia, Dr. Antoine Paris and Roman Urban for being my good friends during these early years in research and making some of the most difficult days in my life that little bit more (or sometimes less) bearable. Additionally, I would like to thank people who were working with me on the same projects for their insightful and fruitful cooperation: Dr. Quentin Smith, Ateeqa Naim, and Dr. Sonette Steczina (along with her supervisor Prof. Michael Regnier).

Last but not least, I would like to thank my partner, Isotta, and my parents for bearing with me during these difficult but ultimately fun and rewarding times.

Abstract

Hypertrophic Cardiomyopathy (HCM) affects 1 in 500 people worldwide and in severe cases can be a cause of sudden cardiac death. This genetic condition can be linked to protein mutations that regulate the energy consumption in cardiac muscle tissues.

To develop a treatment, one must identify the underline cause and correct it. Unfortunately, many current treatments, like β-blockers, involve medications treating the symptoms but not underlying conditions and thus a broader and deeper understanding of the mechanism by which muscles suffer HCM is needed. This thesis was focused around sarcomeric proteins, mutations in which, were shown to be the main causes of HCM. Furthermore, an investigation was conducted into multiple novel small molecule myosin ATPase inhibitors that were developed as a promising treatments for HCM. The mechanism of action of these novel treatments was focus on the correction of misregulation of myosin heads ATP consumption where a more ATP consuming disordered relaxed state (DRX) was transferred into a more energy-saving super relaxed state (SRX).

To evaluate the effects of abovementioned pharmaceutical agents, a single-molecule approach was utilised to monitor the ATP consumption of different muscle tissues. Firstly, a methodology was established to image fast-twitch skeletal muscles (rabbit psoas) and evaluated both the effects of phosphorylation on HCM-related protein, myosin binding protein-C (MyBP-C), and the effect of a small molecule myosin inhibitor Mavacamten on ATPase rates of Cy3ATP in relaxed psoas tissue. Following the PKA treatment there was an observed increase in myosin activity and a reduction in the number of active myosin heads following the Mavacamten treatment. The effects of Mavacamten on skeletal tissue were limited even at higher, fully saturated, concentrations thus showing the cardiac specificity of Mavacamten.

The study of skeletal tissue was followed up with a more clinically relevant study of porcine cardiac left ventricle (β-myosin). After an initial optimisation, the effects of phosphorylation were established on both regulatory light chain (RLC) and cardiac myosin binding protein C (cMyBP-C), mutations in which together account for ~75 % all HCM cases. This work was the first single-molecule imaging for ATPase activity for

β-myosin thus providing an interesting insight into the energy consumption of ventricular muscle.

Finally, the method was developed for imaging multiple samples quasi-simultaneously using the bulk fluorescence imaging approach, for imaging of large quantities of patient or model organism data. In this method, a self-developed moving stage was employed to locate and move though different samples (cardiomyocytes), which could be contained in separate buffer solutions. Unfortunately, due to the time limitations, the only reliable dataset produced was that of porcine cardiac muscle and not of mutated and/or patient tissues as was initially planned. Using this novel approach, two novel small molecule myosin ATPase inhibitors Aficamten and Mavacamten were assessed, along with the myosin activator 2'-deoxy-ATP.

Chapter 1 – Introduction

1.1. Muscle Structure and Function

1.1.1. Muscle Tissue Types and Their Organisation

“Myofibrils…are admirable objects for high-resolution microscopy” Hugh Huxley and Jean Hunson, 1954

Muscles are a type of soft tissue that enables organisms to move parts of their bodies either voluntarily or involuntarily. In such, muscle involvement is not limited to the gross body movements but also extends to the internal processes like blood circulation and peristalsis. Muscles are complicated, albeit well-studied, structured that are classified as; cardiac, skeletal and smooth (see Figure 1). Cardiac muscles (cardiomyocytes) are localised exclusively to the heart and are defined as non-fatiguing and involuntary muscles. In fact, cardiac muscles do not rest throughout the duration of a lifespan of an organism, and together with skeletal muscles, are defined as striated muscles. The name is derived from the pattern produced by the early images of the skeletal and cardiac muscle tissues clearly visible even at a lower magnification on the light microscopes (Sweeney and Hammers, 2018). Unlike cardiac, skeletal muscles are classified as voluntary and fatigue-affected. They are located throughout the body and can be generally classified by their attachment to the skeleton though tendons. Smooth muscles do not belong to the striated muscle classification as they do not form sarcomeres like cardiac and skeletal and thus lack striations. Smooth muscles can be found in both vertebrates and invertebrates, whereas striated muscles are exclusive to vertebrates. Smooth muscles are controlled by the autonomic nervous system (J.R.Sellers, 2006) and can be found in the walls of hollow organs, such as intestines, stomach, bladder etc.

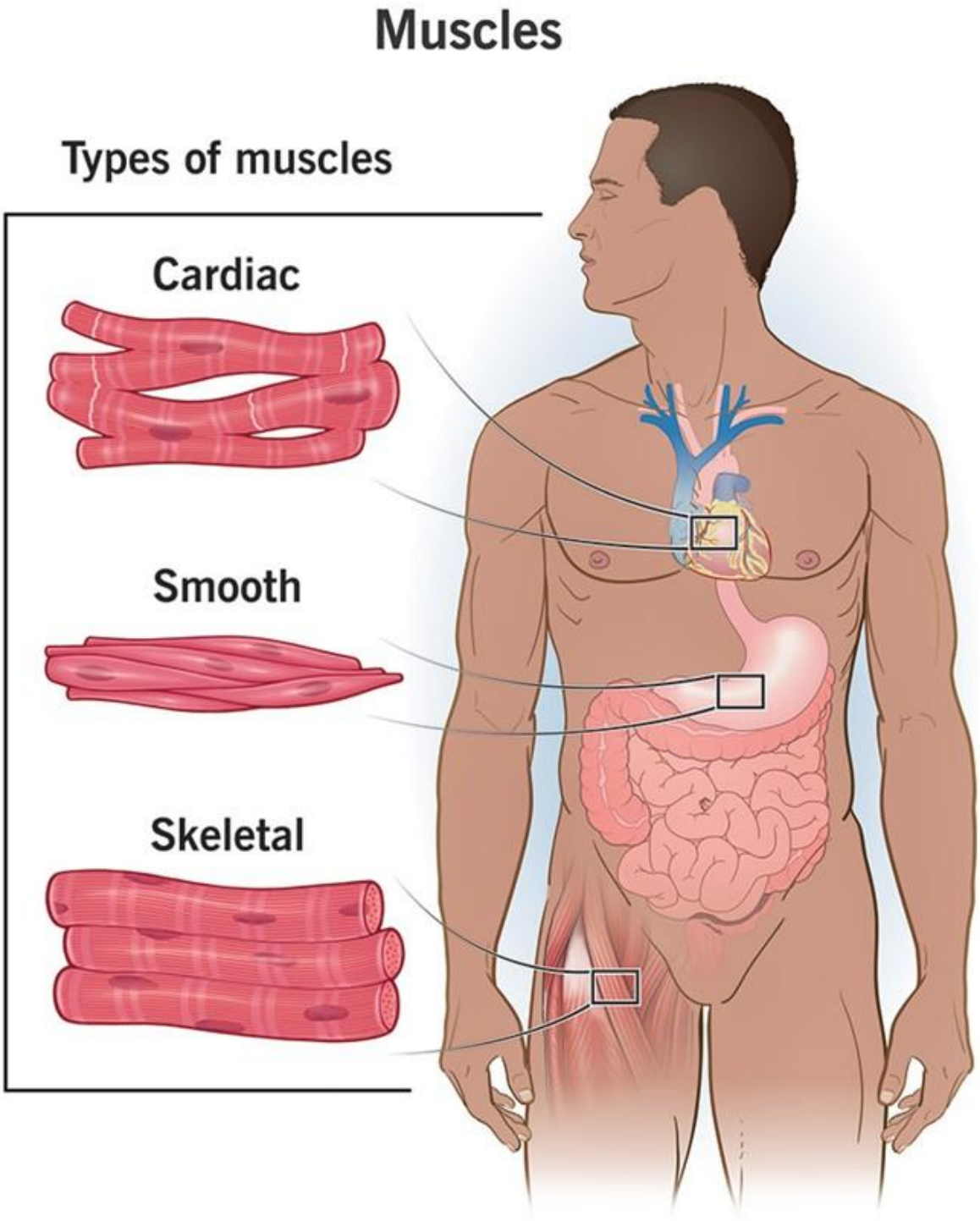


Figure 1. Figure showing three types of muscle tissues.

Cartoon images (left) showing different types of muscle tissues with organ examples for each tissue type; cardiac muscle tissue is present exclusively in the heart, involuntary smooth muscle tissue with stomach lining given as an example, and voluntary skeletal muscle with sartorius leg muscle as an example. Image taken from (*Muscles*, 2023).

1.1.2. Sarcomere Structure

Muscle tissues follow a hierarchical structure from highest level of organisation to the lowest: muscle tissue, muscle bundle, fascicle, muscle fibre, myofibril and finally the basic contractile unit; a sarcomere (see Figure 2). Sarcomeres are separated by the Z-discs (or Z-lines), with the M-line marking the mid-point of the sarcomere. The myosin-containing thick filament crosses the M-line and extends towards both Z-discs (i.e. both ends of the sarcomere), while the actin-containing thin filament extends from both Z-discs towards the M-line (see Figure 3). Excluding myosin, the thick filament has five other major accessory proteins; Myosin Binding Protein-C (MyBP-C), Myosin Binding Protein-H (MyBP-H), titin, myomesin and obscurin (Wang *et al.*, 2018). Although, MyBP-C is well-studied, MyBP-H and MyBP-H-like proteins are more elusive. The thin filament employs the Troponin-Tropomyosin complex for contractile regulation. Troponin has three subunits: Troponin C (TnC), Troponin I (TnI) and Troponin T (TnT). Another essential sarcomeric protein is titin. Titin is a huge (34,451 amino acids, human variant) protein (Labeit and Kolmerer, 1995). Defining and describing the whole structure of titin goes outside of the scope of this thesis but relevant parts will be discussed below along with the other proteins mentioned above.

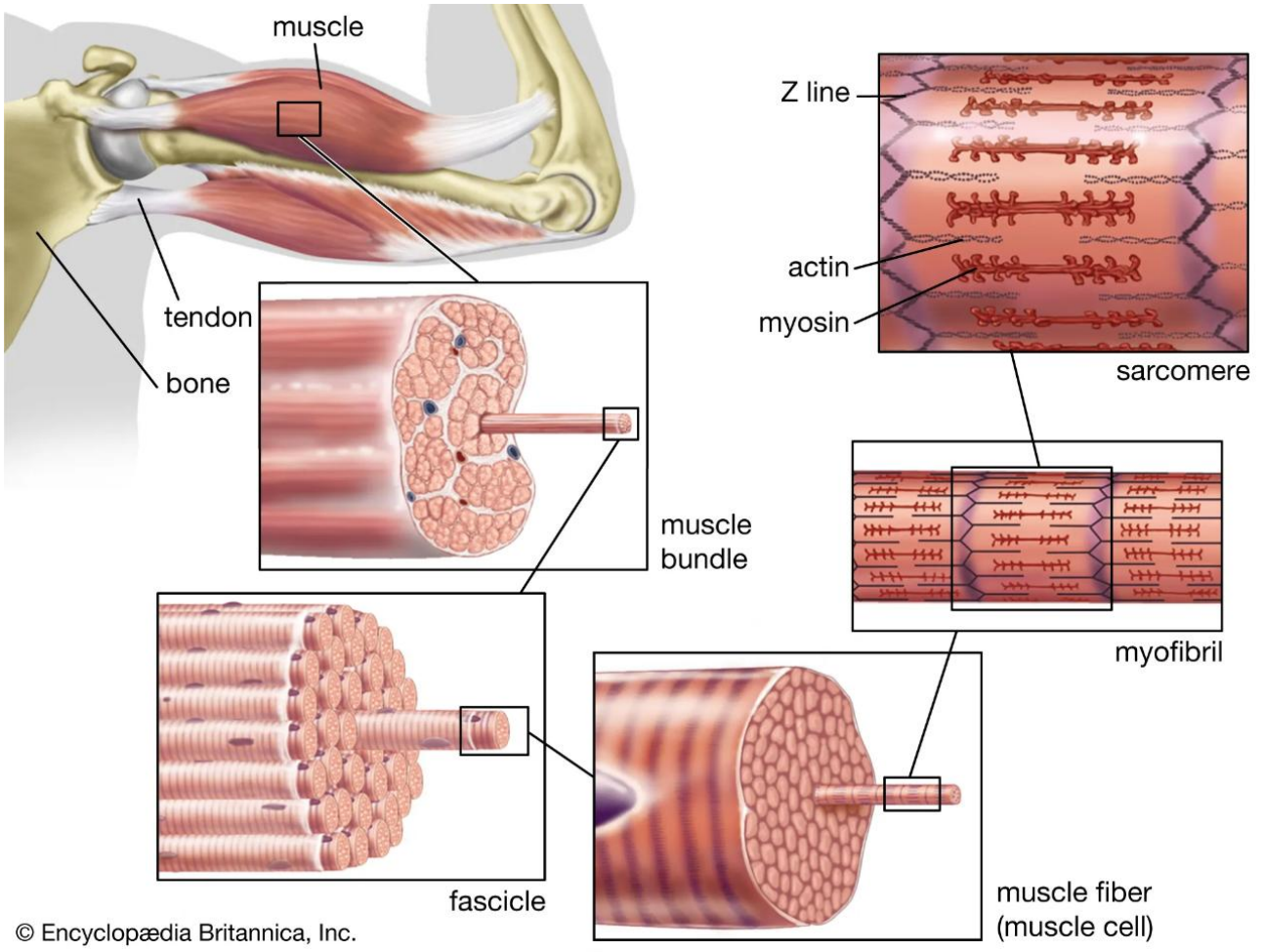


Figure 2. Different levels of structure for skeletal muscle.

Skeletal muscles are connected to the skeleton though tendons and can be subdivided into muscle bundles, muscle bundles divide into muscle fibre and then into myofibrils, with the basic contractile unit of a striated muscle being a sarcomere. Z-discs mark the borders between the neighbouring sarcomeres, while interaction between actin-containing thin filament and the myosin-containing thick filament create a muscle contraction though a sliding motion, pulling the thin filament towards the M-line. Image taken from Encyclopaedia Britannica (Tangen and Wood, 2007).

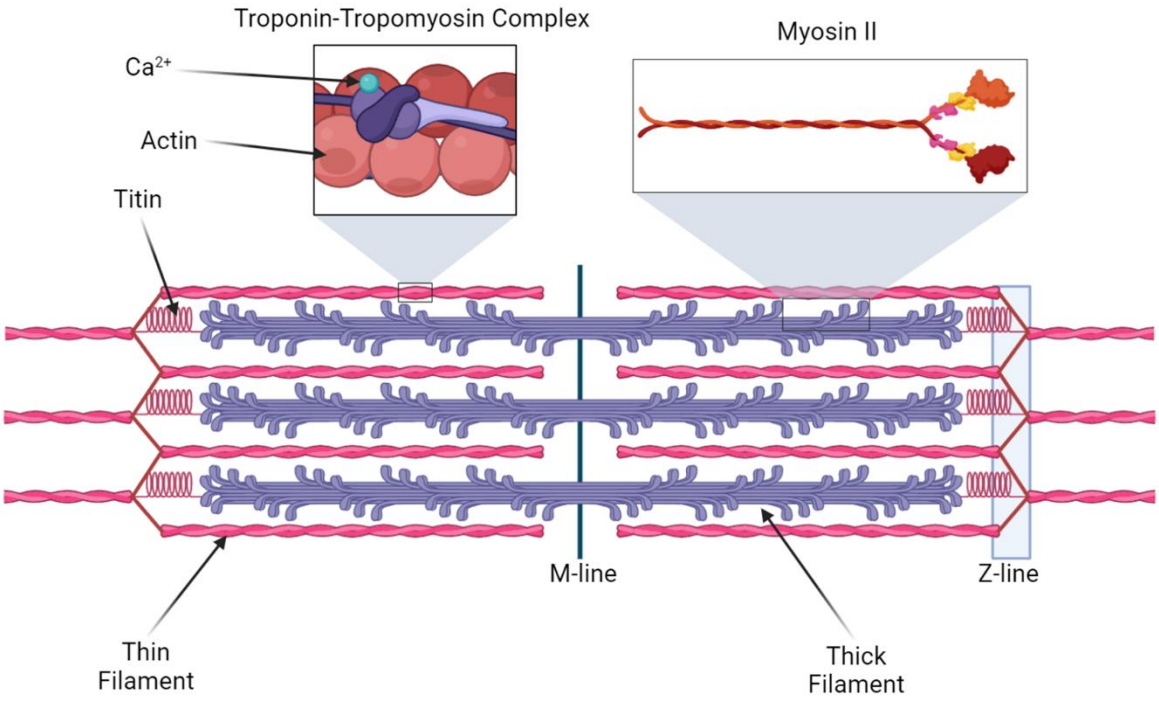


Figure 3. A schematic representation of a sarcomere with an additional details of the structure for both thick and thin filaments.

The M-line is the middle of the sarcomere, while the Z-discs marks its borders. The myosin-containing thick filament is positioned across the M-line protruding in either direction towards the Z-discs. Similarly, the actin-containing thin filament is surging from the Z-discs in the direction of the M-line from both ends of the sarcomere. Titin is attaching the thick filament to the Z-discs and acts as an elastic element, allowing for return to the original conformation following the contraction. Troponin-tropomyosin complex is a part of the thin filament and is discussed below together with the structure of a major thick filament protein myosin II. Image compiled from BioRender.

1.1.3. Sliding Filament Theory

The mechanism of muscle contraction first was proposed independently by two groups (Huxley and Hanson, 1954; Huxley and Niedergerke, 1954) in 1954 and eventually dubbed sliding filament theory. The now predominant theory in the field, describes the movement of thin filament across the thick filament towards the M-line. Myosin heads, protruding from the thick filament, form an actomyosin complex with myosin binding sites on Ca^{2+}-activated thin filament, ATP is hydrolysed in myosin head ATPase cleft, pulling the thin filament towards the M-line, thus contracting the sarcomere (see Figure 4). As the thin filament slides across up to the H-zone, the I-band is shortening, in some cases reaching a near-zero length by the end of the contraction. The thick filament stays in place, while myosin heads are pulling the thin filament towards the

M-band. Titin elastic region shrinks in size, only to be returned back into the original position when its role as an elastic filament has been fulfilled.

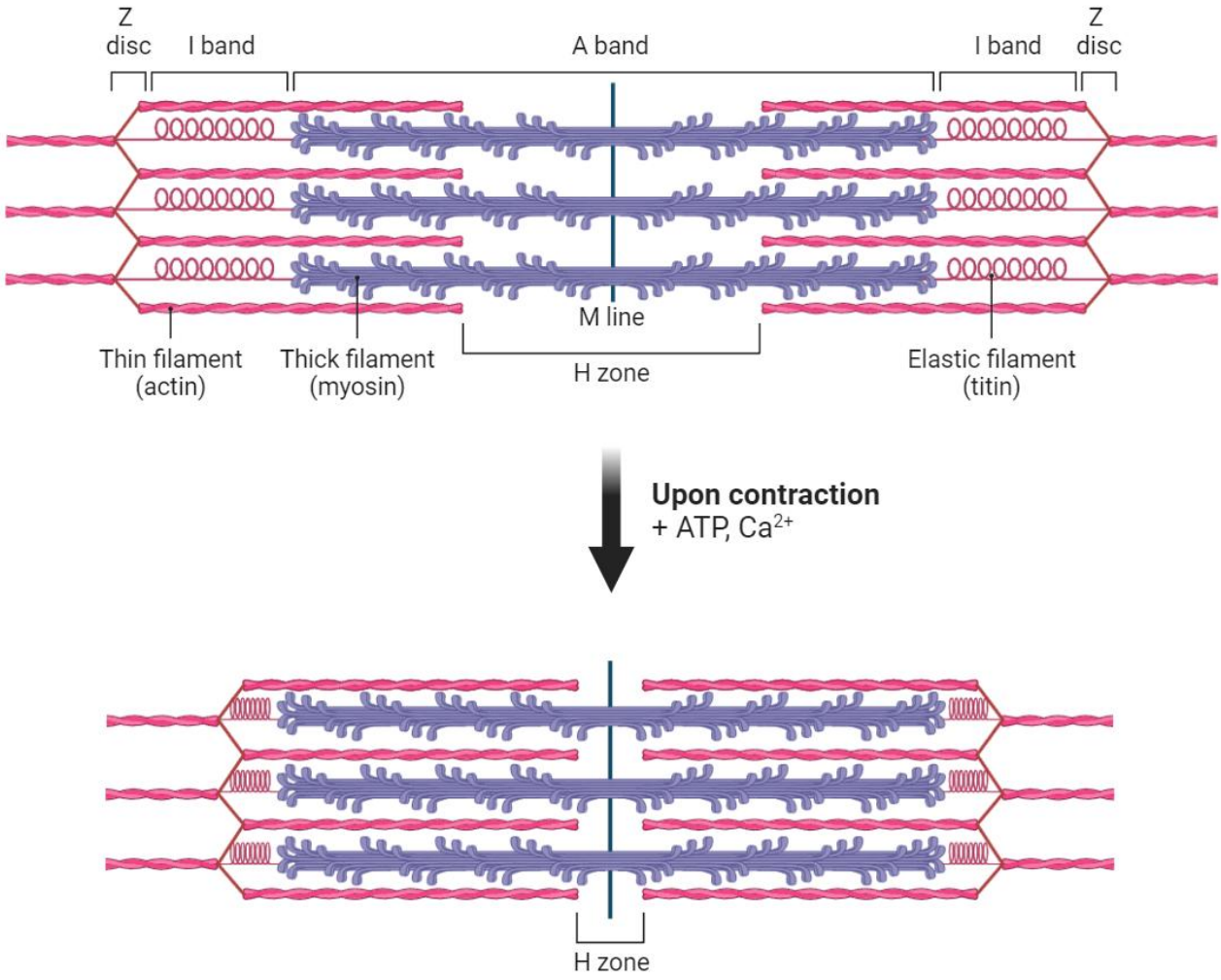


Figure 4. A structural diagram to show the changes in filament positions before and after contraction.

Sarcomere in relaxed conditions (top). Titin elastic region is stretched and thin filaments only partially overlaying the thick filament. The I-band is at maximum length. Contracted sarcomere (bottom), titin elastic region is relaxed and compressed. The thin filament is overlaying the thick filament fully with the I-band nearly gone and thin filament reaching the H-zone. Image taken from BioRender.

1.1.4. Thin Filament Proteins

1.1.4.a. Actin

Actin is a globular protein with an ATPase pocket, which is highly conserved in most eukaryotes. In vertebrates, actin is expressed in three isoforms: alpha (α), beta (β) and gamma (γ). While the alpha isoform is only expressed in muscle-actin, beta is

exclusive to non-muscle actin, and gamma can be found in both non-muscle actin and the smooth muscles (Dominguez and Holmes, 2011). Each type of muscle tissue has a separate isoform of alpha actin. Cardiac, skeletal and smooth muscle alpha actin is encoded by ACTC1, ACTA1 and ACTA2 genes, respectively (Perrin and Ervasti, 2010; Dominguez and Holmes, 2011). Non-muscle actin isoforms are mostly used in cytoskeleton for intracellular movement.

Muscle globular (G)-actin is a ~ 42 kDa protein with 67 x 40 x 37 Å dimensions, established using scanning electron microscopy (SEM) (Elzinga *et al.*, 1973; Elzinga and Collins, 1975). G-actin can be polymerised into filamentous (F) actin using ATP and associate proteins to either inhibit or enhance the polymerisation (β-thymosin and profilin, respectively). β-Thymosins are small (~5 kDa) peptides that can sequester G-actin at both ends to prevent them forming or incorporating into the existing F-actin (Xue *et al.*, 2014). On the other hand, profilins are slightly larger (~16 kDa) and act to elongate actin filament at the barbed-end (Xue *et al.*, 2014). F-actin forms an anticlockwise, single-stranded helix with an axial rotation of 166° and axial translation of 27.5 Å (Von Der Ecken *et al.*, 2015). Normally, the helices intertwine forming a two helix strands approximately 14 G-actin monomers in length (~ 72 nm long, 7-9 nm wide) (Lodish *et al.*, 2016).

The process of F-actin assembly was first discovered by Albrecht Wegner in 1976 (Wegner, 1976) where they observed the addition and removal of radioactively labelled actin monomers. F-actin has polar ends with higher and lower affinity for G-actin molecules. Normally, G-actin molecules get added from the positive (“+” end) and removed from negative end (“-“end). However, the process of adding actin monomers is affinity-dependant and thus can occur at both ends of F-actin (dos Remedios *et al.*, 2003).

Proteins profilin (~15kDa) and cofilin (~19kDa) are involved in actin polymerisation (see Figure 5). Profilin is assisting the proliferation of actin filament, as stated above, by interacting with both ADP-G-actin and ATP-G-actin complexes. Profilin “times” (i.e. tracks the time spend by a G-actin monomer in the F-actin polymer) the hydrolysis of an ATP molecule as monomers closer to the “-“ end get released, followed by the repriming of the G-actin monomers by ADP recycling back into ATP for future addition to the “+” end. (Carlsson *et al.*, 1977). Cofilin from highly conserved and ubiquitous

ADF/cofilin family assists with the depolymerisation at the "-" end of the F-actin and reincorporation of recycled ATP-G-actin molecules into the "+" end. Further reading on ADF/cofilin family is available here (Maciver and Hussey, 2002). The process of actin polymerisation at the "+" end and depolymerisation at the "-" end is termed treadmilling.

In this thesis, actin is discussed for its role in the muscle tissue, but it is also worth mentioning that actin plays an important role in the cell cytoskeleton. Actin filaments in cytoskeleton have different roles and different associated proteins when compared to the actin filaments in muscle tissues. For example, the process of branching occurs only in cytoskeleton actin using ARP2/3 complex (Actin Related protein 2/3 complex). During this process additional branches of actin are created with a distinct 70° angle to the mother-filament (Suraneni *et al.*, 2015). Branching is involved in cell processes, including cell cycle progression regulation (Cao *et al.*, 2023).

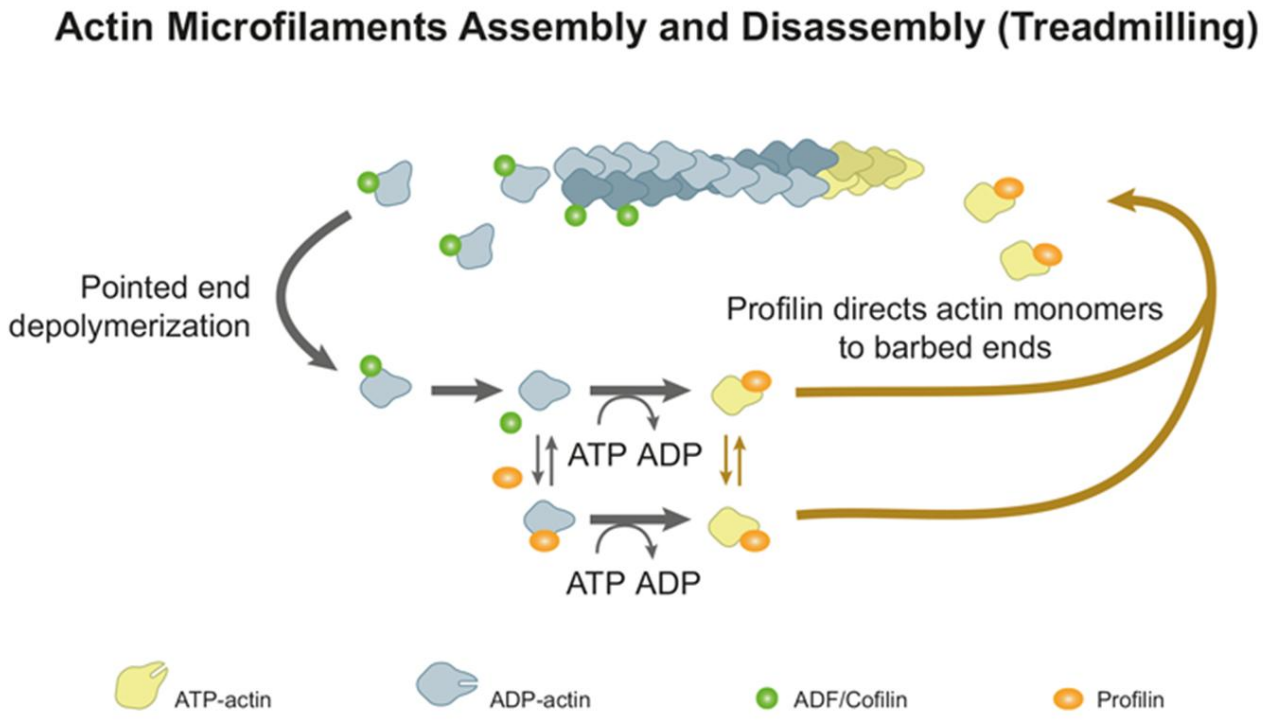


Figure 5. The process of actin treadmilling.

At the positive "+" end actin monomers (G-actin), assisted by profilin (filled, orange circles), are being assembled into filamentous (F) actin, while being simultaneously disassembled at the other end with the help of cofilin (filled, green circles). The ATP is regenerated, and accessory proteins are swapped for the process to be continued. Image taken from https://www.caltagmedsystems.co.uk/information/latrunculin-a-b-potent-actin-polymerisation-inhibitors/.

1.1.4.b. Troponin – Tropomyosin complex

Troponin-Tropomyosin complex is essential for regulating the access of myosin heads to the thin filament myosin binding sites and thus the muscle contraction. Troponin complex (~80 kDa) is comprised of three subunits; TnI (~21 kDa), TnT (~31 kDa) and TnC (~18 kDa). In troponin complex, TnC acts as a Ca^{2+}-sensitive subunit, regulating muscle contraction based on the availability of calcium ions (contractile regulation by Tn complex is described below in 1.2.2.a). Troponin was first discovered as a tropomyosin-like protein involved in muscle contraction in 1964 (Ebashi and Ebashi, 1964), with consequent x-ray crystal structural data published showing a Ca^{2+} -sensitive subunit in 1973 (Kretsinger and Nockolds, 1973). The x-ray crystal structure of cardiac TnC was shown later by a landmark Takeda paper in 2003 (Takeda *et al.*, 2003). In this paper, they describe the iconic “L” shape of the Tn complex, with different regions connected by flexible linkers. They have also identified other regions of interest; IT arm, connecting TnT and TnI, regulatory head, the N-terminal of TnC and C-terminal of TnI with the link peptide located between them. Later studies have identified the difference between cardiac and skeletal isoforms of Tn (Vinogradova *et al.*, 2005). Comparing cardiac (c)TnC to skeletal (s)TnC has shown a sTnC to be shorter at the N-terminal by 30 amino acids (Marston and Zamora, 2020). Cardiac TnC was shown to comprise of four Ca^{2+}-sensitive EF-hands, with short, anti-parallel β-sheet between them. The effects of Ca^{2+} binding to the N-terminus EF-hands (low-affinity, $Ka \approx 10^5\ M^{-1}$) were later recognised as “catalytic” or ”structural”, leading to the “closed” or Ca^{2+}-bound state of tropomyosin. The C-terminus EF-hands (high-affinity, $Ka \approx 10^7\ M^{-1}$) are known as only “structural”; they are always occupied by Ca^{2+} in physiological conditions. High-affinity EF-hands can also bind other cations, such as Mg^{2+} and Cd^{2+} (Li and Hwang, 2015; Marston and Zamora, 2020).

TnI is comprised of four α-helical domains; the N-terminal domain (only in cardiac), the IT rigid arm, the inhibitory peptide, the switch peptide and the C-terminus domain (Marston and Zamora, 2020).

TnT can be divided into three domains: N-terminal, linking, and C-terminal domains. C-terminal domains is the only troponin domain that is localised to the troponin complex, with the others associated with both troponin and tropomyosin. TnT segment

- TnT1 is an extended structure parallel to Tm, and was positionally and orientationally resolved using x-ray diffraction in 1997 (Cabral-Lilly *et al.*, 1997), consisting of an alpha-helix and binding Tm. The likely role of TnT1 is stabilisation of the overlapping regions between two Tm molecules (Palm *et al.*, 2001; Murakami *et al.*, 2008). TnT2 region is believed to be essential to stabilising the placement of Tn on the thin filament (Marston and Zamora, 2020). Both the linker and TnT1 region were not resolved but instead modelled, thus maintaining some structures yet to be discovered (Manning, Tardiff and Schwartz, 2012).

Tropomyosin encompasses the whole length of the thin filament and consists of homomeric parallel coiled-coils. Each homodimer is associated with one troponin complex and seven actin monomers. In the “blocked” state tropomyosin lays over myosin binding sites and blocking them, but can shift to the “closed” position, where upon Ca^{2+} binding to TnC complex, and subsequent shifting of Tm, myosin binding sites are exposed for weak-binding of myosin heads. Upon binding of myosins to actin, Tm is pushed further away from myosin binding sites into “open” state, allowing myosins to strongly bind to actin and thus allowing for contraction (Li and Hwang, 2015).

The earlier view of the Tn/Tm regulatory system was simple. TnT was thought to bind tropomyosin, thus regulating the interaction of troponin complex with tropomyosin. TnI was thought to be a go-between for TnT and TnC, transferring the conformational change initiated by the binding of calcium ions on TnC through to TnT (Gomes, Potter and Szczesna-Cordary, 2002) (see Figure 6). However, more recent cryo-EM (cryogenic electron microscopy) studies (Oda, Yanagisawa and Wakabayashi, 2020; Yamada, Namba and Fujii, 2020; Risi *et al.*, 2021) and an independent *in silico* study (Pavadai *et al.*, 2020), have provided some additional insight into both Tn and Tm. In 2020 Yamada and colleagues have presented a first-in-kind cryo-EM structure using nonhelical algorithm for thin filament reconstruction. In their work, they have shown the first ever structural transition of regulatory units of the thin filament from Ca^{2+}-bound to Ca^{2+}-free conformation at 6.6 Å. In their study Yamada et al. have revealed multiple important mechanisms that were debated (and sometimes predicted) in previous studies, addressing Ca^{2+} activation of the thin filament. A good review article summarising the revolutionary work using Cryo-EM techniques, showing a clearer positions of all changes and thin filament subunits is available here (Tobacman, 2021).

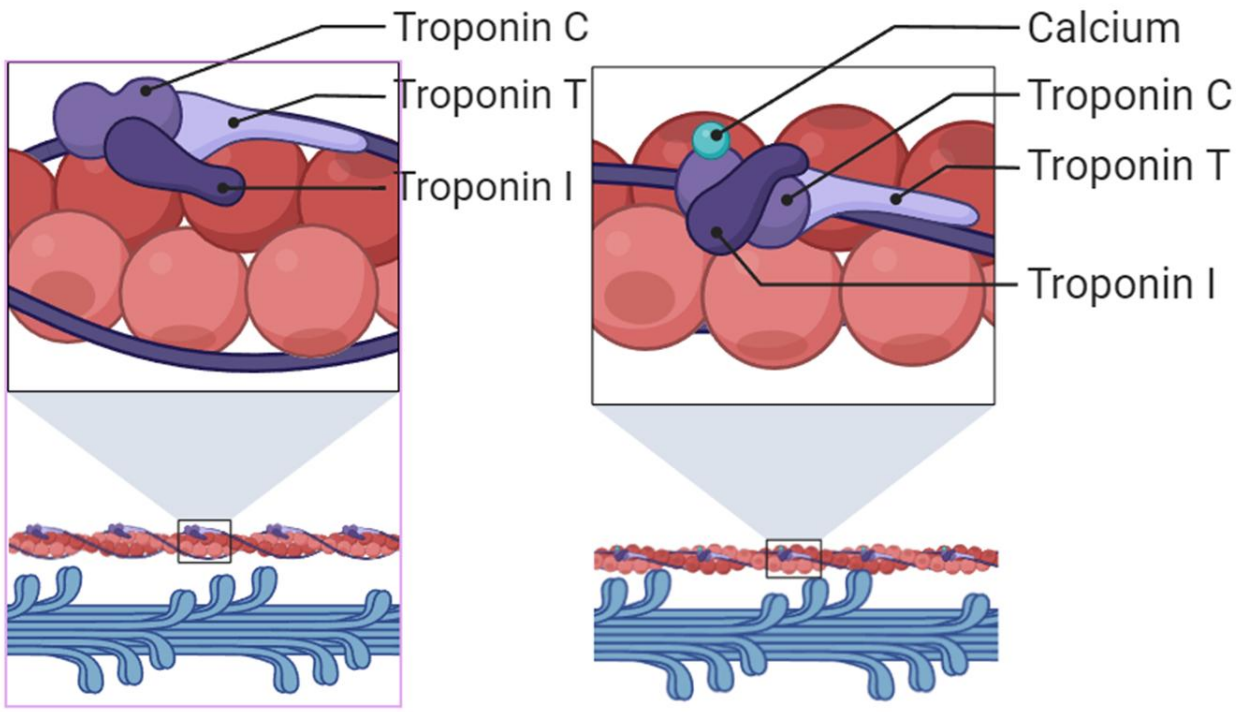


Figure 6. Diagram showing the effects Ca^{2+} binding to TnC.

A schematic representation of troponin-tropomyosin complex on the thin filament in a relaxed muscle (left), showing tropomyosin (dark blue line) covering myosin binding cites (dark circles) on actin filament (red and light red spheres). Troponin subunits are labelled appropriately. Troponin-tropomyosin complex in Ca^{2+}-bound (cyan sphere) state in an active muscle. Tropomyosin has shifted away from myosin binding sites, which are available for binding and the following contraction. Image was made using BioRender.

In their work Yamada and colleagues have shown the position of two Tn complexes on the either strand of an actin helix. They have noted the different sizes of those complexes and thus indicate them Tn1 and Tn2 (see Figure 7). The larger Tn complex spans 7 actin monomers, while Tn2 spans 6. Another difference between Tn1 and Tn2 was present at the linker that connect Tn-core to TnT at the Tm overlapping region (see Figure 7), with Tn1 having a larger linker than Tn2. Earlier experiments have shown the importance of pseudorepeats 3 and 4 of Tm helices and positions of Tn1 and Tn2 on them. These studies have found that upon deletion of pseudorepeats 3 and 4 calcium activation had no effect on the thin filament (Landis et al., 1999; Lu, Tobacman and Kawai, 2003), while deletion of the 4th pseudorepeat resulted in a 60% reduction in activation sensitivity (Hitchcock-DeGregori, Song and Greenfield, 2002). Comparing Ca2+-free and Ca2+-bound states Yamada and colleagues have observed the most prominent changes at the C-terminus of the TnI where it folded away from Tm N-terminus and onto TnC N-lobe region. Additionally, they have measured the IT

region of Tn core domain rotation of ~30° (see Figure 8), which does not appear to have a clear cause yet (Tobacman, 2021). The IT region of the Tn core domain consists of 46 residues of TnI-TnT and the TnC C-lobe, with TnI helix 1 closely attached. Additionally, non-core TnC domain is visibly interacting with TnI, Tm and Actin when Ca^{2+} is bound. Interestingly, a classically inhibitory (Talbot and Hodges, 1981) region of TnI (residues 137-147), which is also a cardiomyopathy site (Kobayashi, Patrick and Kobayashi, 2009; Kozaili, Leek and Tobacman, 2010) does not move during Ca^{2+}-activation (Tobacman, 2021).

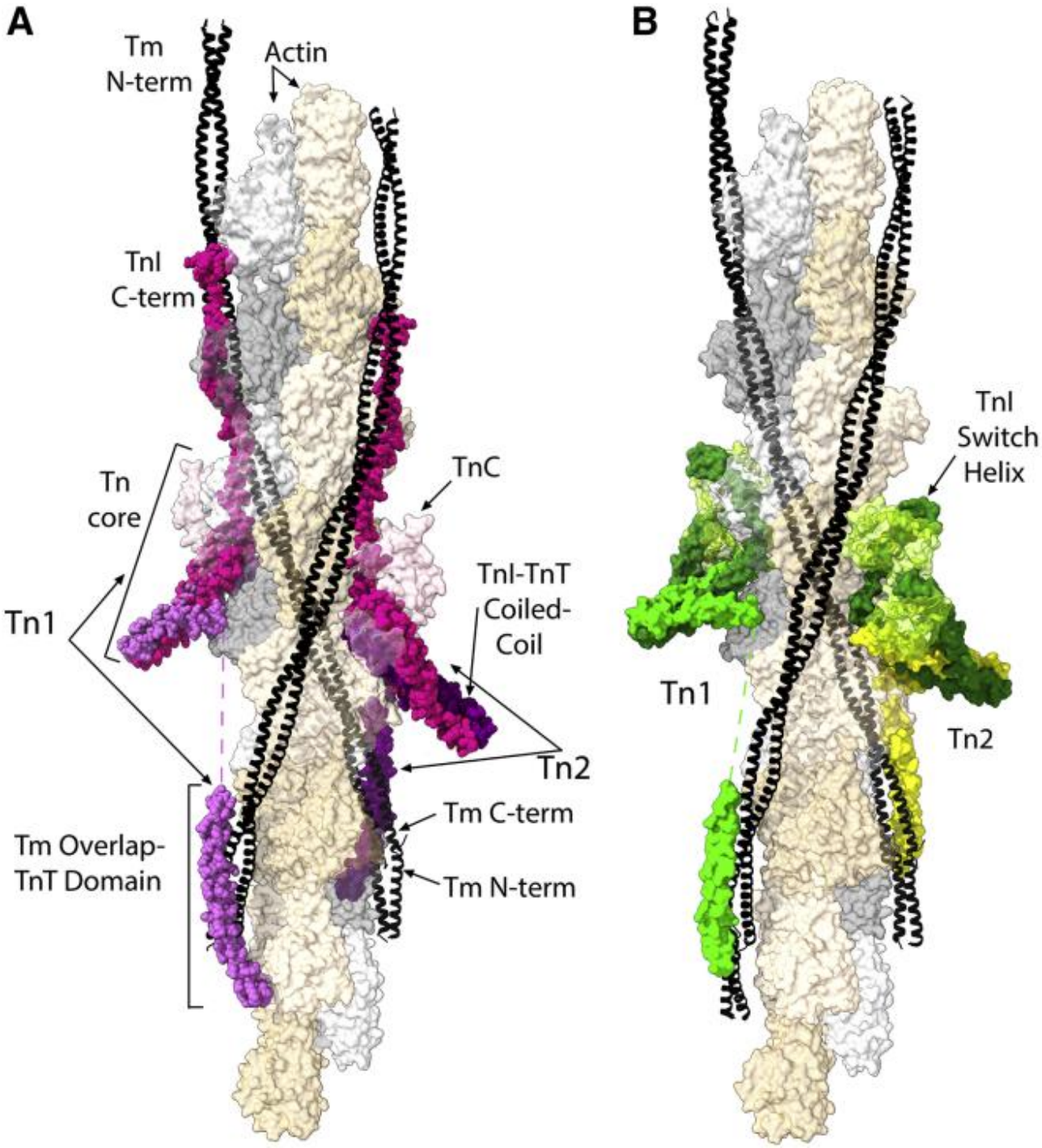


Figure 7. Reconstructed images of the thin filament in Ca^{2+}-free (A) and Ca^{2+}-bound (B) conformations.

Actin is shown semi-transparent in grey and brown for clarity. Tropomyosin (black) is shown spanning both strands of actin helix. Tn complexes (purples (A) and greens (B)) are shown for both strands (i.e. Tn1 and Tn2). Tn complex is broken down into components via colour. TnI (magenta, dark green) C-terminus is extending towards the N-terminus of the Tm molecule, with TnC (pale pink, lime) moving closer towards the backbone of the thin filament as calcium changes its conformation. The large distance to the Tm/TnT (pink, acid green) overlap domain at Tn1 when compared to Tn2 are shown. Image taken from (Tobacman, 2021).

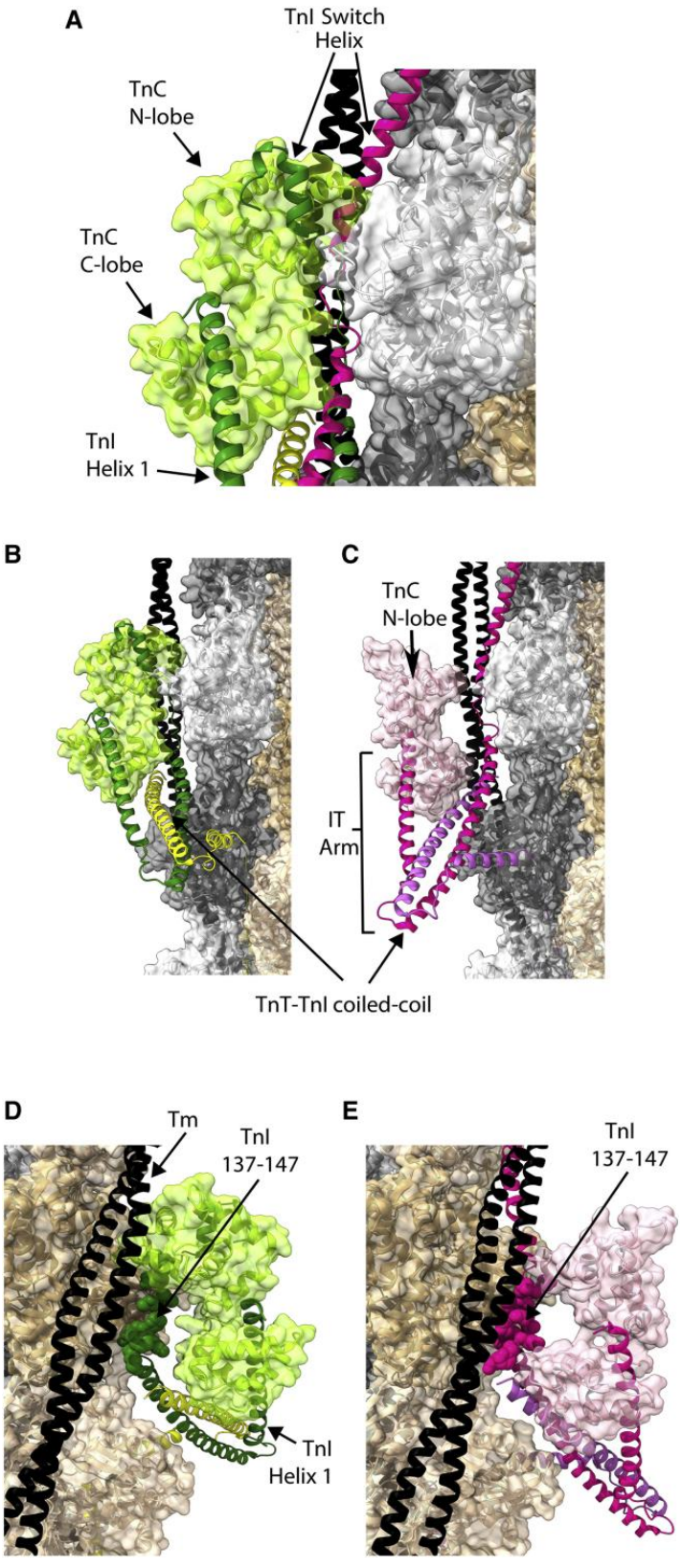


Figure 8. A reconstruction of the core region of troponin complex in calcium bound and free states.

A) Showing the difference between calcium-free (pink) and calcium bound (green) states of the TnI switch helix that swings back onto the TnC N-lobe upon calcium bounding. B & C) States of the Tn core module with (green) and without (pink) calcium showing the IT arm movement upon conformational change. D & E) Absence of movement from the inhibitory region of TnI (residues 137-147) region of the Tn core upon the conformation change. Image taken from (Tobacman, 2021).

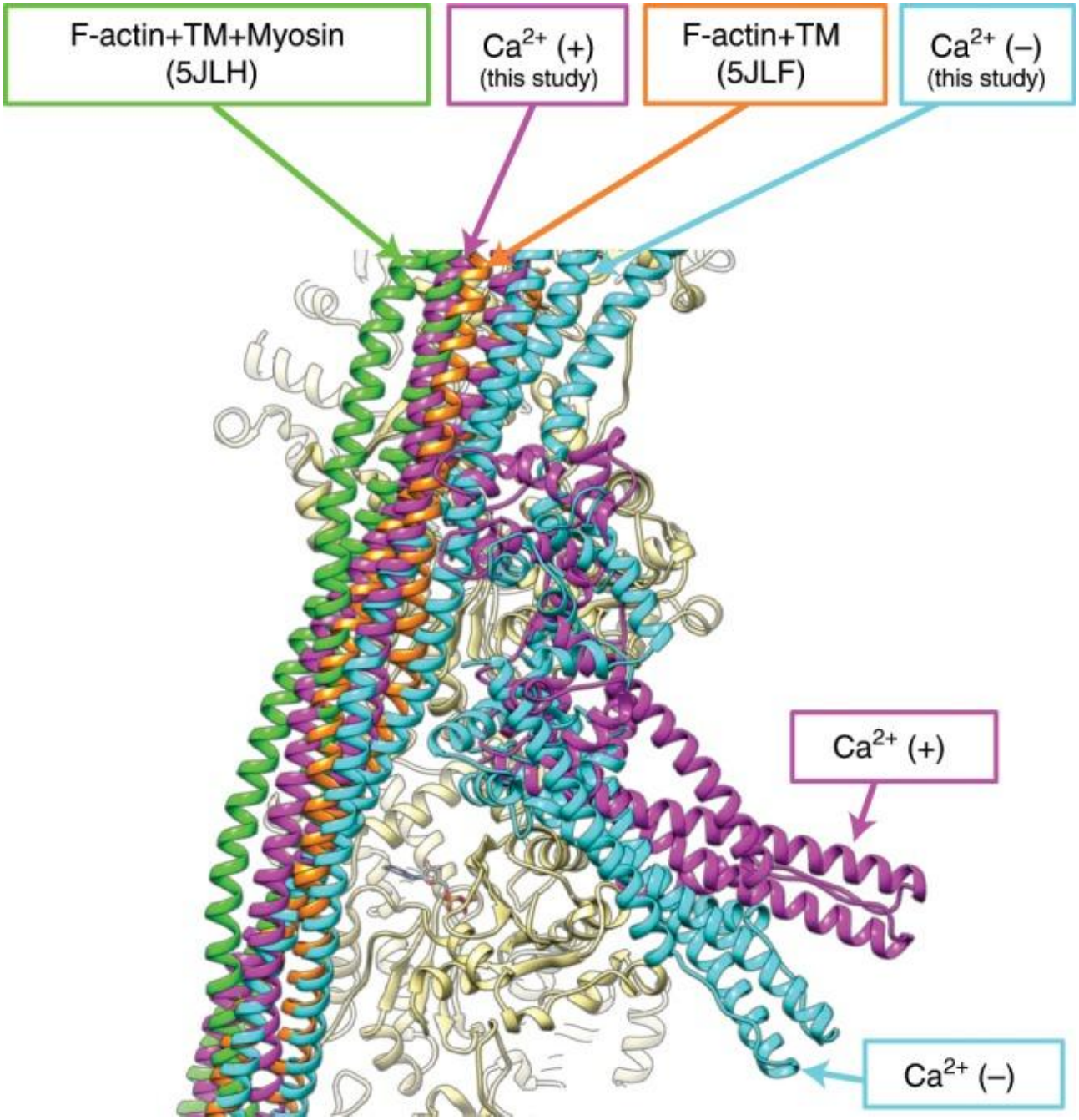


Figure 9. A reconstruction of tropomyosin positions during calcium free, bound and myosin + calcium bound states.

Structures shown in magenta and cyan were observed during Yamada study, with tropomyosin rotating away from myosin binding sites. Another study (5JLH, (von der Ecken et al., 2016)) placing the location of tropomyosin upon binding myosin in an calcium-bound (green) and -free (orange) states. Image taken from (Yamada, Namba and Fujii, 2020)

Cryo-EM studies mentioned above also addressed the movement of Tm upon calcium activation. They have noticed that Tm was not shifted, like previously thought but rather rotated away from myosin-binding sites upon calcium activation (Oda, Yanagisawa and Wakabayashi, 2020; Yamada, Namba and Fujii, 2020; Tobacman,

2021). The rotation was not uniform, radiating from a large rotation at the Tn core towards the smaller rotation at the TnT-Tm overlap domain. The difference in rotation was estimated by an in silico study to be 0-15 and 50-60 degrees for the overlap and core regions, respectively (Pavadai et al., 2020). Tm was seen in three positions (see Figure 9); Ca2+-free, Ca2+-bound (Yamada, Namba and Fujii, 2020), and Ca2+ and myosin bound (von der Ecken et al., 2016). Upon binding of myosin heads Tm was further rotated by 15 degrees (or 1 nm).

These brilliant cryo-EM and one *in silico* study were followed by a complimentary study from Risi and colleagues (Risi *et al.*, 2021) further clarifying the changes occurring in the thin filament under more physiological conditions (including physiological calcium concentrations and experiments conducted on the native cardiac tissues). In addition to confirming results of previous studies they have demonstrated a stochastic nature of thin filament activation by calcium and the short-range cooperativity visible only on a single thin filament strand. They have further suggested that the contractions in cardiac tissues are conducted in a narrow range of calcium concentrations.

1.1.5. Thick Filament Structure

1.1.5.a. Myosin

Myosin was first discovered in 1864 by Wilhelm Kuhne, when he purified viscous protein from skeletal muscle (Kühne, 1864). Kuhne thought that myosin was involved in the tension state in muscle, which was only partially correct as myosins superfamily was later described as a large and diverse group of mechanoenzymes that were involved in actin-motility (Szent-Györgyi, 2004; Hartman and Spudich, 2012). For myosin-driven actin-motility, myosin mechanoenzymes would bind to actin at the ATP binding sites, which hydrolyse ATP while attached to actin to result in the working stroke and contraction.

Structurally, tails of myosin molecules comprise the backbone of the thick filament, with latest studies showing myosins and their tails with up to 19.3 to 23.6 Å resolution (Tamborrini *et al.*, 2023). Tamborrini and colleagues described classical 43 nm repeats of myosin crowns (see Figure 10) in mammalian striated muscles. Previously studies have reported similar 43 nm repeat crown organisation in both insects (Hu *et al.*, 2016;

Daneshparvar *et al.*, 2020) and spiders (Alamo *et al.*, 2008). Furthermore, Tamborrini and colleagues have investigated the difference in myosin tail interactions and structures for the three distinct myosin crowns. Following the investigation; crown 3 was implied to be the nucleus of the filament assembly, all crowns having different degrees of tail curvature of 3.05%, 4.44% and 2.53%, for tails from crowns 1, 2 and 3, respectively, and their different degrees of interactions with titin (Tamborrini *et al.*, 2023).

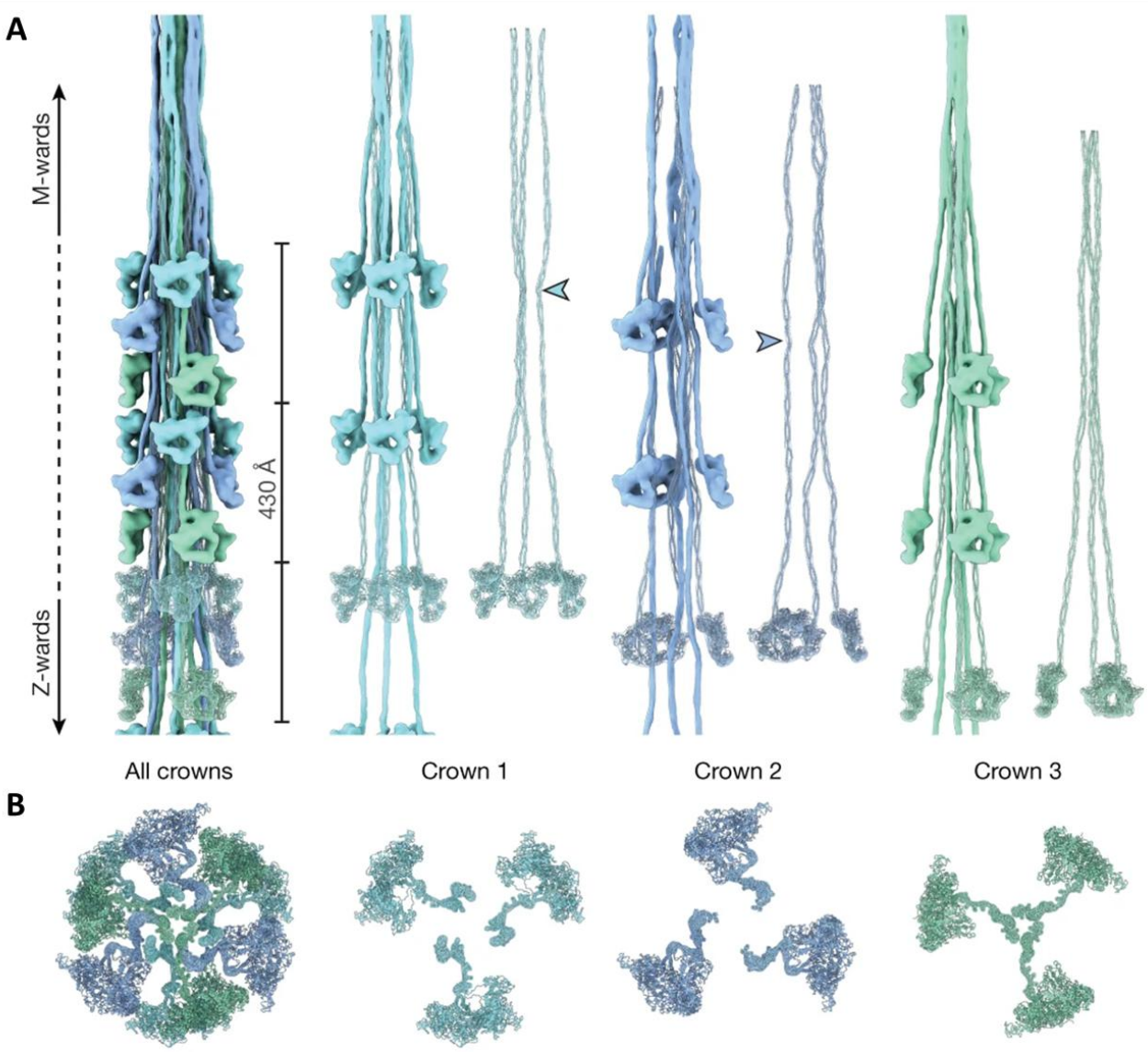


Figure 10. Side (A) and top-down (B) view of myosin molecules assembled in myosin crowns imaged and reconstructed using Cryo-EM.

Myosin crowns follow a three-fold rotational symmetry with 43 nm repeats. Myosin crowns are group into three different crows, each consisting of six myosins (2 per head), and tailing forming the backbone of the thick filament. Crown 2 tail forms the outer layer of the thick filament backbone, followed by crown 1 and 3 tails, with crown 3 tail being the closest to the centre. Arrows indicate an inflection point, common to both crown 1 and 2, with crown 3 being relatively straight. Image taken from (Tamborrini *et al.*, 2023).

Not all myosins are mechanoenzymes, as myosin is a major protein family, which has more then 40 different myosin-coding genes in the human genome alone, some of them are non-muscle myosins (Berg, Powell and Cheney, 2001). In the bounds of this thesis, the isoform of myosin that will be predominantly discussed is Myosin II, coded by MYH7 gene, as a myosin type largely present in experimentally observed sarcomeres (Lynne M. Coluccio, 2008). Myosin II is a large protein consisting of two

heavy chains (MyHC), ~ 2000 amino acids each, with the total molecular weight of ~ 440 kDa (or ~ 220 kDa for each MyHC) (see Figure 11). Each myosin heavy chain consists of; an alpha-helix coiled coil myosin tail that makes up the backbone of the thick filament, a globular motor head that hydrolyses ATP to pull the thin filament and a lever arm that is connecting the two together through isoleucine-glutamine (IQ) motif to allow for the rotational freedom required for the sliding during the contraction (Lynne M. Coluccio, 2008). IQ motif is a calmodulin (CaM) (or CaM-like proteins) mediated Ca^{2+}-binding complex (Bähler and Rhoads, 2002), which was observed to experience auto-inhibitory properties on myosin molecules (Petzhold *et al.*, 2010). Interestingly, the IQ motif was described to have two parts in tandem; IQ1 and IQ2 that bound essential light chains and regulatory light chains, respectively (Petzhold *et al.*, 2010). The inhibitory role is played by the IQ2 motif, as was shown by a significant increase in myosin ATPase activity upon IQ2 deletion (Uyeda and Spudich, 1993).

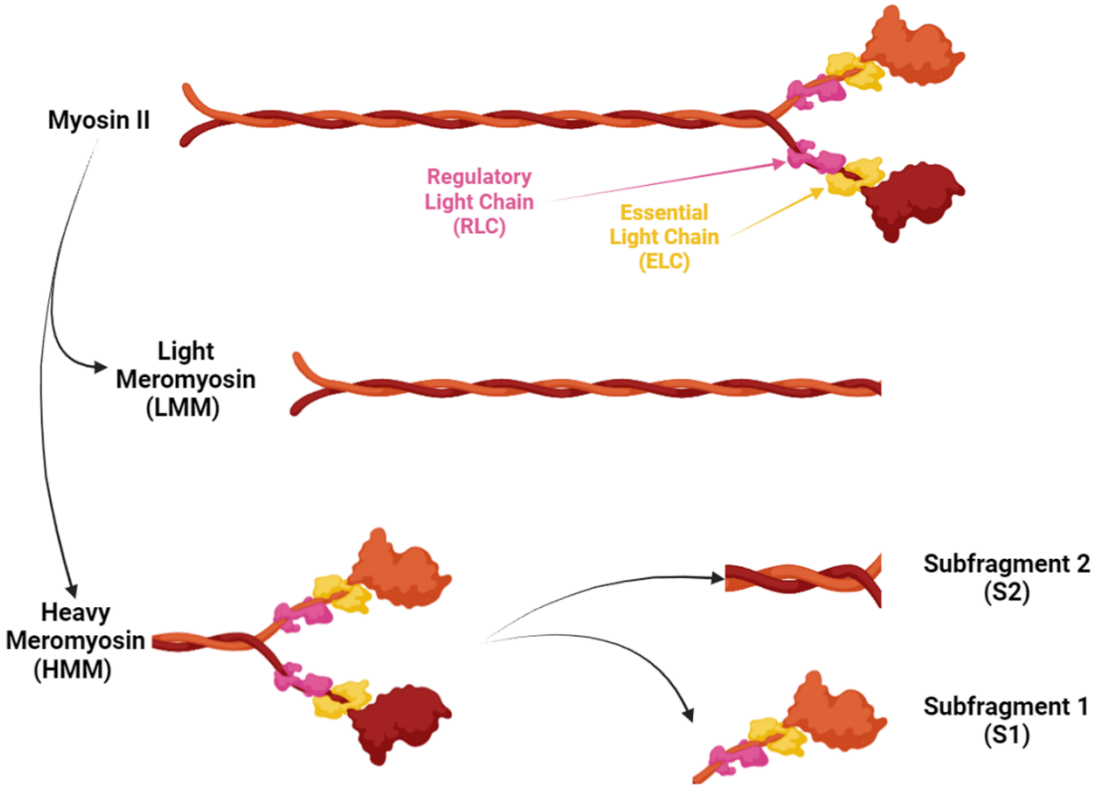


Figure 11. A schematic breakdown of myosin II molecule.

Myosin II protein (top) can be divided into light meromyosin (LMM) (middle) and heavy meromyosin (HMM) (bottom). LMM consists exclusively of two myosin tails. HMM consists of both two myosin heads and part of the myosin tail. HMM can be further subdivided into subfragment 1 (S1) and subfragment 2 (S2) separating myosin head from the tale for S1 and S2, respectively. S1 had three parts labelled on the myosin II (top) diagram; ~ 17 kDa (pink) Regulatory Light Chain (RLC), ~ 20 kDa (yellow) Essential Light Chain (ELC), and ~ 95 kDa globular head region (orange). Image compiled in BioRender.

There are multiple names for the myosin parts mentioned above, mostly coming from the early works that introduced different fragments of myosin molecule trough chemical/enzymatic digestion mostly based on their weight. In such, Light Meromyosin (LMM) (i.e. myosin tail), was obtained through a limited trypsin digestion, also yielding Heavy Meromyosin (HMM) (Kamin-Belsky *et al.*, 1996). Further digest of HMM enzymatically would yield different results depending on conditions and enzymes used (Kamin-Belsky *et al.*, 1996). Limited digestion of Myosin II with trypsin or chymotrypsin yields LMM and HMM, while further digestion of HMM yields S1 (Mueller and Perry, 1962). When digested with papain Myosin II would yield two subfragments (S1 and S2) with only one having any substantial ATPase activity (S1) (Kominz *et al.*, 1965). The difference between S1 produced during chymotrypsin and papain digestions are

in fragment size, with chymotrypsin producing slightly larger fragments and papain cutting into the RLC (Margossian, Stafford and Lowey, 1981).

Subfragment 1 (S1) of myosin head consists of three subdomains: N-terminal 25 kDa domain, central 50 kDa domain, and the C-terminal 20 kDa domain. Just like with the parts of the thick filament names for S1 subdomains came from the earlier studies with enzymes, where trypsin would cleave S1 into 3 subdomains. The original structure of the S1 was published in 1993 by (Rayment *et al.*, 1993), with structures of other myosin isoforms to follow shortly: smooth (Smith and Rayment, 1995), skeletal (Dominguez *et al.*, 1998), and non-muscle S1 (Houdusse *et al.*, 1999; Houdusse, Szent-Gyorgyi and Cohen, 2000). There are more recent articles (Auguin *et al.*, 2023; Grinzato *et al.*, 2023) exploring the structure of β-cardiac myosin S1 using novel methods (e.g. Cryo-EM), the latest structure of a pre-powerstroke S1, in complex with MAVA, is available with 2.61 Å resolution at the protein data bank (PDB) from Auguin and colleagues (Auguin *et al.*, 2024). However, there is an earlier theoretical structure of β-cardiac S1 from (Colegrave and Peckham, 2014). They have used iTASSER (Roy, Kucukural and Zhang, 2010) to create a model of β-cardiac motor domain with light chains (see Figure 12) using existing partial structures. The N-terminal 25 kDa domain consists of; “SH3”-like fold, followed by six β-sheets and finishing with a conserved phosphate binding loop located at the base of the nucleotide binding pocket (Colegrave and Peckham, 2014). This domain is followed by 50 kDa domain with loop 1 acting as a junction.

50 kDa domain contains loops named Switch 1 and 2 that can be used to identify the sate of ATP binding to the ATP-binding pocket. In such, when ATP molecule is bound by the myosin head Switches 1 and 2 are in close proximity, while with ADP bound in the same pocket, Switches are far apart. This conformational change is transferred to the rest of the molecule, thus creating an identification system for ATP binding. It has been suggested that Loop 1 has some role in modulating the ATPase kinetics of the myosin motor, specifically the release of ADP from the ATP binding pocket (Uyeda, Ruppel and Spudich, 1994). There is a separation in 50 kDa subdomain that is attributed to the actin binding faculties localised to the respective domain. In such, lower 50 kDa subdomain contains the majority of actin binding sites, while the upper 50 kDa subdomain contains only some actin binding sites (Colegrave and Peckham, 2014). In fact, an interesting study looking at early Cryo-EM structures of actin-

tropomyosin-myosin complex identified multiple actin binding sites in both lower (L50) and upper 50 (U50) kDa subdomain (Behrmann *et al.*, 2012). Behrmann and colleagues found that as a consequences of U50 domain parts (Loop 2, the Cardiomyopathy loop (CM), and the HW Helix) interactions with Subdomains 1 and 3 of actin, and L50 domain pars (Loop 3) interaction with Subdomain 1 of the neighbouring actin, the cleft between upper and lower parts of the 50 kDa subdomain have closed. Furthermore, a separate role is reserved to helix-loop-helix of L50 domain, as it was observed to interact with both Subdomains 1 and 3 of actin, while also interacting with Subdomain 2 of the neighbouring actin (Behrmann *et al.*, 2012).

Lastly, there is a C-terminus 20 kDa subdomain. The N-terminus of this subdomain is formed by a relay helix (long α-helix) that interacts with both β-sheets found in the first 25 kDa region and actin interacting region of the lower 50 kDa subdomain (Colegrave and Peckham, 2014). Following are the converter domain and the pliant region, which finishes in another long α-helix to which light chains are bound. There are numerous isoforms of myosin that are adapted to specific purposes, with some of them changing their Loop and surface domain compositions to better suit their needs (Onishi, Mikhailenko and Morales, 2006).

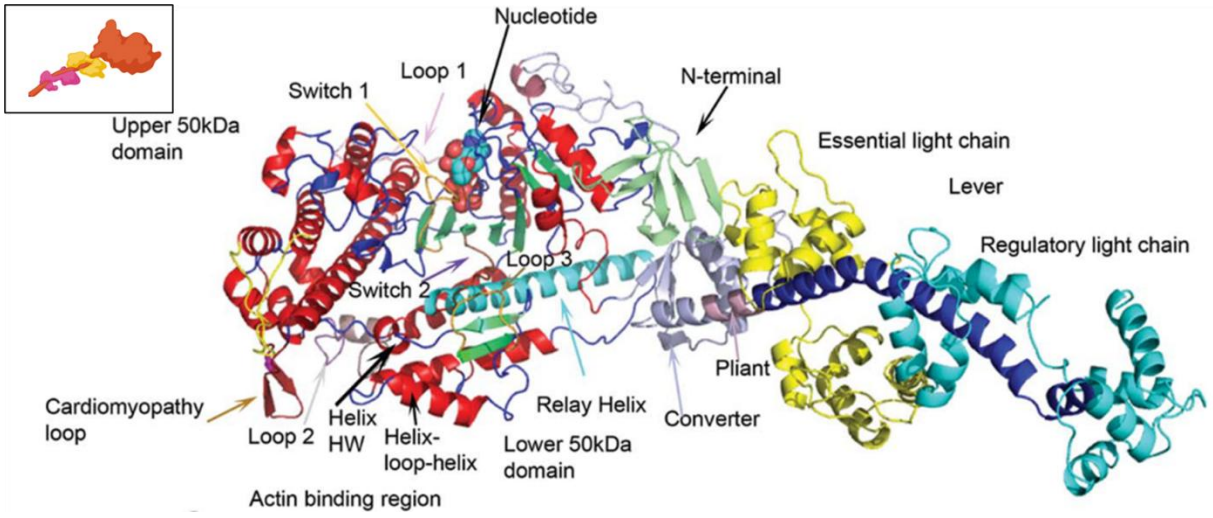


Figure 12. Structural reconstruction of β-cardiac myosin S1 fragment.

Image is showing different subdomains of the Subfragment 1 (S1) of myosin 2 motor. Starting with a N-terminus 25 kDa subdomain, though both lower and upper 50 kDa subdomain, and finally finishing with C-terminus 20 kDa domain and the light chains. Key Loops and essential regions of interest are labelled (see main text for more details). Image taken from (Colegrave and Peckham, 2014).

1.1.5.b. Myosin Binding Protein C

Myosin Binding Protein C (MyBP-C) is a sarcomeric accessory protein that was first discovered as a contaminant from skeletal muscle protein purification in 1971 (Starr and Offer, 1971). Myosin Binding Protein C is a large (120-140 kDa, ~40 nm length, 3nm width) protein localised to the A-band of the thick filament (see Figure 14A) (Hartzell and Sale, 1985; Gautel *et al.*, 1995; Yasuda *et al.*, 1995). MyBP-C isoforms (that are also paralogs (Heling, Geeves and Kad, 2020)) are coded by different genes localised to different chromosomes (see Figure 13); fast skeletal (fs) is coded by MYBPC2 gene on chromosome 19, slow skeletal (ss) coded by MYBPC1 localised to chromosome 12, and cardiac (c)MyBP-C isoform coded by MYBPC3 gene on chromosome 11. Different isoforms were discovered separately, with both skeletal isoforms discovered before cMyBP-C (Hartzell and Titus, 1982; Yamamoto and Moos, 1983). Genetically, all isoforms have similar primary structure with cardiac sharing 54.4 % and 52.4 % of its sequence with fast skeletal (Weber *et al.*, 1993) and slow skeletal (Yasuda *et al.*, 1995), respectively. The two skeletal isoforms are similar in structure; they consist of eight immunoglobulin (Ig) and three fibronectin-III (Fn3) domains (Wang *et al.*, 2018), named C1-C10 (Heling, Geeves and Kad, 2020). There is an additional M-domain (or motif) connecting C1 to C2 domains and a proline-alanine rich region superseding the C1 domain at the N-terminus. cMyBP-C isoforms differ is size (see Figure 13) from two skeletal isoforms, with cardiac isoforms having an additional Ig domain C0 at the N-terminus, 4 phosphorylatable serine residues in the M-domain (Yasuda *et al.*, 1995), and finally an additional 28 amino acid loop on C5 domain (Flashman *et al.*, 2004). The 4 phosphorylation sites at the M-domain are localised to Ser 273, 282, 302, 307 residues (Previs *et al.*, 2016) (see Figure 14 C). The phosphorylation status of those sites defines the interactions of MyBP-C. For example, upon Protein Kinase A (PKA) phosphorylation, MyBP-C releases S2 region of myosin heavy chain, increasing myosin binding to acting thus increasing the contractile potential (McClellan, Kulikovskaya and Winegrad, 2001).

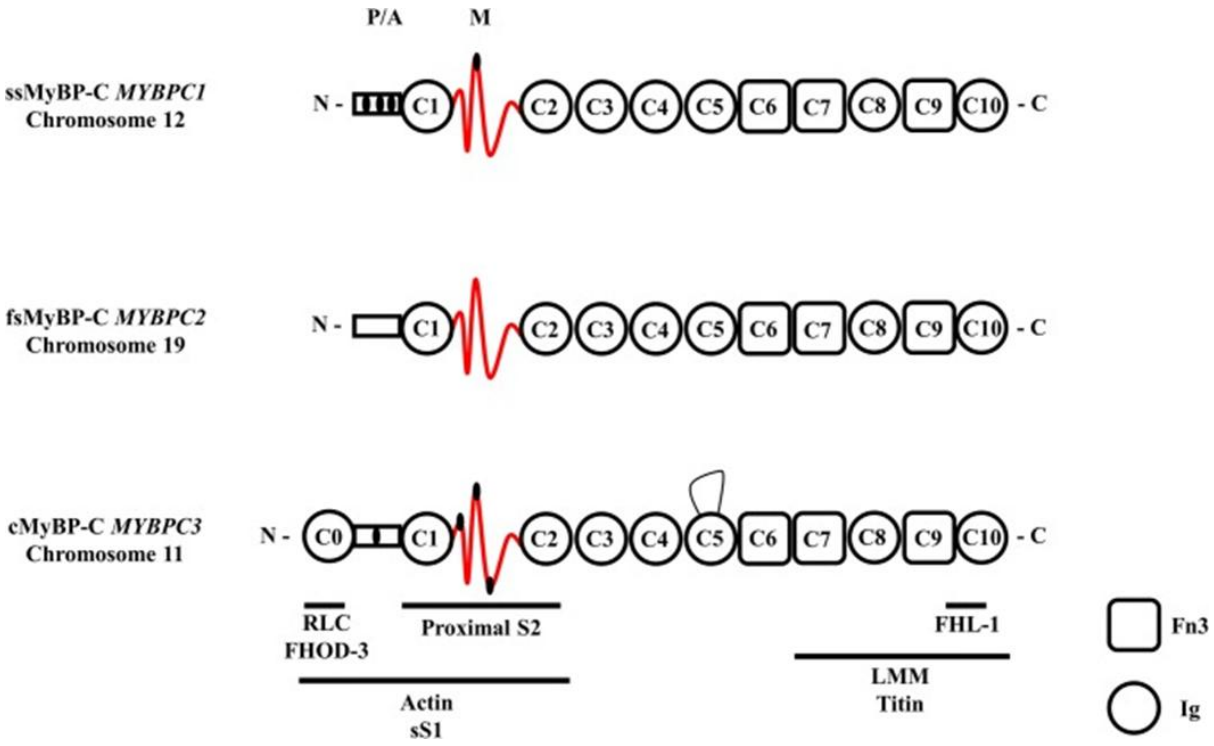


Figure 13.Domain schematics for three isoforms of Myosin Binding Protein C (MyBP-C).

The Image shows; slow skeletal, fast skeletal, and cardiac isoforms of MyBP-C. The coding genes and chromosomal positioning are displayed along with the isoforms. All MyBP-C isoforms are consistent of Fibronectin-III (Fn3, empty squares) and Immunoglobulin (Ig, empty circles) domains. There are 10 domains (C1-C10) for both skeletal isoforms and 11 (with an addition of C0) for the cardiac isoform. The M-domain (red line) connects C1 to C2. Image taken from (Heling, Geeves and Kad, 2020).

The investigation of cMyBP-C was amplified in 1995 when two studies have linked mutations is MYBPC3 gene to hypertrophic cardiomyopathy (HCM) (Bonne *et al.*, 1995; Watkins *et al.*, 1995). HCM will be discussed below in 1.3.1. The link between HCM and MYBPC3 has been investigated further in knockout mice (Harris *et al.*, 2002), where Harris and colleagues found that cMyBP-C absence did not prevent the contractions of cardiac muscle tissues in mice, but rather decrease in systolic and diastolic function, pointing to the regulatory role of cMyBP-C in muscle contractions. More recent investigation have provided some insight into MyBP-C interacting with both thick and thin filaments (Heling, Geeves and Kad, 2020).

Recent studies mapping the C-zone of the A-band by matching MyBP-C stripes to titin's super-repeats, thus providing the positions of the MyBP-C repeats on the thick filament with the total of 9 repeats (earlier study has provided 7 as a number of repeats (Craig and Offer, 1976)), each consisting of 11 domains (see Figure 14) (Tonino *et al.*, 2019; Bennett, Rees and Gautel, 2020). Originally, MyBP-C was identified and viewed

as a myosin binding protein (as the name suggests) (Craig and Offer, 1976), with earlier studies describing interactions between different isoforms of MyBP-C and S2 (Gruen and Gautel, 1999; Kunst *et al.*, 2000; Harris *et al.*, 2004). Later studies have showed a further MyBP-C C7-C10 regions interactions with both S2 and titin (Tonino *et al.*, 2019), with some authors suggesting correlation between MyBP-C localisation to the C-zone and titin super-repeat placements (Heling, Geeves and Kad, 2020). Similarly, the N-terminus of cMyBP-C was shown to interact with the thick filament: C0 interactions with myosin (Ratti *et al.*, 2011), C1 interaction with myosin (Ababou *et al.*, 2008), and C1-C2 interaction with S2 though a cAPK-phosphorylation (Gruen, Prinz and Gautel, 1999).

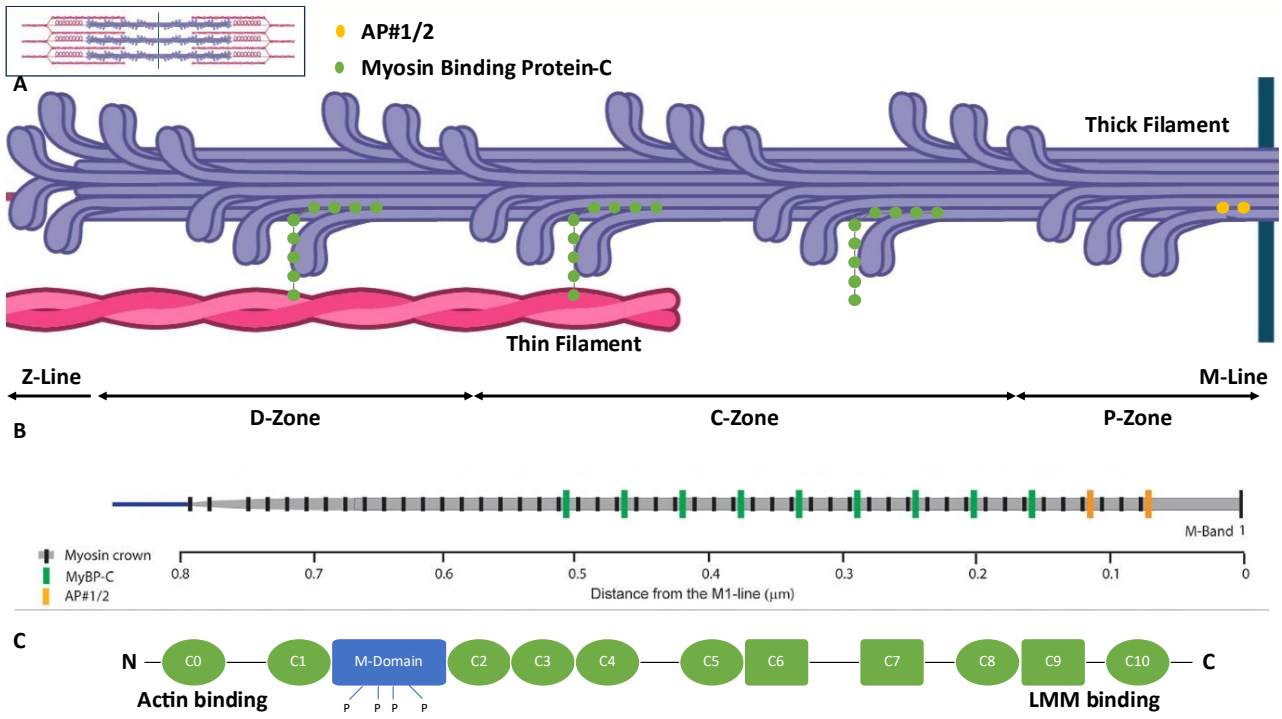


Figure 14. The position and structure of MyBP-C.

A) A diagram indicating the localisation of MyBP-C to the C-zone of the A-band. Nine subunits of MyBP-C are shown in green, two subunits of other myosin-binding protein (AP#1-2) are shown in yellow. B) The position of MyBP-C in respect to the M-line, mapped using titin (Bennett, Rees and Gautel, 2020). The repeats are starting after 6th myosin crown and end before the 30th. AP#1/2 subunits are localised from the bare zone to the 6th myosin crown. C) Eleven subunits of MyBP-C. The N-terminus was shown to interact with the actin on the thin filament and with the S2, while the C-terminus was shown to interact with LMM and titin. Green circles are Ig like domains, while green squares are fibonedian 3 domains. The blue rectangle is M-domain, where 4 phosphorylation sites at Ser 273, 282, 302, 307 are located (Previs et al., 2016).

Interactions of MyBP-C and actin (Moos *et al.*, 1978) were described shortly after its position and myosin binding properties were described in 1976 (Craig and Offer, 1976). Since then numerous studies were conducted to investigate the effects of MyBP-C N-terminus interacting with the thin filament, including multiple works (Razumova *et al.*, 2006; Saber *et al.*, 2008; Previs *et al.*, 2012; Belknap, Harris and White, 2014; Mun *et al.*, 2014) that showed either an increase (at low Ca^{2+} concentration) or decrease (at high Ca^{2+} concentration) in Ca^{2+} sensitivity of the thin filament. According to this model, at low calcium concentration cMyBP-C pushes tropomyosin into the “closed” position, thus allowing for easier myosin attachments (Craig *et al.*, 2014; Mun *et al.*, 2014; Walcott, Docken and Harris, 2015), and competes or block myosin head interaction with myosin binding sites on the thin filament. However, it is essential to note that investigations into thin filament interactions with the N-terminus of MyBP-C is still ongoing, with extra interactions added (e.g. M-domain with the thin filament (Risi *et al.*, 2022)) or more fragment-specific interactions clarified (e.g. only full C0C3 fragments can block S1 and sensitise the thin filament (Inchingolo *et al.*, 2019)) in recent years.

The interactions described above enable MyBP-C to modulate the contractility of muscle tissue by modulating the availability of myosin binding sites on the thin filament, Ca^{2+} sensitivity, and by changing the cross-bridge kinetics on the thick filament (Stelzer, Dunning and Moss, 2006; Stelzer, Patel and Moss, 2006b). Furthermore, MyBP-C has been implicated in altering the myosin ATPase rates, pushing myosins into a more energy conserving Super Relaxed state (SRX) in favour of more active Disordered Relaxed state (DRX) (Hooijman, Stewart and Cooke, 2011; Song *et al.*, 2021; Pilagov *et al.*, 2023, 2024; Hessel *et al.*, 2024). Myosin ATPase states (SRX and DRX) will be discussed below in 1.2.2.c.

Other myosin binding proteins (AP#1/2 in Bennet et al., 2020) are much less defined in the literature when compared to MyBP-C, with some recent studies, calling it Myosin-binding protein H-like (MyBP-HL), and looking at the effects of loss of MyBP-HL in mouse atria. In this study, MyBP-C has double in abundance, following the illumination of MyBP-HL (Barefield *et al.*, 2023) suggesting complementary mechanisms of action (or protein interactions) between MyBP-HL and MyBP-C.

1.1.6. Titin

Titin is a giant protein, which in humans consists of 34 451 amino acids, it has a molecular weight of 3 816 kDa and is over 1 μm in length. Just like MyBP-C, titin consists of Ig and fibronectin-III domains (122 and 133 repeats, respectively) (Labeit and Kolmerer, 1995), but unlike MyBP-C, titin spans ½ of a sarcomere from a Z-disc to the M-line (see Figure 15). First discovered in 1954, titin is thought to contribute to muscle elasticity, when muscle would return to the original shape following the contraction (Natori, 1986). Titin was later purified (Maruyama *et al.*, 1977) and subsequently sequenced for the human genome in 2001 (Bang *et al.*, 2001). N-terminus of titin is localised to the I-band and acts as an elastic region which returns sarcomeres into the relaxed conformation following the contraction. Cardiac isoform of Titin N-terminus is composed of two immunoglobulin domains with PEVK and N2B regions (Wang *et al.*, 1991). N2B region, has been shown to be phosphorylated by Protein Kinase A (PKA). Upon phosphorylation of N2B by PKA or other kinases (like PKG), the stiffness of titin filament decreases, thus increasing the ease of contraction (Ahmed and Lindsey, 2009; Hamdani, Herwig and Linke, 2017). The C-terminus was mapped to the A-band and thought to act as a molecular ruler which is used to position proteins during myogenesis (Giganti *et al.*, 2018). Within the C-terminus are altering fibronectin type III and immunoglobulin domains, which align with 43 nm myosin axial repeats (Bennett and Gautel, 1996; Bennett, Rees and Gautel, 2020).

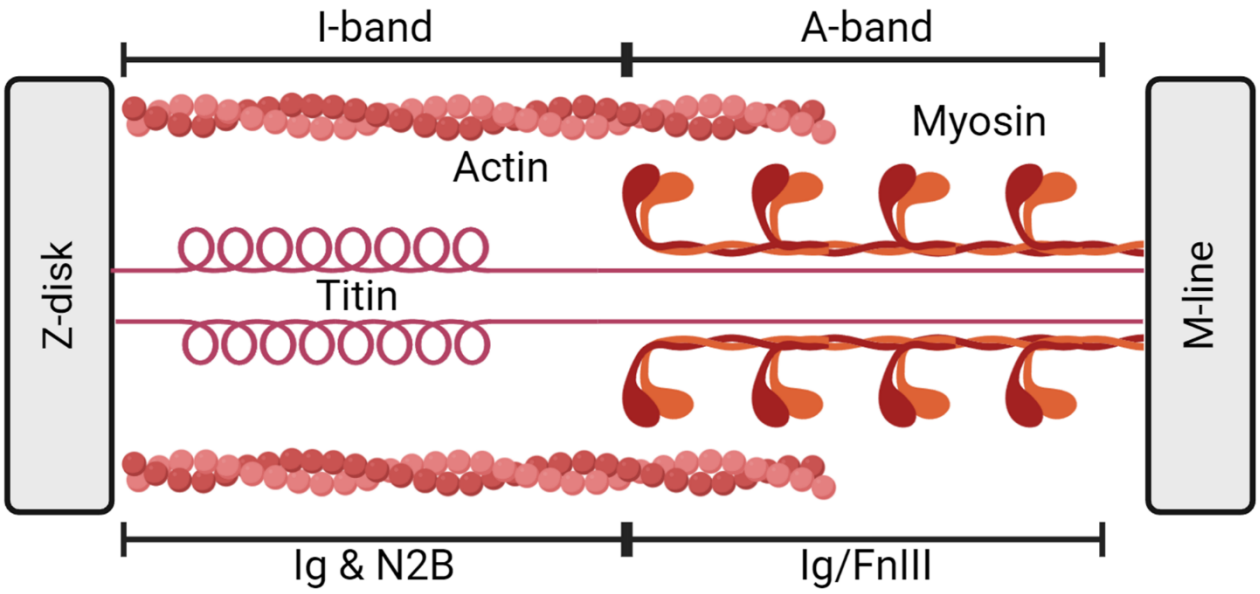


Figure 15. A structural representation of a ½ sarcomere.

Titin (pink line) is shown spanning from Z-disk to M-line. I-band (N-terminus) contains immunoglobulin (Ig) domains on titin, along with N2B region, acting as an elastic region of the sarcomere. The A-band (C-terminus) contains Ig and fibronectin-III (FnIII) domains, acting as a molecular ruler for protein mapping during myogenesis (Giganti *et al.*, 2018). *Myosin and Actin are labelled in orange/red and light/dark pink, respectively. Image made in BioRender.*

1.2. Muscle contraction

1.2.1. Cross-Bridge Cycle

The cross-bridge cycle is a series of transformations native to the myosin heads. During the cross-bridge cycle myosin heads: bind actin, preform a power stroke and return to the original position through the recovery stroke. The cross-bridge cycle was first described by H.Huxley in 1969 (Huxley, 1969), followed by an important addition on weak and strong myosin bounds states in 1971 (Lymn and Taylor, 1971), and later developed by Spudich, Holmes, Geeves and others (Spudich, 2001; Geeves and Holmes, 2005; Geeves, Fedorov and Manstein, 2005). Later myosins were classified into different groups depending on their duty ratio, thermodynamic coupling with actin/nucleotide binding strength and stain-sensitivity based on ADP release. Producing the four groups of myosin motors: fast movers, slow/efficient movers, load-bearers and gates (Bloemink and Geeves, 2011).

Cross-Bridge Cycle of myosin head (see Figure 16)**:**

1. Cross-bridge cycle begins with myosin dissociating from myosin binding site on the actin filament, following the ATP molecule attachment to the ATPase cleft on the myosin head.
2. This is followed by an ATP hydrolysis and repriming of the myosin motor through a complementary change in the converter/light-chain binding domain of the S1. This step is called the recovery stroke.
3. After the recovery stroke, myosin head's ATP cleft closes and rebind actin filament with the 50 kDa subdomain. Inorganic phosphate (Pi) is release and the power stroke (force generated by the S1 during the stroke) occurs. The exact order of cleft closure, Pi release and the power stroke occurring is still under debate (Bloemink and Geeves, 2011).
    a. When force generated by myosin heads is not large enough to move the load, no sliding of the thin filament occurs. Further power strokes are heavily inhibited. The degree of inhibition depends on the myosin isoform.
4. The thin filament slides across the thick filament towards the M-line. Provided the force generated by myosin heads attached to actin is large enough,

resulting in a thin filament is movement of 5-10 nm. This process is called the working-stroke.

5. Myosin releases hydrolysed ADP molecule from myosin ATPase cleft following the conformational change in the light chains.

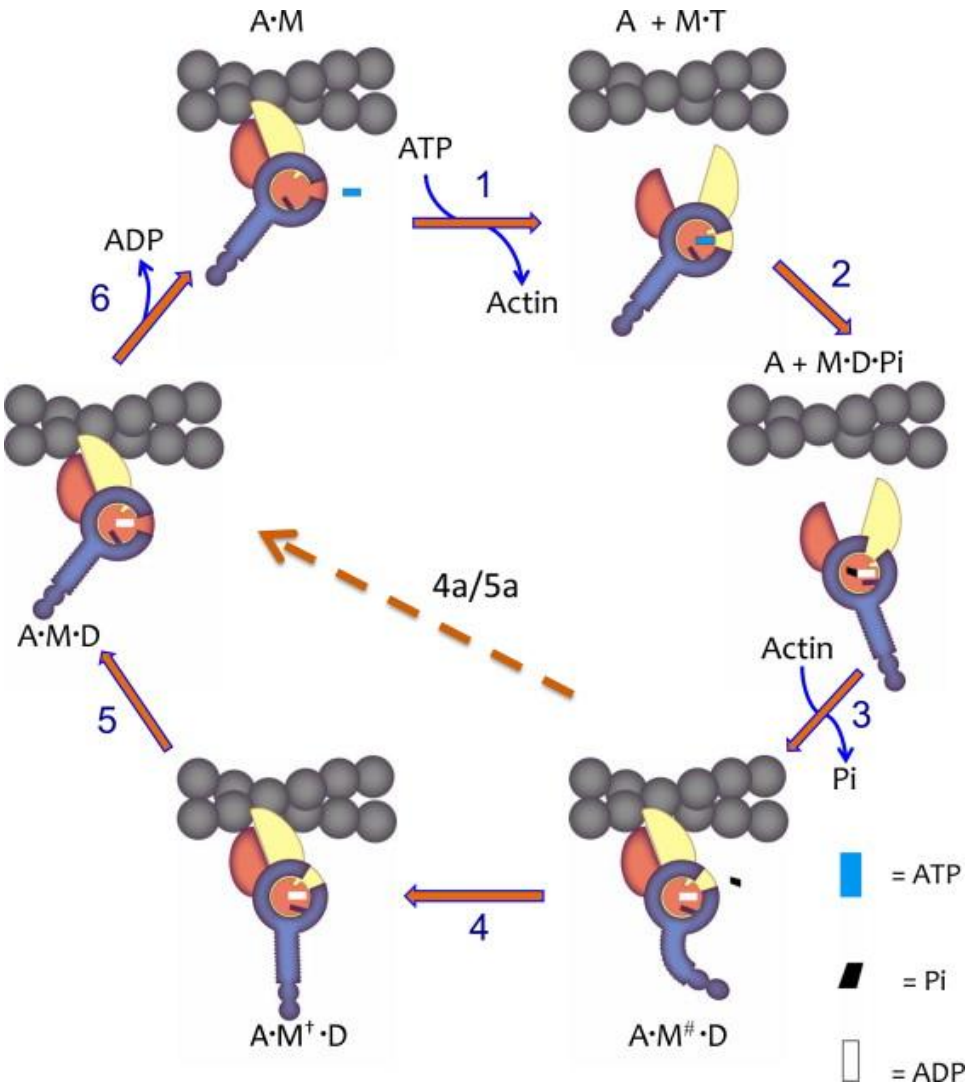


Figure 16. Structural representation of cross-bridge cycle of myosin head.

Myosin head upper domain/core (orange) and lower domain (yellow) are detached from the thin filament (grey) following the binding of an ATP molecule (blue square). This is followed by ATP hydrolysis into ADP (white square) and Pi (black square) and a repriming of the light chains/converter segment (dark blue). Pi is released from myosin ATPase cleft. Myosin head rebinds actin and preform the power stroke, if the power stroke pull is not large enough to move the load further power strokes are inhibited (4a/5a). Working stroke is preformed, sliding the actin filament across towards the M-line. Conformational change in the light chains allows ADP to leave the cleft and the motor is returned to the primary position. Image taken from (Bloemink and Geeves, 2011)

1.2.2. Dual-filament regulation

The first evidence of thick filament regulation arose when discrepancies between estimated ATP consumption (Clinch, 1968; Kushmerick and Paul, 1976) were compared to the isolated ATP consumption of myosin S1 in frog (Ferenczi *et al.*, 1978) and later rabbit muscles (Myburgh, Franks-Skiba and Cooke, 1995). The five-fold decrease in ATPase rate was the first glimpse into the accessory proteins and post-translational modifications, that allowed thick filament to regulate myosin ATPase (Irving, 2017). Further investigation by Stewart and colleagues in a landmark paper of 2010 (Stewart *et al.*, 2010), where to term “super relaxed state” (SRX) was first introduced, described the presents of the slowest ATPase rate by measuring the turnover rate of single fluorescent nucleotides, and arguing that it was related to the interactive head motif of the myosin heads.

This is a very fresh topic in our field with a lot of details still under debate. In our current understanding of dual filament regulation muscle force production is regulated on two levels: bulk activation via Ca^{2+}-sensitive thin filament (McKillop and Geeves, 1993) and fine tuning via repression states of myosin heads controlled though accessory/regulatory proteins (Irving, 2017). Furthermore, more recent studies elucidated other mechanisms of muscle activation involving dual-filament mechanosensing (Brunello *et al.*, 2023). Troponin-Tropomyosin complex, described above, controls the availability of myosin binding sites on the actin thin filament, either allowing or disallowing myosin to bind, thus being described as a general ON/OFF switch of myosin force generation. Myosin repression, on the other hand, acts to dynamically change the number of myosin heads that are ready to attach to the thin filament, thus controlling the strength of the working-stroke produced by the muscle. The topic is discussed further in the individual result chapters (i.e. Chapters 3,4 & 5).

1.2.2.a. Regulation of Muscle Contractions by the Thin Filament

Proteins involved in thin filament regulation of muscle force production are tropomyosin, troponin and actin, which exist in 1:1:7 stoichiometry. Ca^{2+} concentration is sarcoplasmic reticulum (SR) defines the ON/OFF states of the thin filament. The concentration is maintained and controlled by ATP-driven membrane pumps, located in SR. In a resting muscle, Ca^{2+} concentration is ~100 nM, with extracellular concentration in 2-4 mM range and ~0.4 mM in SR (Bootman, 2012). Ca^{2+}

concentration can reach up to ~1 μM during active contractions at 100 Hz stimulation (Fukutani *et al.*, 2024).

Removal of any essential protein (like TnC) have been shown to inhibit the force production in muscle (Moss, Giulian and Greaser, 1985). TnC acts as a ON/OFF switch upon the conformation change following the binding of Ca^{2+}. The conformational change in TnC transfers to TnI that stops its inhibition of actomyosin ATPase, and then translates into TnT that allows Tm to rotate away from myosin binding sites (full mechanism described above 1.1.4.b). TnT, acting as an intermediate between troponin and tropomyosin complexes, activates tropomyosin (~65 kDa) shifting it away from myosin binding sites on the thin filament, allowing myosin to attach to the actin filament. A more recent CryoEM, high-resolution structural study, describing the positions of troponin and tropomyosin complexes with Ca^{2+} - bound and unbound states sheds more light on conformational changes leading to tropomyosin movement (Yamada, Namba and Fujii, 2020) (see Figure 16). Yamada and colleagues were the first to show the predicted Ca^{2+} -induced (from EM structures (Lehman, Craig and Vibert, 1994; Xu *et al.*, 1999; Von Der Ecken *et al.*, 2015)) azimuthal shift in tropomyosin (of ~ 10 Å). Furthermore, they have shown a significant variation in Tm shift distance depending on the position of troponin complex, revealing a diminishing shift further away from the Tn-core.

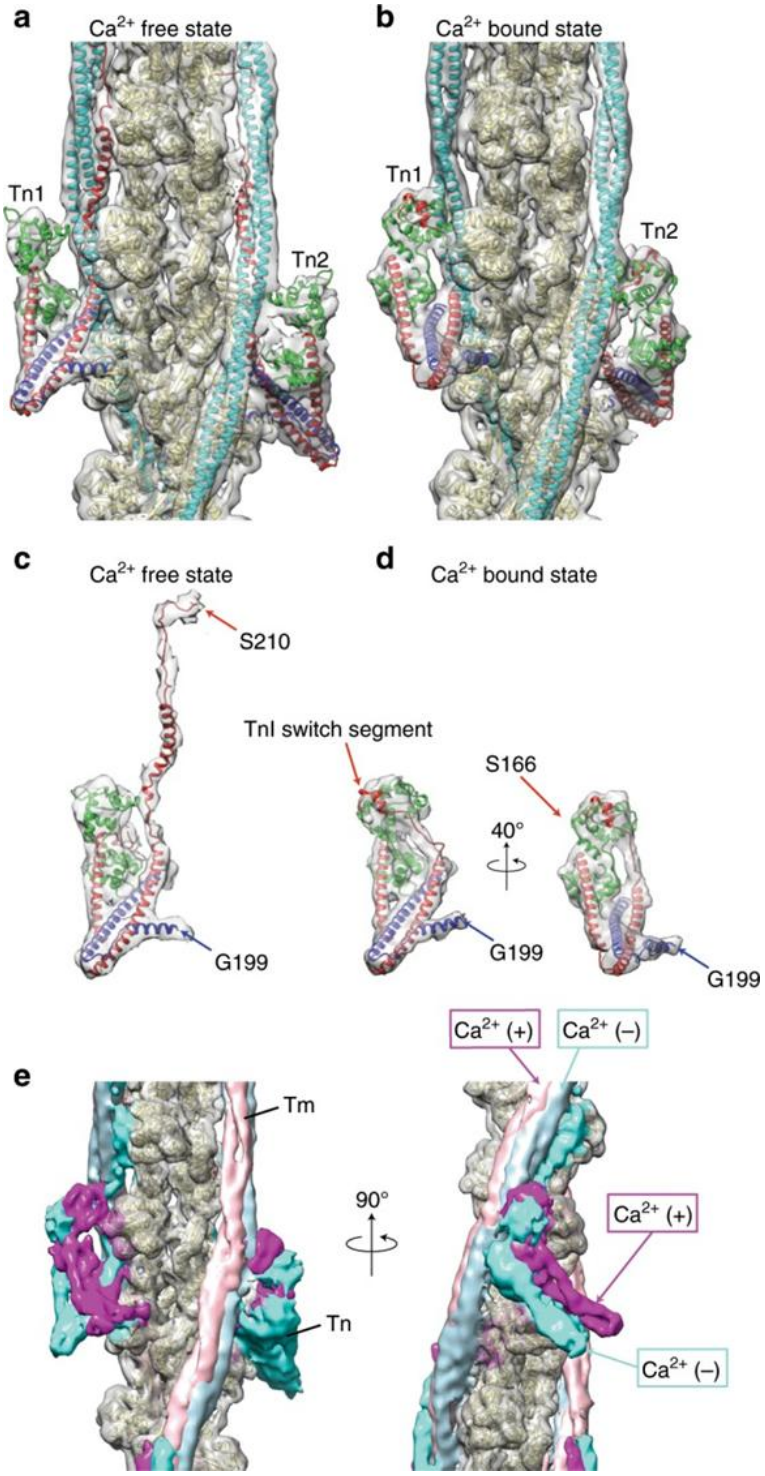


Figure 17. Conformational changes of troponin complex in a Ca^{2+} bound (a, c) and free (b, d) states.

a, b) The structural image of Tn/Tm complex as found on the thin filament. All relevant parts are labelled. c, d) Troponin complex showing the difference of Ca^{2+} free state when compared to Ca^{2+} bound state. Models are coloured as indicated: actin-beige; Tm-light blue; TnI-magenta; TnT-dark blue; and TnC-green. e) A comparative density map for both states at two angles of view on the length of the thin filament. Densities in magenta and light pink are indicating Ca^{2+} bound state for Tn and Tm, respectively. The opposing, Ca^{2+} free state is indicated by cyan and light blue for Tn and Tm, respectively. The images in taken from (Yamada, Namba and Fujii, 2020).

1.2.2.b. Myosin Cooperativity and Mechanosensing

Mechanosensing or myosin cooperativity is a process during which the attachment of myosin head to a myosin-binding site on the thin filament rescues neighbouring myosin heads from a structural OFF state, thus scaling the number of myosin heads in the ON state available for the attachment to the thin filament and thus available for the contraction (Kad *et al.*, 2005; Desai, Geeves and Kad, 2015; Linari *et al.*, 2015; Park-Holohan *et al.*, 2021; Caremani *et al.*, 2022). In earlier studies (Kad *et al.*, 2005), Kad and colleagues have used laser traps to measure motility of reconstituted thin filaments. They have found the movement to be produced in short bursts, thus necessitating incorporation "cooperativity constant" that increased the probability of subsequent myosins binding 10-fold. Complementary to the mechanism of Tm controlling the availability of myosin binding sites on the thin filament, with myosin attachment pushing Tm into the final "open" state (Desai, Geeves and Kad, 2015), the process of myosin binding to the thin filament also creates strain on the thick filament, rescuing myosins from the folded state (Park-Holohan *et al.*, 2021). Park-Holohan and colleagues describes a study where probes were placed into RLC to track its position relative to the thick filament backbone. Using these probes, rise in temperature was shown to increase the mechanosensing by lowering the activation energy of myosins in interacting head motif (IHM) (Park-Holohan *et al.*, 2021). Another recent study (Caremani *et al.*, 2022) showed similar results in soleus fibres by measuring sarcomere lengths. With increase in temperature (from 12 °C to 35 °C), the force produced by the fibre was increased at any Ca^{2+} concentration. In their study Caremani and colleagues hypotheses an existence of an intermediate state of myosin heads relative to the state of Tm molecule. From a literature overview, it is this candidate's opinion, that the process of mechanosensing has been shown to be established, yet more research is required to explain its mechanism of action.

1.2.2.c. Disordered States of Myosin Heads (SRX, DRX) and Interactive Head Motif (IHM)

The process of fine-tuning of contraction by the thick filament is a subject of discussions in the field. Myosin heads have been shown to have different conformations and kinetics depending on the force requirements of the muscle. The structural (conformational) difference of myosin heads are well-documented for both

purified myosins (Wendt *et al.*, 1999, 2001; Burgess *et al.*, 2007; Hyun *et al.*, 2008; Jung *et al.*, 2011) and isolated thick filament in striated muscles (Woodhead *et al.*, 2005; Zoghbi *et al.*, 2008). The structural change was named Interactive Head Motif (IHM). During this change myosin heads fold back onto the myosin tail, thus limiting the myosin head access to the actin binding sites (Irving and Craig, 2019). The kinetics of the "repressed" myosins were shown to have two states Disordered Relaxed and Super Relaxed, DRX and SRX, respectively. Lately, SRX and DRX are also referred to as OFF and ON states of myosin, respectively (Hessel *et al.*, 2024). With DRX hydrolysing ATP at 0.05 s^{-1} (lifetime ~20 s) and SRX at 0.005 s^{-1} (lifetime ~230 s) (Hooijman, Stewart and Cooke, 2011; McNamara *et al.*, 2014). Previously, it was thought that kinetic changes were following the structural changes of myosins, however, recent combination of small-angle x-ray diffraction and biochemical studies have shown some evidence to the contrary, separating structural from kinetic into separate processes (Ma *et al.*, 2023).

The discovery of different kinetics in myosin heads was first made in rabbit skeletal muscles, shortly followed by rabbit cardiac, tarantula smooth exoskeletal muscles, mouse skeletal and lastly human cardiac (Cooke, 2011; Hooijman, Stewart and Cooke, 2011; Wilson *et al.*, 2014; Alamo *et al.*, 2016; Anderson *et al.*, 2018). SRX and DRX exist in a constant state of equilibrium to preserve the energy required for muscle maintenance. In such, keeping myosin heads in the less-active, SRX state, saves about 1000 kCal a day (Cooke, 2011). The transition from SRX to a more active DRX is associated with the times of high-stress or excessive force demand from the muscle tissue (Linari *et al.*, 2015). Interestingly, some pharmaceutical companies are trying to develop an agent to activate repressed heads for a day-to-day usage as means to combat obesity and (as a consequence) type two diabetes (Nogara *et al.*, 2016).

The kinetics of striated muscle myosins were shown to be different in skeletal and cardiac tissues. For example, during saturations of muscle with ADP, skeletal muscles were fully activated with near-zero SRX presents, while cardiac tissue has retained some SRX (Hooijman, Stewart and Cooke, 2011). Based on the current structural understanding of cardiac and skeletal muscle isoforms (McNamara *et al.*, 2014; Pilagov *et al.*, 2023) the difference in SRX population can be attributed to the thick filament accessory proteins (e.g. MyBP-C). More specifically, isoforms of accessory proteins like MyBP-C vary from cardiac to skeletal isoforms (and even from slow to

fast twitch skeletal muscles) thus providing different regulatory functions to their respective muscle types. Myosin cooperativity can also play an important role in thick filament activation. In such, myosins would “rescue” neighbouring myosins from SRX into DRX, once attached to the thin filament (Brito *et al.*, 2011; Sulbarán *et al.*, 2013). Cooperation was shown in tarantula thick filament (Woodhead *et al.*, 2005). The latest, superb high-resolution cryo-EM study (Tamborrini *et al.*, 2023) has shown interactions of MyBP-C with both filaments, as well as different titin chain interactions with the thick filament. This study directly implicates MyBP-C in stabilising the OFF state (structural, IHM state) of myosin by using its C10 and C8 regions to interact with motor domains of free heads on crowns 3 and 1, respectively (see Figure 18). MyBP-C was also shown to interact with titin-α chain that is likely to have a role in length-dependent activation of the thick filament. Similarly, other studies (McNamara and Sadayappan, 2018; Song *et al.*, 2023) with fast skeletal isoform of MyBP-C knockout in mice showed myosin heads shifting towards the ON (DRX) state, implicating fsMyBP-C in repressing myosin heads into the OFF state and/or supressing the transition from OFF to ON state.

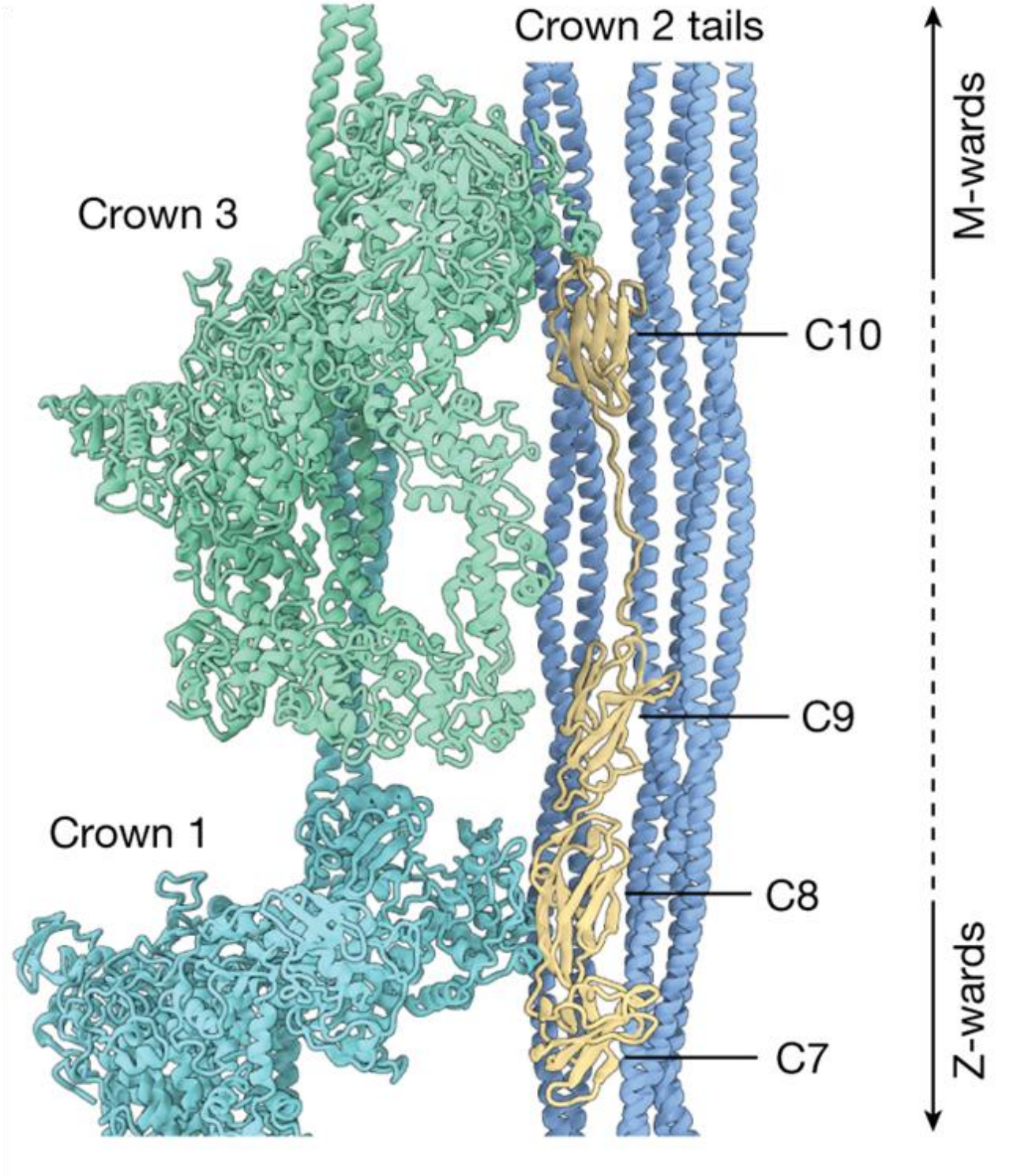


Figure 18. Figure to show regions interacting between MyBP-C and myosin crowns as described by a recent cryo-EM study.

Myosin crowns 1 and 3 (light cyan and light green, respectively) are shown interacting with MyBP-C residues (light yellow) C8 and C10, respectively. Crown 2 tails are shown in light blue. Image taken from (Tamborrini *et al.*, 2023).

In a recent study Hessel and colleagues (Hessel *et al.*, 2024) have used SNOOPC2 mouse line to observe the results of an immediate cleavage of MyBP-C C1-C7 domains. They have observed shortened thin filament following the cleavage, consistent with observations from other recent high-resolution studies (Huang *et al.*, 2023; Tamborrini *et al.*, 2023), to reduced calcium sensitivity at shorter sarcomere lengths, and most importantly shift towards the ON state for the myosin heads. Furthermore, Hessel and colleagues proposed a unifying scheme for thick filament ON-to-OFF transition that combined; the functional role of MyBP-C (Harris, 2021), recent high-resolution Cryo-EM studies (Grinzato *et al.*, 2023; Tamborrini *et al.*, 2023; Dutta *et al.*, 2024), and their previous studies on titin (Hessel *et al.*, 2022). In their view, sarcomeres disrupt the OFF-state during contractions by putting strain on both titin and MyBP-C though crown 2 that interacts with titin, and crowns 1 and 3 that interaction with MyBP-C C-terminal (C8-C10) in the C-zone (Hessel *et al.*, 2024). Meanwhile, the N-terminus of MyBP-C (C1-C7) keeps myosin heads in an OFF conformation, but upon removal causes the destabilisation of crown 1 into the ON state, which in turn destabilises crown 3 into the ON state. Lastly, destabilisation of crown 1 to the ON state, leads to a sarcomere-length independent structural elongation of the thick filament (Linari *et al.*, 2015; Ma *et al.*, 2021, 2023) leading to the perturbation of both titin and MyBP-C, leading to a potential disturbance in their interactions with myosin heads (Hessel *et al.*, 2024).

Although the mechanism behind MyBP-C regulation of the myosin ATPase is not completely clear, post-translational modifications of MyBP-C (e.g. phosphorylation) were shown (Ackermann and Kontrogianni-Konstantopoulos, 2011b; Kumar *et al.*, 2015; Pilagov *et al.*, 2023) to play a crucial role in regulating the level of repression MyBP-C imposes on myosin heads.

1.2.3. Post-Translational Modifications of Regulatory Proteins

1.2.3.a. MyBP-C

MyBP-C has been shown to regulate the cross-bridge kinetics of myosin molecules (Koretz, 1979; McClellan, Kulikovskaya and Winegrad, 2001). The process of kinetic regulation by MyBP-C is thought to be part of β-adrenergic activation, mimicked by Protein Kinase A (PKA). Several experiments have demonstrated increased contractility, through myosin activation, in PKA treated mice trabeculae (Colson *et al.*, 2008, 2012). Cardiac MyBP-C has 3-4 phosphorylation sites (species dependent) for PKA, localised to the M-domain. PKA is a serine/threonine-specific kinase, regulated by cellular levels of cyclic adenosine monophosphate (cAMP).

PKA is comprised of two catalytic (C)-subunits and a dimeric regulatory (R)-subunit (Lu *et al.*, 2019; Taylor *et al.*, 2021). The kinase core is localised to one of catalytic subunits and binds both Mg^{2+} and ATP. Conformation of all subunits depends on the availability of cAMP, which binds to the regulatory domain (Bauman and Scott, 2002). A recent study has shown the effect of combined or partial phosphorylation of those sites (McNamara, Singh and Sadayappan, 2019). In this study, the effects of PKA phosphorylation was shown on transgenic mice where PKA phosphorylated Ser residues (273,282 and 302). Phosphorylated sited were replaced with either phosphomimetic (aspartic acid) or phosphor-ablated (alanine). They found phosphomimetic residues on all Ser sites to increase the contractile potential of the muscle, while phosphor-ablated substitutions were stabilising SRX. Surprisingly, phosphomimetic residue on Ser-283 was concluded to be vital. The experiment leading to this conclusion has shown no change in SRX % when Ser 273 and 302 were phosphorylated, while Ser-283 was left unphosphorylated.

Another study (Ponnam *et al.*, 2019) investigating the effects of cardiac MyBP-C (cMyBP-C, right ventricle trabeculae, Wistar rats) phosphorylation at all four Ser residues using both PKA and S6 kinase II (RSK2) has also suggested a hierarchical structure of cMyBP-C phosphorylation. In their study, Ponnam and colleagues have used protein-protein interactions measured with PhosTag gel electrophoresis, as well as fluorophore interactions measured with microscale thermophoresis (MST) to establish the levels of cMyBP-C phosphorylation. Phosphorylating different sites and isolating monophosphorylated, bis-phosphorylated and tris-phosphorylated molecules

with ion-exchange chromatography and comparing the effects of different phosphorylation structurally, they have established a hierarchical nature of cMyBP-C phosphorylation. Confirming information provided by previous studies (McNamara, Singh and Sadayappan, 2019), Ser 288 phosphorylation was not significantly affected by dephosphorylated residues at Ser 279 or Ser 313, thus making Ser 288 the primary and most vital phosphorylation site on cMyBP-C. Ser 279 phosphorylation was indicated as a second in the line of hierarchy, yet still unable to be phosphorylated without Ser 288 phosphorylation. Ser 313 was inhibited by alanine substitution on either Ser 279 or 288. Furthermore, this study has shown the affinity of cMyBP-C at different phosphorylation states. In such, non-phosphorylated cMyBP-C, binding to the S2 in a biphasic manner would have dissociation constants (K_d) of 20.7 and 400 µmol/L for high and low affinity binding sites, respectively. Upon monophosphorylating cMyBP-C at either Ser 308 or 288 the K_d increased slightly to 30 µmol/L. Biphosphorylation with either PKA or RSK2 (i.e. either 2 sites by PKA or 1 by PK + 1 by RSK2) lead to a complete dissociation of cMyBP-C from S2.

Interactions of MyBP-C with myosin heads are well documented (Kunst *et al.*, 2000; Harris *et al.*, 2004; Herron *et al.*, 2006) and are discussed fully in the relevant section above 1.1.5.b.

1.2.3.b. RLC

Regulation of myosin cross-bridge kinetics by RLC phosphorylation is well-documented (Yu *et al.*, 2016; Ito *et al.*, 2022). RLC phosphorylation by Myosin Light Chain Kinase (MLCK) for both types of striated muscles show an increase in activity following the treatment. In skeletal muscle RLC phosphorylation occurs on Ser 14,15 (Blumenthal and Stull, 1980; Davis, Satorius and Epstein, 2002). Cardiac RLC phosphorylation is species-specific, with human RLC having Asparagine (Asn) instead of Ser on residue 14, and thus having only one phosphorylation site on Ser 15 (Scruggs *et al.*, 2010; Kampourakis and Irving, 2015). Other mammals, like mouse have Ser on both 14 and 15 residues (Lyon *et al.*, 2009). Some species have a completely different RLC mechanism of activation. For example, in tarantula smooth muscle RLC is phosphorylated by both Protein Kinase C (PKC) and MLCK at Ser 35 and 45, respectively (Espinoza-Fonseca *et al.*, 2015).

In physiological conditions, cardiac RLC phosphorylation is ~40% (Scruggs *et al.*, 2009; Warren *et al.*, 2012; Chang *et al.*, 2015), with the levels varying from endocardium to epicardium (Davis *et al.*, 2001). To create equilibrium with MLCK phosphorylation, PKA and Rho-kinase pathways control the phosphatase concentration (Ito *et al.*, 2022). MLCK is a serine/threonine -specific protein kinase, regulated by Ca^{2+}-Calmodulin (CaM) receptor located on either side of the myosin binding domain (Khapchaev and Shirinsky, 2016). MLCK has a basal activity without CaM/Ca^{2+} binding, which increases ~2 fold upon CaM/Ca^{2+} binding. Furthermore, some isoforms of MLCK (e.g. MLCK4) are not reliant on CaM/Ca^{2+} completely (Chang *et al.*, 2016). Upon RLC phosphorylation; Ca^{2+} sensitivity of Tn is increased, isometric force is increased, and cross-bridge cycle is fastened (Morano *et al.*, 1985; Sweeney and Stull, 1986; Olsson *et al.*, 2004; Stelzer, Patel and Moss, 2006a; Kampourakis and Irving, 2015). Finaly, in cardiac tissue cMLCK also phosphorylates cTnI , with smooth muscle MLCK having similar effects with decreased potency (Sevrieva *et al.*, 2020).

1.3. Diseases Associated with Mutations in Sarcomeric Proteins

1.3.1. Cardiomyopathy

Cardiomyopathies are a group of primary diseases of the heart muscle. Types cardiomyopathies are varied; hypertrophic cardiomyopathy (HCM) is recognisable left ventricular hypertrophy with preserved systolic function and impaired relaxation, while dilated cardiomyopathy (DCM) hears show an increase left ventricle chamber volume and systolic dysfunction (Garfinkel, Seidman and Seidman, 2018). Other types of cardiomyopathies include arrhythmogenic cardiomyopathy (ACM) and Takotsubo cardiomyopathy (TTS).

HCM is a common, genetic driven, disease affecting approximately 1 in 500 people (Cirino and Ho, 2021). The distinctive indication of HCM is an enlarged cardiac wall thickness ≥15 mm in adults and >3 mm in children (Gersh *et al.*, 2011). The increase in left ventricle and septum wall thickness may lead to a reduction in the volume of the left ventricle and reduce the amount of blood pumped and the pressure created. Symptoms associated with HCM vary dramatically, ranging with asymptomatic to a sudden cardiac death (Elliott *et al.*, 2014). Although symptoms may vary, people affected by HCM are at a higher risk of atrial fibrillation (AF), that may lead to thromboembolism. In such, 60 % of patients diagnosed with HCM at 40, are suffering from AF by the age of 60 (Ho *et al.*, 2018). Patients with both HCM and AF are affected with thromboembolism in 27% of cases (Elliott *et al.*, 2014). More severe consequences of end-stage HCM is an impaired systolic function that affects 5-10 % patients. The end-stage patients mortality rate is ~ 11% and may require a heart transplant (Harris *et al.*, 2006). The most severe consequence of HCM is sudden cardiac death (SCD), affecting ~ 6% of patients (Ho *et al.*, 2018). SCD in HCM causes ventricular arrhythmias, leading to cardiac arrest (O'Mahony, Elliott and McKenna, 2013). The genes most commonly involved in HCM are; MYBPC3 (cMyBP-C) – causing ~ 50% of all HCM related cases, MYH7 (myosin heavy chain) – causing ~33% of all HCM cases, and others like TNNI3 (5%) and TNNT2 (4%) for TnI and TnT, respectively (Cirino and Ho, 2021).

Individual mutations associated with MYBPC3 are predominantly (60%) truncating, including insertion, nonsense, deletion and other cMyBP-C mutations, like MYBPC3-c.772G>A, result in haploinsufficiency (Steczina *et al.*, 2024). Mutated cMyBP-C is unable to bind myosin and/or titin, thus losing the regulation control for myosin ATPase activity (Behrens-Gawlik *et al.*, 2014).

The majority of mutations are heterozygous, with a late onset (Carrier *et al.*, 2015). Multiple studies (Niimura *et al.*, 1998; Kubo *et al.*, 2005; Christiaans *et al.*, 2010; Adalsteinsdottir *et al.*, 2014; Calore *et al.*, 2015) have identified the founder mutations responsible for HCM-causing mutations in MYBPC3 gene. They have concluded that shorter cMyBP-C, lacking phosphorylation sites in the M-domain and/or myosin or titin binding domains, lead to HCM.

DCM is associated with a left ventricle enlargement (left ventricle wall thinning) and as a result the reduction in systolic myocardial force of contraction (Hershberger and Jordan, 2022). Like HCM, DCM phenotype varies significantly from asymptomatic to heart failure. Main genetic components of DCM are TTN (titin) – ~15-20%, MYH7 - ~4%, and other.

1.3.2. Pharmacology

Here and below HCM will be of primary focus, as the other cardiomyopathies mentioned above were outside of the scope of this thesis.

Primary treatments for HCM are inotropic agents including; β-blockers and non-dihydropyridine calcium channel blockers (Daubert *et al.*, 2018; Marrakchi *et al.*, 2020). Beta blockers are competitive antagonists that inhibit β-adrenergic response, thus increasing cardiac automaticity and conduction velocity (Farzam and Jan, 2025). Calcium channel blockers (CCBs), as the name suggests, reduce the movement of calcium ions that are essential for initiating muscle contractions. More specifically, non-dihydropyridine calcium channel blockers are a class of CCBs that are relatively selective for myocardium and thus are used for HCM patients (McKeever, Patel and Hamilton, 2025). The experimental pharmaceutical agents for HCM, that were used

during our experiments are listed blow, with short a descriptions and a mechanism of action (if known).

1.3.2.a. Mavacamten (MAVA)

Mavacamten (or MYK-461) is a first-in-class, FDA approved (approved in 2022), treatment specific for threating obstructive HCM (Basit *et al.*, 2025). MAVA is a selective, allosteric, and reversible small molecule myosin ATPase inhibitor. Furthermore, MAVA has been shown to affect skeletal muscles, albeit at higher saturation (Pilagov *et al.*, 2023). The mechanism of action for MAVA has been proposed recently (Grillo *et al.*, 2019), revealing the inhibition of the phosphate release (rate defining) step of the cross-bridge kinetics. Additionally, MAVA inhibits ADP release and repriming of myosin head (Kawas *et al.*, 2017). The recommended dose of MAVA for HCM patients is 5 mg/day, with final plasma concentration of 1-2 μM (Bello and Pellegrini, 2023).

1.3.2.b. Aficamten (AFI)

Aficamten, or CK-3773274, is another allosteric small molecule cardiac myosin ATPase inhibitor, which is a direct next-in-class drug to MAVA, currently in phase 3 trials. AFI binds into the blebbistatin pocket, as implied previously by a competitive binding study (Hartman *et al.*, 2024). The proposed binding site for AFI is located in the hydrophobic pocked at the apex of the 50 kDa cleft (Allingham, Smith and Rayment, 2005). AFI acts similar to MAVA, preventing the release of P_i from actomyosin complex, however showing a very ageing-related correlation with drug-myosin incubation time (Hartman *et al.*, 2024).

1.3.2.c. 2'-deoxy-ATP (dATP)

2'-deoxy-ATP is an naturally occurring nucleotide, that was shown as an alternative substrate for ATP during striated muscle contractions (Korte *et al.*, 2011; Powers *et al.*, 2019; Ma *et al.*, 2020). When replaced, muscle contractions have shown an increase in contractility, thus making dATP a myosin activator. dATP is suggested to increase the cross-bridge binding and ATP hydrolysis kinetics, however the exact mechanism of action is still unclear (Ma *et al.*, 2020).

1.4. Aims of this Thesis

For the duration of this thesis, our aim was to establish a series of novel and reliable methods to image and analyse myofibril ATPase activity with high precision, on both single-molecule and bulk fluorescent levels. The end-goal of this thesis was to use fluorescent microscopy to describe the effects of modulations (both post-translational and drug-induced) on striated muscles and fill in the gaps left in literature. For example, to the best knowledge of this candidate our laboratory was the first to report on single-molecule ATPase activity of β-cardiac myosin.

Our initial goal was to develop on single-molecule methodology to monitor the ATPase activity of skeletal, permeabilised rabbit (psoas) myofibrils. Single-molecule microscopy was used to observe the affects β-adrenergic response (stimulated by PKA) and of a novel myosin ATPase inhibitor MAVA. For our initial study the ATPase rates of myosin molecules were observed at a single-molecule level using the methodology developed for binning fluorescent ATP molecules into individual zones of the A-band (Pilagov *et al.*, 2023). This was followed by a study where a similar method was developed to observe a more clinically-relevant porcine cardiac tissue. For the study of cardiac tissue, experiments were conducted to observe the effects of phosphorylation on RLC (phosphorylated by MLCK) and cMyBP-C (phosphorylated by PKA) on myosin ATPase in C-, P-, and D- zones of the thick filament (Pilagov *et al.*, 2025). Lasty, a method to image multiple cardiac samples quasi-simultaneously was devised using a bulk fluorescence imaging approach that was utilised alongside a modified pulse-chase methodology. The last method was to expand the capabilities of our system by incorporating a moving stage that would cycle though samples in separate flow chambers (with potential of imaging using different solutions) and increasing the throughput of our imaging setup thus allowing us to screen for different pharmaceutical agents as well as mutated isoforms of striated muscles.

Chapter 2 – Materials and Methods

2.1. Buffers and Solutions

Cardioplegic Solution

5.5 mM Glucose, 0.5 mM $MgSO_4$, 24 mM KCl, 20 mM $NaHCO_3$, 109 mM NaCl, 0.9 mM H_2NaO_4P, 1.8 mM $CaCl_2$, 0.01% NaN_3, pH 7.4

2.1.1. Rabbit Psoas (Skeletal)

Skeletal Skinning Buffer

6 mM imidazole, 8 mM Mg-acetate, 70 mM propionate, 5 mM EGTA, 7 mM ATP, 0.5% Brij 58 (P5884; Sigma-Aldrich), 1 mM Na-azide, pH 7.0

Skeletal Preparation Buffer

6 mM imidazole, 8 mM Mg-acetate, 70 mM propionate, 5 mM EGTA, 7 mM ATP, and 1 mM Na-azide, pH 7.0

Skeletal Wash Buffer

6 mM Mg-acetate, 10 mM EGTA, 54 mM Na-acetate, 18 mM Na2SO4, 10 mM MOPS, 5 mM ATP, and 1 mM DTT, pH 7.4

Skeletal Imaging Buffer

1 mg/ml BSA, 5 nM phosphoenolpyruvate [PEP], 1 µl pyruvate kinase [PK], 6 mM Mg-acetate, 10 mM EGTA, 54 mM Na-acetate, 18 mM Na2SO4, 10 mM MOPS, 1 mM DTT, 5 nM Cy3-ATP, and 5 mM ATP, pH 7.4

Stopped-Flow Buffer

25 mM KCl, 20 mM MOPS, 5 mM MgCl2, and 1 mM Na-azide, pH 7

2.1.2. Porcine Cardiac

Cardiac Preparation Buffer

20 mM MOPS, 132 mM NaCl, 5 mM KCl, 4 mM MgCl2, 5mM EGTA, 10 mM Na Azide, 5mM DTT, 20 mM BDM, protease inhibitor cocktail (A32965; Thermo Scientific), pH 7.1

Cardiac Myofibrils Skinning Buffer

20 mM MOPS, 132 mM NaCl, 5 mM KCl, 4 mM MgCl2, 5mM EGTA, 10 mM Na Azide, 5mM DTT, 20 mM BDM, protease inhibitor cocktail (A32965; Thermo Scientific), 0.5 % Triton X-100 (T8787; Sigma), pH 7.1

Cardiac Imaging Buffer

20 mM MOPS, 132 mM NaCl, 5 mM KCl, 4 mM MgCl2, 5mM EGTA, 10 mM Na Azide, 1mM DTT, 1-10 nM Cy3-ATP, and 5 mM ATP, protease inhibitor cocktail (A32965; Thermo Scientific), pH 7.1

2.1.3. Cy3-ATP Ensemble Experiments

All buffers were degassed.

Chase Prep Buffer

20 mM MOPS, 132 mM NaCl, 5 mM KCl, 4 mM MgCl2, 5mM EGTA, 10 mM Na Azide, 5mM DTT, protease inhibitor cocktail (A32965; Thermo Scientific), pH 7.1

Chase Imaging Buffer

20 mM MOPS, 132 mM NaCl, 5 mM KCl, 4 mM MgCl2, 5mM EGTA, 10 mM Na Azide, 5mM DTT, 1 μM Cy3-ATP, 500 μM ATP, 5 mM Phosphoenolpyruvate (2-phosphoenolpyruvate, PEP), 2.2 units Protein Kinase A (PKA), protease inhibitor cocktail (A32965; Thermo Scientific), pH 7.1

Chase Chasing Buffer

20 mM MOPS, 132 mM NaCl, 5 mM KCl, 4 mM MgCl2, 5mM EGTA, 10 mM Na Azide, 5mM DTT, 5 mM ATP, 5 mM Phosphoenolpyruvate (2-phosphoenolpyruvate, PEP), 22 units Protein Kinase A (PKA), protease inhibitor cocktail (A32965; Thermo Scientific), pH 7.1

2.2. Muscle Preparation

2.2.1. Cardiac tissue preparation from full heart

No live animals were used in these studies. Muscle tissue was collected in accordance with the U.K. Animals (Scientific Procedures) Act 1986 and associated guidelines.

Hearts of freshly euthanized pig was submerged into an ice-cold Cardioplegic Solution. Hearts remained in cardioplegic solution during dissection. Dissection was performed on ice. Samples were made from trabeculae muscles (~ 5 mm each) and flash-frozen. Samples were placed at -80 °C for long-time storage.

2.2.2. Chemical Skinning

Muscle tissue was skinned using buffers specific for each type of tissue ,yet both detergents used for all experiments were non-ionic, as both are considered to be mild surfactants (Johnson, 2022) that are most likely to preserve protein-protein interactions and less likely to denature proteins. Out of non-ionic surfactants Triton X-100 (X100; Sigma-Aldrich) and Brij 58 (P5884; Sigma-Aldrich) where chosen as common representatives of surfactant used in the field for skinning muscle fibres (Lewalle *et al.*, 2022). However, Triton X-100 was chosen for the later (cardiac and ensemble) experiments as a representative of the most recent surfactant used for similar experiments (Nelson *et al.*, 2020; Park-Holohan *et al.*, 2021) in the field.

2.2.2.a. Rabbit Skeletal

Rabbit psoas muscles were skinned using a modified form of the previously described protocol (Walklate *et al.*, 2019). Briefly, strips of tissue 1-2 mm in diameter were attached to wooden sticks (e.g. ordinary toothpicks) using a sturdy string on both ends. Strips were equilibrated in ice-cold Skeletal Preparation Buffer for 30 min twice. For skinning Skeletal Preparation Buffer was replaced by Skeletal Skinning Buffer and samples were incubated on a rotating surface for 2 h at 4 °C. To store skinned strips, they were moved back into Skeletal Preparation Buffer mixed 1:1 with glycerol and equilibrated for 2 h. Equilibrated samples were stored at -20 °C until use.

2.2.2.b. Porcine Cardiac

Porcine samples were skinned using two previously established protocols (Walklate *et al.*, 2022; Nelson *et al.*, 2023) with some modifications. Quality of the sample prepared was very similar for both methods, but due to a time optimisation reasons the former protocol was chosen as a main protocol for the cardiac study: first cardiac tissue was cut in small, rectangular ~4/6 mm (w/l) pieces and pinned to a silicon-based petri dish with tungsten rods on both sides under tension. Cutting and pinning both occurred in the presence of ice-cold Cardiac Myofibril Prep Buffer in relaxed (pCa < 9) conditions. Once the samples were pinned and equilibrated, the buffer was exchanged to Cardiac Myofibrils Skinning Buffer and samples were skinned overnight at 4 °C on a shaking/agitated surface. Skinned samples were utilised within 12 h from the end of skinning. Care was taken to keep them in the temperature range of 0 – 4 °C prior to myofibril preparation. The latter protocol (Nelson *et al.*, 2023) was chosen for the ensemble study for its simplicity and reduced time of skinning. Reduced time also meant a low probability of protein degradation between skinning and imaging. Similarly to the other method, myofibrils were dissected into rectangular ~4/6 mm (w/l) pieces, homogenised (using the method below) and then skinned with 1 % Triton-X100 for 30 min at 4 °C with constant agitation. Skinned myofibrils were spun down using a bench centrifuge at 1K x g for 5 min at 4 °C three times. In between centrifugations myofibrils were resuspended in Chase Prep Buffer.

2.2.3. Myofibril Preparation

The protocol for myofibril preparation from skinned tissue is very well established (Eastwood *et al.*, 1979; Knight and Trinick, 1982; Herrmann *et al.*, 1993; Walklate *et al.*, 2019; Nelson *et al.*, 2020; Walklate *et al.*, 2022; Nelson *et al.*, 2023; Pilagov *et al.*, 2023). Minor modifications were applied to account for tissue specificity. Both cardiac and skeletal tissues were prepared very similarly, with only minor changes in buffer composition. Both tissues were dissected into smaller pieces using dissection kit: common bench scalpel, micro-scissors (Vannas-Tübingen Spring Scissors, Fine Science Tools, 15003-08) and tweezers (Dumont #5 Fine Tip Tweezers, Fisher Scientific, 15483542).

For dissection, tissue was transferred from the cold storage to a petri-dish filled with tissue-specific preparation buffer. All steps described below are performed on ice and using ice-cold buffers, unless stated otherwise.

For skeletal sample, a piece ~2 – 3 cm was cut from the skinned muscle attached to the wooden stick. The texture of psoas muscle allowed muscle fibres to be pulled apart using tweezers, creating small threads of muscle fibre. This process was repeated until threads were too thin to pull apart. It is important to note that thinner threads increased the quality of myofibrils present during image acquisition. Cardiac myofibrils were much harder to prepare compared to their skeletal counterparts. Unlike psoas muscles, cardiac samples were impossible to pull apart and thus they needed to be cut using micro-scissors. Just like with the skeletal sample thinner samples provided better end-result while imaging. The ideal size for cutting cardiac tissue was found to be ~1/3 mm (w/l). Cut tissues were transferred one-by-one into a 2 ml centrifuge tube using tweezers. Centrifuge tube contained 800 µl of preparations buffer. Tissues were homogenised using Tissue Ruptor II (Qiagen, 9002755) for 10 s twice with a 60 s rest period (on ice). Homogenised sample was either concentrated or diluted to OD_{600} - 0.8, 0.4 or 0.5-0.75 (Skeletal, Cardiac or Ensemble) measured using a bench Jenway 7315 Spectrophotometer (Fisher scientific, 15179702). The OD was measured using polysterol/polystyrene cuvettes (Sarstedt, 67.742). It is important to note that myofibrils settle relatively quickly and thus may provide an inaccurate reading if undisturbed for too long. To account for that the density was measured either straight after the transfer or sample was agitated in the cuvette prior to the reading.

2.3. Myofibril Imaging

2.3.1. Flow Chamber Preparation

Flow chamber assembly and design was identical for both Cardiac and Skeletal experiments and was described previously (Pilagov *et al.*, 2023, 2024) . Briefly, a slide with two drilled holes (1.5 mm diameter) was attached to a gasket. Gasket was made of double-sided tape and cut into 10x15 mm. A standard 24x40 mm coverslip (Borosilicate) was attached to the other side of the gasket. The assembly created a space that could contain ~30 µl liquid. Coverslips were plasma treated prior to assembly using a plasma cleaner (Harrick Plasma PDC 32G 2) for 5 min. Plasma cleaning allowed for smoother surface and thus a better attachment of myofibrils. Prior to assembly but following the plasma clean coverslips were coated in 15 ug/ml poly-L-lysine (PLL; P1524; Sigma-Aldrich) and allowed to dry for 30 min. PLL treatment was ensuring the attachment of myofibrils to the surface of the coverslip. Flow cells (chambers) were assembled by attaching a gasket onto a slide followed by the coverslip, PLL-covered side facing the slide (see Figure 19). Prior to any experiment the flow chamber was washed out with 3 x 100 µl of the experiment-specific buffer to remove any dust/impurities that have accumulated on the inside surfaces of the flow chamber. Ensemble experiments employ their own way of washing the flow chamber but were prepared similarly; plasma-cleaned and PLL-coated.

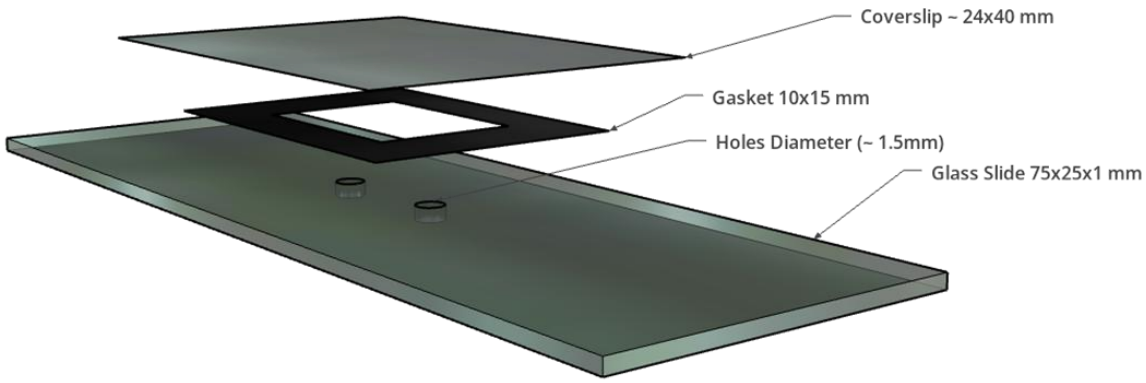


Figure 19. A schematic diagram showing the structure of a flow chamber (cell).

A coverslip (24x40mm, borosilicate), covered in PLL facing the slide, is attached to a slide (standard, 75x25x1mm), with two holes (1.5mm diameter) drilled in it and, covering both with a gasket (10x15mm) made of double-sided tape.

2.3.1.a. Rabbit Skeletal

Experiments with rabbit psoas muscles were described in our previously published work (Pilagov *et al.*, 2023). Briefly, rabbit psoas muscles were laid out on to the surface of the flow chamber by injecting 30 µl of myofibrils through a single port and incubated for 30 min. To prevent non-specific attachment the surface was blocked by 100 µl of 10 mg/ml BSA (A7906; Sigma-Aldrich) for 2 min followed by 100 µl Washing buffer. Myofibrils were treated with either Mavacamten (MAVA; myk-461; MCE HY-109037) or cAMP-dependent protein kinase (PKA; P2645; Sigma-Aldrich). The treatments were applied differently as MAVA did not require specific conditions and thus was added directly to the Imaging Buffer to the final concentration of 30 µM. A short, 10 min incubation was allowed following the treatment but prior to the imaging. It was made sure that the concentration of the solvent (Dimethyl sulfoxide; DMSO) for MAVA treatment was not exceeding recommended 0.5 % (Mariano *et al.*, 2001). PKA on the

other hand required Mg^{2+} and ATP containing buffer with an optimal pH of 7-7.8 and an incubation period of at least 1 hour. The time was estimated based on the specific activity of the catalytic domain and recommendation provided by the manufacturer. PKA treatment was conducted outside of the flow chamber with 62.5 units/µl PKA at 4 °C for 1 hour in a Skeletal Prep Buffer, on a rotator for constant agitation, to preserve the integrity of myofibrils. Cy3-ATP and dark ATP was regenerated using PK/PEP regeneration system described below (see 3.2.6). In the case of the skeletal study, regeneration system was applied in the imaging buffer for at least 1h on ice prior to imaging.

2.3.1.b. Porcine Cardiac

Our study on β cardiac muscle (Pilagov et al. 2024 in review) was conducted similarly to our previous skeletal muscle study. Skeletal methods were slightly modified to fit the cardiac system. Myofibrils were exposed to recombinant human Myosin light chain kinase (MLCK; ab55674; Abcam) and PKA. PKA treatment was conducted in a similar manner to the skeletal muscle imaging. MLCK treatment was conducted at 0.4 µM, 4 °C for 1 hour, following previously described protocol (Stelzer, Patel and Moss, 2006a) in Cardiac Preparation Buffer + 5mM BDM, 67 µM CaCl2, 6 µM Calmodulin. Incubation time for MLCK was higher than recommended to compensate for the lower incubation temperatures. Cy3-ATP regeneration system was applied to the cardiac study similarly to the skeletal study, but instead of regenerating Cy3-ATP in imaging buffer it was regenerated separately for 1 h at 4 °C with constant agitation.

2.3.2. Microscope Experimental Setup

Microscope experimental setup has been described previously (Desai, Geeves and Kad, 2015).

2.3.3. Image Acquisition

2.3.3.a. Single-Molecule Imaging

Image acquisition was described previously (Pilagov *et al.*, 2023, 2024). Briefly, an oblique angle fluorescent (OAF) microscope was used in all experiments to image single-molecule activity. Lasers utilised were; 561-nm laser (OBIS LS laser) and Oxxius 488 nm laser to illuminate Cy3-ATP and Alexa-488-labeled Z-disks, respectively. Illumination times were kept constant at 200 ms for all single-molecule experiments, while laser OFF time varied according to the needs of the experiment. Camera and lasers were synchronised using a custom-designed Arduino-based control system.

2.3.4. Image Processing

Image processing was conducted in two stages. First (data extraction), images were analysed using ImageJ with some degree of automation. Second (data analysis), ImageJ output was analysed, plotted and fitted with Microsoft Excel. Throughout the progress of this thesis methods have evolved providing a more automated approach for both data extraction and data analysis.

2.3.4.a. Skeletal Study

In our skeletal muscle study, the analysis was fully manual, utilising ImageJ plugin TrackMate (Tinevez *et al.*, 2017) to super-localize the position of every Cy3-ATP and Alexa-488-labeled Z-disks attachment (Pilagov *et al.*, 2023). Z-disc imaging was conducted in the first 30 sec of the image acquisition at which point the 488 laser was switched OFF and the 561 laser was switched ON for Cy3-ATP imaging. TrackMate was set to include objects with 390 nm diameter using a LoG detector, used 100 nm

linking and gap-closing distance for the LAP tracker and max gap-closing frame distance of 20 frames. The results were manually compared to a kymograph of the same video to ensure the tracks recorded by TrackMate matched that of tracks obvious on the kymograph (Figure 20). TrackMate data was input into a custom-written Microsoft Excel spreadsheet for further analysis, where it was analysed sarcomere by sarcomere. First, the tilt in the Z-discs had to be corrected to ensure the correct placement of ATP events on the super- localize sarcomeric map. A simple trigonometric approach was utilised, where all events were shifted in respect to how far they were from a line parallel to the y-axis. In this approach, the Z-discs were assumed to be straight, able to fit to a simple linear equation $(y = mx + c)$ and parallel to the next Z-disc. The tilt of the fitted Z-disc was estimated based on the *m* component and corrected as if the *m* component was zero. All ATP events in a sarcomere (i.e. in-between two Z-discs) were moved together with the Z-disc points to the degree dictated by the change in gradient required to make the gradient zero (Figure 21). The concern with this approach was the assumption that the Z-discs were straight and that they were parallel to each other, which was not always the case. Some Z-discs were curved and not always perfectly aligned to the subsequent Z-disc. This approach was modified to address those concerns in our next, cardiac study.

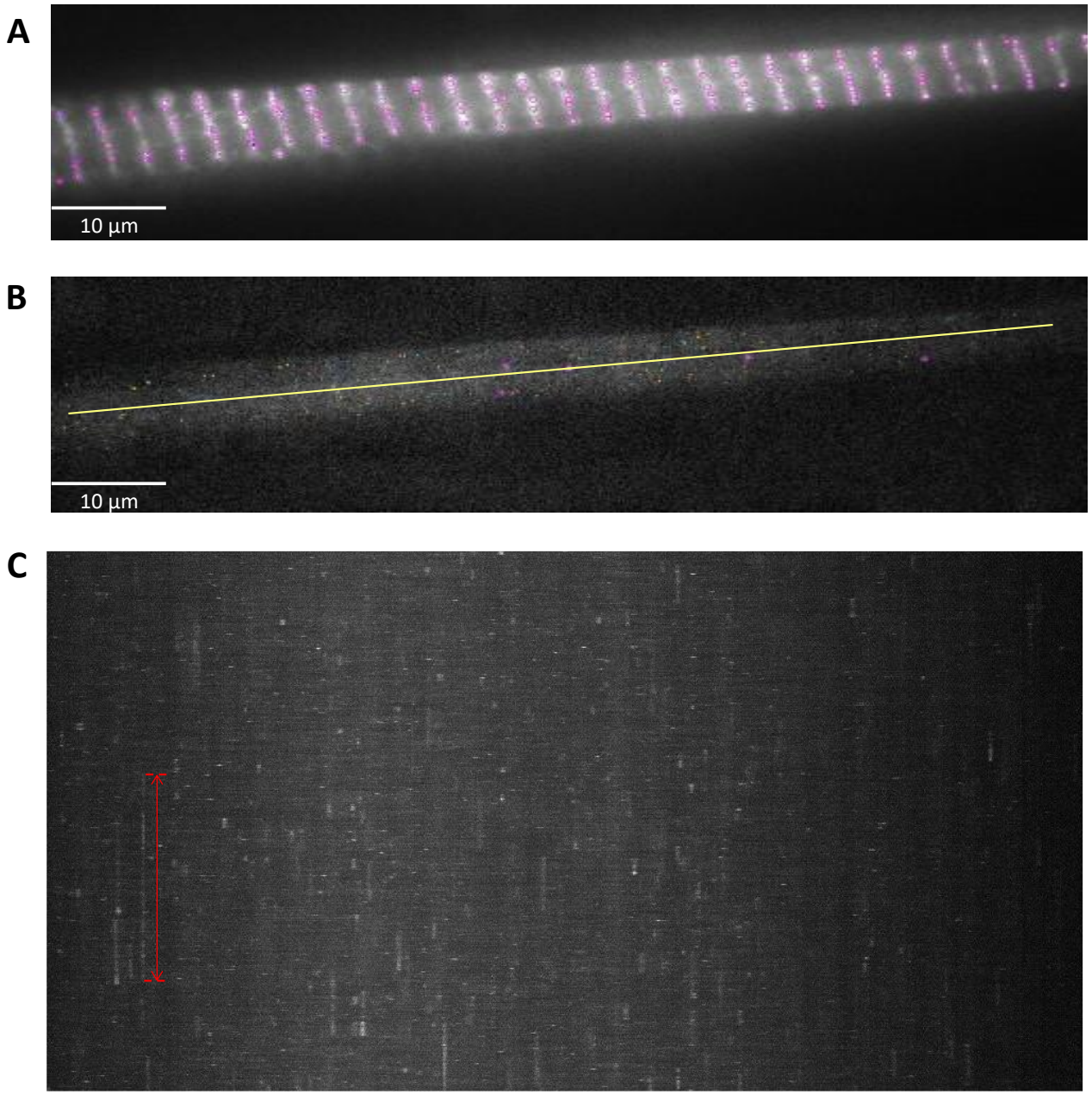


Figure 20. A visual representation of a tracking process using TrackMate plugin for ImageJ.

A) Tracking of Z-disc labelled with Alexa-488-labelled Z-disks on a chosen myofibril. Purple circles are events on a current frame that follow the criteria set in TrackMate and that are going to be tracked in the following frames if they do not disappear. B) The same myofibril but with Cy3-ATP illuminated instead. Similarly, purple circle showing the events being tracked on a current frame and coloured dots showing the positions of events that were tracked on previous frames. The yellow line showing the kymograph imaging plane as was typically used for the ImageJ analysis. C) A kymograph of Cy3-ATP events that is used to check the validity of TrackMate output. The arrowed red line is showing a typical long-lived track that would be compared against TrackMate output.

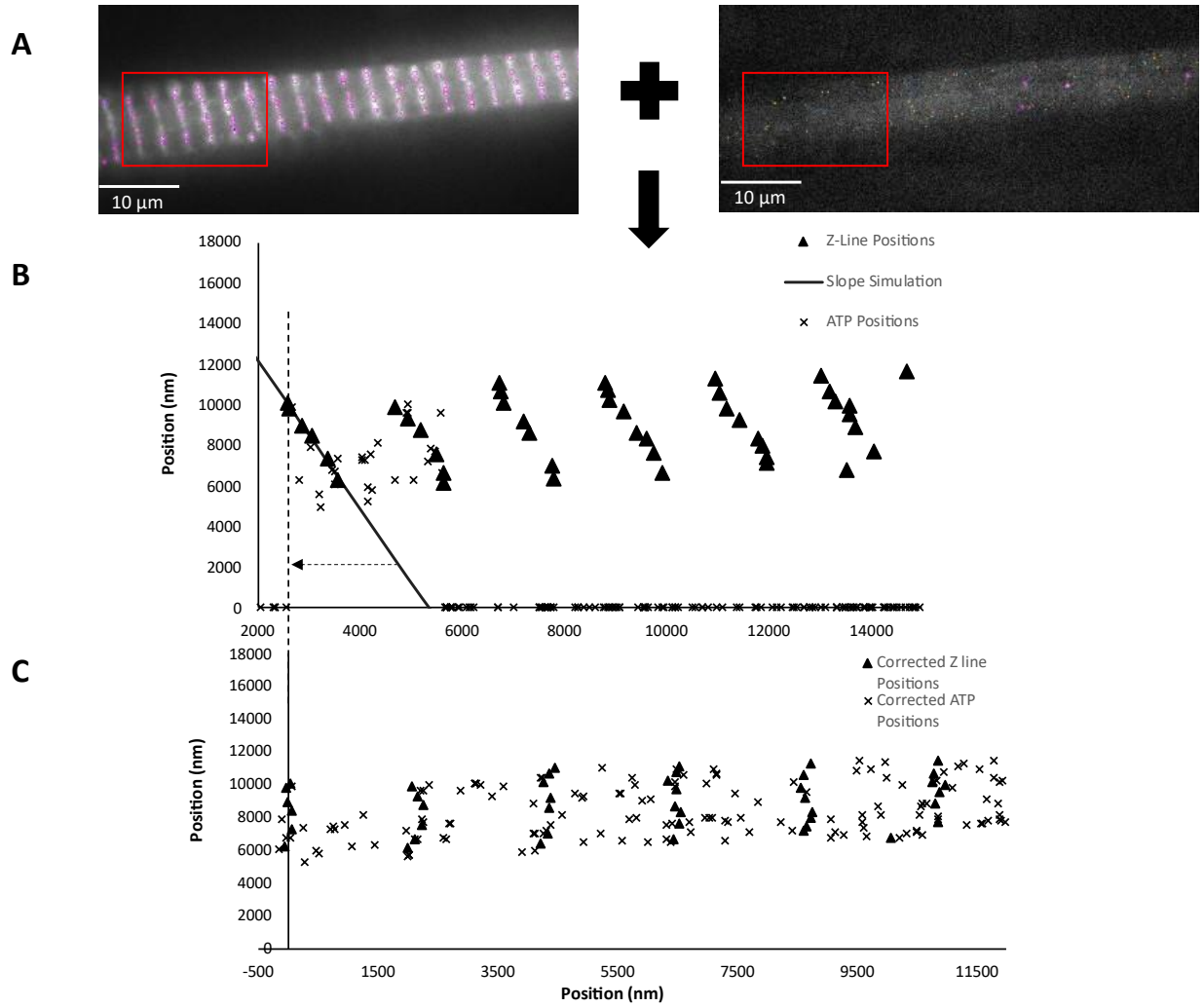


Figure 21. A visual explanation of a step-by-step process of superposition and tilt-correction employed in the analysis of skeletal myofibrils.

A) A typical image of fluorescently labelled myofibril (left) with that of Cy3-ATP events (right). When overlayed creating a superimposed image in B. B) A superimposed image of a myofibril featuring the Z-disc (filled triangles) and ATP events (crosses). C) When tilt of a currently analysed sarcomere is corrected both Z-disc and ATP events are shifted, resulting in a tilt-corrected myofibrils. Tilt correction was done using simple trigonometry, by aligning the left Z-disc to the y-axis. Axis are given as position of attachments (for both ATP and α-actinin) in nm.

The Z-discs were used as fiducial marker to establish the zones on the A-band and bin ATP events into them. Z-disc positions were fitted to two Gaussian distributions (one for each Z-disc of a sarcomere). This user-free approach has enabled us to estimate the position of the M-line (halfway point between the two Z-discs) and provided an error in approximation equal to 31.8 nm from the average SD of 1318 Gaussian fits. Furthermore, this helped to provide us with an error for binning zones for the A-band (P, C and D zones). The zonal distribution was calculated from the distance away from the M-line using; P-zone [0–159 nm], C-zone [160–500 nm], and

D-zone [501–800 nm] (Tonino *et al.*, 2019; Bennett, Rees and Gautel, 2020). ATP events precision was calculated separately using an unbiased empirical approached developed by (Gelles, Schnapp and Sheetz, 1988). Calculated ATP precision was 29.2 nm in X and 26.7 nm in Y. This approach compares the positions of 75 Cy3-ATP events with duration of 10-21 frames, while not relying on any assumption about hardware or software being used, instead the error is calculated on the assumption that the objects in the field of view are stationary, while incorporating all sources of error. This unbiased, empirical approach was utilised to determined the accuracy of localisation based on the SD of relative positions of fluorescent particles.

Results for ATP event durations and positions were collected and plotted on a cumulative survival plot and fitted to a triple exponential. Triple exponential was chosen as a least possible number of exponentials that would fit our data. The fitting was done utilising the Solver GRG nonlinear engine with linear weighting. Fitting was constrained to 1.8–2.2-fold difference from the global (untreated) values for the whole sarcomere to ensure no overlay in rates. The range was chosen to maximise the available range while preventing overlays with ~10-fold slower rates (i.e. DRX~0.01 sec^{-1} & SRX~0.001 sec^{-1}) To further eliminate any error in fitting the tracks of the residual fits were analysed, by looking for consistent under/over fitting of the data, meanwhile comparing the output from triple exponentials to double exponentials. For example, in case of overfitting, duplicaterates were expected to appear following the fitting (i.e. the same rate would show up twice). From these fits the amplitudes were extracted and rates consisted with Super Relaxed (SRX) and Disordered Relaxed (DRX) states of myosin and the fastest rate being contributed by unspecific attachments or Cy3-ATP hydrolysis of other (non-myosin) ATPases (Amrute-Nayak *et al.*, 2014; Ušaj *et al.*, 2021). Slower rates were confirmed to be in line with rates previously described in literature, subject to photobleaching correction (Hooijman, Stewart and Cooke, 2011) Analysing each sarcomere at a time has enabled the determination of the position of each ATP track in every zone of the A-band and determine the percentage of events that were contributing to SRX, DRX and Fast events.

2.3.4.b. Cardiac Study

Building on the above approach and attempting to improve it by solving limitations described above, a more automated version was developed for our next, cardiac study (Pilagov *et al.*, 2024). Briefly, TrackMate with the same parameters, except for the gap-closing max frame set to 5 frames. TrackMate was called through a custom-scripted Python (Jython) code (https://github.com/Kad-Lab/Myofibril-phosphorylation). Unlike our skeletal study it was decided to track Z-disc positions with higher precision and thus inserted one Z-disc frame every five Cy3-ATP frames. These frames needed to be separated to be analysed which was scripted in the above code. Separated frames were analysed by calling TrackMate though the script but otherwise following the skeletal example, with kymograph checks applied.

In a case where drift was present, it was corrected using a star-map approach (https://github.com/fiji/Descriptor_based_registration, (Preibisch *et al.*, 2010)), also incorporated into the code. The star map approach was developed to tack fluorescently labelled beads in 3D on a surface. Briefly, the beads (or in our case, fluorescently labelled anti-alpha-actinin antibodies on Z-discs) are mapped as constellations, with position of each bead (antibody) determined by constellation patters produced by beads around it.

For this study the Excel portion of the analysis was modified as well, again, to address the limitations of our previous approach. In such, the Z-disc tilt correction approach was modified. For that a slightly more complicated trigonometric approach was employed. In this approach each point was rotated through both planes, thus clearing any concern of curved Z-discs effecting the tilt correction precision. The rotation was done separately for x ($x' = xcos(\theta) - ysin(\theta)$)and y ($y' = xsin(\theta) + ycos(\theta)$) position of every Z-disc and ATP event with regards to the leftmost position of the Z-disc event (for an example see below, 2.3.4.c). This approach has also illuminated any concern for how parallel two consequent Z-discs are to each other, as they no longer needed to be parallel (i.e. they only needed to be rotated the same amount in x and y). The binning process was unchanged from the skeletal study. For this study, the precision was shown to be Z-disc (X - 68.2 nm, Y – 135.4 nm) and Cy3-ATP (X - 28.1 nm, Y – 38 nm) using the same methods described above. The fitting process was modified

slightly to allow for a degree of freedom equal to 20% of untreated “all zones” (i.e. data fitted without dividing it into zones) values for both rates and amplitudes.

2.3.4.c. Z-disc Tilt Correction Control Simulation

To provide evidence of functionality and robustness of our data analysis algorithm for the cardiac study, Microsoft Excel was employed to simulate a simplistic set of data and ran it though our analysis algorithm. The data was simulated using a matrix comprised of both simulated Z-disk and Cy3-ATP data. 2D Gaussian distributions were used to simulate the area-defined-Cy3ATP events (see Figure 22 A), which were distributed semi-randomly throughout the myofibrils. During the random generation, it was ensured, that at least two events would be present per each zone of the A-band, and that at least two events would be placed in both I-bands. The Z-discs were simulated (see Figure 22 B) using the same method. All Z-disc events were placed in a straight line with a total sarcomeric length of 2.5 um.

Simulations were loaded into the FIJI ImageJ using ImageJ -> Import -> Text Image. Produced separate slices of Z-discs and Cy3ATP events were combined using ImageJ -> Image -> Stacks -> Tools -> Concatenate. To mimic a single stroboscopic repeat of experimental data, a Cy3ATP simulation image was replicated to the total number of 5 slices and then concatenation with the Z-discs slice. The process was repeated 25 times to partially emulate the length of a typical experimental video. To better represent changes that were implemented throughout the testing process, Z projects of Cy3 and Z-disc stacks were overlayed. The results of Cy3ATP (magenta) and Z-disc (cyan) slices overlay, through ImageJ -> Process -> Image calculator -> Add, are shown in Figure 22C(left). For easy reference, the overlay is shown with a red dashed line representing the M-line and different zones of the A-band approximately labelled in blue (D-zone), orange (C-zone), yellow (P-zone).

Following concatenation, the stack was rotated by 30° to simulate the sarcomeric tilt that was present during experimentation. Tilted stack was then treated like a typical experimental video and put through the analysis process described above. A super-localized TrackMate output scatter plot (see Figure 22 D) is a horizontally mirrored representation of tilted-simulated events from Figure 22 C (right). The mirroring occurs due to the TrackMate algorithm of analysis. Tilted-mirrored events were then put

through the tilt correction and separated into the I-band and the zones of the A-band according to their position in the sarcomere. Lastly, the results of the analysis were compared to the known original positions of Cy3ATP events using our binning zone method described above. The position of each Cy3-ATP event was compared pre- and post- rotation by calculating the displacement using $d^2 = (\Delta x^2 + \Delta y^2)$, where d is displacement, Δx is the difference in x-axis coordinates, and Δy is the difference in y-axis coordinates. The results showed an average displacement of 10.97 (±5.89) nm.

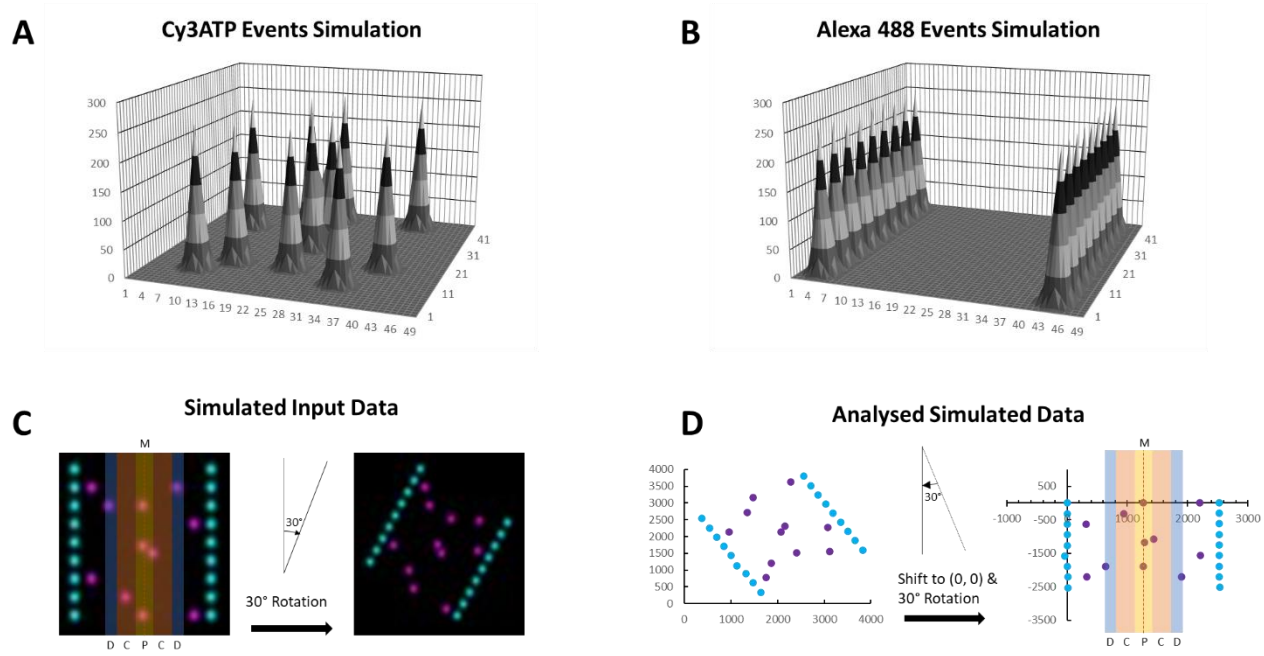


Figure 22. A representation of a data simulation workflow and the following analysis.

The simulation was implemented to determine the robustness of the analysis. The data was simulated using 2D gaussian equation and can be seen plotted for both Cy3ATP and Z-disc events in parts A and B, respectively. The combined simulated data produced image as seen in part C (left) and as it is seen after the 30° rotation in part C (right), in both Z-disc events are seen in cyan and Cy3ATP in magenta. For reference, an M-line (red dotted line) and zones of the A-band were added. A-band zones: D, C and P zones, were labelled blue, orange and yellow, respectively. The output of the TrackMate analysis can be seen in D (left), and the product of the Z-disc tilt correction in D (right). D (right) is shown with A-band zones and the M-line.

2.3.4.d. Statistical Analys

Single-molecule data described above was analysed for statistically significant changes throughout this manuscript in order to compare the effects of different treatments (e.g. MAVA & PKA). An unpaired two-tail t-test with the standard error of the mean (SEM) was utilised to establish the statistical significance of the change in the untreated vs treated samples for both cardiac and skeletal single-molecule experiments. The unpaired t-test was utilised as the analysis was comparing all the

samples to the untreated data, and thus was only required to compare the two unrelated groups of means from a treated sample to an untreated sample. The unpaired t-test was conducted using GraphPad (GraphPad Software, Inc.) open access web-based software. SolverStat (Comuzzi *et al.*, 2003) was utilised to determine the fitting error, when fitting the cumulative frequency graphs, for both skeletal and cardiac studies. The ensemble imaging did not utilise the same approach as employed with the single-molecule experiments, instead relying on the consecutive ROIs for establishing the standard deviation of observed intensities (described fully in 5.2.5). Standard error propagation was applied for all errors established throughout the analysis.

2.4. Gel-Based phosphorylation assays

Gel-based phosphorylation assays were conducted to quantify the phosphorylation levels of sarcomeric proteins. Gels were utilising ProQ Dimond phosphostain (P33300, Invitrogen) and Phos-Tag Yellow (380-15241, FUJIFILM).

2.4.1. Rabbit Skeletal

A standard polyacrylamide Tris-Glycine SDS-PAGE gel was used for protein separation. The gels were hand casted using Bio Rad Mini-PROTEAN® Tetra Handcast Systems. Gels were run on the same system at 180 V for ~50 min. Samples were boiled in standard Coomassie running buffer for 10 min at 95 °C. For loading see appropriate chapter sections (e.g. 3.2.4). The staining was done according to manufacturers instructions.

When needed, sMyBP-C was precipitated, to make the band more pronounced, from myofibrils using a well-established technique of ammonium sulphate precipitation, that changes protein solubility based on a high salt concentration. Briefly, sample was diluted with 100% $(NH_4)_2SO_4$ to the final concentration of 55%. The sample was placed on a rotor, at 4 °C, and incubated for 30 min to allow sMyBP-C to fall out of solution. The sample was then centrifuged, at 4 °C, for 10 min at 4K g. Supernatant was discarded, pellet resuspended in the Washing Buffer and dialysed overnight in 500 ml of Washing Buffer. The size of pores on the dialysis tubing was chosen to prevent sMyBP-C from leaving. For this experiment the Dialysis tubing cellulose membrane (Sigma, D9277) was utilised.

2.4.2. Porcine Cardiac

Similarly to our skeletal study the sarcomeric protein phosphorylation levels were quantified using phosphorylation gels. In this study a Phos-Tag Yellow stain was employed instead of ProQ staining which was applied to a precast Novex™ 4 to 20%, Tris-Glycine (EC6021, ThermoFisher) for better separation unattainable with hand casted gels. Electrophoresis and staining were done according to manufacturers instructions.

2.4.3. Relative Gel-Based Phosphorylation Levels

Phosphorylation levels of protein bands observed on both Coomassie and photosensitive gels were determined using the relative intensities of actin bands in-between the gels and band-of-interest intensities when compared to the actin band on the same gel. The quantification of band intensity and their consecutive comparison was essential as to compensate for the loading variation and devise an unbiased approach of determining the phosphorylation values of separate proteins. The band intensities were established using the rectangular and magic wand tools of ImageJ.

Actin band (~40 kDa), was taken as a standard as it was not expected to change in intensity throughout the multitude of samples. The calculation for relative band intensities was:

$$P_{2rel} = \frac{A_1}{A_2} \cdot \frac{P_2}{P_1}$$

Where P_{2rel} was the relative intensity of a protein band, when compared to the same protein band but in the untreated well, A_1 and A_2 were the band intensities for actin (in untreated and treated wells, respectively) that were used to equilibrate any inconsistencies in the loading. Finally, P_2 and P_1 were the band intensities for the protein of interest, in our case it was either MyBP-C and RLC, where P_1 was the intensity for the untreated sample and P_2 was the intensity for the sample treated with MLCK, PKA, or CIAP.

Chapter 3 – Using A Novel Single-Molecule Approach to Map ATPase Activity in Psoas Rabbit Myofibrils

3.1. Introduction

This chapter was set out to explore the effects of novel small molecule ATPase inhibitor MAVA and a known myosin activator PKA on psoas rabbit skeletal myofibrils. This

study was conducted to deepen our understanding of the thick filament regulation of contractions in skeletal muscles and test skeletal tissue-specificity of recently FDA approved drug MAVA. For this, individual Cy3-labelled ATP molecules were tracked as they were detaching from surface-fixed myofibrils to determine their respective positions in the A-band using Alexa-488 labelled Z-disks as fiducial markers. The experiments were conducted using custom-build, oblique angle fluorescent microscope with a single-molecule precision. In this study, protein kinase A (PKA) was shown to activate the thick filament, although its effects were limited to the C-zone of the A-band. On the other hand, MAVA was shown to repress myosin ATPase activity throughout the sarcomere, but a previously described reserve (Nelson *et al.*, 2023) of myosins in a disordered relaxed state (DRX) has remained even when treated with MAVA at well-above saturation levels.

3.1.1. Skeletal MyBP-C Splicing is Tissue-Dependent

MyBP-C has three isoforms: slow skeletal, fast skeletal, and cardiac that are coded by MYBPC1, MYBPC2, and MYBPC3 genes, respectively (Heling, Geeves and Kad, 2020). Most isoforms can be found in respective muscle types (i.e. cardiac in cardiac, and fast skeletal in fast skeletal muscles etc.), but the naming convention does not elaborate on the complex nature of MyBP-C isoform expression. For example, mammalian atrium was shown to contain small quantities of slow skeletal isoform of MyBP-C (Dhoot and Perry, 2005). Furthermore, other studies have shown a cardiac tissue in mouse heart failure model to contain fast skeletal isoform of MyBP-C (Lin *et al.*, 2013). The investigation of both splicing and the effect of all isoforms on contractile apparatus are vital, as mutations in cardiac (Harris, Lyons and Bezold, 2011) and both skeletal (Gurnett *et al.*, 2010; Markus *et al.*, 2012; Bayram *et al.*, 2016) isoforms were shown to be a cause of hypertrophic cardiomyopathies and skeletal myopathies, respectively. To complicate matters further, different gene expression per tissue type (i.e. the expression of slow skeletal isoform in fast-twitch muscles) (Yamamoto and Moos, 1983; Dhoot *et al.*, 1985) is not the only difficulty facing the characterisation of MyBP-C isoforms. For example, slow skeletal MyBP-C isoform was suggested to have multiple expression profiles, thus leading to different ssMyBP-C isoforms (Ackermann and Kontrogianni-Konstantopoulos, 2010, 2013). Unfortunately, fast skeletal and slow skeletal isoforms are less characterised than cardiac isoform (Ackermann and

Kontrogianni-Konstantopoulos, 2011a; Li *et al.*, 2016), most likely due to the link between cMyBP-C isoform and HCM.

MyBP-C appears to play a crucial role in contractile regulation. For example MyBP-C centralised location (i.e. C-zone) appears to be crucial at correcting the inhomogeneity arising from different Ca^{2+} concentrations (Previs *et al.*, 2015), although a clear definition of the role of each isoform is still under debate, as the conditional co-expression of multiple isoforms in a tissue is still unclear (Lin *et al.*, 2018). Using a combination of biophysical techniques Lin and colleagues have reported similarities between ssMyBP-C and cMyBP-C at low calcium and fsMyBP-C and cMyBP-C at high calcium. Their structural studies suggest that all isoforms of MyBP-C interact with tropomyosin, shifting it away from myosin binding sites on the thin filament and that the extent of this shift is isoform-dependant. Finally, they suggest that the cardiac isoform can operate at a full range of calcium concentrations to match the dynamic range of intracellular calcium concentrations present on beat-to-beat bases, and similarly they suggest that low and high calcium-concentration specificity for slow skeletal and high skeletal have evolved to fine-tune contraction in skeletal muscles.

3.2. Results

Results presented in this chapter are taken from a published study (Pilagov *et al.*, 2023) conducted on skeletal muscle as a means of describing a novel single-molecule approach to tracking myosin ATPase activity throughout a skinned skeletal myofibril and demonstrating the effects of MAVA and PKA on myosin ATPase activity. The methods for this chapter are described in an appropriate section of this thesis (see Chapter 2 – Materials and Methods). Please refer to the sections describing experiments with skeletal muscles.

3.2.1. Tracking Cy3-ATP Events On the Sub-sarcomeric Level

Myosin ATPases were tracked throughout the skeletal muscle sarcomeres using Cy3-ATP doped into non-fluorescent ATP molecules, the Cy3-ATP events were isolate individually and super-localized for both accurate duration of precise binding location. This was performed by evaluating the event durations and positions, following the data extraction described above (see 2.3.4.a). When plotted (see Figure 23 A), positions of each Cy3-ATP event relative to both Z-discs and subsequently to the M-line (calculated as midway between the Z-discs). Cy3-ATP events could be analysed either separately, using P-,C- and D-zones of the thick filament, or combining them all together to show all zones events simultaneously (from now on referred to as “all zones”). The advantage of simultaneous analysis was an increased number of events, leading to a more precise fit. Overall, both analyses were implemented to minimise the error, while maximizing the resolution (i.e. the ability to monitor all zones separately). The zonal positions in relation to the M-line were taken from a previous titin study (Tonino *et al.*, 2019; Bennett, Rees and Gautel, 2020).

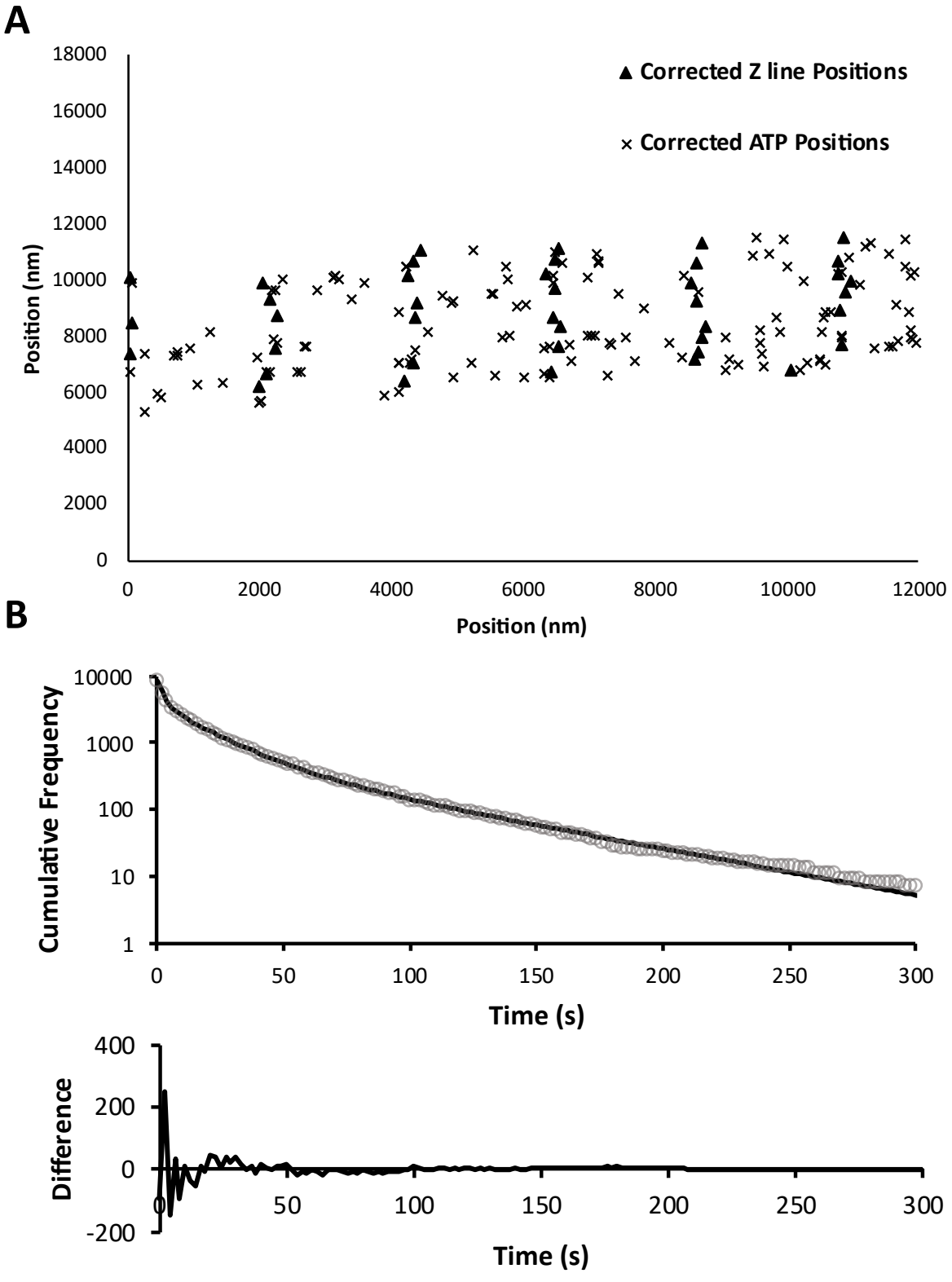


Figure 23. A graphical representation of a myofibril that was analysed by fitting a survival frequency graph.

A) Myofibrils presented as locations of Z-discs (filled triangles) and Cy3-ATP events (crosses), Axes are given in nm. B) A survival frequency graph of the collected Cy3-ATP events (empty, grey circles) from all sarcomeres observed in myofibril A). The survival graph is fitted to 3 exponentials, with the combined fit shown in black. The residual of the fitting is shown below the survival fit.

The fitted data was arranged in a cumulative frequency graph and fitted up to three exponentials. Cumulative frequency (or survival frequency) graphs had time on the X-axis and total number of events of that duration on the Y-axis (see Figure 23 B). The rates of reduction in event frequency could be fitted using natural logarithmic exponentials, thus producing the derived rates and raw amplitudes used for final calculations. The natural logs were used as it was easier to visualise the fitting of exponential components during the analysis. The initial estimate for the number of exponentials to be fitted to survival graphs was chosen based on well-established stopped-flow experiments (Walklate *et al.*, 2022) showing two exponentials representing DRX and SRX states of myosin. Our work had placed DRX and SRX at 0.04 s^{-1} and 0.004 s^{-1}, respectively. Fitting to two exponentials resulted in incomplete fits with large residuals, thus resulting in a third exponential being introduced (see Figure 23B). The third, fastest rate of 0.36 s^{-1} (after photobleaching correction, described in 3.2.5.b) was attributed to fast/non-specific events, that were considered to be attaching to myosins only partially, not attaching at all, or attaching to other ATPases (e.g. on the Z- or M-lines). Photobleaching corrected rates were comparable to those described in the literature (Hooijman, Stewart and Cooke, 2011). The absence of the faster rater in stopped flow experiments could be explained by the nature of the experiment, with stopped flow having a much larger fluorescent concentration and measuring a change in fluorescence upon MANT ATP attachments. Thus, stopped-flow was unable to detect events that are: not fully attached to myosin molecules and thus not emitting, not attached to myosins but are just diffusing through, or are attached to other ATPases that do not provide fluorescence observed upon MANT ATP attachment to myosin. Furthermore, while stopped flow experiments are measuring the change in fluorescence based on the number of MANT ATP molecules attached, our experiments measure the rate of Cy3 ATP detachment, which is a subtle but essential difference.

The proportion of three exponentials were reported as an adjusted percentage of total amplitude of fluorescent ATP events. The amplitude correction was used to normalise all myosin ATPases to the middle rate (i.e. DRX). In such, the correction was applied to both Fast and SRX populations to reconcile larger/lower amplitudes detected due to the faster/slower rates of Cy3-ATP attachment frequency. To elaborate further; slower evets would naturally have a lower amplitude because of lower turnover rate,

and would need a proportional increase based on the rate ratio between the fast and slow populations. This relationship between faster and slower events could be described with the flowing equation:

$$AMP_{corr} = AMP_{fit} \frac{k_{DRX}}{k_{fit}},$$

where AMP_{corr} is the amplitude after the correction, AMP_{fit} is the amplitude prior to the correction, k_{DRX} is the rate of DRX and k_{fit} is the rate of the amplitude that is undergoing the correction. Here and below, DRX was chosen as a normalising rate, but this could have been any other rate (i.e. SRX or Fast), as long as all calculations were using the same rate. After correction, relative percentage of each state (i.e. Fast, DRX or SRX) population was reported as 10.8 (±0.5)% Fast, 53 (±1.1)% DRX, and 36 (±2.8)% SRX (see Figure 24). The rates were reported without photobleaching correction, which was used exclusively to compare acquired rates with rates in the literature. Photobleaching correction was unnecessary, as rates were compared in between each other, thus cancelling out the correcting during calculations.

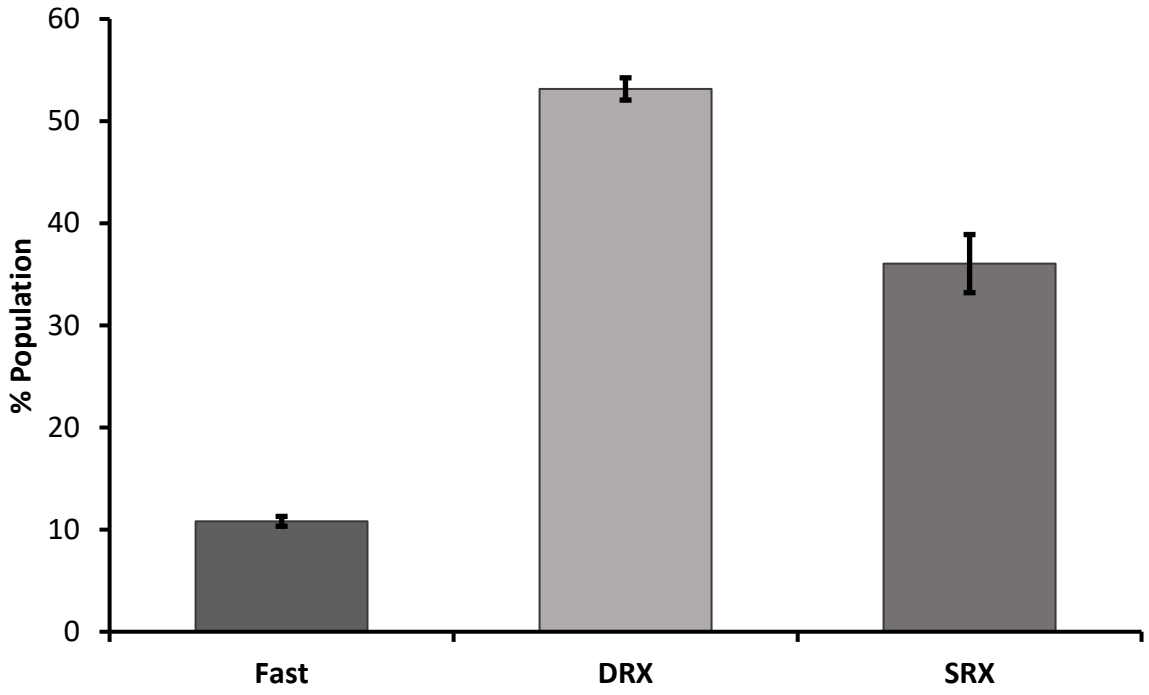


Figure 24. A bar chart of myosin states distribution throughout all measured myofibrils.

The population is given in precent of total corrected (see 3.2.1) amplitude. The correct rates were reported as 10.8 (±0.5) % Fast, 53 (±1.1) % DRX, and 36 (±2.8) % SRX. Error bars are given as standard deviations of percentage population.

3.2.2. Mapped Cy3-ATP Events Reveal Three Lifetimes

The calculations for myosin ATPase states (i.e. Fast, DRX, and SRX) for the whole sarcomere were closely followed by the same calculations conducted for the individual zones of the A-band. The resulting cumulative frequency graphs (see Figure 25) were plotted similarly to the graphs containing the data for the whole sarcomere (above). Zones were established from previous studies using the position of titin along the thick filament to establish the position of MyBP-C super repeats (Tonino *et al.*, 2019; Bennett, Rees and Gautel, 2020) and using the α-actinin-Alexa 488 labelled Z-discs as fiducial markers. By utilising the Alexa 488-labelled fiducial markers, an approximate position of the M-line was calculated for each sarcomere, thus establishing the bins of the each zones of the A-band. The zones were designated to be; P-zone (0–159 nm), C-zone (160–500 nm), and D-zone (501–800 nm). Distance given in nm from the M-line. Following calculations above, the relative populations of myosin states for each zone was determined individually (see Figure 26, Table 1). The

largest SRX population (52.5 ±4 %) was observed in the C-zone, implicating sMyBP-C in pushing myosin heads into a more energy-conserving, SRX state. The largest DRX population (54 ±2.5 %) was observed in the P-zone. Events that didn't fall into any zones of the A-band were not counted during the analysis and only comprised ~6 % of total number of events.

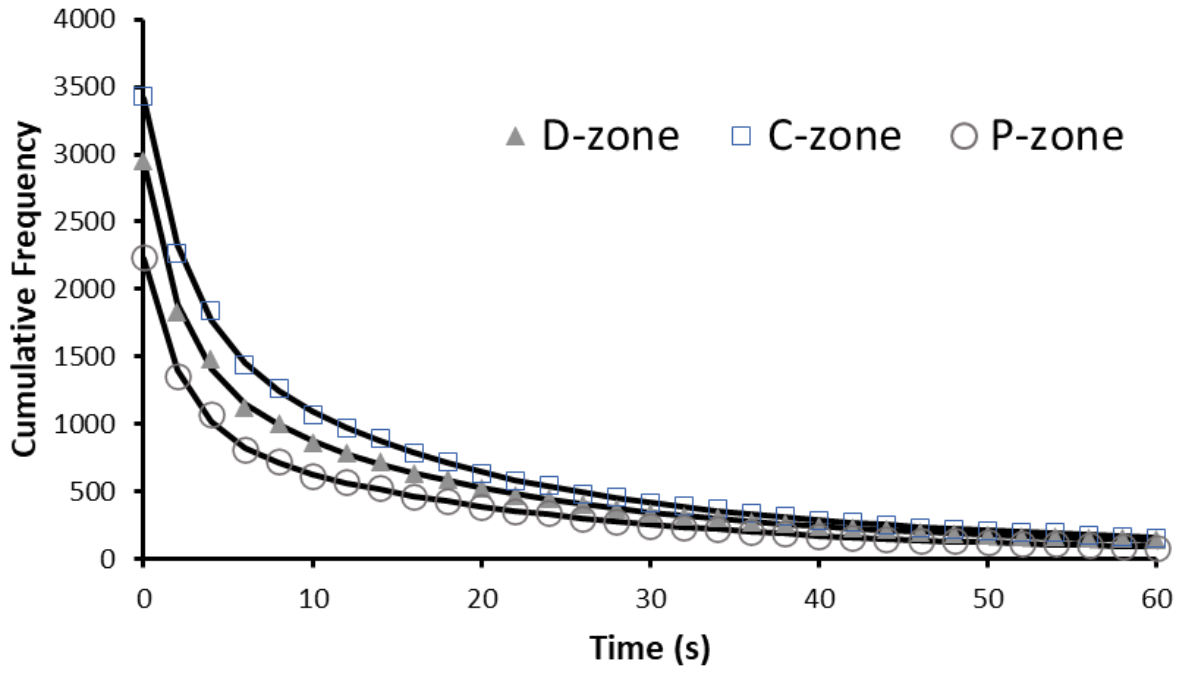


Figure 25. A cumulative frequency histogram to show the distribution of Cy3-ATP events through the zones of the thick filament.

Cumulative frequency histogram describing the population of Cy3-ATP molecules over time in individual zones of the A-band. D-zone events are shown in filled, grey triangles, C-zone events are shown in empty, blue squares and P-zone events are shown in empty, grey circles. All fits are shown as black lines.

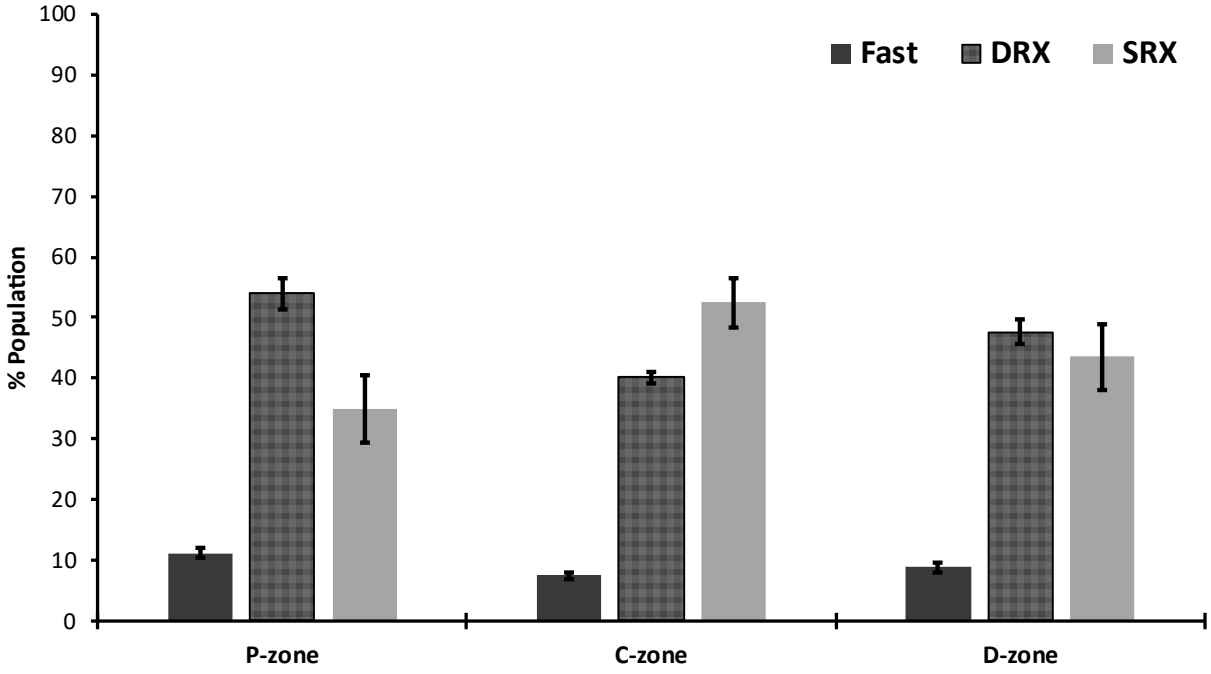


Figure 26. Bar chart showing the relative percentage of each myosin state in each zone of the A-band.

The C-zone has the largest SRX population, while the P-zone has the largest DRX population. Fast events fluctuate ~10% for each zone. The largest DRX population is localised to the P-zone, while the C-zone harbours the smallest DRX population.

Untreated % (±SEM)	P-zone	C-zone	D-zone
Fast	11.1 (±0.8)	7.4 (±0.5)	8.8 (±0.8)
DRX	54 (±2.5)	40.1 (±1)	47.7 (±1.9)
SRX	35 (±5.5)	52.5 (±4)	43.6 (±5.4)

Table 1. Table showing distribution of relative % myosin states for all zones of the A-band.

The distribution of ATPase activity across untreated myofibrils shows the largest population of SRX in the C-zone; 52.5 (±4) %, while the largest DRX population is reported in the P-zone; 54 (±2.5).

3.2.3. Altering myosin ATPase using PKA and MAVA

In addition to studying untreated myofibrils, myofibrils were perturbed with a well-known myosin repressor – MAVA and a well-known myosin activator PKA. To represent the results of our study in a clear way, SRX to DRX ratio was calculated by dividing the relative number of SRX events by the relative number of DRX events. The resulting ratio produced a clear way of comparing experiments with different conditions (i.e. untreated, MAVA and PKA) simultaneously. Figure 27 shows the difference in SRX/DRX ratio upon the respective treatment, with statistically significant treatments indicated by "*". The precise data is also provided in a table below (see Table 2). Furthermore, a significant reduction was observed in sarcomere lengths (SL) following the PKA treatment from 2,219 (±168 SD, P = 0.0319) nm to 1,920 (±377 SD) nm. MAVA did not cause a significant change in SL, 2,121 (±132, P = 0.2433) nm.

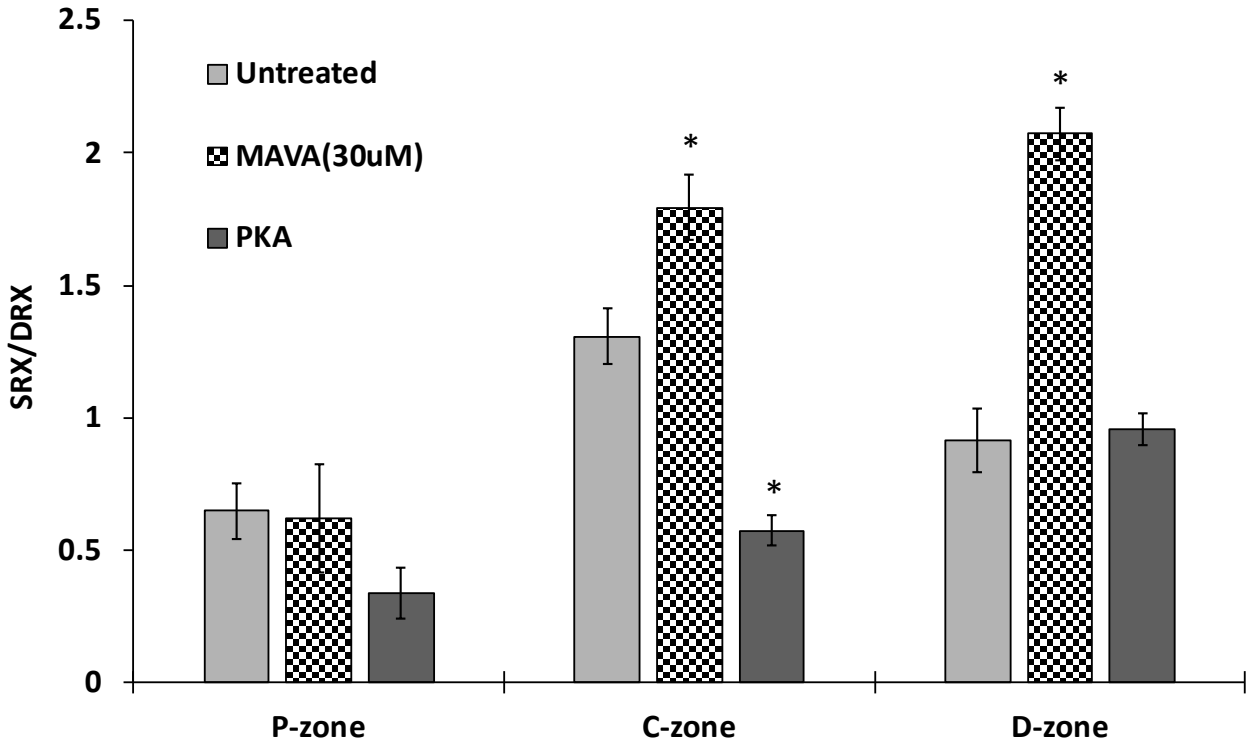


Figure 27. A bar chart showing difference in Cy3-ATPase attachment lengths in untreated and perturbed skeletal myofibrils.

The chart is broken down into P,C and D zones of the thick filament. Treatments are shown in dark grey, striped and light grew for untreated, MAVA treated and PKA treated, respectively. A clear increase in SRX/DRX ratio in the C and D zones(P = 0.0093 and P = 0.0001, respectively) following the MAVA treatment indicates the involvement of sMyBP-C in controlling the myosin ATPase activity in the C-zone but not in the D-zone. On the other hand, PKA had only shown a statistically significant decrease in SRX/DRX ratio in the C-zone (P = 0.0001) hinting at sMyBP-C as its target. The change values are given as a ration of SRX/DRX for the ease of interpretation. Error bars were calculated using standard error of the mean (SEM). Changed with the p values < 0.05 are labelled with a star atop the bar.

A) SRX:DRX ratio (Figure 27)	P-zone	C-zone	D-zone
Untreated	0.6 (±0.1)	1.3 (±0.1)	0.9 (±0.1)
+MAVA	0.6 (±0.2)	1.8 (±0.1)*	2.1 (±0.1)*
+PKA	0.3 (±0.1)	0.6 (±0.1)*	1.0 (±0.1)

Table 2. Table, showing the distribution of SRX/DRX ration for each zone of the thick filament.

*The data is given for all; untreated, MAVA treated and PKA treated experiments. * is indicating the significant change form untreated data.*

3.2.3.a. Mavacamten decreases ATPase in Skeletal Muscles

MAVA has been shown to decrease myosin ATPase activity though lowering the rate of P_i release (Green *et al.*, 2016; Kawas *et al.*, 2017; Grillo *et al.*, 2019) (for brief pharmacology see 1.3.2.a), thus pushing myosins into SRX. The effects of 30 μM (full saturation) MAVA was measured on skeletal myofibrils using a standard 2-second interval stroboscopic illumination. This concentration was exceeding half-maximum inhibitory concentration (IC_{50}) for skeletal muscle ~4-5-fold (Scellini *et al.*, 2021; Auguin *et al.*, 2023). Higher concentration was aimed at testing the limits of repression achievable with cardiac-specific MAVA in skeletal muscle at concentration higher than IC_{50}. A separate breakdown of each zone myosin population can be seen in Figure 28.

Figure 28 A is showing the relative change in myosin states population for all zones of the thick filament following MAVA treatment. The P-zones shows very little change. Both C and D zones show a significant decrease in DRX and an increase in SRX populations. The change is especially apparent in the D-zone, it has a smaller untreated SRX population and a larger subsequent increase in SRX population following MAVA treatment. The C-zone, on the other hand, has a larger untreated SRX population, with a smaller subsequent increase. Interestingly, the final percentage of SRX in both D and C zones are similar (63% to 60%, respectively), with no significant difference between them ($p = 0.45$). The D-zone is the second largest contributor of myosin crowns, with the C-zone being the largest (~6, 25, 18 for P, C and D zones, respectively (Bennett, Rees and Gautel, 2020)). Table 3 shows the exact data presented in Figure 28.

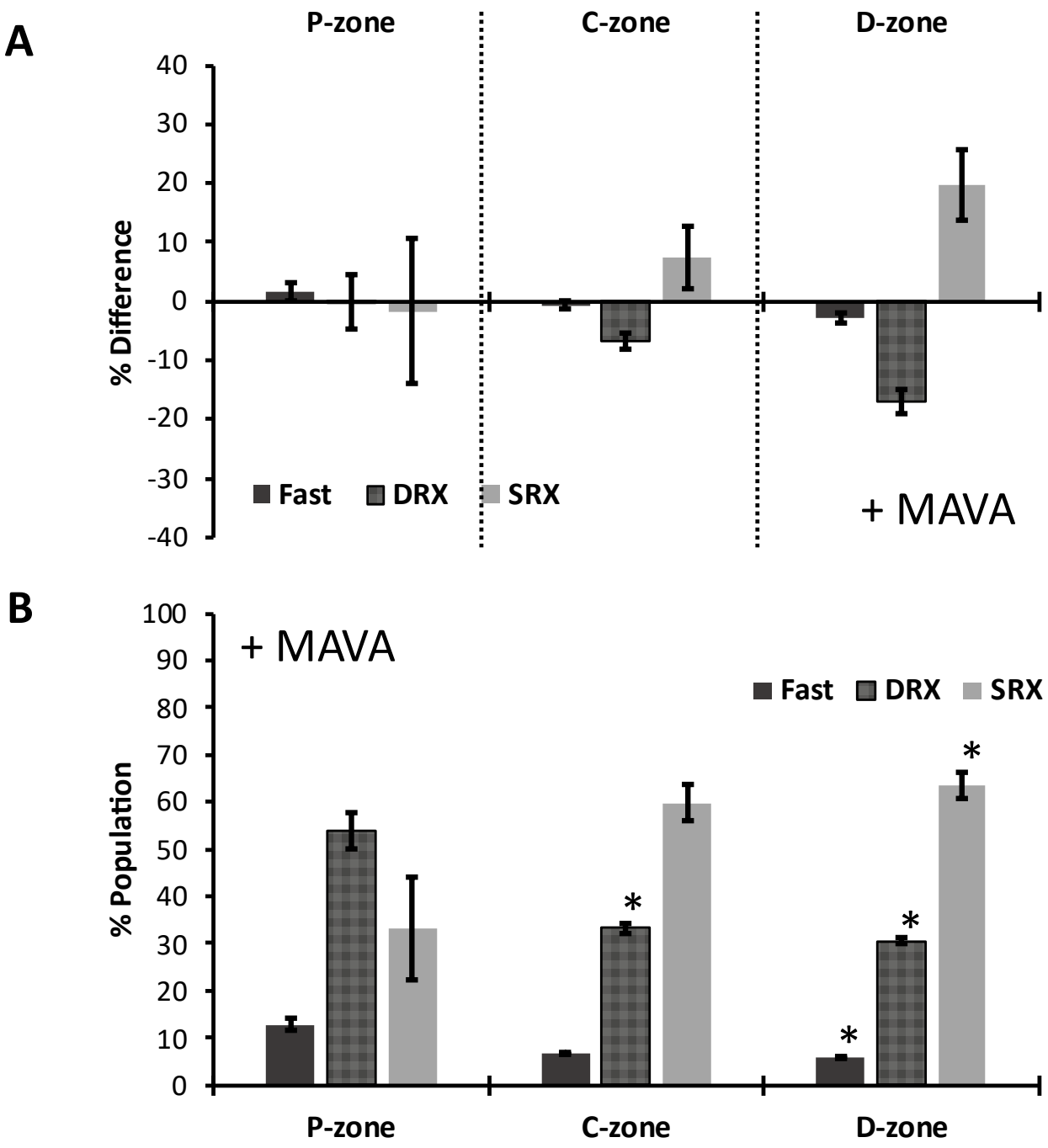


Figure 28. Bar charts showing the effects of MAVA on skeletal myofibrils.

*A) The difference (in percentage) in myosin states population in each zone of the thick filament following MAVA treatment when compared to untreated samples. Zones are labelled at the top and separated with dotted lines. B) Bar charts showing the final composition of myosin heads in each zone of the thick filament in percentage. For all; fast, DRX and SRX events are represented by bars coloured with dark grey, striped and light grey, respectively. Upon the treatment, a significant change as observed in the DRX population of the C-zone (P = 0.0003), alongside in each population of the D-zone (fast P = 0.0013, DRX P = 0.0001, SRX P = 0.0028). Changes that were statistically significant from untreated data are indicated with an *.*

A) Change from untreated to MAVA (Figure 28 A)	P-zone	C-zone	D-zone
Fast	1.7 (±1.6)	−0.7 (±0.6)	−2.8 (±0.8)
DRX	−0.1 (±4.5)	−6.7 (±1.5)	−17.1 (±2)
SRX	−1.6 (±12.2)	7.4 (±5.4)	19.8 (±6.1)
B) MAVA (Figure 28 B)			
Fast	12.8 (±1.3)	6.7 (±0.4)	6 (±0.2)*
DRX	53.9 (±3.7)	33.4 (±1.1)*	30.6 (±0.6)*
SRX	33.3 (±10.8)	59.9 (±3.6)	63.4 (±2.7)*

Table 3. Tables mirroring the results obtained in Figure 30.

*A) Shows the precise difference observed in fig.30 A in each state of myosins following MAVA treatment for each zone of the thick filament. B) Similarly, showing the exact values obtained from the bar-chart shown in fig.30 B. Values that are statistically significant form the untreated data are labelled with an *.*

3.2.3.b. PKA Increases ATPase Activity of Skeletal Myofibrils

For our study to be complimentary, a cAMP-dependent kinase (PKA) was employed to investigate the effects of a well-known myosin activator; PKA. PKA has a well-documented phosphorylation sites in the M-region of MyBP-C. Similarly to MAVA treatment, a protocol outlined in the literature was followed (Tong *et al.*, 2008) to establish the effects of MyBP-C phosphorylation in each zone of the thick filament. The largest effect of PKA treatment was observed in the P and C zones, with the largest decrease occurring in SRX population, to favour DRX population (see Figure 29). Interestingly, no significant change was observed in the D-zone following the treatment. The exact data for PKA treatment can be reviewed in Table 4.

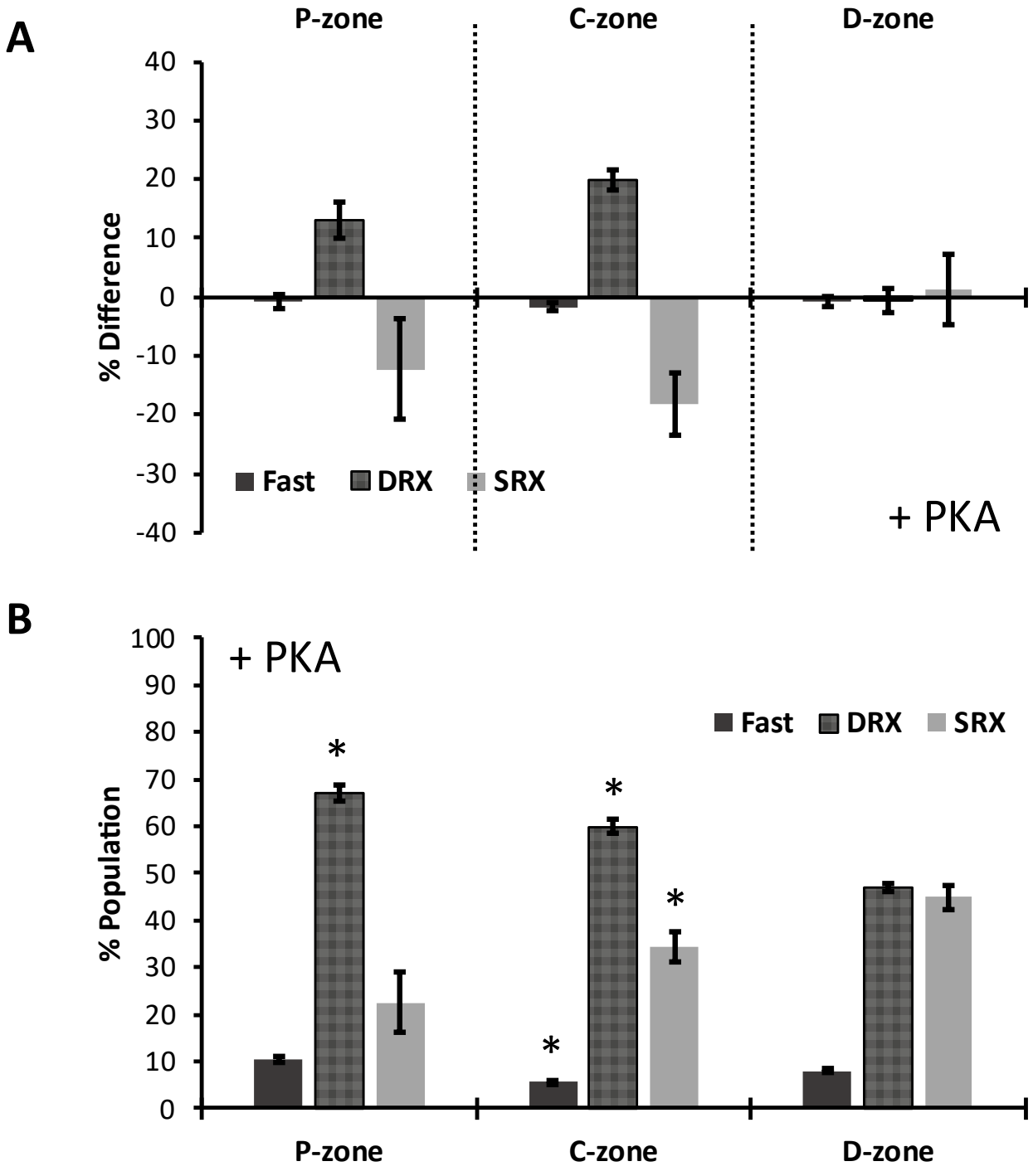


Figure 29. Bar charts showing the effects of PKA on skeletal myofibrils.

A) The difference (in percentage) in myosin states population in each zone of the thick filament following MAVA treatment. Zones are labelled at the top and separated with dotted lines. B) Bar charts showing the final composition of myosin heads in each zone of the thick filament in percentage. For both, fast, DRX and SRX events are represented by bars coloured with dark grey, striped and light grey, respectively. PKA treatment has indicated a significant change in DRX population in the P-zone (P = 0.0001) and in all rates of the C-zone (fast P = 0.0101, DRX P = 0.0001, SRX P = 0.0034). Changes that were statistically significant from untreated data are indicated with a star.

A) Change from untreated to PKA (Figure 29 A)	P-zone	C-zone	D-zone
Fast	−0.8 (±1.1)	−1.7 (±0.6)	−0.7 (±0.8)
DRX	13.1 (±3)	19.9 (±1.7)	−0.7 (±2.1)
SRX	−12.4 (±8.6)	−18.1 (±5.2)	1.4 (±6)
B) PKA (Figure 29 B)			
Fast	10.3 (±0.7)	5.7 (±0.3)*	8.1 (±0.4)
DRX	67.1 (±1.6)*	60 (±1.4)*	47 (±0.9)
SRX	22.6 (±6.6)	34.3 (±3.3)*	44.9 (±2.7)

Table 4. Tables mirroring the results obtained in Figure 31.

*A) Shows the precise difference observed in fig.31 A in each state of myosins following PKA treatment for each zone of the thick filament. B) Similarly, showing the exact values obtained from the bar-chart shown in fig.30 A. Values that are statistically significant form the untreated data are labelled with an *.*

3.2.4. Visualising the Effects of PKA Using Pro-Q Dimond Phosphoprotein Gel Stain

To investigate the effects of PKA phosphorylation further, a SDS-PAGE gel was stained with two different stains: Pro-Q-Diamond and Coomassie Blue (see Figure 30). The phosphorylation levels in ProQ gel were provided along with approximate protein concentration in Coomassie. Gels were run for full rabbit psoas myofibrils, precipitated

sMyBP-C and a control of a known PKA target C0C3 region of cMyBP-C. Both precipitated sMyBP-C and full psoas myofibrils show similar phosphorylation levels when compared to the respective untreated samples band of sMyBP-C. Furthermore, the effects of PKA on C0-C3 subunits of cMyBP-C, which contain the M-domain with the known PKA phosphorylation sites, was shown as a control for Pro-Q sensitivity to PKA phosphorylation. These results indicate an intriguing possibility of a yet unknown phosphorylation pathway for PKA that alters the ATPase rates of myosin heads. This has been expanded upon below in the discussion.

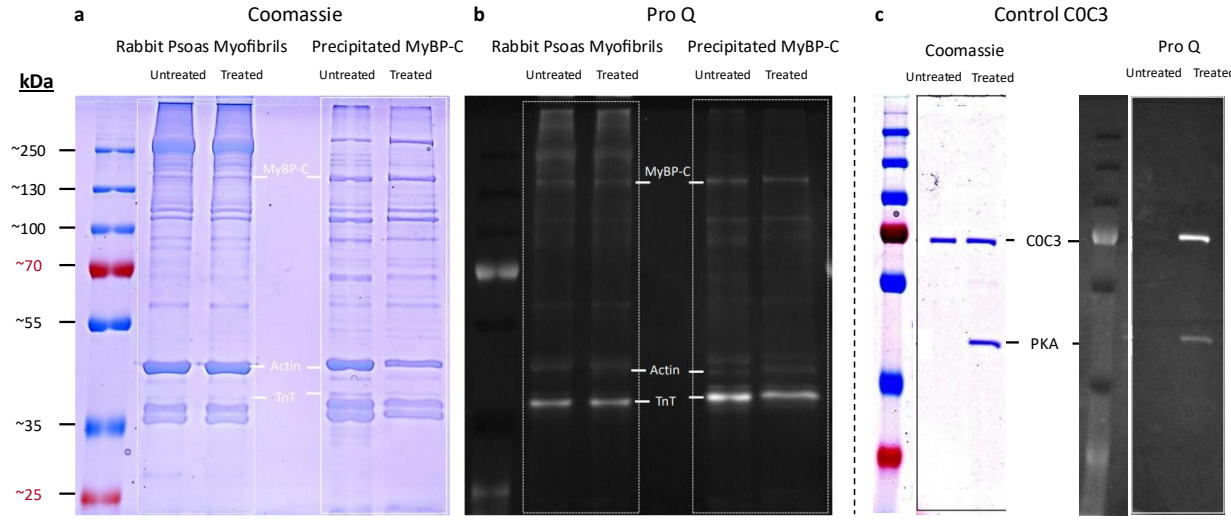


Figure 30. SDS-PAGE gels showing both protein concentration and phosphorylation levels using Coomassie and ProQ-Dimond stains.

SDS-PAGE gels showing phosphorylation levels of proteins of interest and relative protein concentration using ProQ-Dimond and Coomassie Blue stains, respectively. a) SDS-PAGE gel of skinned rabbit psoas myofibrils. The first well is showing untreated samples, while the second well is showing samples treated with PKA. The last two wells, labelled appropriately, are showing the separation of MyBP-C purification. Proteins of interest (i.e. MyBP-C, Actin and TnT) are labelled appropriately. b) Similar to the previous gel but this time labelled with phospho-sensitive ProQ-Dimond stain. c) Control gels showing the difference in phosphorylation levels between C0C3 region of cMyBP-C pre and post treatment with PKA. The size of proteins in the ladders (PageRuler Plus Prestained Protein Ladder, Fisher Scientific, 11832124) are labelled appropriately on the first gel (a), and are kept consistent throughout all other gels.

3.2.5. Imaging Technique and Photobleaching Rate Derivation

Single-molecule studies are novel and high-resolution techniques for defining the localisation of fluorescent events, yet as other fluorescent techniques they intrinsically face a number of problems including photobleaching. To combat photobleaching the stroboscopic illumination technique was employed to reduce the exposure time of

fluorophores and thus reduced the photobleaching. Furthermore, the experiments were conducted to determine the photobleaching rate as a component of observed detachment rate of Cy3-ATP molecules. Photobleaching experiments were conducted to compare observed rates with rates defined in the literature.

3.2.5.a. Stroboscopic Imaging

Stroboscopic illumination employed in all our experiments was designed to prevent extensive photobleaching of the fluorescent samples. Stroboscopic illumination is the easiest to explain using an example below (see Figure 31). In this example a theoretical Cy3 fluorophore was designated to photobleach after 3 frames of exposure. While the illumination is consistent, the imaging time is constrained to 3 frames each 200 ms (T_{exp}) but if the frames were to be separated and assuming the fluorophore position stays constant, the survival time of fluorophore can be increased by allowing for longer period of laser OFF time ($T_{tl} - T_{exp}$). In the example below (Figure 31), the T_{tl} was extended while keeping the T_{exp} constant, thus delaying the photobleaching process by 600 ms and 1.5 sec for middle and bottom images, respectively. By increasing the OFF time of the laser, the fluorophore photobleaching was delayed and thus increased the imaging period without sacrificing in resolution. In most of our experiments, 2 (single-molecule) or 5 (ensemble) sec time-lapse were utilised, thus providing up to 1800 ms or 4985 ms laser OFF times for single-molecule and ensemble imaging, respectively.

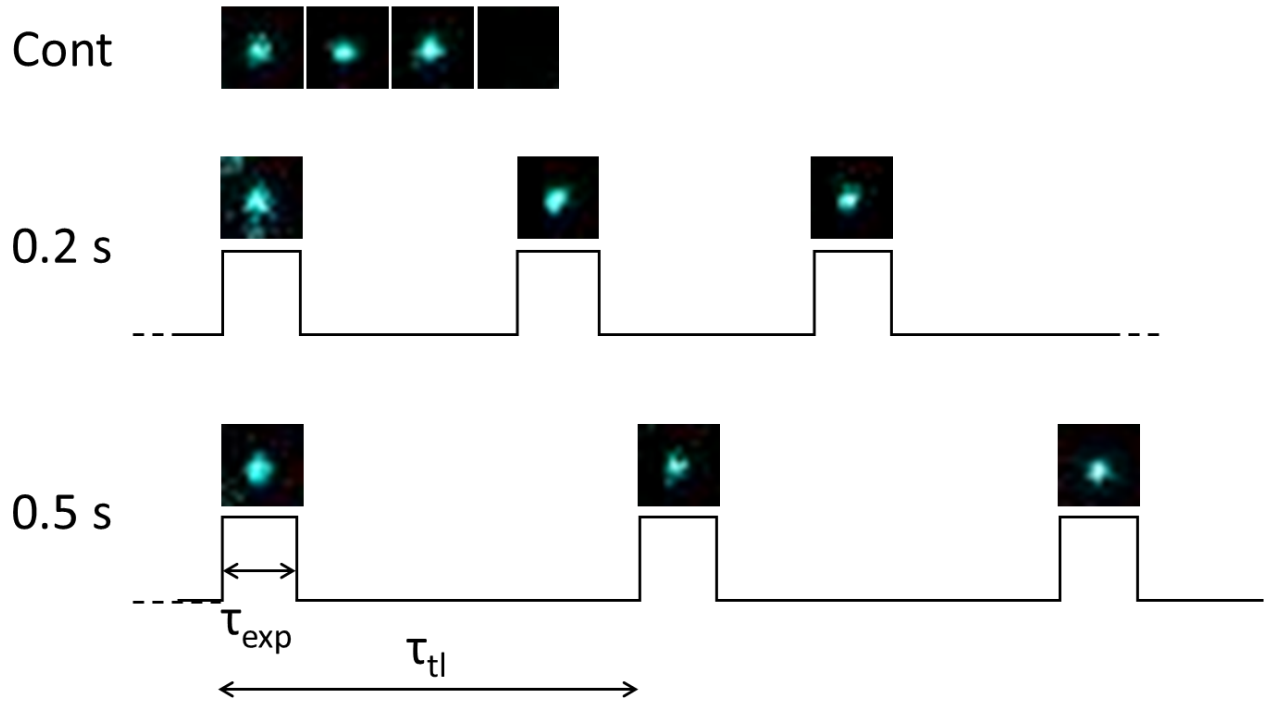


Figure 31. A diagram explaining the concept of stroboscopic illumination.

A diagram of stroboscopic illumination for fluorescently labelled Cy3-ATP molecules with Texp being the exposure time of each illumination and total time per frame (Ttl). The diagram is showing the difference between Cy3-ATP exposure time from continues illumination (top) to 1 sec stroboscopic illumination (bottom), pointing to an increased imaging time of stroboscopic illumination when compared to constant exposure.

3.2.5.b. Defining Photobleaching Rate of the System

Using stroboscopic approach, the photobleaching rate for Cy3-ATP was calculated for both laser powers used in; single-molecule and ensemble experiments (for ensemble see 5.2.9). Both single-molecule experiments (on cardiac and skeletal muscle tissues) were conducted using the same dye and the same laser power, so the same control was used to determine the photobleaching rate for both.

Below an approach used to define the photobleaching rate for single-molecule experiments is defined. For this approach a formulae describing such relationship was derived from the works of (Gebhardt *et al.*, 2013):

$$k_{off} = k_{obs} - k_{bl} \cdot \frac{T_{exp}}{T_{tl}},$$

where k_{off} is the rate of ATP release deconvoluted from the rate of photobleaching, k_{obs} is the rate of ATP release observed initially combining both k_{bl} and k_{off}, k_{bl} is the

photobleaching rate constant, T_{exp} is the exposure time of the experimental system, and T_{tl} is the total time lapse between the consequent frames. The relationship described by this equation can be visualised simplistically (Figure 32).

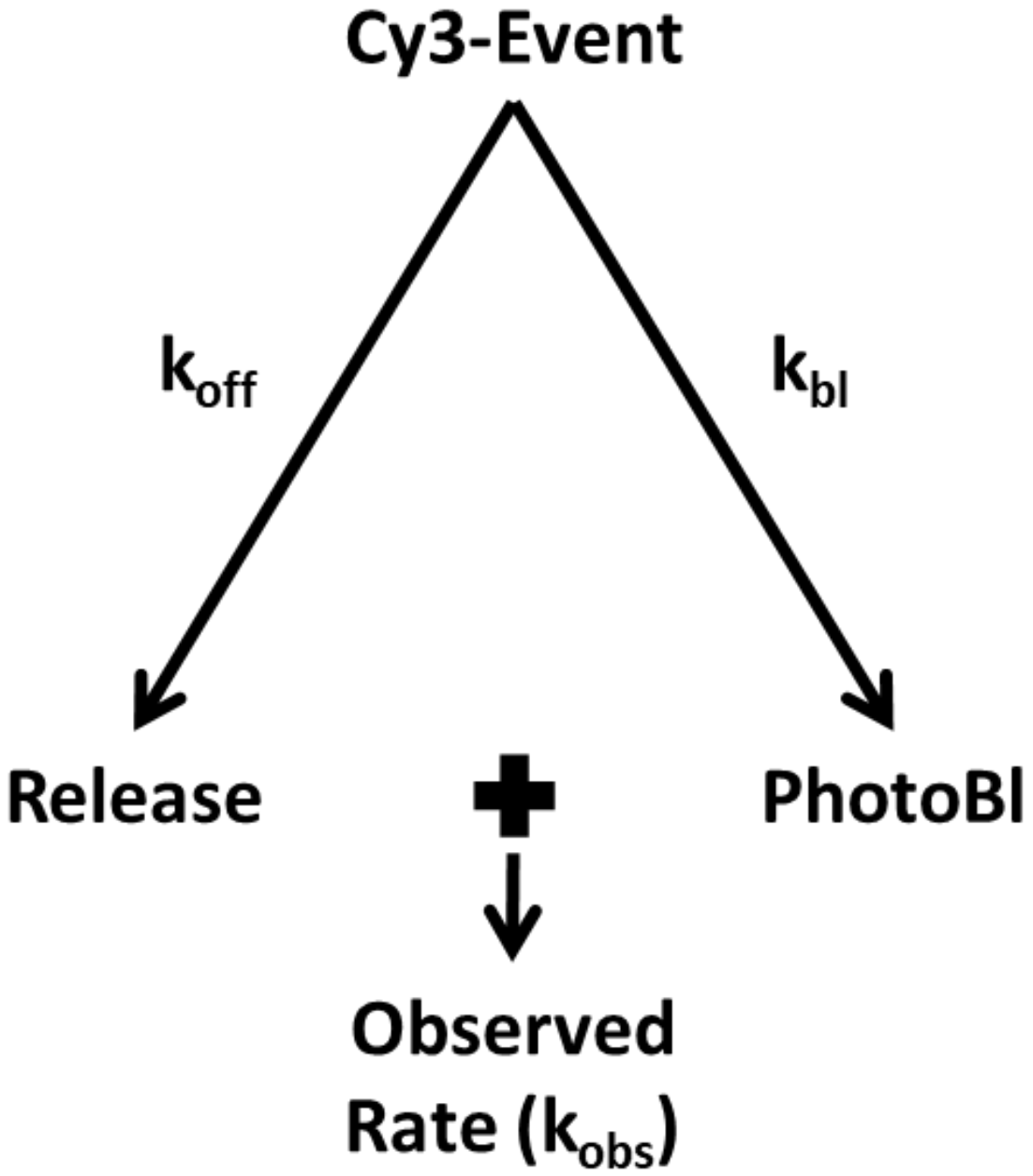


Figure 32. A schematic/mathematical representation of photobleaching process.

Cy3-ATP evens are either hydrolysed and released by myosins (Release) at a rate of k_{off}, or photobleached (PhotoBl) at the rate of k_{bl}. Together, they compose the observed rate constants derived during the analysis (Observed Rates), that detach from the imaged myofibril at the rate of k_{obs}.

Using experiments with a stationary fluorescent signal (Gebhardt *et al.*, 2013; Pilagov *et al.*, 2023) myofibrils were imaged at different time lapses of 0.2, 0.5, 1 and 2 sec for single-molecule experiments. Those results were plotted with *time lapse* against exposure *time*observed photobleaching rate* (see Figure 33), so that the *c* component of the linear fit for this graph would be a function of the photobleaching rate constant. The resulting photobleaching rate was 0.13 ± 0.05 s^{-1} (200 ms exposure, 20 mW laser power) that produced rate constants of 0.36 s^{-1}, 0.04 s^{-1}, and 0.004 s^{-1} for fast, DRX, and SRX, respectively. These rates were in line with rates observed previously by other groups (Hooijman, Stewart and Cooke, 2011).

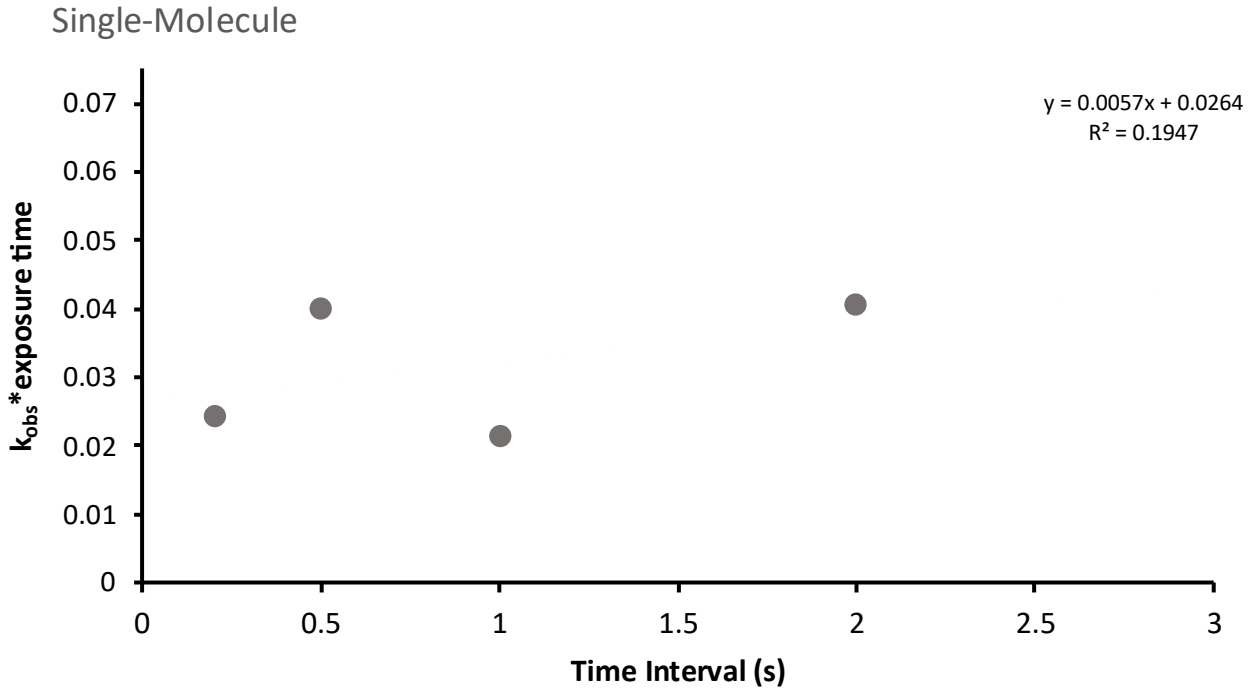


Figure 33. Graphs to present the results of photobleaching experiments.

Graphs representing experiments conducted to determine the rates of photobleaching for single-molecule (Pilagov *et al.*, 2023) *and Ensemble experiments. A) Graph is showing the observed rate*exposure time of the slowest, thus the most photobleaching affected, population of Cy3-ATP molecules releasing from the myosins in single-molecule experiments plotted against each time interval (i.e. 0.2, 0.5, 1, 2 & 5 sec). The intercept of this graph is a derivative of rate of photobleaching (k_{bl}).*

3.2.6. Regenerating Cy3-ATP Using PK/PEP Regeneration System

ATP (both Cy3-ATP and dark ATP) was regenerated using a well-established regeneration system (Radnai *et al.*, 2019) using ~1 unit of rabbit muscle PK (P0294;

Sigma-Aldrich) and PEP (concentration equimolar to Cy3-ATP). In all experiments, 1 h was allowed for the regeneration, incubated either on ice or at 4 °C with constant agitation. To test the effects of the regeneration a well-established stopped flow technique (Walklate *et al.*, 2022) was employed. Using a HiTech Scientific (SF-61 DX2) stopped-flow with 700 µl sample syringes rabbit subfragment 1 (S1) myosin heads were mixed with Cy3-ATP (1 µM) at a range of S1 concentrations of 2.5 µM – 39 µM. Observation chamber was illuminated using an LED lamp (290 nm; Ocean Optics) and employing a WG320 filter to prevent illuminating beam from interfering with the readout. Briefly, MANT-ATP binds to myosin with a conformational change increasing emission at 446 nm, by the change in the signal during mixing populations of all ATPase rates are calculated. Experiment was conducted using Stopped-Flow Buffer. The experiment has concluded a near-full recovery of ADP molecules back into ATP.

The stopped flow was used to analyse samples pre and post PK/PEP regeneration (see Figure 34 A and B, respectively). To determine the precise difference in ADP contamination, the quadratic tight-binding equation (Morrison, 1969) was used, instead of a standard Michaelis-Menten equation, as it did not require a free ligand approximation assumption (i.e. system ligand concentration is approximately equal to the total ligand concentration and thus the ligand concentration is >> enzyme concentration). Ligand concentration for this experiment was close to the enzyme concentration and thus the use of the tight-binding equation was more applicable, as all ligand could not be assumed to remains free in solution during the experiment.

$$\boldsymbol{v} = \boldsymbol{V_{max}} \frac{([\boldsymbol{E_T}] + [\boldsymbol{S_T}] + \boldsymbol{K_M}) - \sqrt{([\boldsymbol{E_T}] + [\boldsymbol{S_T}] + \boldsymbol{K_M})^2 - \boldsymbol{4}[\boldsymbol{E_T}][\boldsymbol{S_T}]}}{\boldsymbol{2}[\boldsymbol{E_T}]}$$

where V_{max} – is the max rate of the reaction, $[E_T]$ is the total enzyme concentration, $[S_T]$ is the total substrate concentration, [ES] is the concentration of enzyme-ligand complex, and K_M is the Michaelis Menton constant. Untreated samples have shown the E_T 500 nM, S_T 278 (±38) nM, and V_{max} = 1.96 (±0.08) (Figure 34 A), while treated samples shown the E_T 500 nM, S_T 544 (±85) nM, and V_{max} = 1.46 (±0.06) (Figure 34 B), indicating a decrease in ADP contamination following the treatment from ~ 50 % to ~100 % ATP. It is necessary to mention, that the concentrations provided by K_M are given after mixing and thus should be compared to 50 % of original Cy3 ATP concentrations (i.e. final Cy3ATP concentration after mixing is 500 nM).

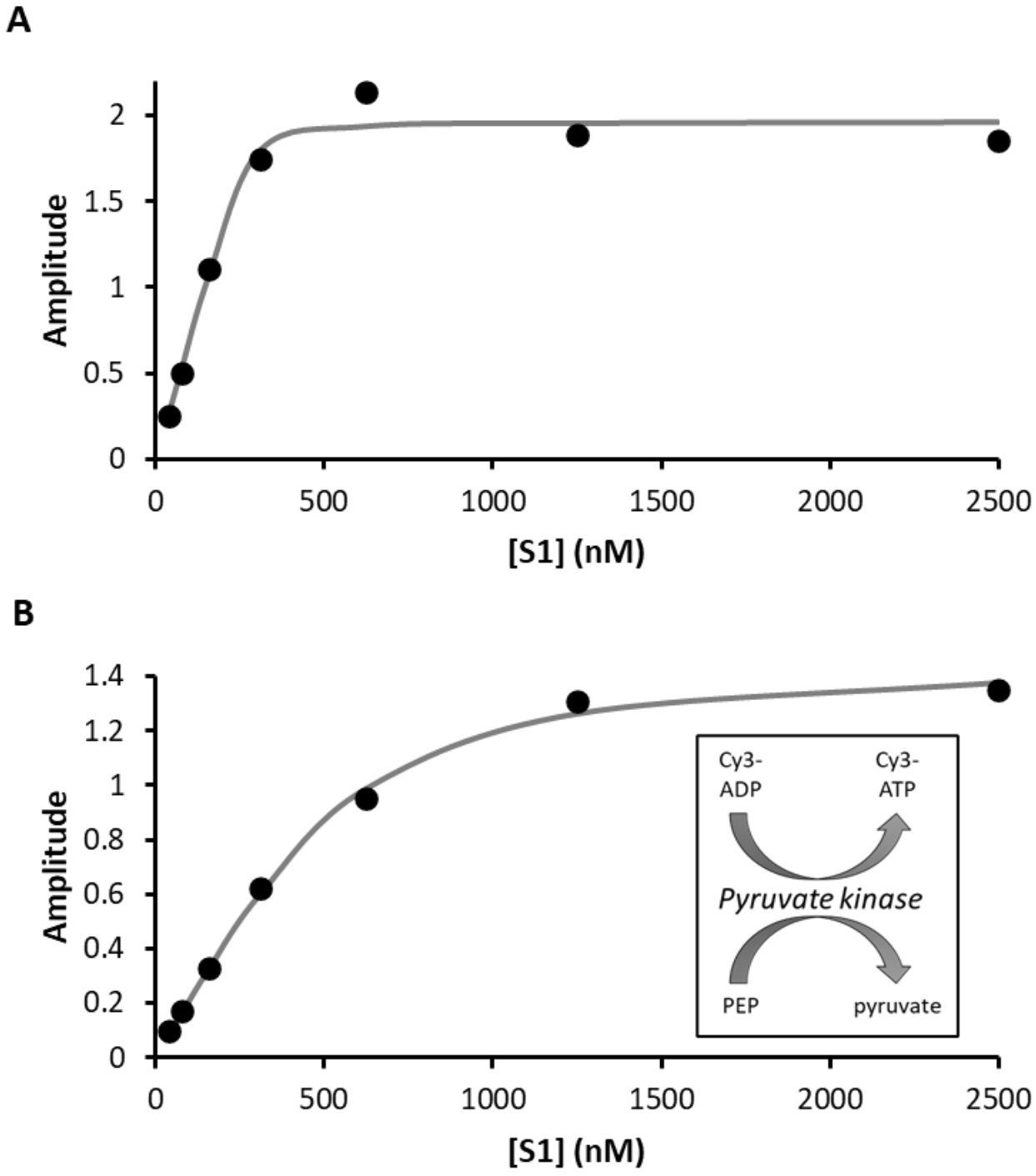


Figure 34. Cy3-ATP binding curves prior and following the regeneration.

A) A graph depicting S1 binging in 2:1 conformation to Cy3-ATP prior to PK/PEP treatment, indicating an approximate 50 % ADP contamination. Fitted values: E_T 500 nM, S_T 278 (±38) nM, V_{max} = 1.96 (±0.08). B) Using the process of nucleotide regeneration employing pyruvate kinase the binding curve has shifted right, indicating a 1:1 stoichiometry of S1 binding to Cy3-ATP and this a near-full regeneration following the 1h treatment with regeneration system. Fitted values: E_T 500 nM, S_T 544 (±85) nM, V_{max} = 1.46 (±0.06). Each point was an average of at least three repeats.

3.3. Discussion

This chapter describes the work conducted using a novel technique that used a custom-build single-molecule microscope to monitor the ATPase rates of myosin heads in skeletal myofibrils. During these experiments three distinct ATPase rates were recorded by following the rates of detachment of fluorescent Cy3-ATP molecules. The fastest rate observed attributed to non-specific (or fast) attachments, with the two slower rates attributed to DRX and SRX, as they were shown to be similar, subject to photobleaching correction, in value with previously reported DRX and SRX rate values as described in literature (Hooijman, Stewart and Cooke, 2011). While relaxed, myofibrils tend to favour more energy-conservative state (i.e. SRX), while during periods of activity, the equilibrium existing between the two is shifted towards the more active state (i.e. DRX). Using our single-molecule approach the population of myosin states were determined in each zone of the A-band individually. Specifically, the sMyBP-C-containing C-zone was investigated, when compared to the D-zone, which does not house any myosin-associated proteins.

Using single-molecule analysis, a baseline SRX population was established for the untreated samples; showing the C and D zones were housing a statistically larger population of SRX than found in the P-zone. Furthermore, the effects of myosin repressor MAVA and myosin activator PKA were investigated. Unsurprisingly, MAVA was found to push myosin heads into SRX, drawing from DRX population in both C and D zones. MAVA was found to be incapable of repressing all myosin heads even when working at ~6-fold excess concentrations, indicating an underline mechanism of ATPase upregulation (or homeostasis) that is independent of the myosin head. Similar study with MAVA (10 μM) but using stopped-flow methodology, had also shown a reduction but not a complete absence of ATPase activity, albeit with S1 and HMM instead of full length myofibrils and using cardiac samples (Rohde *et al.*, 2018). Another stopped flow study using rabbit psoas myofibrils (Walklate *et al.*, 2022), again showed an uncomplete repression of myosin heads even when using 30 μM MAVA.

Further underlining our findings in this chapter, other groups have shown the difference between the effects produced by MAVA on cardiac and skeletal tissues (Scellini *et al.*, 2021). In their studies, they have used a well-established force measurement to

observe the difference between MAVA treated and untreated rabbit fast skeletal and human ventricular myofibrils. The results show a decrease in maximum Ca^{2+}-activated isometric force for both tissue types, but with cardiac tissue having a larger sensitivity to MAVA and thus producing the same levels of isometric force at 10-fold lower MAVA concentrations when compared to rabbit skeletal. The reduction in force for the rabbit psoas, however, even at 10 μM, only results in a ~2-fold reduction, thus indicating a reduction in DRX but not a 100% SRX composition following the treatment. Although some studies showed 100% SRX following only 10 μM MAVA treatment (Gollapudi, Yu, *et al.*, 2021), there were larger concerns in the field regarding some methodology used during these experiments (see 5.3.1).

On the other hand, when treated with PKA, myofibrils were observed to have larger DRX population that was evidently drawn from the SRX population. Interestingly, the effect of PKA treatment was primarily localised to the C-zone, with near-zero changed observed in the D-zone. PKA has been shown to phosphorylate slow isoform of (s)MyBP-C, which is found in fast-twitch skeletal muscle, like rabbit psoas, thus, explaining the effects on the C-zone observed following the PKA treatment. However, the effects PKA may have on other proteins in myofibrils (e.g. titin) could not be ruled out as contributing factor to the observed changes. This study is reporting the direct effects of myosin modulators on the rates of ATPase activity as observed at a single-molecule level on all zones of the A-band individually.

3.3.1. MAVA cannot fully repress myosin heads

MAVA represses myosin heads via inhibiting the rate determining step of P_i release (see 1.3.2.a for pharmacology). Here, MAVA was used at an excess (30 μM, ~6 fold > K_d (Kawas *et al.*, 2017; Scellini *et al.*, 2021)) to establish the maximum repression levels throughout the thick filament. To this effect, MAVA was found to reduced DRX population in both C and D zones, decreasing DRX population in the C-zone from 40.1% (30 heads) to 33.4% (25 heads), with a much larger decrease in the D-zone from 47.7% (26 heads) to 30.6% (17 heads). The resulting increase in SRX was close to the decrease in DRX population. Similar studies (Nelson *et al.*, 2020), working with rat tissue, have reported an increase in DRX in the D-zone, with the C-zone DRX population remaining semi-constant. The final amount of SRX in both D and C zones are comparable between the studies, and just like our study, Nelson et. al shows the

effects of MAVA are limited to max achievable SRX population. In other words, even using ~6-fold K_d, it was found to be impossible to repress all myosin heads into SRX, instead ~ 36 % DRX remained. These findings further validate the use of MAVA for treatment in cardiac tissues, even at higher concentrations. Further investigation is required to establish if MAVA is capable of repressing cardiac tissue to a near-zero DRX population.

The above approach relies heavily on studies (Li *et al.*, 2019; Tonino *et al.*, 2019; Bennett, Rees and Gautel, 2020) conducted to determine the exact position of sMyBP-C in the sarcomere. However, the exact start of sMyBP-C repeats may be fewer as suggested by earlier studies (Luther, 2009). Alternative approaches using affirmers to super-resolve the position of individual MyBP-C molecules have been proposed (Carrington, Tomlinson and Peckham, 2019), potentially providing a more accurate approach for future MyBP-C isoforms position determination.

3.3.2. PKA activity is localised to the C-zone of the Thick Filament

PKA phosphorylation primarily targets Troponin I and the cardiac isoform of MyBP-C (see 1.2.3.a for the full list) in cardiac tissue. Other sarcomeric protein post-translational modifications, thought to be involved in SRX/DRX equilibrium regulation (like RLC), are controlled by other kinases (like MLCK for RLC) (Colson *et al.*, 2010; Heling, Geeves and Kad, 2020). Furthermore, as this study was conducted in relaxed (pCa <9) conditions, the influence of troponin I phosphorylation (by AMPK (Sancho Solis, Ge and Walker, 2011; Gross and Lehman, 2016)) in skeletal muscle is less relevant.

Therefore, the effects on SRX/DRX equilibrium observed in this study are most likely to be caused by sMyBP-C phosphorylation. Tissues used in this study is rabbit skeletal psoas, that consists predominantly of the fast (f) isoform of MyBP-C (Bennett *et al.*, 1986), but also contains lesser amounts of the slow (s)MyBP-C isoform (Reinach, Masaki and Fischman, 1983; Weber *et al.*, 1993). There is some evidence of PKA phosphorylating fMyBP-C, although it may only occur under specific conditions (Lim and Walsh, 1986; Ackermann and Kontrogianni-Konstantopoulos, 2011b; Colson *et al.*, 2012), thus leading us to the conclusion that the changes observed following the PKA treatment, are most likely to be related to sMyBP-C, which was shown to be a

phosphorylation target for PKA (Ackermann and Kontrogianni-Konstantopoulos, 2011b). The composition of MyBP-C isoforms in skeletal muscle is species-and-tissue-specific. For example, a recent study in rat EDL muscle (fast-twitch) has shown 42% of MyBP-C was fast, with the rest 58% combining both slow and spliced isoforms (Li *et al.*, 2019). Other studies have provided insight into the function of fMyBP-C, where it was implicated in the regulating of the force generated by myosin motors, either though interfilamentous force sensing or directly affecting the SRX/DRX ratio (Irving, 2017). Additional studies have also explored the effects of fMyBP-C knockout (Song *et al.*, 2021) and knockdown (Li *et al.*, 2016) with both showing a reduced force-generation capacity for studied muscles, although an increased degree of order was shown, which is at odds with reduced force-generation (Song *et al.*, 2021). Additionally, in vitro and fibre studies have shown fMyBP-C capable of reducing the shortening velocity (Hofmann, Greaser and Moss, 1991; Lin *et al.*, 2018), potentially though fMyBP-C interactions with the thin filament (Walcott, Docken and Harris, 2015).

To summarise, due to the uncertainty of MyBP-C isoform distribution, it was challenging to relate particular isoform to an increase/decrease in SRX observed in this study. However, it is probable, that effects observed during the PKA treatment were a result of PKA phosphorylation of sMyBP-C (Robinett *et al.*, 2019). Experimentally, a decrease in SRX population was observed from 53 % (39 myosins) to 34 % (26 myosins) following the PKA treatment. Interestingly, the initial amount of SRX population in untreated samples is similar to sMyBP-c levels in fast-twitch skeletal myofibrils (Li *et al.*, 2019).

Additionally, a gel-based phosphorylation analysis was conducted on precipitated MyBP-C from psoas muscles (for gels see 3.2.4) to identify proteins responsible for a decrease in SRX population. The phosphorylated MyBP-C was found in untreated samples, with levels of phosphorylation very similar to levels observed following the PKA treatment (see Figure 30). This indicated a potential new phosphorylation event for PKA that affects MyBP-C-myosin head interaction such as titin, that results in a C-zone-exclusive reduction in SRX/DRX ratio, as the only change in SRX/DRX ratio observed in PKA treated samples, was localised to the C-zone. This implies the presence of yet unknown phosphorylation target, which affects MyBP-C-regulated myosin head activity, but does not directly affect the level of MyBP-C phosphorylation. The investigation is further impaired by the nature of sMyBP-C splicing, isoforms

having different molecular weights and thus complicating the gel-based analysis. Although the exact combination of phosphorylation targets of PKA are uncertain, the effect of PKA on myosin ATPase rate in the C-zone is clear. Further investigation into the nature of MyBP-C splicing and position required for better understanding of PKA mechanism of ATPase control.

3.4. Conclusion

In this study, the skeletal rabbit psoas myofibrils were perturbed with a myosin activator - Protein Kinase A (PKA) and a myosin repressor – Mavacamten (MAVA). MAVA has dramatically decreased the number of myosin heads in more active state (DRX), while increasing the population of a more repressed myosins (SRX). However, the levels of repression are limited, unable to pass a threshold ~ 64 % SRX, even when MAVA applied at 6-fold K_d. This finding further justifies the use of MAVA for cardiac patients, as our findings show the off-target effects in skeletal muscles to be limited, even at higher MAVA concentrations. PKA was shown to significantly decrease the repressed (SRX) myosin population in both C and P zones, leaving the D-zone unchanged. The major target for PKA in the effected zones is ssMyBP-C, thus suggesting the link between the decrease in SRX population with ssMyBP-C phosphorylation by PKA. Here a novel technique was presented allowing for a direct visualisation of myosin ATPase activity under perturbed conditions, along with some insight into the mechanism of action of tested pharmaceutical and enzymatic agents.

Chapter 4 – Exploring The Effects of Post-Translational Modifications On β-Myosin Using Single-Molecule Microscopy

4.1. Introduction

In this chapter our previous work with skeletal muscle was expanded on to investigate the effects of post-translation modifications (PTMs) on β-myosin taken from porcine left ventricle. Specifically, the phosphorylation's were observed on the cardiac myosin binding protein-C (cMyBP-C) by protein kinase A (PKA) and regulatory light chain (RLC) by myosin light chain kinase (MLCK). PTMs on both RLC and cMyBP-C contribute to the contractile regulation by the thick filament, thus aiming this study at understanding of how each PTM affect zone of the A-band individually and as part of the whole sarcomere. Similarly to our skeletal approach the release rates of Cy3-labelled ATP molecules was tracked while using Alexa-488 labelled Z-disks as fiducial markers to bin Cy3-ATP events into the A-band zones.

4.1.1. The Effects of β-adrenergic Response on Cardiac Tissue

During a stress response catecholamines hormones, like adrenaline and noradrenaline, stimulate sympathetic nervous system through the class of G protein-coupled receptors, which include adrenergic receptors (Graham, 1990) (see Figure 35). Adrenergic receptors are of three types: α_1, α_2, and β that are couple to G_q, G_i, and G_s protein α subunits of the heterotrimeric G protein, respectively. Extracellular signalling ligands like adrenaline or noradrenaline begin their signalling cascade by binding to G protein-coupled receptors (GPCR) on the target cell, which in turn transfers the conformational change to the aforementioned heterotrimeric G protein

(Robinson-White and Stratakis, 2002). The above-mentioned G alpha subunits on the targeted heterotrimeric G protein are released through a reaction where guanosine diphosphate (GDP) is exchanged for guanosine-5'-triphosphate (GTP) with catalytic support from GPCR, to activate an adenylyl cyclase to convert adenosine triphosphate (ATP) into cyclic adenosine monophosphate (cAMP), thus increasing the cAMP intracellular levels (Robinson-White and Stratakis, 2002; Lodish *et al.*, 2016). Protein Kinase A (PKA) is also called cAMP-dependent protein kinase as it requires the binding of four cAMP molecules to its two regulatory subunits, that each have two cAMP binding sites (CNB-B and CNB-A). The attachment of four cAMP molecules to the regulatory subunits of PKA causes the detachment of two activated catalytic subunits (Lodish *et al.*, 2016). Similarly, inhibitory hormones like prostaglandin E1 is used to inhibit the activity of adenylyl cyclase (see Figure 35) (Lodish *et al.*, 2016).

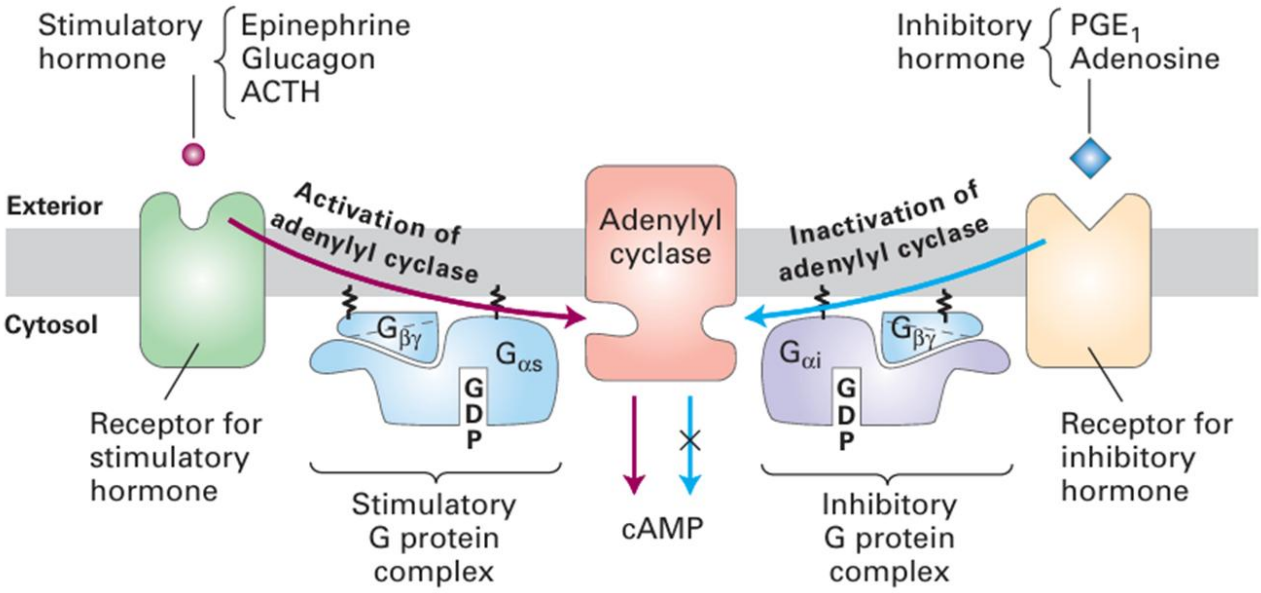


Figure 35. Figure illustrating the activation and inhibition pathways for adenylyl cyclase enzyme.

Extracellular stimulating hormones (dark red circle) like epinephrine and glucagon attach to a respective receptor (green) which transfers the signal though the stimulatory G protein complex (blue) with the use of GDP and activates adenylyl cyclase (red). Similarly, extracellular inhibitory hormones (dark blue rhombus) like prostaglandin E1 (PGE_1) attach to the inhibitory receptors (yellow) and signal though the inhibitory G protein complex (light purple) to stop the production of cAMP though the inhibition of adenylyl cyclase. Figure taken from (Lodish *et al.*, 2016).

The catalytic subunit targets multiple Ser/Thr phosphorylation sites including troponin I (Dong *et al.*, 2007), the M-domain of cardiac isoform of myosin binding protein C (Jia

et al., 2010), the slow isoform of MyBP-C (Ackermann and Kontrogianni-Konstantopoulos, 2011b), and N2Bus on titin (Yamasaki *et al.*, 2002; Krüger and Linke, 2006) in the sarcomere. Additionally, PKA has numerous other non-muscle targets (Lodish *et al.*, 2016).

MyBP-C isoforms have different number of phosphorylation sites with MYBPC1, MYBPC2, and MYBPC3 having 2, 1, and 12, respectively (see Figure 36). PKA phosphorylates 4 Ser residues on the human cardiac isoform of MyBP-C at Ser 288, 279, 313, and 308. Additionally, PKA may have targets outside of the M-domain on cMyBP-C at Ser 690 (Doh *et al.*, 2022).Ser 308 can be phosphorylated by PKA at high concentrations but usually uses other kinases (protein kinase D and protein kinase C epsilon type), with some evidence of Ser 308 acting as a negative regulator for Ser 313 (Ponnam *et al.*, 2019). PKA phosphorylates residues above sequentially to control MyBP-C interactions with the thick and thin filament (Kunst *et al.*, 2000; McNamara, Singh and Sadayappan, 2019; Ponnam *et al.*, 2019). Upon phosphorylation of Ser 288 the affinity of the cMyBP-C N-terminus for S2 is decreased, with a complete inhibition with biphosphorylation at both Ser 288 and 279 (Ponnam *et al.*, 2019). N-terminus interactions with the thin filament are not affected by biphosphorylation of Ser 288 and 279, but reduce the N-terminus affinity on triphosphorylation (Ser 288, 279, and 313) (Ponnam *et al.*, 2019). Other studies (Mamidi *et al.*, 2017) proposed a hierarchical nature of PKA-phosphorylated residues on MYBPC3 gene by using phosphor-ablated Ser 282 and 302. The hierarchical structure of cMyBP-C phosphorylation is described above in 1.2.3.a.

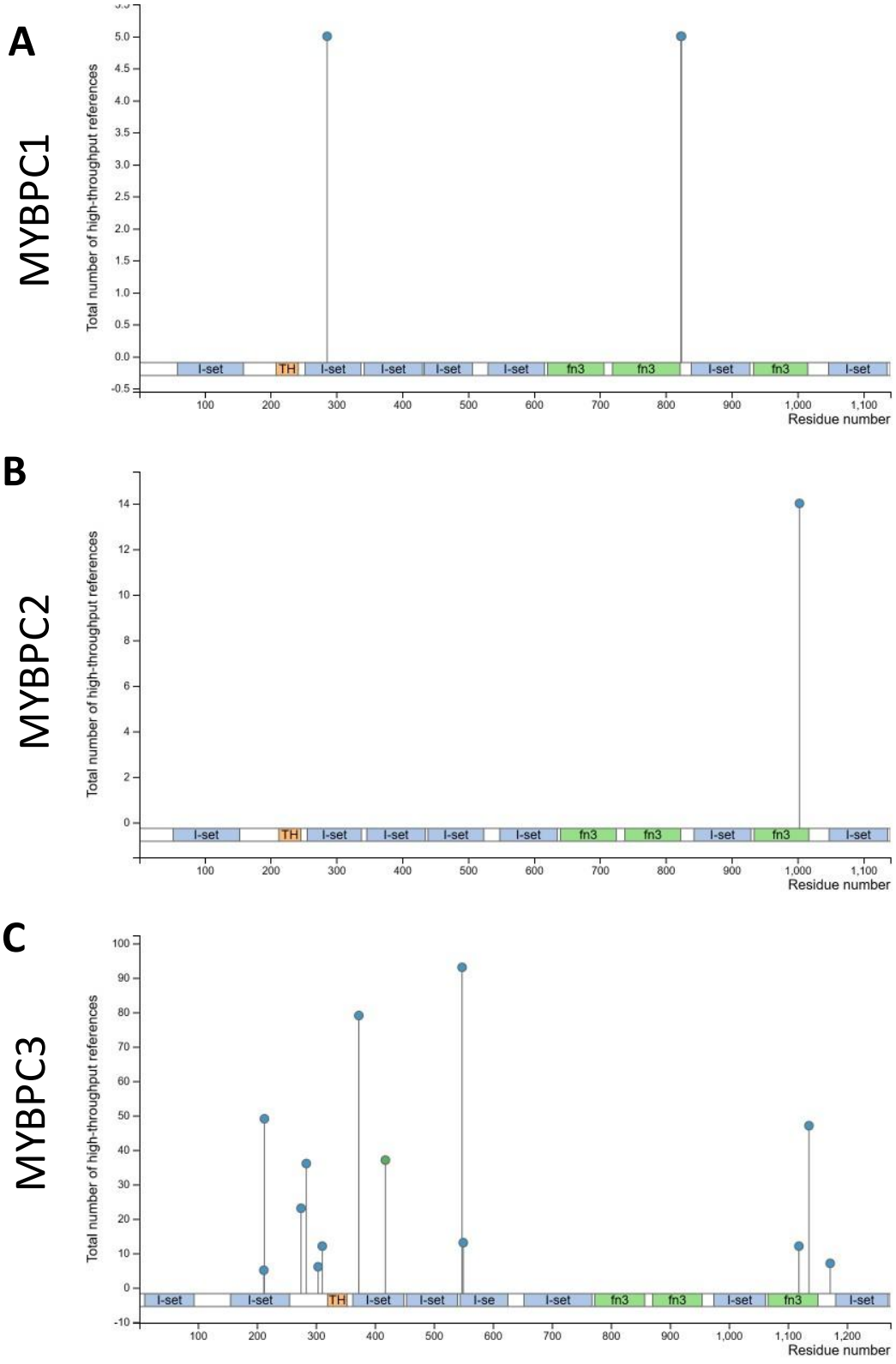


Figure 36. Residue maps for all isoforms of MYBPC gene showing the reported positions of phosphorylation sites (blue circles).

A) Shows the locations of phosphorylation sites (blue circles) on the slow-skeletal isoform of MyBP-C, coded by MYBPC1 gene. B) The position of a phosphorylation site on the fast-skeletal isoform of MyBP-C, coded by MYBPC2 gene. C) Position of the well-studies MYBPC3 gene that codes for the cardiac isoform of MyBP-C (a green circle is an acetylation site). Images taken from PhosphoSitePlus resource (Hornbeck *et al.*, 2015).

4.2. Results

4.2.1. Imaging Porcine Cardiac Myosin ATPase in Relaxed Conditions

Similar to our skeletal study, Z-discs labelled with Alexa-488 anti-α-actinin were used as fiducial markers and Cy3 labelled ATP molecules were used to pinpoint the positions and biochemical states of myosin ATPases under different conditions (see Figure 37 A). However, this time the observed tissue was predominantly β-myosin porcine cardiac tissue (left ventricle) (Walklate *et al.*, 2021). Images acquired were initially split between frames showing Cy3-ATP frames and Alexa-488-Z-disc frames, as both needed to be imaged using different lasers. The process of image consolidation and other relevant image processing techniques are described in the relevant methods section (see 2.3.4.b). When overlapped, Z-disc images and Cy3-ATP images, would result in a typical image shown in Figure 37 B. Figure 38 shows the distribution of sarcomere lengths across recorded conditions for each myofibril. Based on the dimensions of the A-band (1.6 μm (Tonino *et al.*, 2019)), the cut-off point for acceptable sarcomeric lengths was established for an incomplete filament overlap of 1.7 μm. In such, all sarcomeres that were smaller than 1700 nm were discarded, with no data from those sarcomeres included into the data analysis.

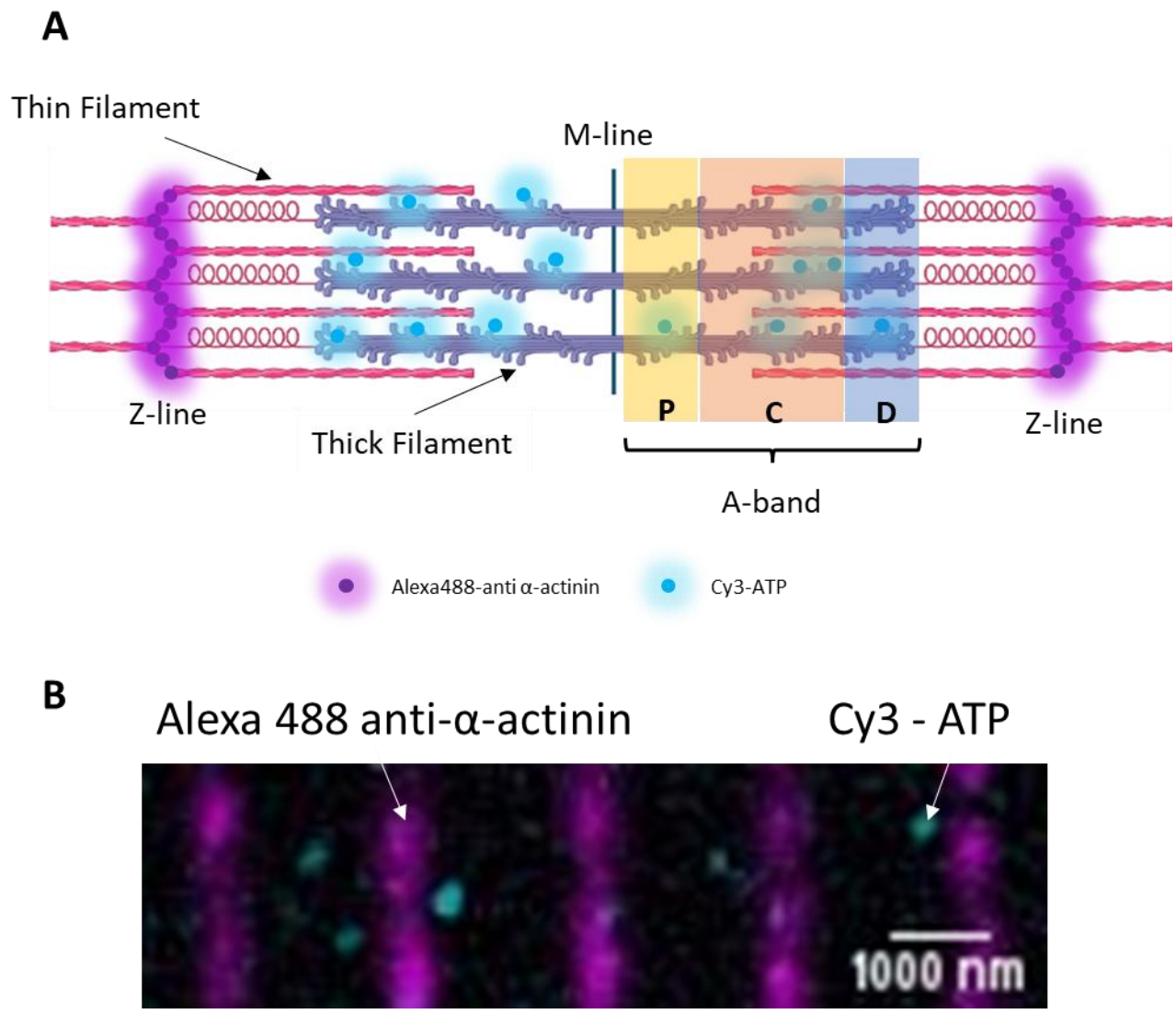


Figure 37. Figure showing a cartoon and a coloured video images of sarcomeres with Cy3-ATP attached.

A) A schematic representation of a sarcomere, labelled with Cy3-ATP (cyan) and Alexa 488-anti-α-actinin antibody (magenta). The zones of the A-band are labelled with yellow, orange and blue for P, C and D zones, respectively. Other parts of the sarcomere are labelled appropriately. B) An overlay of channels from the imaging sequence, showing Z-discs in magenta and Cy3-ATP attachments in cyan. The scale bar is provided.

Our previous experience with skeletal tissue was expanded upon by adding a drift-correcting procedure. For this, the number of Z-disc frames taken per experimental video was increased from 15 frames in the first seconds of the video to Z-disc frame being inserted every 5 Cy3-ATP frames. This way, the position of Cy3-ATP could be corrected in post data collection analysis with a higher degree of accuracy (compared to our previous study) by constantly tracking and adjusting the positions Cy3-ATP events for each pair of Z-discs. The Cy3 dye was continued to be utilised for cardiac experiments, as it was previously shown not to interfere in myosin ATPase activity

(Toseland and Webb, 2011; Ušaj *et al.*, 2021; Pilagov *et al.*, 2023). For the optimal background-noise the ratio of Cy3-ATP to dark ATP molecules was kept at $1:10^6$, respectively.

Analysing each sarcomere individually, the Cy3-ATP events were extracted and separated into zones of the A-band using a super-localisation ImageJ plugin TrackMate. To ensure better fits for the separate zones of the A-band, additionally the un-binned data ("All Zones") was collected for cardiac tissue. All zones data was broken down into a cumulative frequency graph and fitted with the optimal number of exponentials. As in our previous (skeletal) study, the optimal number was found to be three. The optimal number of exponentials was established by plotting the residuals of the exponential fits and comparing them for different number of exponentials. Observed rates from 3 exponentials were attributed to; unspecific or fast events (0.82±0.01 sec-1), DRX events (0.11±0.001 sec-1)and SRX events (0.020±0.0004 sec-1)(see Figure 39 A). The rates were photobleached-corrected and compared to the literature as described above (see 3.2.5).

Upon the analysis of All zones and separate zones data, the percent SRX and DRX was quantified, respectfully (see Figure 39 B). Figure 39 B does not show the data for the Fast events as to preserve clarity of representation and comparison. Additionally, the nature of unspecific events is still unclear, as reported both by us (Pilagov *et al.*, 2023) and other groups (Ušaj *et al.*, 2021). Furthermore, unspecific events could belong to non-myosin ATPases (Amrute-Nayak *et al.*, 2014; Ušaj *et al.*, 2021). Lastly, ATP events with ~1 sec lifetimes could be Cy3-ATP molecules diffusing across the imaging plane, thus not belonging to any ATPases in myofibrils.

The relative adjustment utilised in the previous chapter (see 3.2.1) was also applied to the data collected from the cardiac tissue. Briefly, the events with lower rates (like SRX) would have a lower chance of appearing throughout the image acquisition process than events with higher rates (like Fast). This would incorrectly represent the percentage of SRX population, when compared to the events with faster rates, thus the amplitude correction had to be employed. Following the correction, the percentage of myosin heads in SRX across all zones was 49.8% ± 0.03%. Additionally, the percentage of SRX heads in all zones of the A-band was identified individually: 56.8% ± 1.1%, 53.8% ± 0.4% and 43.9% ± 0.5% for P, C and D zones, respectively.

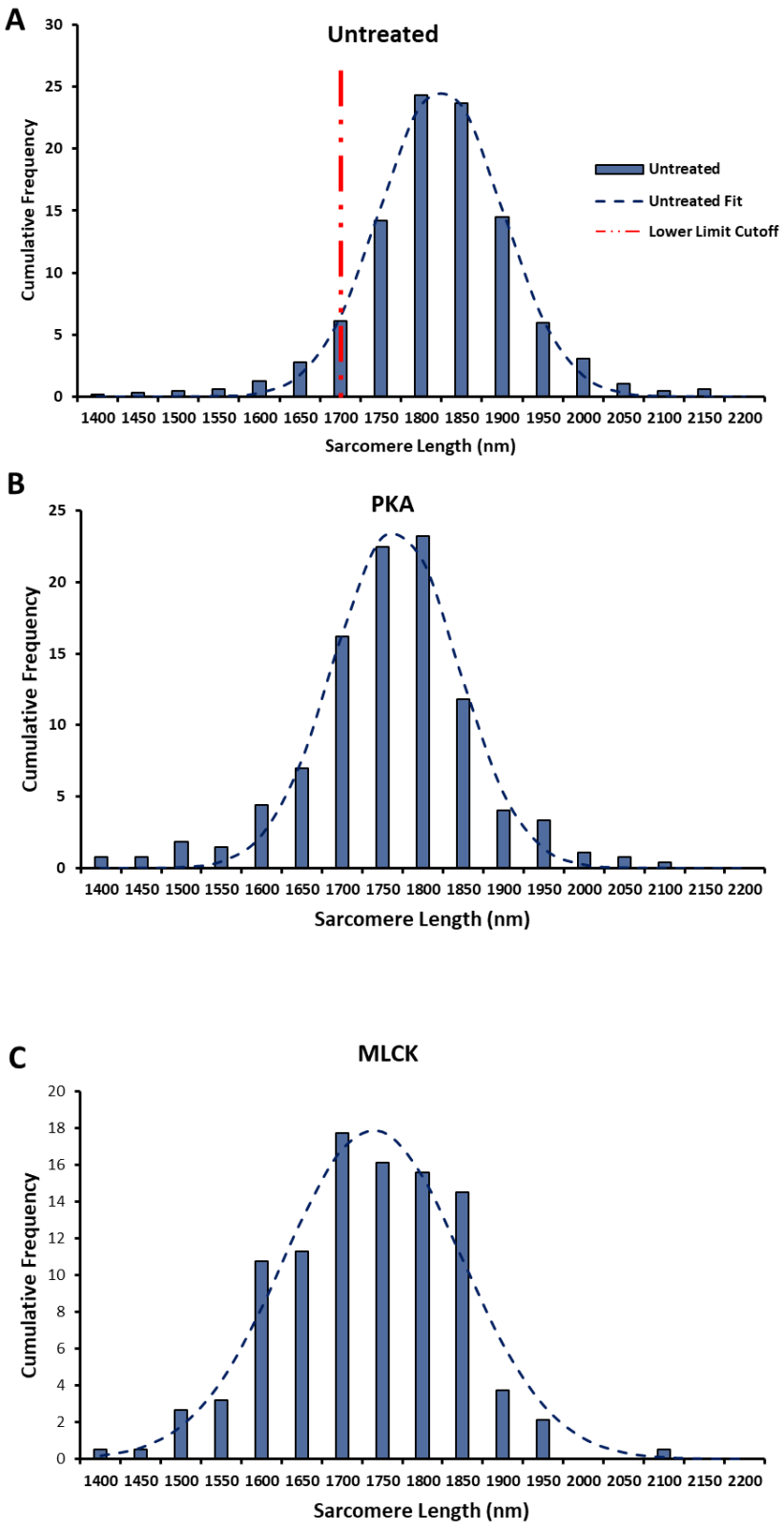


Figure 38. Graphs showing the distribution of sarcomere lengths in all experimental conditions.

Sarcomere length distribution for untreated (A), PKA (B) treated and MLCK (C) treated samples. Sarcomeres smaller than 1700 nm were discarded, as indicated with the red dotted line in A. The size exclusion was allied to all conditions.

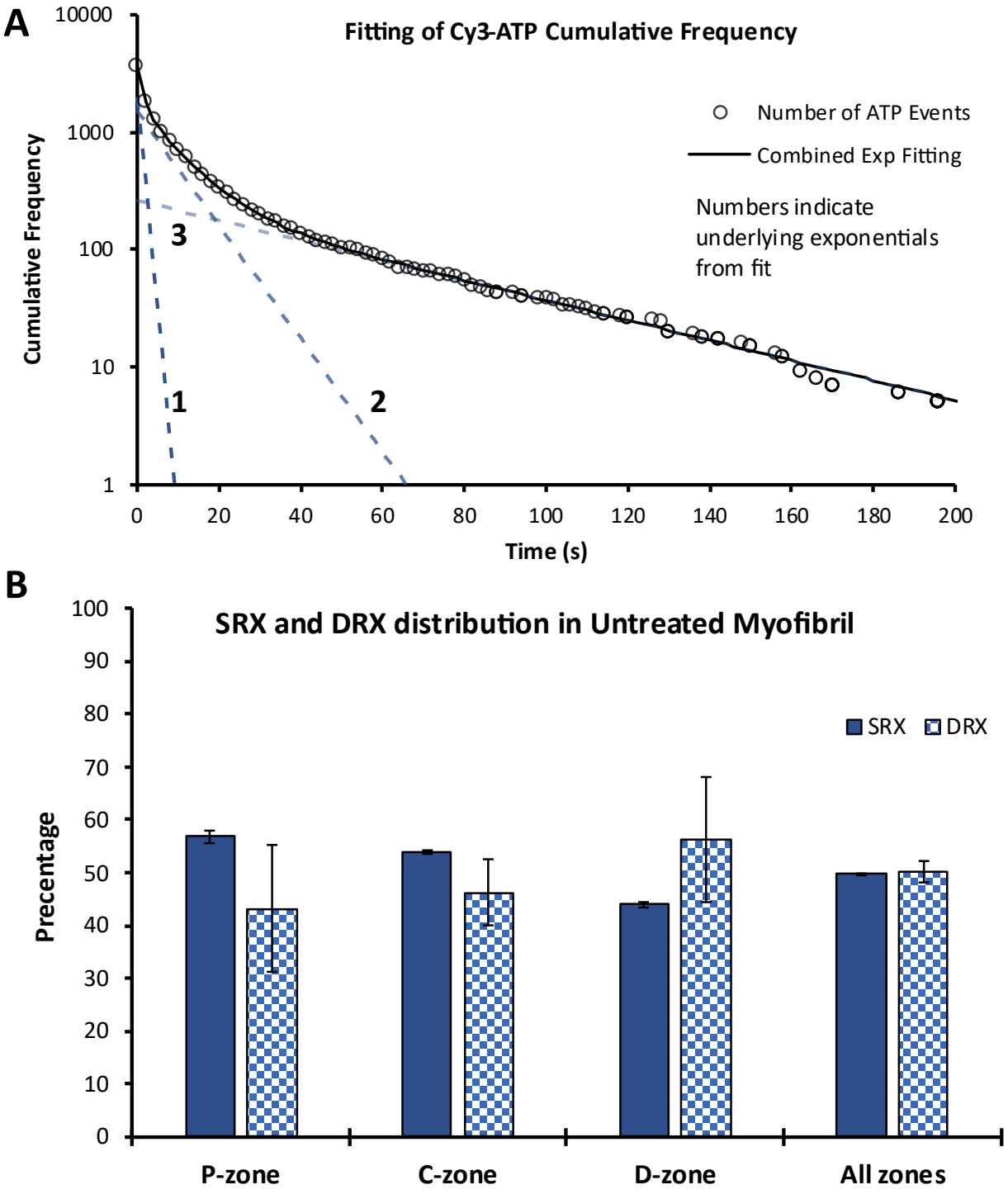


Figure 39. Graph and a chart showing the breakdown of the analysis process, resulting in an estimation of percentage myosin heads in SRX/DRX.

A) The breakdown of fitting sequence employed for cumulative frequency graph for untreated cardiac Cy3-ATP events. The graph is shown on a logarithmic scale. Individual exponentials are numbered 1-3 and are shown with dotted lines. The combined exponential fit is shown with a solid black line. Cy3-ATP survival cumulative frequency is shown with empty black circles. B) The results of data extrapolation from A) for percentage DRX and SRX for all zones of the A-band and all zones combined.

4.2.2. PKA Treatment of Porcine Left Ventricle Reveals a Zonal Compensatory Mechanism

Following the investigation into untreated porcine myofibrils, the β-adrenergic response was investigated though the use of the catalytic subunit of PKA. The major targets for PKA in cardiac system are; cMyBP-C, Titin and cTnI (Krüger and Linke, 2006; Ahmed and Lindsey, 2009). To quantify and reiterate the effects of PKA on the cardiac myofibrils, an SDS PAGE gel with phosphorylation-sensitive staining was employed, and compared to the Coomassie staining (see Figure 40). To compare the two gels and their relative bands, the relative band intensity was calculated for both ProQ and the Coomassie stained gels. The gels have revealed a significant increase in cMyBP-C phosphorylation levels (~x2,5) for the cMyBP-C band. The gels have also revealed an increase in the level of cTnI phosphorylation, which was not surprising but was not pursued further as it was unlikely to affect the system under relaxed conditions. The overall decrease in SRX following the PKA treatment for 'All Zones' was significant, yet small (46.1% ± 0.6% vs 49.8% ± 0.03% for untreated) (see Figure 41; Table 5). However, when the A-band zones were observed individually, the zonal breakdown revealed a different picture. A large decrease in SRX population of 16.4 % was observed in the C-zone (to 37.4% ± 4.7%), with a smaller decrease of 9.5 % observed in the D-zone (to 47.3% ± 8.6%). To the best knowledge of this author, P-zone does not contain a target for PKA, the results are thus implying a degree of cooperativity between the C and P zones upon PKA phosphorylation. Intriguingly, the D-zone has shown an increase in SRX population following PKA treatment, potentially indicating a present of a compensatory mechanism resulting in a smaller-then-expected 'All zones' change upon PKA phosphorylation.

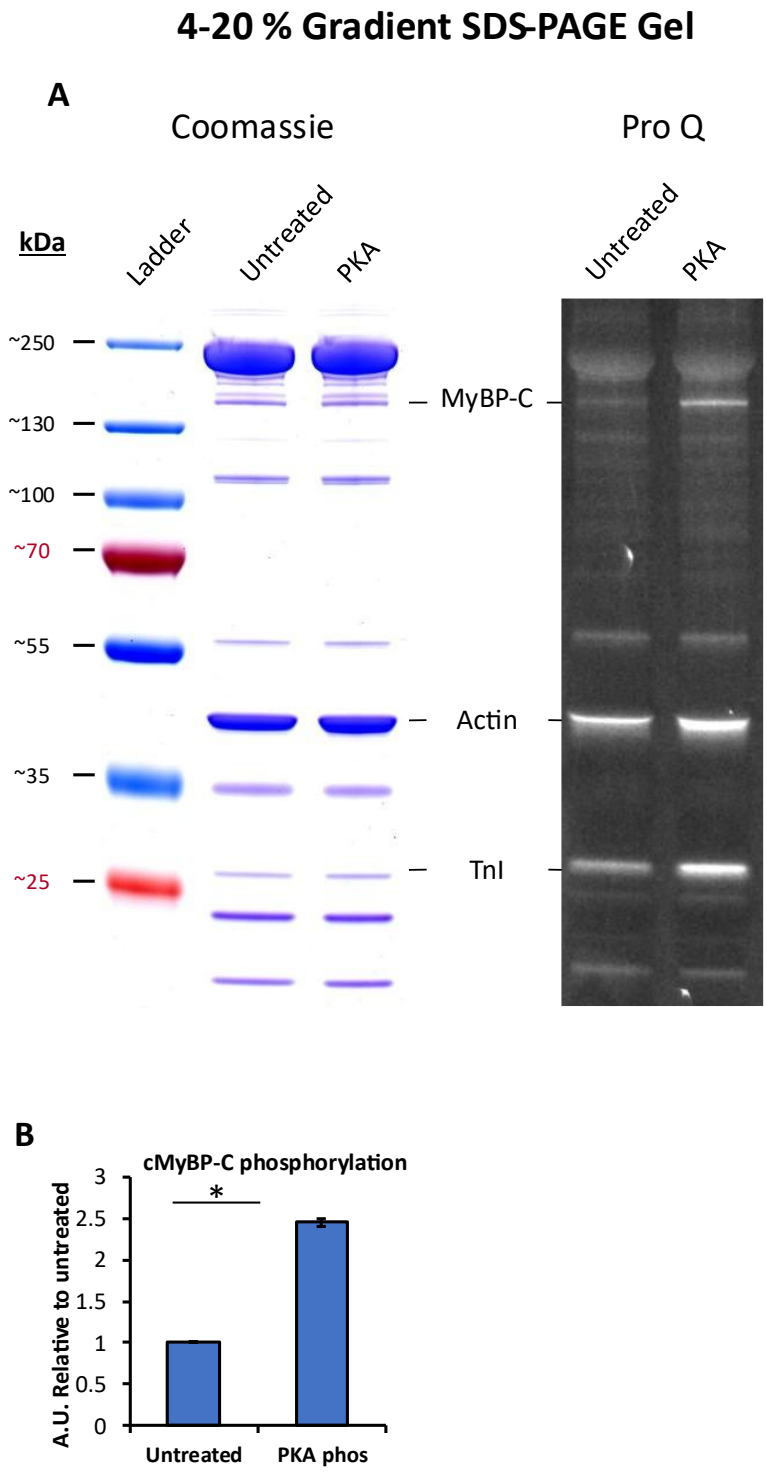


Figure 40. Image showing an SDS-PAGE gel for observing the effects of PKA, with a subsequent analysis.

SDS PAGE gels and their intensity analysis. A) Coomassie gel (left) showing an approximate protein concentrations, with ProQ Dimond phosphor-sensitive gel (right) showing the relative phosphorylation levels of individual proteins. B) For quantitative comparison, the relative intensities were calculated when compared to the untreated bands. The results indicating a significant shift are labelled with a "". The size of proteins in the ladder (PageRuler Plus Prestained Protein Ladder, Fisher Scientific, 11832124) are labelled appropriately. The ladder is kept consistent throughout this thesis.*

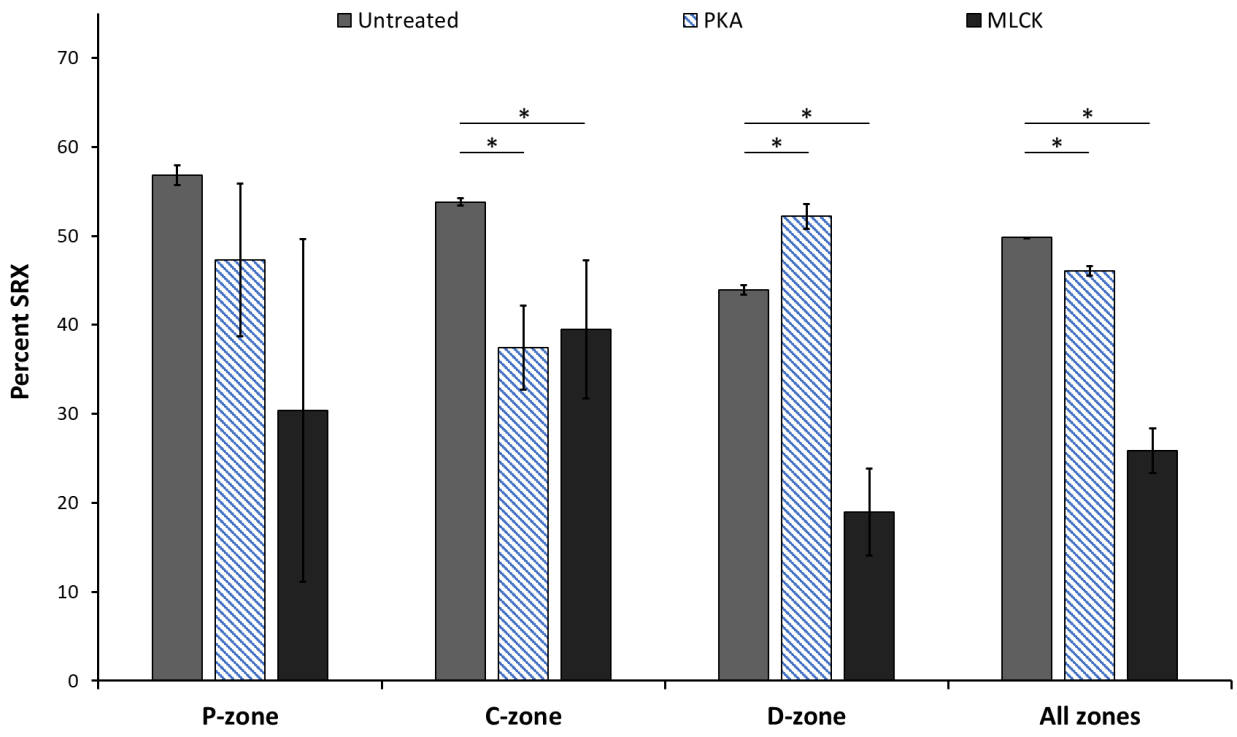


Figure 41. Figure showing the percentage of myosin heads in SRX across all conditions.

Untreated (grey), PKA treated (blue stripes) and MLCK treated (dark blue). The bar chart is showing the changes occurring in all zones of the A-band separately (P,C and D zones) and when combined into the All zones. Samples treated with PKA have shown a significant reduction in SRX population in the C-zone (P = 0.0001) and a significant increase in the D-zone (P = 0.0001), with the total number of SRX heads in all zones decreasing slightly but significantly (P = 0.0001). The effects of MLCK on the A-band zones yielded a significant decrease in the SRX population of both C and D zones (P = 0.0216 and P = 0.0001, respectively), and an overall decrease in All zones (P = 0.0001). The significant changes are indicated by a line with "". Error bars are derived using the standard error of the mean.*

	% SRX				n		
	P	C	D	All zones	All	DRX	SRX
Untreated	56.8 (±1.1)	53.8 (±0.4)	43.9 (±0.5)	49.8 (±0.03)	3638	1491	260
PKA	47.3 (±8.6)	37.4 (±4.7)	52.2 (±1.4)	46.1 (±0.6)	1463	477	85
MLCK	30.4 (±19.3)	39.5 (±7.8)	18.9 (±4.9)	25.9 (±2.5)	2292	525	39

Table 5. Table quantifying the percentage of myosin heads in SRX for each condition.

Untreated, PKA treated and MLCK treated. Percentage was calculated for each zone (P,C and D) individually and all zones together (All zones). The number of events (n) are provided for the total number of events used to calculate the above percentages SRX. Errors are given as ±SEM using n. The total number of porcine hearts used in experiments are: untreated (N = 3), PKA (N = 3), MLCK (N = 2).

Even more interestingly, the effects observed under PKA treatment of the skeletal muscle differs from results observed during cardiac experiments, indicating a tissue-specific PKA modulation. Figure 42 shows a comparative bar chart for the effects of PKA on both porcine cardiac and rabbit psoas tissues. Table 6 complements Figure 42 by showing a decrease in SRX population for the cardiac tissues in both P and C zones by 9.5(±8.7)% and 16.4(±4.7)%, respectively, and showing similar effect on skeletal sample with a reduction of 12.4(±8.6)% and 18.1(±5.2)% for P and C zones, respectively. The main difference between the skeletal and cardiac tissues is localised to the D-zone, showing an increase in the SRX population for the cardiac tissue by 8.3(±1.5) %, and only a marginal increase of 1.4(±6) for skeletal tissue, indicating the potential presents of a compensatory mechanism only in the cardiac tissue but not skeletal.

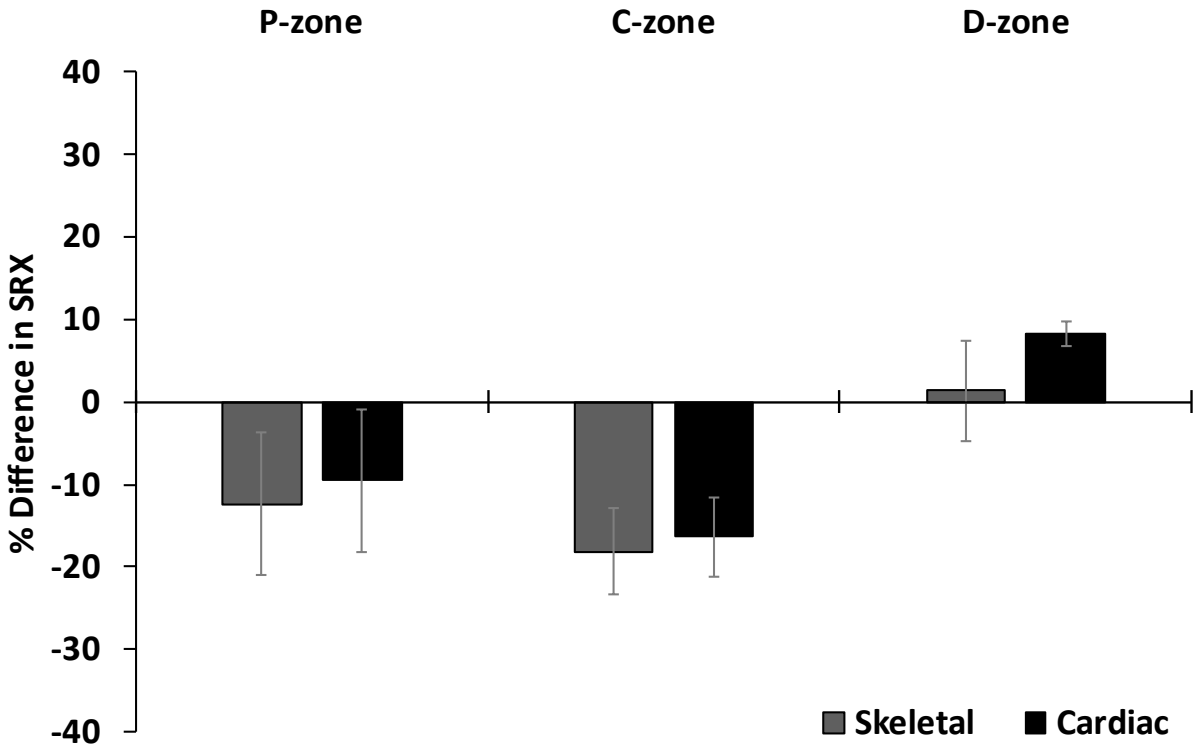


Figure 42. Bar chart to show the difference between the effects of PKA on porcine cardiac and rabbit skeletal muscles.

The effects are broken down into zones of the thick filament. The P and C zones shows a reduction in SRX for both skeletal and cardiac muscles. In the D-zone cardiac samples shown a statistically significant increase in SRX population following the treatment, with no statistically significant change in SRX for skeletal sample.

% Difference in SRX	P-zone	C-zone	D-zone
Skeletal	-12.4(±8.6)	-18.1(±5.2)	1.4(±6)
Cardiac	-9.5(±8.7)	-16.4(±4.7)	8.3(±1.5)

Table 6. Table showing the differences in SRX percentage for skeletal psoas and porcine cardiac tissues following PKA treatment.

This table displays values presented in a bar-chart in Figure 42 and shows the difference between cardiac and skeletal muscle, when comparing the percentage of myosin heads in SRX over every zone of the thick filament following the PKA treatment.

4.2.3. Targeting the RLC on Porcine Left Ventricle Using MLCK

The effects of a known RLC phosphorylation agent MLCK (Morano *et al.*, 1985; Sweeney and Stull, 1986; Olsson *et al.*, 2004; Stelzer, Patel and Moss, 2006a; Kampourakis *et al.*, 2018), were investigated following the data collected for the phosphorylation of cMyBP-C by PKA. Gels-based assays were conducted by other groups for human, marmoset and rat cardiac systems to show an increase in phosphorylation levels of RLC upon MLCK treatments (Sevrieva *et al.*, 2020). A gel-based phosphorylation-sensitive assay was utilised to investigate MLCK phosphorylation of RLC, that was conducted using similar approach as with PKA in skeletal study. The results of that assay are provided in Figure 43. Figure 43B indicate a lack of apparent phosphorylation when comparing the untreated samples with MLCK-treated samples. Unlike the gel-based assays, the single-molecule analysis showed a clear reduction is SRX population of 23.9% observed across all zones (to 25.9% ± 2.5%, see Figure 41; Table 5).

Examining the zonal SRX distribution post MLCK treatment has revealed: 26.4 % reductions in the P-zone (to 30.4% ± 19.3%), similar, 25.0 % reduction in the D-zone (to 18.9% ± 4.9%), and a much smaller, 14.3%, reduction in the C-zone (to 39.5% ± 7.8%). The breakdown of changes for both PKA and MLCK treatment when compared to untreated samples are compiled in Table 7. Investigating the combined effects of PKA and MLCK phosphorylation was intriguing, but unfortunately unfeasible due to a

rapid myofibril degradation unavoidable in cases of longer incubation periods (~4 h for both kinase phosphorylation).

Unlike the results of MyBP-C phosphorylation by PKA, the ProQ gel of MLCK treatment has not revealed any apparent shifts in RLC phosphorylation. Thus, a separate investigation was launched to determine the reason for the lack of apparent change. First, an alternative phopho-sensitive gel staining was used ; PhosTag Yellow (AlphaLaboratories, 380-15241). The results are shown in Figure 44. The change in staining was driven by a decreased staining time for PhosTag staining, which was much lower (~1h) than ProQ staining (~4h). The reduced time was imperative as the stability of RCL phosphorylation was a concern when preserved for a long period of time. Thus, an attempt was made to reduce the time between defrosting of boiled samples and gel imaging. Unfortunately, this had proven to have no effect on the outcome of RLC phosphorylation status. Figure 44 presents a PhosTag gel and reports similar levels of phosphorylation across RLC in both untreated and MLCK-treated samples, while additionally providing some insight into the effects of Calf Intestinal Alkaline Phosphatase (CIAP, ThermoFisher Scientific, 18009019). CIAP was employed as a known dephosphorylation agent for RLC (Husberg *et al.*, 2012) to establish and compare the levels of phosphorylation of RLC in untreated conditions. When treated with CIAP, the sample shows a near 2-fold decrease in phosphorylation levels when compared to the untreated data, indicating a high level of RLC phosphorylation in untreated samples and potentially explaining the absence of change during MLCK treatment.

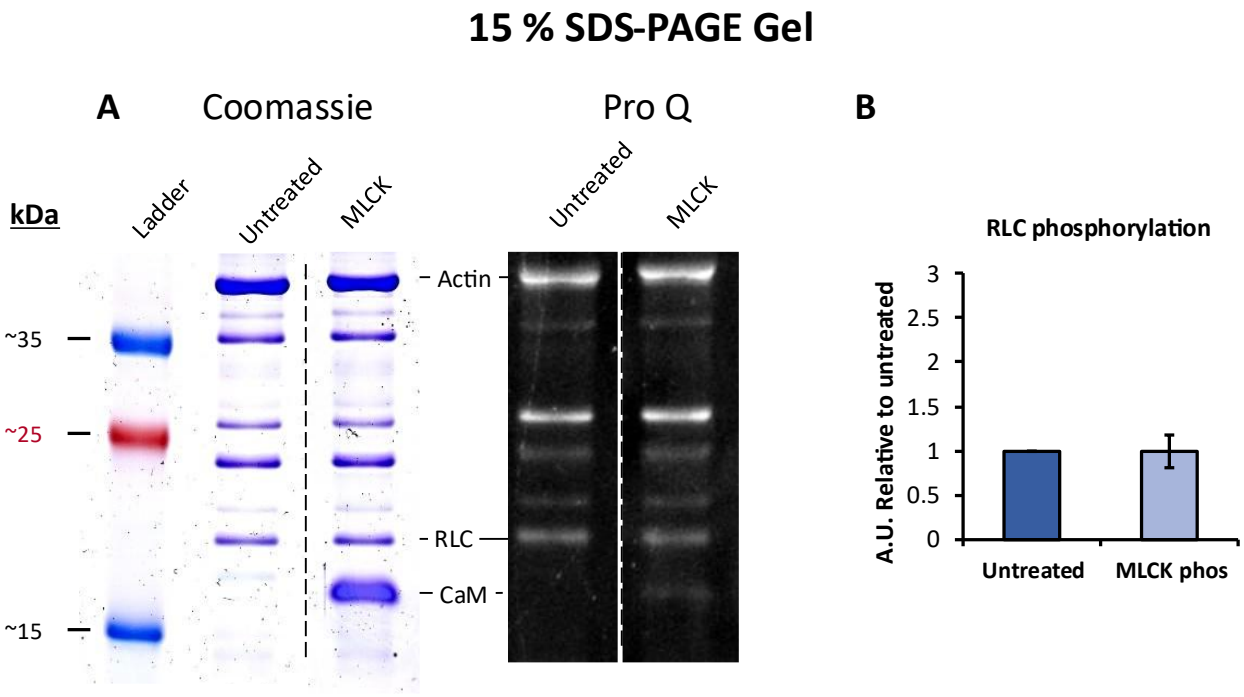


Figure 43. SDS PAGE gels showing the levels of phosphorylation of MLCK-treated myofibrils.

When compared on Coomassie stained (A, left) and ProQ-stained (A, right). Gels were run as 15% acrylamide gels to better resolve smaller molecular weight proteins. Relative proteins are labelled. Comparative analysis of RLC band intensity is provided in (B). The size of proteins in the ladder (PageRuler Plus Prestained Protein Ladder, Fisher Scientific, 11832124) are labelled appropriately. The ladder is kept consistent throughout this thesis.

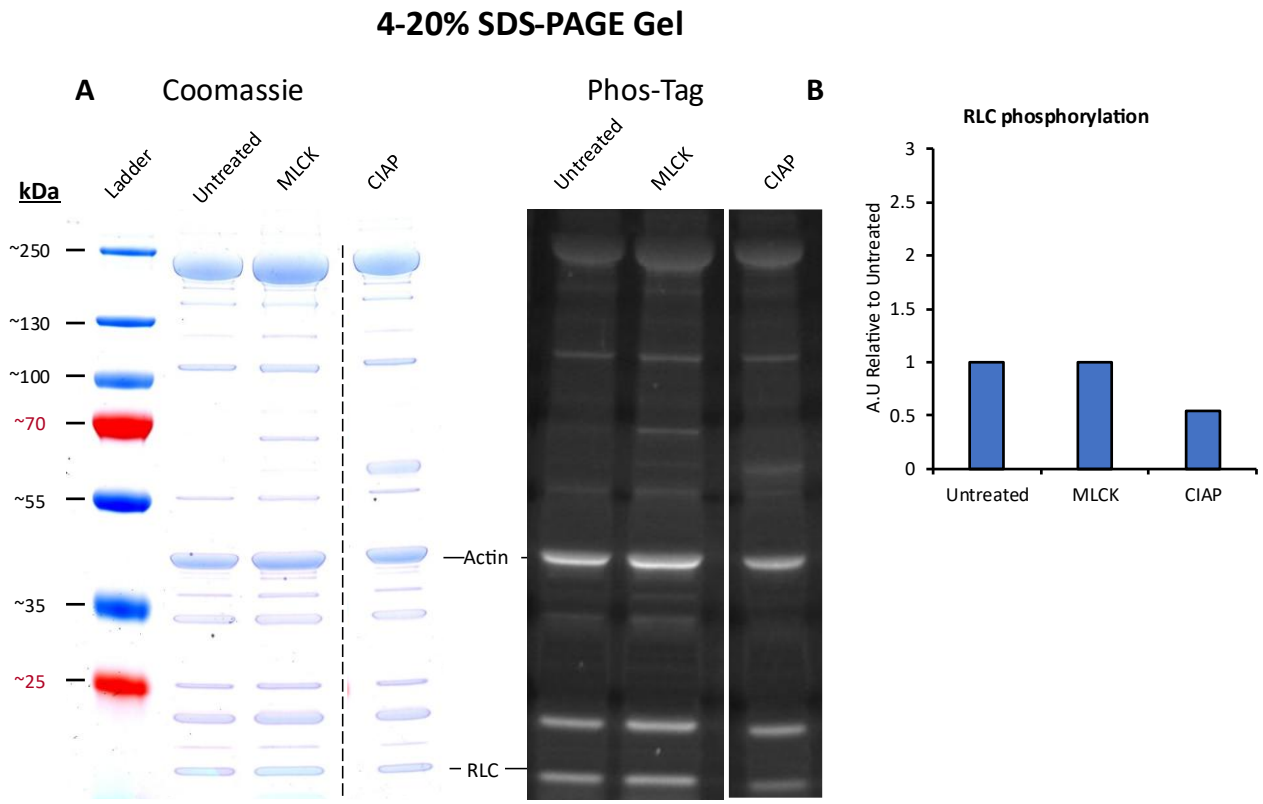


Figure 44. SDS PAGE gels to show the phosphorylation levels of RLC after MLCK and CIAP treatments.

A) A Coomassie gel (left) and a respective PhosTag (right) gel showing the distribution of proteins, with relative proteins labelled. B) A relative intensity comparison for untreated vs MLCK-treated RLC band. The size of proteins in the ladder (PageRuler Plus Prestained Protein Ladder, Fisher Scientific, 11832124) are labelled appropriately. The ladder is kept consistent throughout this thesis.

	Δ SRX (%)			
	P	C	D	All zones
PKA	-9.5 (±8.7)	-16.4 (±4.7)	8.3 (±1.5)	-3.8 (±0.6)
MLCK	-26.4 (±19.3)	-14.3 (±7.8)	-25 (±4.9)	-23.9 (±2.5)

Table 7. Table summarising the percentage change for each condition for both: zones separately and all zones together.

The percentage change is given relative to the untreated data. The errors are given by mean ±SEM.

4.3. Discussion

Cardiac myofibril contractions are controlled on two levels: Ca^{2+} - sensitive thin filament and myosin kinetic repression states SRX/DRX. Thin filament control is a large-scale control, regulating the activation/deactivation of contractile apparatus localised to sarcomeres, while thick filament control regulates a more precise contractile forces by regulating the amount of myosin heads available for the sliding of the two filaments. The states of myosin heads are characterised by their ATPase rates, where DRX is more active than SRX. Along with the biochemical (kinetic) characterisation of myosin-based regulation, myosins are also found in different structural conformations associated with Interactive Head Motif (IHM). The current view in the field is suggesting correlation, but not necessary intercalation of the two (Ma *et al.*, 2023). Here, the single molecule microscopy was used to observe the ATPase rates of the myosin heads under the influence of PKA and MLCK. Our results of PKA treated myofibrils reveal the effect to be localised primarily to the C and D zones, with the resulting effect on the overall sarcomeric SRX population (all zones) being minimal. The results provided from the MLCK treatment reveal a decrease in SRX population across all zones and each zone individually, with the C-zone being the least affected by the treatment.

4.3.1. PKA Represses Myosins in the D-zone, While Activating Them in the C-zone

PKA is recruited though the β-adrenergic stimulation and results in phosphorylation of multiple targets in the sarcomere. First, PKA has three-to-four phosphorylation sites on MyBP-C depending on the isoform (Jia *et al.*, 2010; Kooij *et al.*, 2013; McNamara *et al.*, 2014; Mamidi *et al.*, 2017; Ponnam *et al.*, 2019; Doh *et al.*, 2022). For a full breakdown of phosphorylation sites on MyBP-C see appropriate section see 1.2.3.a and above, 4.1.1. Upon phosphorylation, MyBP-C was shown to interact with both thick and thin filaments (Shaffer, Kensler and Harris, 2009; Mamidi *et al.*, 2017; McNamara, Singh and Sadayappan, 2019). Here, a fractional yet statistically significant decrease in the SRX population was reported for ‘All Zones’. When broken down into individual components however, the largest SRX decrease is observed in

the C-zone, where the most likely target is cMyBP-C. Surprisingly, the increase in SRX in the D-zone was counterbalancing the effects observed in the C-zone, resulting in the overall near-zero net change. The mechanism by which PKA is affecting the D-zone is unknown, potentially suggesting allosteric interaction with another PKA phosphorylation target like titin. The effects of PKA on titin are localised to the N2B unique sequence (Krüger and Linke, 2006; Hamdani, Herwig and Linke, 2017) and result in a decrease in passive tension of the I-band end of the titin filament (Yamasaki *et al.*, 2002). Here, the work was conducted using the relaxed cardiac myofibrils stuck to the glass surface averaging ~ 1.76 μm sarcomere length (SL), and thus having an overlap between the A-band and the thin filament. The overlap results in the N2B region of titin being close (or overlapping) the D-zone and thus potentially explain the effects of PKA observed during the experiment.

4.3.2. Hierarchical Nature of Post-Translational Modifications in the Thick Filament

Regulatory light chain (RLC) is localised to the S1 subfragment of myosin heavy chain. RLC stabilises the lever arm to maximises the force produced during contractions (Sherwood *et al.*, 2004; Sheikh *et al.*, 2012), effects the cross-bridge mechanics (Diffee *et al.*, 1996; Scruggs *et al.*, 2009; Pulcastro *et al.*, 2016; Toepfer, West and Ferenczi, 2016) and the positions of myosin heads relative to the backbone of the thick filament (Levine *et al.*, 1996; Colson *et al.*, 2010). The above effects are modulated though the states of RLC phosphorylation, with phosphorylated RLC leading to a greater disorder of myosin heads (Levine *et al.*, 1996) or structural changes pushing myosin heads closer to the thin filament and slowing the cross-bridge detachment (Turner *et al.*, 2023). Smooth muscle myosin light chain kinase (sMLCK) was employed in this study as a RLC-specific kinase (Chan *et al.*, 2008; Ding *et al.*, 2010). Although cardiac isoform of MLCK is widely-regarded as the main phosphorylation agent for RLC, there is some evidence that other isoforms (e.g. smooth muscle MLCK) also targets the RLC, albeit to a lesser degree (Sevrieva *et al.*, 2020). Smooth isoform was chosen due to the availability and the high cost of the replacement cardiac isoform.

In vivo MLCK is maintained at approximately 1:2 ratio to RLC per myosin head pair (i.e. one MLCK molecule per a pair of myosin heads) (Colson *et al.*, 2010; Scruggs *et*

al., 2010; Chang *et al.*, 2015). Consistent with our MyBP-C investigation, a gel-based pho-sensitive assay was conducted to determine the levels of RLC phosphorylation following the MLCK treatment. Interestingly, our gel-based investigation has shown a lack of significant change when comparing MLCK-treated and untreated myofibrils. However, a clear difference was observed in our single-molecule experiments, thus suggesting the gel-sensitivity was not adequate. This has lead us to the optimisation of the staining agent form ProQ to PhosTag (see Figure 44). Unfortunately, the replacement of the gels staining protocol also did not yield any changes in RLC phosphorylation.

The dephosphorylation of the myofibril proteins was attempted by using CIAP to elaborate on the lack of MLCK phosphorylation on the RLC band. CIAP treated myofibrils have shown a 2-fold reduction in RLC phosphorylation levels when compared to untreated samples. The tandem of CIAP and MLCK results might indicate both RLCs being phosphorylated during MLCK treatment and the gel not having enough resolution to clearly show the distinction between the number of phosphorylated heads. The distribution of RLC phosphorylation by MLCK between myosin heads on the same head-pair is thought to be random (Chang *et al.*, 2015). However, in some cases the random nature of the distribution might have resulted in both RLCs on a myosin head to be phosphorylated together. With large population of such random occurrences, it was possible to explain the deviation observed between our gel-based and single-molecule results. The pair of myosin heads with both RLCs phosphorylated would be hard to distinguish on a standard ProQ or Phos-Tag gels, as both RLSs would have the same molecular weights. To separate RLCs with different phosphorylation states acrylamide Phos-Tag gel stain (e.g. Fujifilm, AAL-107M) could have been employed. Phost-Tag acrylamide gel separates molecules based on their phosphorylation status, thus making the same molecules with different phosphorylation statuses appear as separate bands on the gel. On the other hand, single-molecule experiments provided observations from each Cy3-ATP molecule detaching from the thick filament and thus included both RLS of both heads, thus potentially providing a deviation when comparing a gel-based assay to the results observed during our single-molecule experiments.

The above speculative suggestions could be transformed to an exciting new study looking at how the single or double-phosphorylated RLCs affect the ATPase rate in

sarcomeres, potentially using PhosTag acrylamide (Fujifilm, AAL-107M). Phos-Tag acrylamide (as described in their original publication (Kinoshita *et al.*, 2006)) uses alkoxide-bridged dinuclear metal, like zinc or manganese, as a supplemental metals required to produce a phosphate-binding tag (or Phos-Tag). Phos-Tag molecules preferentially bind to phosphomonoester dianions bound to phosphorylated residues (i.e. Ser (in our case), Thr and Tyr). The Phos-Tag system with supplementary metal is incorporated into the gel to enable the retardation of the phosphorylated band progression and thus a separation of phosphorylated and non-phosphorylated molecules.

Regardless, single-molecule results offer an exciting glimpse into how phosphorylation affects myosin ATPases in the sarcomere. The changes observed in P and D zones upon MLCK treatment are much larger than changes observed in the C-zone. Furthermore, the changes observed in the C-zone are nearly identical to changes seen during the PKA phosphorylation of MyBP-C. In tandem with recent study (Turner *et al.*, 2023), where they used transgenic mice with MyBP-C knock-out to show a larger effect of RLC phosphorylation in the absence of MyBP-C to control the energy states of myosin molecules, our results indicate a smaller effect of RLC phosphorylation on the C-zone where MyBP-C is present. Reduced effects of RLC phosphorylation in the C-zone might indicate interaction of MyBP-C and RLC (Ratti *et al.*, 2011; Heling, Geeves and Kad, 2020). The proposed MyBP-C phosphorylation dampens the effects of RLC phosphorylation revealing a potential and yet unknown hierarchical interaction between RLC and MyBP-C phosphorylation.

4.4. Conclusions

Phosphorylation status of selected sarcomeric proteins have been shown to play part in regulation of muscle contractions. Here, the effects of PKA on cMyBP-C were investigated, which resulted in primary phosphorylation effects to be localised to the C and D zones, surprisingly revealing a compensatory mechanism previously unseen in studies involving β-cardiac myosin. Although the effects of PKA localisation to the C-zone are in line with cMyBP-C phosphorylation, the full activation of the C-zone was not achieved. Secondly, MLCK was utilised to phosphorylate RLC on the myosin heavy chain. RLC phosphorylation has decreased the levels of myosin in SRX across all zones, with the C-zone having the smallest change. Interestingly, RLC phosphorylation led to similar levels of SRX in the C-zone found during MyBP-C phosphorylation, indicating an underline hierarchical mechanism relating MyBP-C and RLC, with MyBP-C dominating the regulation of RLC phosphorylation.

Chapter 5 – Using a Novel Ensemble Approach to Investigate the Effects of Mavacamten and 2'-deoxy-ATP on Beta Cardiac Myofibrils

5.1. Introduction

In this chapter, a novel, high-throughput method was established to analyse multiple cardiac samples quasi-simultaneously. For this, a moving stage was created that allowed for an increased throughput of ~3-5 fold, when compared to our previous single-molecule experiments. Furthermore, a previously established pulse-chase protocols (e.g. (Wilson, Naber and Cooke, 2020)) were optimised to fit our novel, high-throughput system. The self-build, 3D-printed stage was used in tandem with an adjusted pulse-chase approach to test well-known myosin repressors, MAVA & AFI, and myosin well-known myosin activator, dATP, by showing an increase and a decrease in myofibril ATPase activity, respectively.

5.1.1. Drug Development and Treatments for Hypertrophic Cardiomyopathy (HCM)

Mavacamten was the first drug of its kind to get approved for treatment of HCM (Olivotto *et al.*, 2020). However, most available treatments still target the physiological manifestations of HCM, rather than treating the underlying causes of energy consumption mis-regulation by myosin motors. The current arsenal of treatments consists of pharmacological options: β-blockers, nondihydropyridine calcium-channel

blockers and/or disopyramide (see 1.3.2 for mechanisms of action). More invasive surgical options are also available for some HCM patients, such as: implantable cardiac defibrillators or septal reduction therapy (Ho *et al.*, 2020; Ommen *et al.*, 2020). Closely following MAVA, the next-in-line drug aficamten (AFI) was developed 3 years later (Maron *et al.*, 2023).

MAVA has a longer half-life and a wash-out period when compared to aficamten, making it less attractive as an alternative to current methods of HCM treatment (Keam, 2022). Furthermore, at high concentrations MAVA is a known cytochrome P450 3A4 (CYP3A4) and cytochrome P450 2B6 (CYP2B6) inducer and thus MAVA concentration should be adjusted prior to the use of CYP2C19 or CYP3A4 inhibitors such as omeprazole or verapamil, respectively. The use of the above inhibitors combined with MAVA is associated with a higher risk of systolic dysfunction, loss of medical effectiveness, or exacerbation of the heart failure (Grillo *et al.*, 2019; Keam, 2022). Lastly, in animal models MAVA was suggested to have foetal toxicity, thus requiring a reliable contraceptive measure for at least 4 months after the last dose (Sebastian *et al.*, 2023). Unlike MAVA, AFI has a shorter half-life, thus being more suitable for daily dosing, and reaches steady-state concentration within two weeks (Chuang *et al.*, 2021; Maron *et al.*, 2023). Furthermore, AFI does not have any significant P450 interactions and exhibits a wider range of therapeutic window with a significant window between toxicity and effectiveness (Chuang *et al.*, 2021; Malik *et al.*, 2022).

5.2. Results

In this third and final chapter of this thesis a novel was developed to investigate multiple cardiac samples quasi-simultaneously while using different buffer solutions. This was done to introduce a novel method of investigating large quantities of human (or model organism) derived samples with potential for drug screening in mind. Due to the time restraints, only the initial methodology was established, with limited experiments conducted to show the effects of known pharmacological agents on porcine samples. These experiments were conducted to establish the reliability of the system, unfortunately, without the ability of using different solutions for physically separated samples.

The initial plan was to image multiple mutated cardiac samples either from patients or from model organisms, by combining fluorescent imaging and a moving stage. The implementation of a moving stage was an essential part of initial development to move between physically separated samples. Using our single-molecule approach would have been too time-consuming, as hundreds of patient samples were intended to be imaged, with data for one sample in single-molecule approach (in triplicate) taking at least three days of data collection. However, by using our novel ensemble approach, the increased in the output by at least 3-fold made the sample screening less time-consuming. Alas, such an increase in productivity came at a cost of resolution, as the Z-disc labelling was discontinued, with a potentiality of re-implementing it in the future. The outcome was a system with an automated stage controlled though two Arduino boards, which was controlled by a custom-written software, and a thoroughly tested and established pulse-chase technique, that was modified from previously established studies (Hooijman, Stewart and Cooke, 2011; Nogara *et al.*, 2016). The stage would move inside a standard flow chamber and pick up 3-4 myofibrils per imaging session though the use of stroboscopic illumination, that has enabled the imaging of all 3-4 myofibrils in a frame of 5 sec. This allowed for the imaging of all myofibrils in the duration of the OFF-time for other myofibrils. In other words, the stage would return to the first imaged myofibrils in a period of 5 sec with images of all other myofibrils already collected. A detailed description of the approach is provided below.

5.2.1. Ensemble Sample Preparation

Ensemble imaging sample preparation differs slightly from our single-molecule work described above (for a refresher on single-molecule methodology see 2.3.1). Briefly, using our single-molecule experience with Cy3-ATP illuminated with 561 nm laser, the fluorescent decay was measured on myofibrils following the Chase Buffer injection. The imaging session were conducted in 30 min windows using stroboscopic illumination with the interval of 5 sec. Laser ON time was 15 ms with the laser power set to 10 mW. To synchronise the movement of the stage and flashes of the laser a custom-written Arduino script (C++) was employed to synchronised all; the camera ON time, the flashes of the laser, and the movement of the stage.

When used, drugs were introduced either together with both Chase Buffer and Imaging Buffer or just Imaging Buffer, depending on the relative speed of drug effect upon the

myofibrils. If the effect of perturbation was not shown previously to be instantaneous, the drugs were introduced together with both buffers. To this effect, samples with 2'-deoxy-ATP (dATP) (NEB, N0440S) (Walklate *et al.*, 2022) and Mavacamten (MAVA) (30 µM, MedChemExpress, HY-109037) (Pilagov *et al.*, 2023) were introduced with the Chase Buffer while Aficamten (AFI) (30 µM, MedChemExpress, HY-139465) was allowed to incubate with the myofibrils in the Imaging Buffer for 20 min prior to the chase and the consequent imaging. All drugs were dissolved in DMSO with the final concentration not exceeding 0.5 % of the total buffer concentration (Mariano *et al.*, 2001).

5.2.2. Ensemble Flow Chamber Assembly

By developing on the established (Hooijman, Stewart and Cooke, 2011; Nogara *et al.*, 2016) pulse-chase experiments our custom build oblique angle fluorescent (OAF) microscope was employed to image the bulk fluorescence of multiple myofibrils quasi-simultaneously. Flow cell construction for these experiments differed slightly compared to the flow chamber shown in Figure 19. The experimental setup was similar to the DNA work previously published by our group (Kad *et al.*, 2010; Barnett and Kad, 2019) but using myofibrils on the surface instead of DNA. Briefly, flow chambers had an additional plastic microfluidics attached to each port (holes) of the flow chamber and sealed with a strong adhesive (AB-1, RS, Germany), thus creating an enclosed and continues environment inside the flow chamber upon the attachment of the syringe pump and perfusion tube on the either end (see Figure 45). Microfluidics (GE-0086-033, 0.86mm ID x 0.33 mm Wall, Polyethylene, US) were used by attaching a 10 ml syringe, operated by a syringe pump (AL-1000, WPI, UK) to one end of the flow chamber and connecting the other end microfluidics to a perfusion tube (1.5 ml, standard).

The use of the syringe pump for the buffer exchange was deemed necessary due to the time precision required for an accurate pulse-chase experiments. To set up the pulse chase experiment the syringe was first filled with 6 ml of Pulse-Chase Prep Buffer with 1 ml being discarded into waste to clear the microfluidics. The pump rate was set to 1 ml/min unless stated otherwise. Here and in the following text the direction of the flow created by the syringe pump would be indicated via "withdrawn" (towards the syringe) or "pumped" (towards the perfusion tube). The syringe was placed into

the pump and fixed in place. The pump was activated, and the syringe end of microfluidics was attached to the flow chamber. It was ensured prior to the attachment that no bubbles are present in the tubing. When flow chamber has been filled, the other end of the flow chamber was attached to the perfusion tube microfluidics. The syringe was pumped for further 500 µl. The perfusion tube was emptied with a pipette (care taken not to introduce bubbles into the system). Skinned myofibrils (200 µl) of OD_{600} = 0.5-0.75 were added to the perfusion tube and withdrawn towards the flow chamber. After all 200 µl of myofibrils were withdrawn, further 200 µl of Pulse-Chase Prep Buffer was added to the perfusion tube. The syringe was withdrawn further until myofibrils were visibly appearing inside the flow chamber, at this point syringe was withdrawn for further 200 µl, then reversed and pumped for 200 µl increasing the number of myofibrils stuck to the surface. Myofibrils were allowed to adhere to the surface on ice for 30 min with microfluidics still attached. The excess myofibrils were washed out by pumping at 7.5 ml/min for 600 µl following the incubation. Perfusion tube was emptied, and the setup was moved to the microscope.

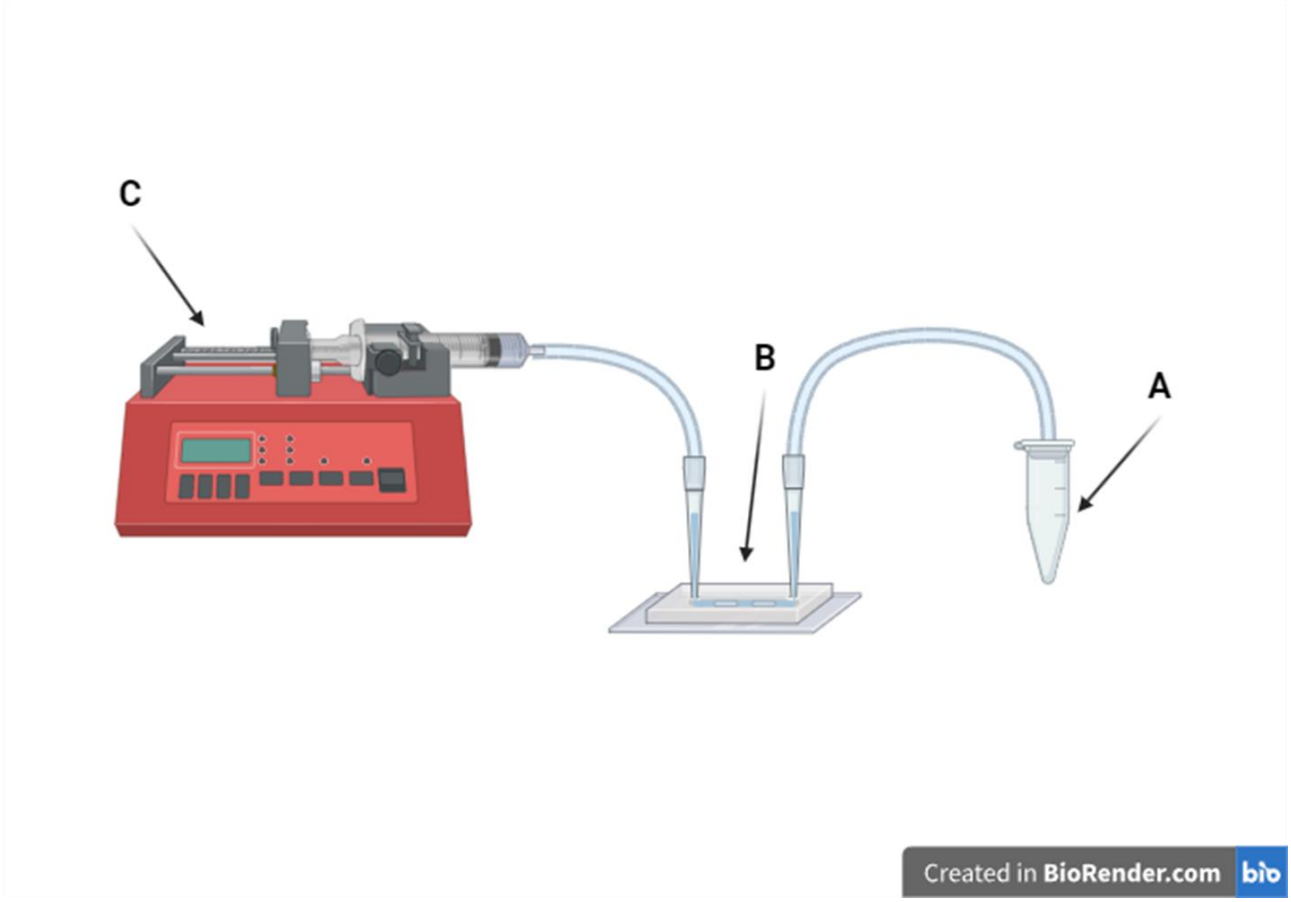


Figure 45. A schematic representing flow chamber setup used in Ensemble experiments.

A) The perfusion tube is a standard 1.5 ml centrifuge tube with 3 holes made; to connect microfluidics, balance the pressure and change solutions. B) The flow chamber is designed in the same way as described in Figure 19 with double the capacity and connected microfluidics. C) Syringe pump (AL-1000, WPI, UK.) and syringe are attached to the other end of the microfluidics and is used to push or pull liquid into (pump) or from (withdraw) the perfusion tube thus changing solution inside the flow chamber.

On the microscope the flow chamber was subjected to the continues exposure of 1 mW 561 nm diode OBIS LS laser (Coherent, USA) to track the introduction of the 200 µl Chase Imaging Buffer that was withdrawn from the perfusion tube. The intensity of the fluorescence would be tracked to stop the withdraw at the peak intensity, this would ensure the concentration consistency for Cy3-ATP. When the perfusion tube would run dry (most likely before the peak is reached) it would be refilled with Pulse-Chase Chasing Buffer. At the peak intensity, the shutter would be closed and perfusion tube filled up to 900 µl with Pulse-Chase Chasing Buffer. The flow chamber would be incubated in that state for 20 min, ensuring that all myosins have take up Cy3-ATP to replace the dark ATP/ADP occupying their ATP binding pockets. Following the incubation the syringe pump would be set to withdraw 800 µl at 7.5 ml/min. The acquisition software would be prepared and 561 nm laser would be switched to 10 mW stroboscopic illumination (stroboscopic imaging is described above, see 3.2.5.a)

with 500 ms frames (450 ms pre-exposure + 15 ms exposure + 35 ms delay). The laser was switched OFF and stage moved to the next sample. When all myofibrils were imaged, the stage would move back to the first myofibril, wait (if necessary) for full 5 sec to pass and then repeat the cycle. Acquisition software was run for one cycle prior to imaging to confirm myofibril placement.

To achieve a high-throughput of image acquisition a programable, automated stage (see Figure 46) was devised to allow for the movement between single flow chamber samples during the OFF periods of the stroboscopic illumination. The schematic for circuitry is provided (see Figure 47). This setup allowed for all samples to be imaged continuously by exposing each sample to 15 ms laser ON in a period of laser OFF time for other myofibrils. For example, if three samples were to be imaged: A,B and C. The first frame to be take would be at the sample A (500ms frame), the stage would then move (100 ms move) to the next cardiomyocyte B (500ms to take a frame), and then proceed to the next cardiomyocyte C (1000 ms move), where another image (500 ms frame) would be taken, and finally move back to the first cardiomyocyte A (1100ms). 500*3 + 100 + 1000 + 1100 = 3700 ms, the stage, therefore, would wait for 1300 ms before beginning the next 5 sec imaging cycle.

To clean microfluidics after the experiment, full syringe volume of methanol was drawn and discarded though the system, following by the same volume of water. This process was done prior and following any day of the experiment.

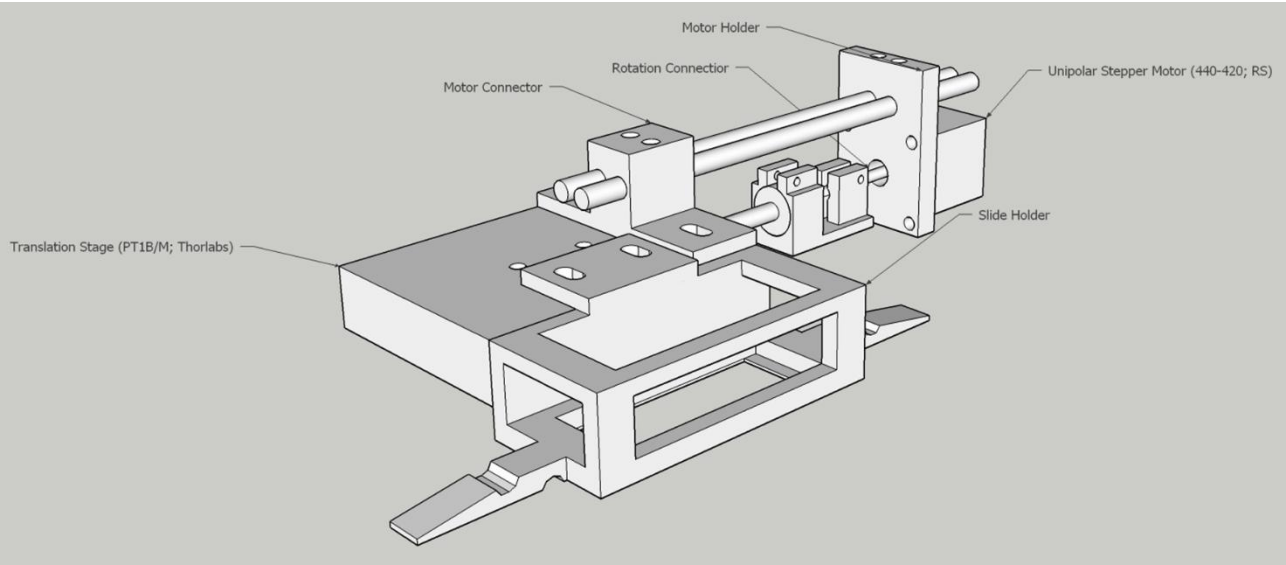


Figure 46. A schematic of an automated stage.

A schematic of a programmable, automated microscope stage designed to move the objective between samples using a unipolar stepper motor (440-420,RS), translation stage (PT1B/M; Thorlabs) and an Arduino UNO board (Arduino UNO Rev3; Arduino). Arduino is acting as a control unit, giving orders to the motor, which rotates the stage while remembering positions of each myofibril that is being recorded. All parts except for the stage, board and the motor were 3D printed using UltiMaker 2+ Connect.

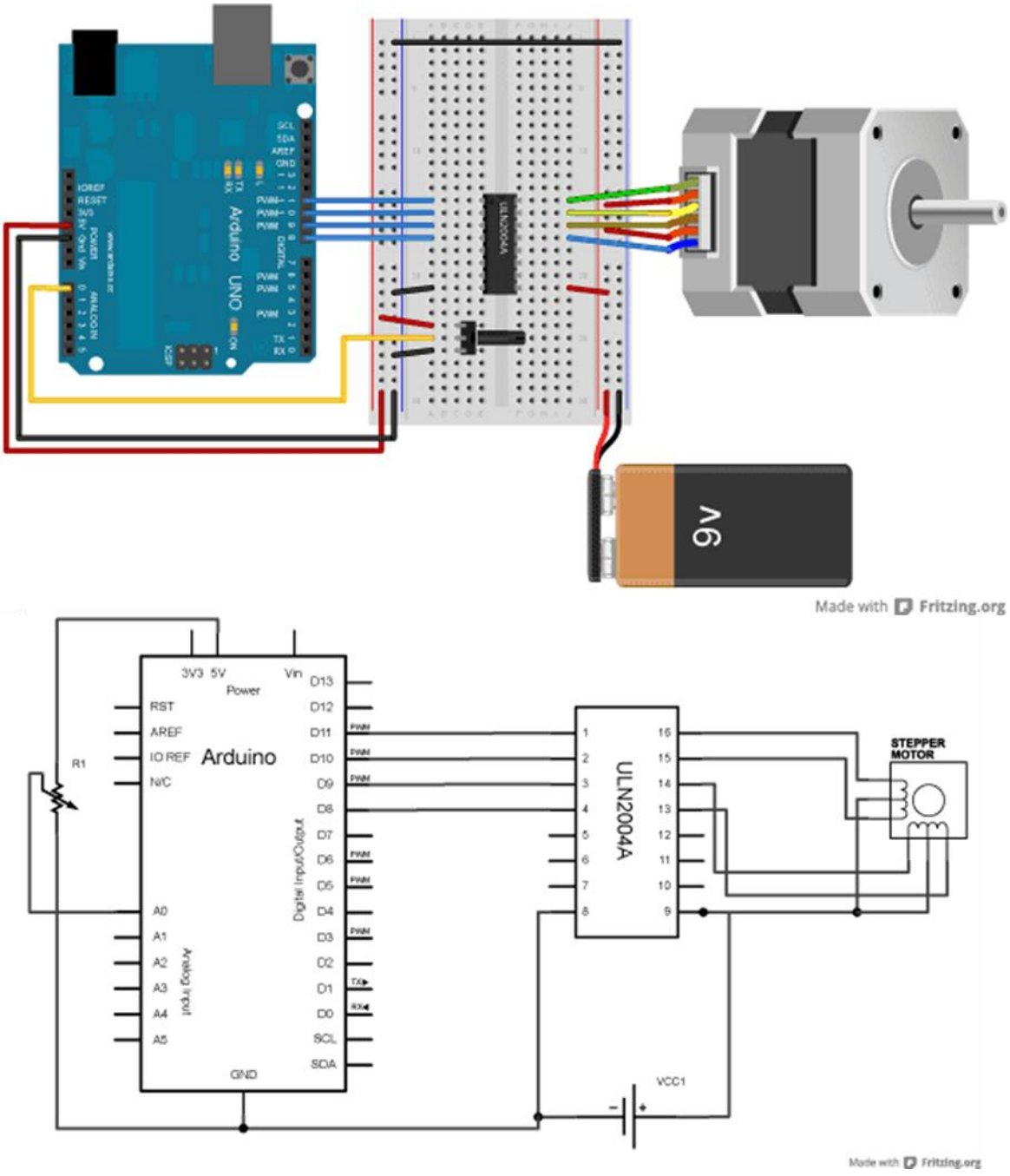


Figure 47. A circuit schematic showing the wiring of the Arduino board to the unipolar stepper motor.

An image (Top) and a schematical diagram (Bottom) of the wiring employed to connect the unipolar stepper motor to an Arduino UNO modulating board. The motor is connected to the board through an ULN2004A chip. Images taken from (https://docs.arduino.cc/learn/electronics/stepper-motors/), the analogue input is not employed in our design.

5.2.3. Ensemble Imaging Technique

Similar to our previous work (Pilagov *et al.*, 2025), a series of custom-written scripts were used to ease and decrease the human involvement during the analysis. First, a Jython script was used to separate a video into stacks of separate cardiomyocytes (for the ease of descriptions referred to as myofibrils). The number of stacks would depend on the number of myofibrils present on the video (usually 3-4). The videos were then analysed using a same-size ROIs (Figure 48A). Intensity change through time for each ROI was then analysed using an ImageJ plugin – Registration/Descriptor based-series-registration (2d/3d +t). This produced an exponential decay of intensity vs time (Figure 48B). The results were saved in .csv format. Further analysis was conducted using Microsoft Excel, where ROIs with clearly visible parts of a myofibril would be hand-picked and exponential decays fitted to up to 3 exponentials. If available, neighbouring ROIs each side of a chosen ROI were also analysed and the error for both amplitudes and rates were calculated using the standard deviation as error.

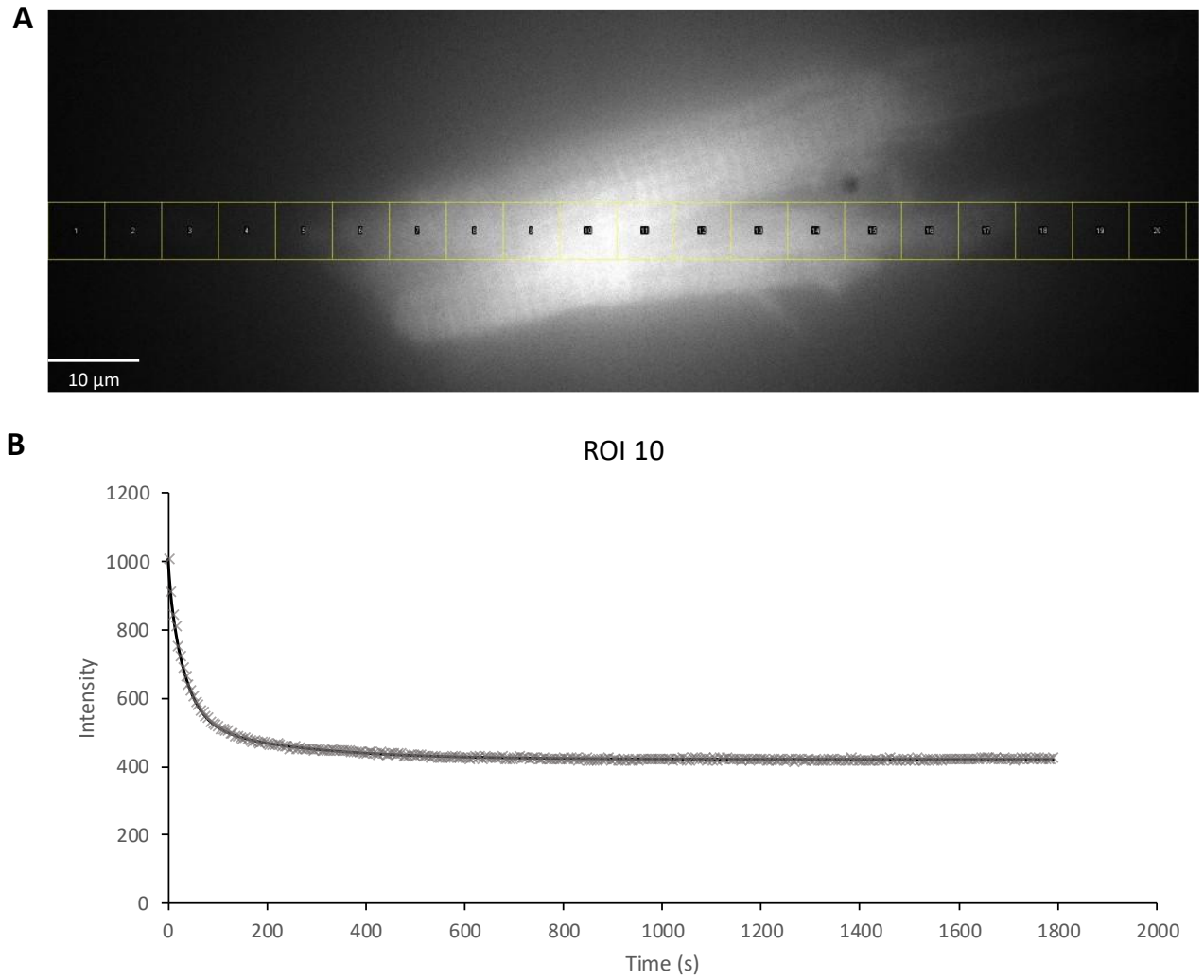


Figure 48. A typical cardiomyocyte as seen during imaging with 20 ROIs overlayed during the analysis.

A) ROI overlay was created using a custom-written Jython code using ImageJ. For this myofibril, ROIs 9,10 and 11 were chosen for analysis all others were not analysed. In this example, ROIs 9 and 11 were used to calculate the error in amplitudes and rates. B) Intensity decay was analysed using ImageJ plugin Registration/Descriptor based-series-registration (2d/3d +t). The results were fitted to triple exponential.

5.2.4. Determining the Accuracy of Stage Repositioning

Before proceeding, the reliability of the stage movement had to be addressed. The movement had to be tested to measure the relative positions of untreated myofibrils before and after the movement. Position tracking was done using Template Matchmaking (Thomas and Gehrig, 2020) plugin in ImageJ (source on GitHub). This plugin scans each frame from top left corner to the bottom right conner searching for a template image provided by the user. The user-defined template is translated over one image at a time and similarity score is calculated between the template and the

image section. This forms a correlation map (see Figure 49) that uses absolute pixel values to compare the user-defined template to a current image patch.

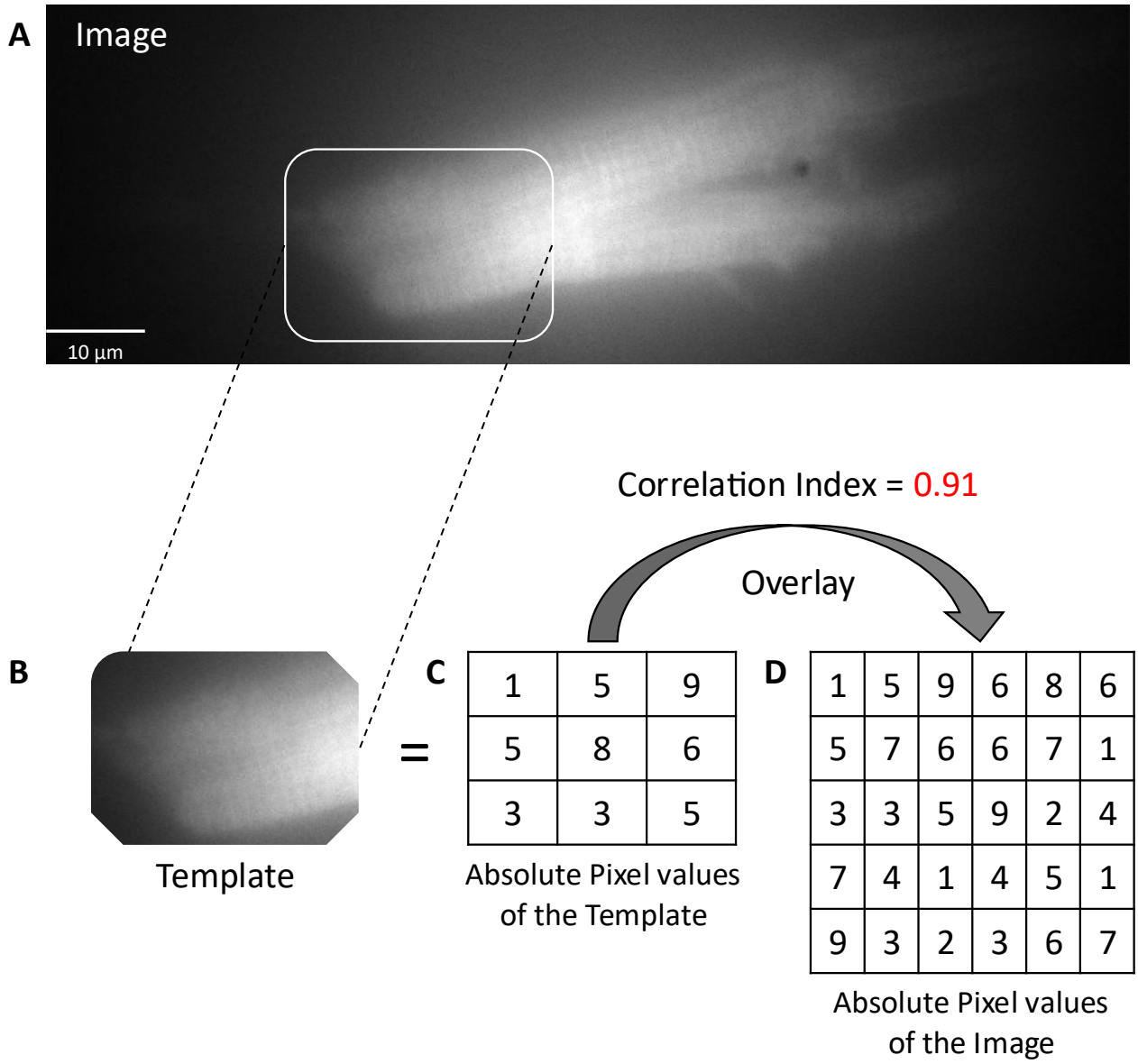


Figure 49. The image representing the pipeline of user-defined image alignment using Template Matchmaking plugin.

A) The image as seen during the analysis with a white box representing the template to be used in the comparative overlaying. B) A user-defined template derived from the original image and seen as a white box in A. C) A table showing an example of the absolute pixel values that are representative of intensities shown on the template. The absolute pixel values from the template are then completed to the rest of the absolute pixel values of the image (D) throughout all stacks to identify the correlation indexes for each segment of the original image. Correlation indexes are used to calculate the relative movement of objects though time.

The resulting correlation map enables the tracking of multiple or (in our case) single object position throughout the stack with positions (x, y) recorded and stored. Taking

the first frame of the sequence as a template, the position of the most distinct (highest signal-noise) part of the imaged myofibril was tracked throughout the image stack, and utilised using the capabilities of Template Matchmaking plugin to track the drifting of the observed myofibrils over 6 samples. The resulting displacement calculations were derived from Pythagorean relationship to the (0,0) coordinate, which was assumed to be the start of the movement (if any). The maximum change in myofibril position (x,y) was subtracted from the myofibril original position thus calculating the final displacement. It is worth mentioning, that some myofibrils were more distinct (higher signal-to-noise ratio) than others, with less-pronounced myofibrils being excluded from the analysis, as detection method was unable to accurately determine their movement.

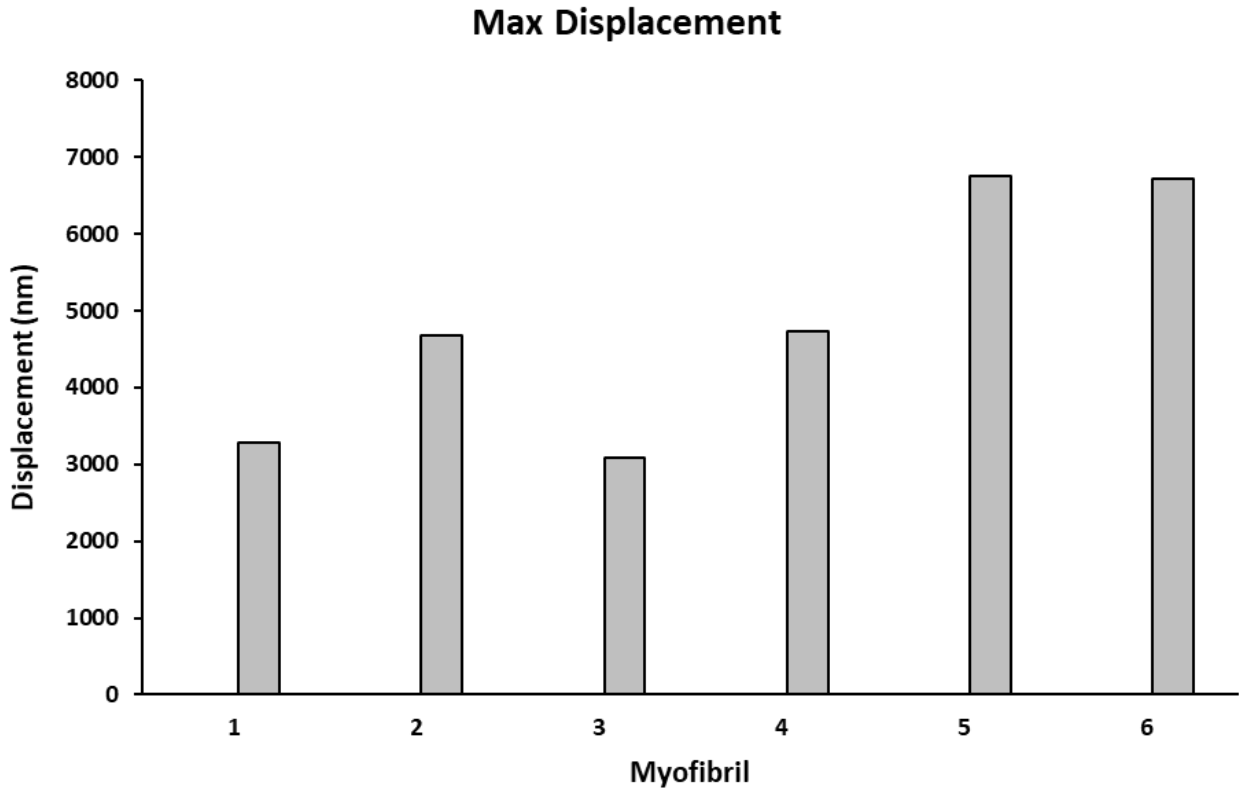


Figure 50. Figure showing the maximum displacement of myofibril during the stage movement for ensemble experiments to show the stage movement error.

Myofibrils analysed for this control are shown in numbers (1-6) on the x-axis, while their tracked maximum displacement is shown on the y-axis in nm. The displacement was calculated from a tracked initial position of the myofibril.

Average Max displacement was calculated to be 4871.72 nm (± 1454.35 nm). For reference, methodology employed (see the next section) during ensemble experiments used the analysis of 100x100 pxl (6300x6300 nm) region-of-interest (ROI) to evaluate the fluorescent decay of the sample. Thus, the maximum displacement was shown to be smaller or equal to the size of an ROI.

5.2.5. Using Adjacent ROIs to Calculate Measurement Errors

Ensemble imaging employs a different approach to the error calculation, when compared to experiments described in the two previous chapters. The myofibrils, as described above, used ROIs that were drawn from one end of the stack image to another (see Figure 51 A), numbered, and analysed to produce an intensity decay graph that is used to extract amplitudes of both DRX and SRX. The advantage of such analysis is the ability to analyse different parts of the image separately. Employing this advantage, three ROIs that were adjacent to each other were chosen (see Figure 51 AB) and analysed as described above. Each ROI produced amplitudes for DRX and SRX, that were used to produce both the average and standard deviation of ATPase rates for this myofibril. The advantage of this method was its non-reliance on the conventional fitting-derived errors, making it less complicated and more robust. When combining the data from multiple myofibrils under the same condition, the errors were propagated using standard error propagation approach.

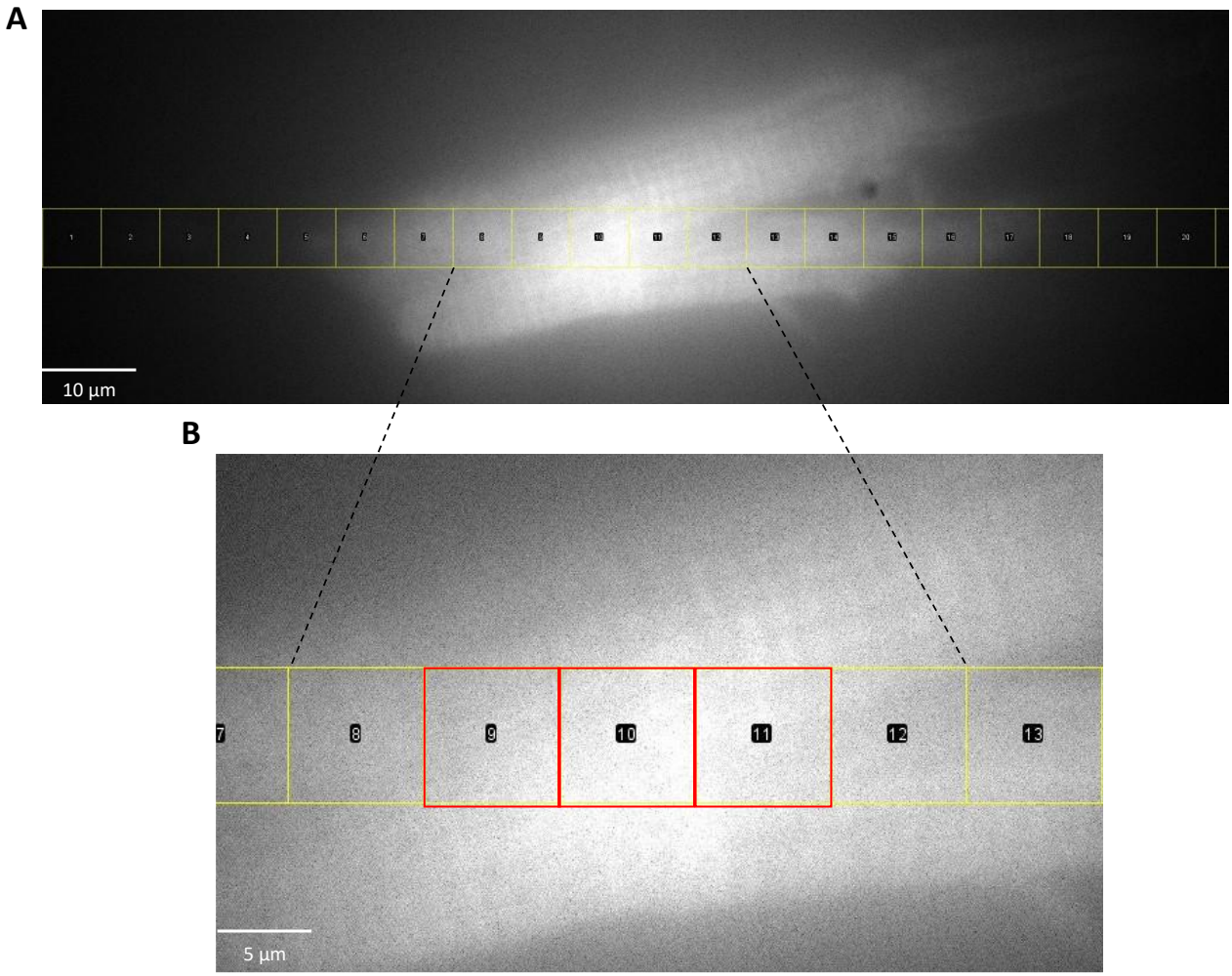


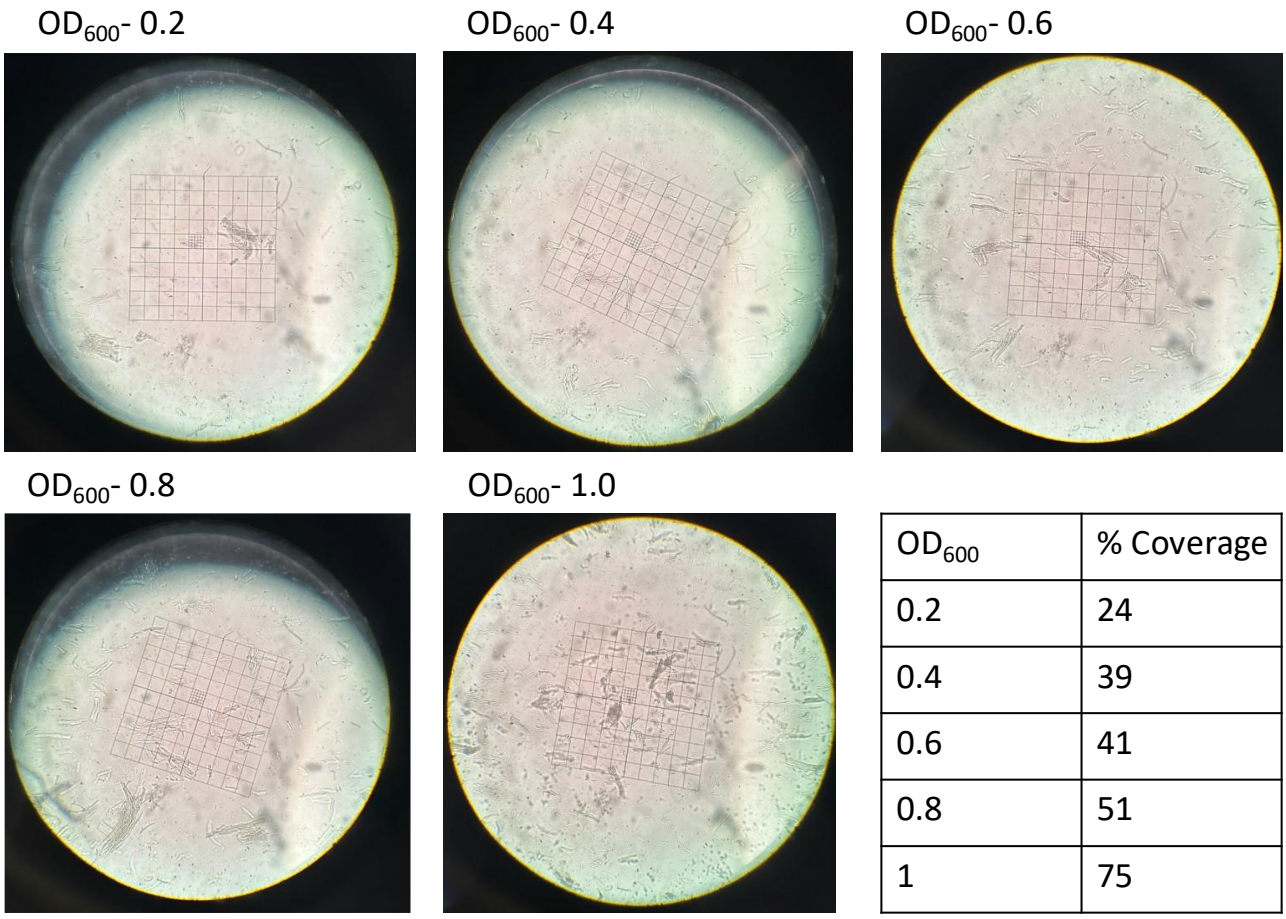
Figure 51. A typical cardiomyocyte showing the pipeline of analysis of three adjacent ROIs.

ROI separation during image analysis is described in 5.2.3. The ROIs are used to plot the intensity decay profile, from which both the amplitude and rates of Cy3-ATP attachments are extracted. Amplitudes are averaged and error is determined by using the standard deviation of between the amplitudes.

5.2.6. Pulse-Chase Optimisation

Pulse-chase part of the ensemble experiment was optimised to fit the bulk fluorescence approach of the ensemble imaging. The optimisation involved changes to the flow chamber design and the adjustments to the myofibril imaging employed by earlier, single-molecule studies. The flow chamber was modified to withstand an increased pressure associated with a rapid pulse of 7.5 ml/min. For that, the flow chamber volume was doubled (to 60 µl) to reduce the pressure inside the chamber, thus increasing the chamber reliability. Myofibril imaging was modified by increasing the myofibril density in the flow chamber, increasing the concentration of Cy3-ATP, and the concentration of dark ATP in the chase buffer.

The myofibril density was adjusted to compensate for the loss of some myofibrils due to a larger pressure from the increased flow of 7.5 ml/min. The increase in density also served to increase the probability of finding myofibrils suitable for imaging in close proximity to each other due to the time 5 sec frame limit of the experimental design. During the experiment, the 5 sec per cycle rule was applied, where the stage had to move through all imaged myofibrils within 5 seconds, thus dictating that the close proximity of suitable myofibrils on the imaging plane was necessary. To quantify the density, a microscope eyepiece reticule counting grid (Cambridge Optics, CO-ZZFHCW09.934) was utilised to estimate the number of myofibrils. The percentage of myofibril coverage was determined by counting the number of squares fully and partially filled with myofibrils (see Figure 52). Cy3-ATP and myofibril concentrations had to be adjusted relative to each other to maintain low background to noise ratio.



OD_{600}	% Coverage
0.2	24
0.4	39
0.6	41
0.8	51
1	75

Figure 52. Figure showing distribution of myofibrils on the surface of the flow chamber.

The image is observed as seen through a bench light microscope (OLYMPUS) with x400 magnification at different OD_{600}. Different ODs are indicated appropriately, with the summary table indicating the approximate percentage of the imaging surface in the flow chamber covered by the myofibrils.

5.2.7. Step-Resolution Optimisation

A glass microscope calibration graticule (S48, Graticules LTD, UK) was employed to determine the resolution of a single step. The step resolution was calculated to be ~1 micron per step using the above graticule. A unipolar stepper motor (440-420,RS), that is a size 17, 4 phase hybrid stepper motor capable of delivering a high torque even without direct electrical input, thus preventing the drift during the periods of inactivity. The step angle for this motor as described in the manufacturer-provided manual is 1.8 degrees, with an accuracy of 5% (or 0.09 degrees or 50 nm) .

5.2.8. The Effects of Known Myosin Modulators on Porcine β-cardiac Myofibrils

The untreated porcine myofibrils were imaged for the first part of our experimental procedure. This was conducted to compare ensemble imaging with previously conducted single-molecule porcine experiments. The results (see Figure 53A) show that untreated samples had a larger DRX population than observed in single-molecule experiments using the same tissue type. Samples from the single-molecule imaging were reported to have 49.8 ± 0.03% SRX, while samples imaged with the ensemble imaging yielded average of 32.6 ± 1.47% SRX. The difference was shown to be statistically significant ($p < 0.005$). Additionally, when looking at the stopped-flow experiments (Walklate *et al.*, 2022), the results reveal a very similar SRX population when compared to our ensemble experiments, with ~35% SRX for the same muscle type (porcine ventricle). The results shown in Figure 53 present an overall breakdown of myosin biochemical states relative to each measured myofibril individually, with myofibrils indicated by numbers on the x-axis and relative SRX/DRX % on the y-axis. It also provides a viable insight into the process of data analysis that leads us to the results reported below in Figure 54.

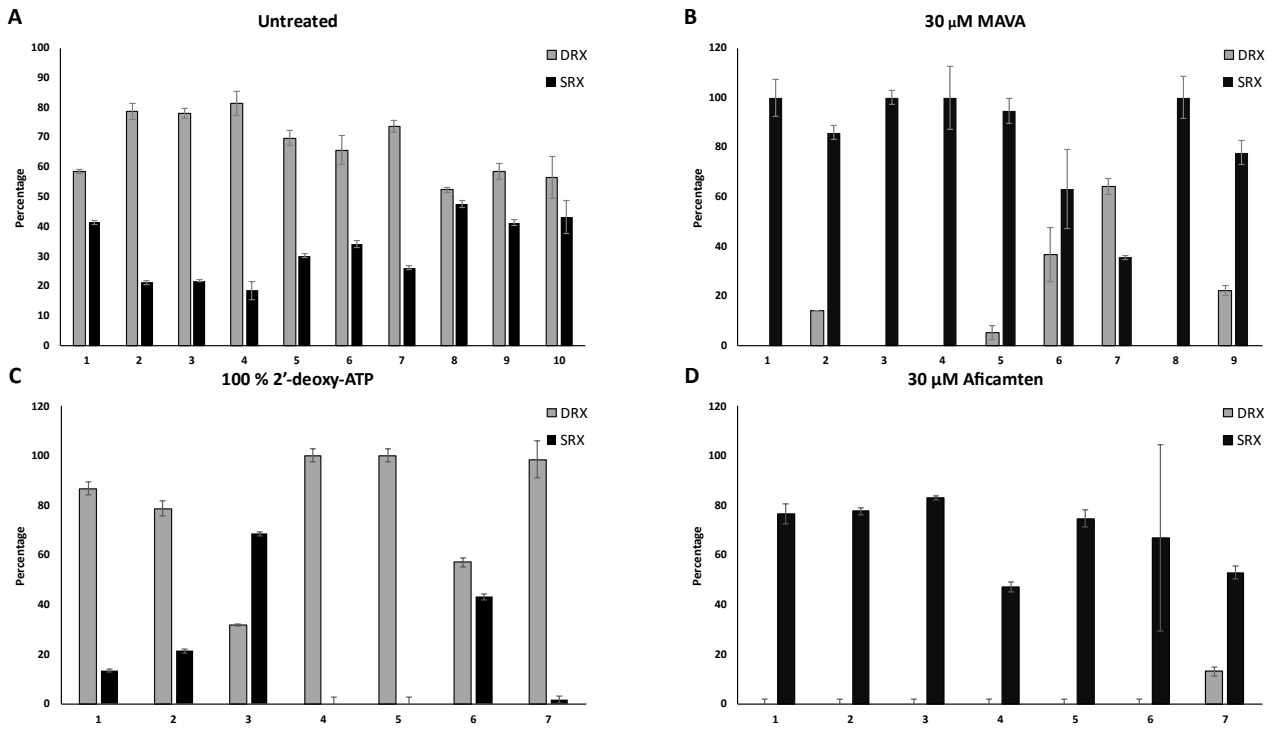


Figure 53. Bar charts reflecting the percentage of DRX and SRX.

The charts show the results for; untreated (A), 30 µM MAVA treated (B), 100 % dATP treated (C), and (D) 30 µM aficamten treated myofibrils. Percentage of Trespective myosin state is shown on the y-axis, while the x-axis shows the myofibril number. Error bars are provided using the standard deviation of adjacent ROIs method (see 5.2.5.). The averages for all conditions are provided in Figure 54.

When samples were treated with 2'-deoxy-ATP (dATP) the mean DRX percentage has increased to 78.9 (± 2.9)%, while dropping the SRX population to 21.1 (± 1.5)%. Changes observed during this treatment were not large enough to facilitate a statistically significant shift ($p = 0.1748$, see Figure 54B), although they were performed with 100 % dATP. Conversely, similar experiments conducted with stopped-flow (Walklate *et al.*, 2022) in the same tissue, have shown a complete activation of the thick filament.

On the other hand, after treatment with MAVA, thick filament has shown a near-complete repression of myosin heads. MAVA was introduced at 30 µM, which is 15-fold excess compared to a recommended dose for human intake (for pharmacology see 1.3.2.a). The concentration was chosen based on our previous experiments and to show the maximum level of repression possible. In such, MAVA has increased SRX percentage significantly from 32.0 ±9.5 % to 93.8 ± 9.99 % (see Figure 53C), with near complete elimination of DRX. MAVA was previously shown to be unable to fully repress

myosin heads in skeletal muscles (Pilagov *et al.*, 2023), with some myosin heads remaining in DRX despite many-fold-K_d-excess MAVA. Other groups have shown similar results in skeletal muscles. For example, a single-molecule experiments on the rat soleus muscle have revealed a 50 % SRX upon 10 μM MAVA treatment (Li *et al.*, 2019), and stopped flow experiments conducted on rabbit psoas muscles with 30 μM MAVA yielding ~45% SRX (Walklate *et al.*, 2022). Thus, a substantial difference was reported when comparting the results for skeletal to cardiac tissues.

Similarly to MAVA, when treated with aficamten (AFI) myofibrils have shown a complete repression of myosin heads from 32.6 (± 1.5) % SRX to 97.2 (± 7.4) % SRX. Interestingly, the percentage of repressed heads was higher when compared to Mavacamten (97.2 (± 7.4) %, 84.2 (± 6.7) %). Both changes in DRX and SRX upon AFI treatment were shown to be statistically significant (p-value < 0.001 for both).

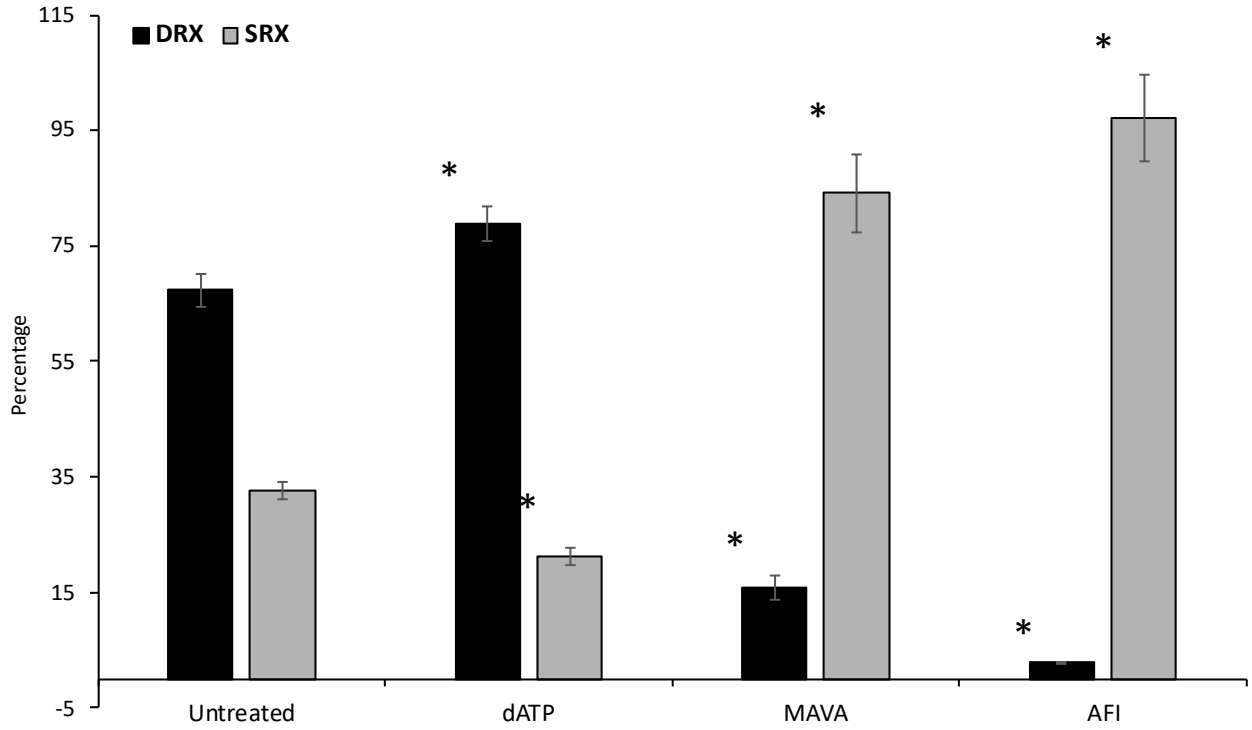


Figure 54. A bar chart showing the changes of average DRX and SRX percentage in each treatment group.

Untreated samples have approximately 2-fold DRX when compared to SRX, while upon 100 % dATP treatment this number increases to nearly 4-fold, yielding a statistically significant changes in both (P = 0.0036 and P <0.0001, respectively). MAVA treatment shown a statistically significant change for both increase in SRX (P < 0.0001) and decrease in DRX (P < 0.0001), when compared to the untreated. Finally, treatment with small molecule myosin ATPase inhibitor aficamten increase percentage SRX even further (than MAVA) and results in a statistically significant decrease (P < 0.0001 for both SRX and DRX changes) in DRX population to near-zero. The difference between two populations is determined using student-t-test and indicated with "" were significant. Errors are provided using standard error of the mean (SEM).*

5.2.9. Determining the Photobleaching Rate of Ensemble Experiments

The technique employed for calculating the photobleaching rate in single-molecule experiments was similarly utilised for the ensemble experiments. This control had to be repeated for the ensemble experiments as both the laser power and the exposure time were changed. The photobleaching experiments for ensemble experiments were conducted with the time lapses of 0.5, 1, 2 and 5 sec. In the end the photobleaching rate of the ensemble experiments was estimated (for the method refresher see 3.2.5.b) to be 0.60 ± 0.30 s^{-1} (for 15 ms exposure, 10 mW laser power) (see Figure 55). The resulting rate was larger than expected and what was estimated for a photobleaching rate of the single-molecule experiments. The initial explanation is a number of limitations to utilising the same approach used for single-molecule experiments when trying to determine the rate of photobleaching for ensemble experiments, namely, the

calculations were intended to describe the behaviour of singular events, rather than deal with the bulk fluorescence used in the ensemble imaging. Therefore, additionally clarification had to made to discuss the potential alternative ways to calculating the photobleaching rate for ensemble imaging, along with some arguments to try to elaborate on a large photobleaching rate estimated with ensemble control photobleaching experiments.

Fist, one has to always keep in mind that the photobleaching correcting was only applied to the data when comparing observed rates to the rates established in the literature and that the photobleaching rate was not used in calculating the reported percentages of myosin heads in DRX and SRX for both single-molecule and ensemble imaging. To put it another way, DRX and SRX percentages were calculated in relation to each other and thus did not involve the photobleaching rate (or rather photobleaching rate would have been cancelled out during calculations).

Second, the photobleaching rate observed above was observed for 15 ms exposure at 10 mW laser power, which makes is ~13 fold shorter and 2 fold less exposed to the laser beam than during the single-molecule experiments. Thus, an increased photobleaching rate that was produced by the ensemble photobleaching experiments does not align with our understand of photobleaching effect as one would expect the photobleaching rate to be smaller when either exposure time or laser power are reduced (and thus also smaller when both are reduced). Yet, an expected decrease was not observed, which indicated the lacking of the experimental design or unaccounted variable(s) in the used formulae (i.e. the formulae does not describe the observed events fully). When comparing Figure 33 to Figure 55, one can see a lower y-intercept for the latter, with an intercept being 0.009 (compared to ~0.03 for single-molecule) and thus producing a result that should be smaller than observed in single-molecule experiments, yet the produced value is larger as the y-intercept is a component of k_{bl} and thus has to be deconvoluted before the final result can be obtained. This leads us to believe that the formulae describing plotted graphs (for figures 36 & 55) are missing a component when describing the photobleaching of Cy3-ATP molecules in the ensemble experiments, although it seems to be very well suited for single-molecule approach.

Lastly, produced photobleaching rate for the ensemble experiments is not the lowest observed for data collected. For example, SRX rate for untreated myofibrils is 0.002 ± 0.0002 s^{-1} which would have been impossible to measure if the photobleaching rate was 0.6 s^{-1} as all events would have photobleached before releasing from the myosin heads. This further shows that the equation describing the calculated photobleaching rate (Gebhardt *et al.*, 2013; Pilagov *et al.*, 2023) is lacking variable(s) when used for ensemble experiments. Further experiments would have to be conducted to establish the best approach to determining their photobleaching rate. For example an alternative way of determining the photobleaching rate for ensemble imaging would be to compare the fluorescent decay of Cy3-ATP molecule attached to the surface of a coverslip to those attached to a myofibril as it would produce a distinctive rate of photobleaching that would be matching the ones observed on the coverslip surface. Unfortunately due to the time limitations of this thesis the time to conduct these experiments was spend elsewhere and thus a refinement of an existing equation describing the photobleaching rate for the ensemble imaging , sadly, was not achieved.

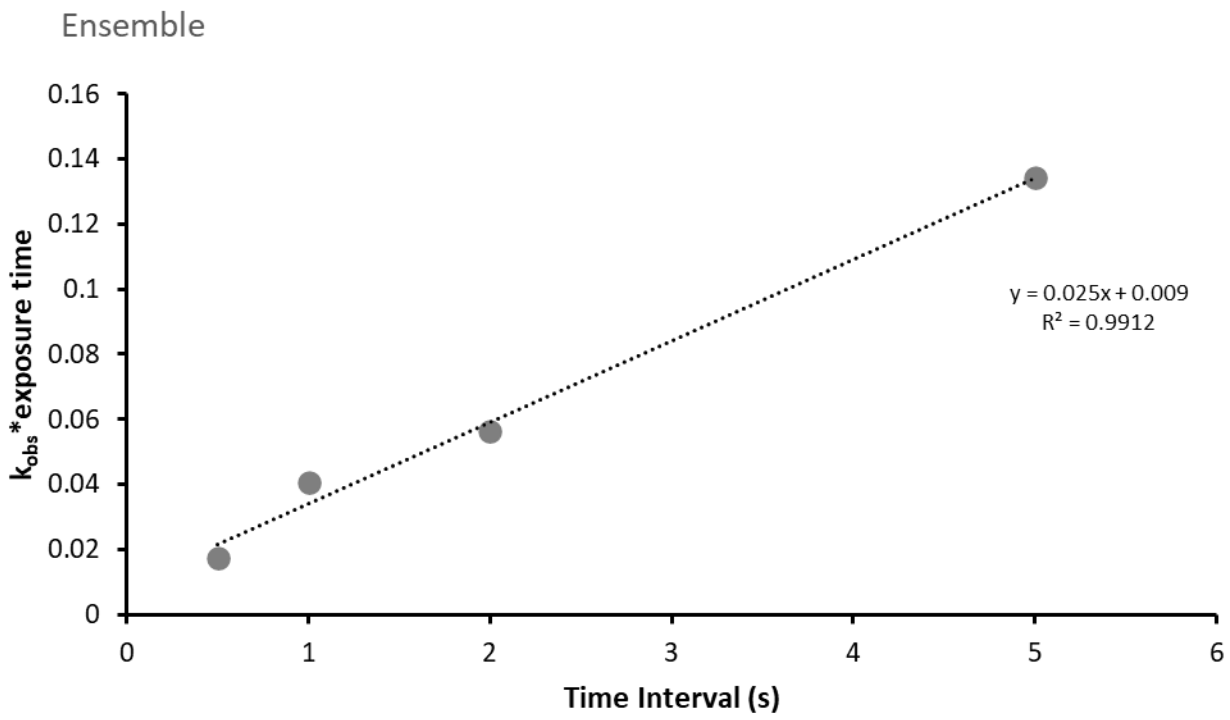


Figure 55. Figure representing a control experiment to calculate the photobleaching rate of the ensemble experiments.

Similar to single-molecule experiments, this graphs is used to determine the y-intercept that provides an approximation of the photobleaching component for observed fluorescence. Points are plotted for each OFF-time interval: 0.5, 1, 2, and 5 sec. Equation and R^2 are provided along with the trendline.

5.3. Discussion

During this final chapter a modified pulse-chase approach was established to image Cy3-ATP attachments to the cardiac myofibrils from porcine left ventricle. The previously described single-molecule approach was used as a template to implement the pulse-chase methodology first used to identify the SRX state of myosin by Stewart and colleagues (Stewart *et al.*, 2010). Further work from the same group (Roger Cooke's) has described and compared SRX in cardiac muscles to SRX in skeletal muscles (Hooijman, Stewart and Cooke, 2011), identified the involvement of MyBP-C in regulating SRX (McNamara *et al.*, 2016), and explored small molecule inhibitors (like piperine) to shift SRX:DRX ratio to a more active state as a means of treating metabolic disorders (like type 2 diabetes) (Wilson, Naber and Cooke, 2020). The difference between the two approaches is subtle but worth mentioning. In our approach, thinner cardiomyocytes (~5 μm dimeter) were used when compared to bundles with diameter < 90 μm used in papers above. Additionally, alternative fluorescent molecules (Cy3-ATP) were used when compared to mantATP used by the above studies. Finally, a microfluidics system was utilised to deliver the chase (and all other) buffers into the flow chamber, while the above studies did it manually.

These changes to the protocols of the above papers resulted in different observations produced during the experiments. For example, our experiments have yielded three rates of Cy3-ATP decay (compared to 2 reported by Cooke's group), which might be the products of a smaller time intervale between the chase and the beginning of the imaging session. This is a result of our novel microfluidics setup, that enables us to see the fastest ATPase rate (~0.1s^{-1}) that was not observed by Cooke and colleagues as the majority of the fastest ATP molecules would have detached by the time the flow chamber would have been imaged. The advantages of using Cy3-ATP when compared to mantATP will be described in the next section when addressing the pulse-chase controversy. Conversely, the difference in muscle fibre diameter should not affect the imaging or the Cy3-ATP availability as the diffusion of free nucleotides was shown to be 10-15 sec from tissues with similar diameter (Cooke and Pate, 1985).

Lastly, when comparing two slow rates observed in our ensemble experiments (45.9 ± 2.4 s, and 473.6 ± 52.2 s) to Cooke's work (12-25 s, and ~140 s) with cardiac muscles

(Hooijman, Stewart and Cooke, 2011), the similar rates were observed for both DRX and SRX rate, respectively. Although our rates are ~3 fold slower, this might be a result of experimentation with different species as Hooijman and colleagues used rabbit ventricle, while our experiments were using porcine ventricle.

5.3.1. Addressing the Pulse-Chase Controversy

Recent publication by Regnier group (Mohran *et al.*, 2024) have brought into light some concerns regarding the standard mantATP pulse-chase experiments. In their work, they describe three paradoxes that plague some classic experiments conducted using mantATP both with and without the use of small molecule inhibitors (e.g. MAVA).

Their first paradox describes the inconsistency in SRX:DRX equilibrium. In such, thermodynamic equilibrium present in myosin head's biochemical states do not correlate with the time scale normally associated with SRX (100 s) and DRX (10 s). They postulated that if DRX and SRX are in constant thermodynamic equilibrium, then the change between the states can occur as fast as the slowest of the rates (i.e. SRX, >100 s), and thus produce a single exponential seen during mantATP experiments on mollusc myosin (Jackson and Bagshaw, 1988; Nyitrai, Szent-Györgyi and Geeves, 2003) where contraction is regulated by Ca^{2+} binding to RLC. Our work was conducted using whole, skinned myofibrils and thus have access to accessory/associated proteins (e.g. MyBP-C, titin, etc.) that were not present in their experiments, as they were conducted on HMM and S1. Such proteins would be potential culprits in us observing more than one myosin ATPase rate, as some of them were shown to interact with both thick and thin filaments, thus potentially changing their kinetics (e.g. MyBP-C (Ponnam *et al.*, 2019)).

The second paradox refers to a comparative differences between the steady-state ATPase experiments and SRX/DRX measurements for isolated myosin preparations. Specifically, Mohran and colleagues point out a large change that should be occurring as a result of using different types of imaged myosin fragments (e.g. S1 and HMM) as larger fragments would be expected to form both head-head and head-backbone stabilising interaction, and thus should be having a larger repression effect on observed myosin population (Ma *et al.*, 2021). Yet, for some mantATP nucleotide displacement assays (e.g. (Gollapudi, Yu, *et al.*, 2021)) using isolated myosin

preparations the results (~30 % inhibition by MAVA) were inconsistent when comparing the reported steady-state ATPase of different myosin fragment and reported (Gollapudi, Ma, *et al.*, 2021) SRX population (>90 % inhibition by MAVA) for the same tissue. However, in our approach full myofibril bundles were utilised instead of isolated proteins and thus were not facing the same problem.

The third paradox is interesting and puzzling but does not contradict anything described in this chapter. Instead, it poses an interesting question; why, if SRX could be formed in 200 ms, does such a large percentage of DRX persist in all observations? Another study (Walklate *et al.*, 2022) goes into potential explanations of this paradox, where they discuss the possibility of zero turnover rate for SRX, which was previously proposed in molluscs (Nyitrai *et al.*, 2003), to also exist in mammalian sarcomeres. SRX with zero turnover rate would imply that ATP turnover would be dependent on the ATP release rate from DRX heads and the rate of SRX-to-DRX conversion. Walklate and colleagues additionally argue that because the IHM has a very tight conformation, ADP.P_i will not be able to release without breaking or destabilizing the IHM structure, thus further justifying zero-rate-SRX model. Keeping in mind the arguments posed for the first paradox, the assumption would be that the involvement of accessory/associated proteins allows for the modulated myosin kinetics and thus making a rapid change an energetic possibility, but ultimately the last paradox requires more experiments to establish the exact nature of different modulations inside both thick and thin filaments that result in observed rates of myosin ATPase rate.

Overall, Mohran *et al.* 2024 concentrates specifically on questioning the experiments conducted with mantATP on partial fragments of myosin molecule (i.e. HMM or S1). Our experiments employ the use of whole myofibrils and use Cy3-ATP instead of mantATP. The advantage of using whole myofibrils are detailed above, while the use of Cy3-ATP was shown not to interfere with the myosin ATPase rate (Toseland and Webb, 2011; Ušaj *et al.*, 2021; Pilagov *et al.*, 2023).

5.3.2. Small Molecule Perturbation Shows the Viability of the Novel Ensemble Imaging

Testing the newly developed system was crucial, thus a series of well-defined myosin ATPase modulators were used to test the novel approach experimentally. Perturbation

was performed to both increase (MAVA, AFI) and decrease (dATP) the repression of myosin heads. In such, conducted experiments were to establish the level of robustness of the newly constructed system by the effects of known myosin modulators and show the effects of newly developed small molecule myosin ATPase inhibitor aficamten (Hartman *et al.*, 2024).

When treated with dATP, a statistically significant increase was observed in the number of myosin heads in DRX, with an average of 78.9 (± 2.9) %. When compared to 67.4 (± 2.9) % DRX in untreated samples, the change was large enough to be considered statistically significant (p= 0.0036), with 11.5 % increase in DRX population observed. Literature analysis has shown that the amplitude of dATP-driven change was surprisingly low, when compared to experiments on the same (and other) tissue types from other groups (Powers *et al.*, 2019; Ma *et al.*, 2020; Walklate *et al.*, 2022). We chose to compare our dATP experiments closely to the work of Walklate et al., as they were utilising the same tissue type and employed similar techniques to ours. In their experiments Walklate et al. had a much larger net change, yielding a full activation of the thick filament, using the same dATP (100%) concentration. Although, the decrease in DRX observed in our experiments with 100% dATP was shown to be statistically significant the same dATP concentration has yielded a full activation of the thick filament in the works of Walklate et al.

The potential reasoning behind the lack of change observed under 100% dATP condition is a lack of incubation time during the chase phase of the experiment or an insufficient number of imaged myofibrils. Above, in 5.2.2, the change of Cy3-ATP containing solution to 100% dATP containing solution was described to be a very fast. In fact, the solution change was conducted in ~4.36 s. Briefly, flow chamber with sample was flushed with 800 µl Chase Buffer at 10 ml/min (or 183.3 µl/s), thus producing ~4.36 s flow. Although solution was fully replaced with dATP-exclusive solution, Cy3-ATP molecules already inside the ATP-binding pockets of myosin molecules would maintain their positions and thus produce results similar to untreated samples. Furthermore, due to the time limitations, the sample size was not larger enough when compared to the untreated. Thus, when comparting untreated SRX population to that in dATP (as displayed in Figure 53) the changes observed might not appear large enough, albeit significant.

MAVA has established a larger SRX population across all samples, averaging 84.2 (± 6.7) % SRX across all imaged myofibrils. Near-full repression came as a surprise, as a full repression was not observed with similar conditions in literature (Rohde *et al.*, 2018; Scellini *et al.*, 2021; Walklate *et al.*, 2022; Pilagov *et al.*, 2023). However, experiments in the literature provided were either conducted in a different tissue type or used differ MAVA concentrations, thus rendering comparison more complex. Regardless, the aim of both dATP and MAVA perturbations was to show the robustness of the system and not to determine the precise effects of MAVA and dATP, which are described excessively in literature.

Lastly, aficamten has shown a near-full repression of myosin heads resulting in 97.2 (± 7.4) % final SRX population. When taken individually, myofibrils as described in Figure 53 show the absence of DRX in most myofibrils with myosin heads fully repressed. Aficamten is a next-in-line small molecule myosin ATPase inhibitor after MAVA and thus has a very limited literature presence as of writing of this thesis (Coats *et al.*, 2024; Hartman *et al.*, 2024; Maron *et al.*, 2024). However, the results described in this chapter indicate that AFI has an increase potency when compared to MAVA in myosin ATPase inhibition in myofibrils obtained from the porcine left ventricle.

	Untreated	**dATP**	**MAVA**	**AFI**
Average DRX %	67.4 (± 2.9)	78.9 (± 2.9)*	15.8 (± 5.6)*	2.8 (± 0.2)*
p-value		0.0036	<0.0001	<0.0001
Average SRX %	32.6 (± 1.5)	21.1 (± 1.5)*	84.2 (± 6.7)*	97.2 (± 7.4)*
p-value		<0.0001	<0.0001	<0.0001

Table 8. Table showing the distribution of DRX and SRX across perturbed and unperturbed conditions for ensemble imaging.

Statistically significant changes, when compared to untreated, are labelled with an "". P-values are provided for SEM error calculations.*

5.4. Conclusions

During this final part of our research a novel, high-throughput method was established for the analysis of multiple myofibrils simultaneously. This method was aimed at looking through multiple patient-derived samples that were acquired from our collaborators. Unfortunately, the time limitation had prevented us from progressing to human sample testing, but a solid groundwork was laid for future testing and the robustness of the method was tested by collecting multiple datasets with previously used porcine cardiac tissue treated with known myosin modulators. The value of this method when compared to our previous work was the reduced experimental time per sample, as multiple samples could be imaged quasi-simultaneously. Furthermore, this method implemented an imaging system where samples could have had separate microfluidics attached to multichannel flow chambers, which would have enable the use of separate buffers for each sample. Our novel system was further tested by imaging porcine cardiac sample using both new (aficamten) and well-known (Mavacamten, dATP) myosin antagonists.

Sadly, the separation of these myofibrils into separate flow chamber, capable of using different buffers was never achieved, as the natural progression of this project dictated the development of the moving stage and pulse-chase optimisation as a primary focus. However, a decrease in myosin ATPase activity was shown following AFI and MAVA treatments, with an increase in myosin ATPase activity after dATP treatment. Interestingly, a novel small molecule myosin inhibitor aficamten has shown a larger degree of repression than Mavacamten, resulting in a near-full repression of the thick filament. Lastly, activation of the thick filament by dATP was not complete even at 100% dATP. This did not align with observations made in studies of other groups at 100% dATP using the same tissue type. This could be attributed to a relatively small sample size or the nature of our novel experimental method.

Regardless, here a novel, high-throughput method of collecting and analysing myofibril data was developed to increase the productivity of our previous, single-molecule, approach, in fact the novel method had at least a 3-fold increase in productivity. This novel approach was tested by modulating the myofibril ATPase with known myosin

repressors (MAVA, AFI) and activator (dATP), with results showing similar trends as observed in literature.

While sacrificing the sub-zonal resolution of single-molecule approach, a novel method was created with the myofibril imaging limits defined by the hardware of the stage, rather than the experimental time, as was the case for single molecule experiments. An improved stage had enabled us to increase the number of samples imaged per 30 min imaging session, with the number of myofibrils limited only by the stage specifications. Following the acquisition of an improved stage and implementation of the multichambered flow cells, it was planned to utilise the system to image a large number of mutated tissue samples. These samples would have come either from donor-biopsies, model organisms or from induced pluripotent stem cells.

Chapter 6 – Final Words and Conclusions

6.1. Conclusions

The work covered in this thesis furthers our understanding of how HCM-related proteins like MyBP-C and RLC are affecting the energy consumption by myosin motors. Furthermore, a bulk fluorescent technique, the ensemble imaging, was developed to investigate multiple patient- or model organism- derived samples quasi-simultaneously.

The effects of pharmaceutical agents on the energy consumption of myosin molecules was investigated in both cardiac and skeletal muscles to establish the energy consumption of different muscle tissues. A single-molecule approach was employed to measured the rate of ATP detachment from the full-length myofibrils by using Cy3 as a fluorophore. Additionally, an anti-alpha actinin specific antibody with an Alexa-488 secondary antibody was attached to the Z-discs and used as fiducial markers to further resolve the positions of attached Cy3-ATP molecules. Specifically, a novel small molecule ATPase inhibitor Mavacamten (MAVA) was found to repress myosin heads in fast-twitch skeletal rabbit psoas muscles, thus reducing their ATP consumption and leading to a larger population of myosin heads in a Super Relaxed State (SRX). On the other hand, the activity of protein kinase A (PKA) was shown to activate myosin heads, thus creating a larger population of a more energy-using Disordered Relax State (DRX). The effects of PKA were shown in both cardiac and skeletal muscles. Additionally, the effects of RLC phosphorylation were shown by employing myosin light chain kinase (MLCK) on porcine cardiac tissue containing β-myosin. MLCK has shown a large increase in the number of activated myosin heads (i.e. myosin in DRX), that has echoed the results observed under a PKA treatment. The key difference between the kinase treatments was the distribution of percentage SRX decrease along the A-band. PKA-induced change was marginal overall but revealed compensatory mechanism is the D-zone that compensated the largest observed increase in SRX in the C-zone. Like the cardiac tissue, skeletal muscles have shown a decrease in SRX

population following PKA treatment, although no compensatory mechanism was observed for this tissue type. The results obtained from the MLCK phosphorylation have shown the effects of MyBP-C, localised to the C-zone, on phosphorylated RLC. In such, the effects of RLC phosphorylation were dampened in the C-zone, hinting at the hierarchical nature of MyBP-C to RLC interactions.

Finally, a novel method of imaging using bulk fluorescence was developed which required an adjustment of the existing single-molecule approach to fit into a high-throughput system for testing multiple patient or model samples simultaneously. Unfortunately, the system was never fully implemented and the tests using patient samples were never conducted. Instead, the system was used to test porcine left ventricle with the known myosin activator dATP and two novel small molecule myosin ATPase inhibitors: MAVA and aficamten (AFI). The results produced by both myosin inhibitors and activators have confirmed the reliability of the system, thus providing us with an alternative, high-throughput method of observing myosin ATPase.

When compared to the work from other groups similar techniques were utilised by Warshaw and Cooke laboratories for single-molecule approaches (Nelson *et al.*, 2020, 2023) and ensemble experiments (Wilson, Naber and Cooke, 2020), respectively. When comparing results produced by similar single-molecule experiments, including other groups (Ušaj *et al.*, 2021), comparable results were produced with only slight alterations that most likely resulted from the use of different species or muscle type. For example, our results for rate constants of observed sarcomeric ATPase were comparable to the abovementioned single-molecule studies (Nelson *et al.*, 2020; Ušaj *et al.*, 2021; Nelson *et al.*, 2023) and produced 2-3 rates of; ~0.1, ~0.01, and ~0.001. Although Nelson and colleagues did not report the fastest rate in their experiments, this could be attributed to their method of data analysis and acquisition. Regardless, our studies have provided a comprehensive description of ATPase activity in slow skeletal (Pilagov *et al.*, 2023) and cardiac isoforms (Pilagov *et al.*, 2025) of striated muscles. Furthermore, our single-molecule approach was the first to report on the activity of β-cardiac myosin isoform, in addition of being the first to report on the effects of RLC phosphorylation by MLCK on single-molecule level. Lastly, our studies were among the first to report on cardiac specificity of Mavacamten, providing a tangible contribution to the pharmaceutical field.

There are other well-established methods to monitor muscle ATPase activity, like stopped-flow (Walklate *et al.*, 2022), which provides relatively quick results, although lacking sub-sarcomeric resolution provided by our single-molecule techniques. Additionally, there has been a recent controversy (Mohran *et al.*, 2024) associated with the use of mantATP in determining myosin ATPase activity that did not include our single-molecule approach (for detailed explanations see 5.3.1), thus making it an attractive tool to use for future experiments.

With some additional implementations, our single-molecule set up could be used to address another controversy in the field, the differences between biochemical and structural states of myosin motors. Juts like a recent publication by Ma et al (Ma *et al.*, 2023) where the small angle x-ray diffraction was used to distinguish that difference, our approaches could be modified to implement similar techniques found in the works of the Brunello et al. (Brunello *et al.*, 2023), where they inserted orientation-sensitive fluorescent probed into RLC and TnC to describe not only the biochemical states of myosin motors but also extract their structural data. Additionally, experiments conducted by other groups like (Walklate *et al.*, 2022; Brunello *et al.*, 2023) describe experiments conducted at close-to-physiological temperatures (~30-35 °C), rather than a more widely-used room temperature (or ~20-25 °C) (Hooijman, Stewart and Cooke, 2011; McNamara *et al.*, 2016). Although the relation between temperature, IHM and SRX is still under debate (Walklate *et al.*, 2022), with some authors suggesting that higher temperatures result in more IHM thus reducing force generation (Caremani *et al.*, 2019) and other discussing a more complex nature of force-temperature dependence (Walklate *et al.*, 2022). An additional layer of complication is added when considering an unclear nature of IHM:SRX relationship, with some data suggesting two separate processes (Ma *et al.*, 2023) and others considering them to be the same (Alamo *et al.*, 2016). Regardless, additional experimentation to clarify temperature-SRX relation is clearly required in the field and our methodology might be the best way to provide that, as sample preparation could be separated from the imaging conditions and thus eliminating the largest issue of sample degradation due to higher temperatures. This could be achieved with a relatively simple stage heating mechanism.

To conclude, a novel and uniquely flexible methodology was developed throughout this thesis that could be adjusted to both; implementing different techniques from

around the field and advancing our understanding by providing an alternative ATPase tracking method for less understood areas of the field.

References

Ababou, A. *et al.* (2008) “Myosin binding protein C positioned to play a key role in regulation of muscle contraction: structure and interactions of domain C1,” *Journal of molecular biology*, 384(3), pp. 615–630.

Ackermann, M.A. and Kontrogianni-Konstantopoulos, A. (2010) “Myosin binding protein-C slow: an intricate subfamily of proteins,” *Journal of biomedicine & biotechnology*, 2010, p. 652065.

Ackermann, M.A. and Kontrogianni-Konstantopoulos, A. (2011a) “Myosin binding protein-C: a regulator of actomyosin interaction in striated muscle,” *Journal of biomedicine & biotechnology*, 2011(1), p. 636403.

Ackermann, M.A. and Kontrogianni-Konstantopoulos, A. (2011b) “Myosin binding protein-C slow is a novel substrate for protein kinase A (PKA) and C (PKC) in skeletal muscle,” *Journal of proteome research*, 10(10), pp. 4547–4555.

Ackermann, M.A. and Kontrogianni-Konstantopoulos, A. (2013) “Myosin binding protein-C slow: a multifaceted family of proteins with a complex expression profile in fast and slow twitch skeletal muscles,” *Frontiers in physiology*, 4, p. 391.

Adalsteinsdottir, B. *et al.* (2014) “Nationwide study on hypertrophic cardiomyopathy in iceland evidence of a MYBPC3 founder mutation,” *Circulation*, 130(14), pp. 1158–1167.

Ahmed, S.H. and Lindsey, M.L. (2009) “Titin phosphorylation: myocardial passive stiffness regulated by the intracellular giant,” *Circulation research*, pp. 611–613.

Alamo, L. *et al.* (2008) “Three-Dimensional Reconstruction of Tarantula Myosin Filaments Suggests How Phosphorylation May Regulate Myosin Activity,” *Journal of molecular biology*, 384(4), pp. 780–797.

Alamo, L. *et al.* (2016) “Conserved Intramolecular Interactions Maintain Myosin Interacting-Heads Motifs Explaining Tarantula Muscle Super-Relaxed State Structural Basis,” *Journal of molecular biology*, 428(6), pp. 1142–1164.

Allingham, J.S., Smith, R. and Rayment, I. (2005) “The structural basis of blebbistatin inhibition and specificity for myosin II,” *Nature structural & molecular biology*, 12(4), pp. 378–379.

Amrute-Nayak, M. *et al.* (2014) “ATP turnover by individual myosin molecules hints at two conformers of the myosin active site,” *Proceedings of the National Academy of Sciences of the United States of America*, 111(7), pp. 2536–2541.

Anderson, R.L. *et al.* (2018) “Deciphering the super relaxed state of human β-cardiac myosin and the mode of action of mavacamten from myosin molecules to muscle

fibers," *Proceedings of the National Academy of Sciences of the United States of America*, 115(35), pp. E8143–E8152.

Auguin, D. *et al.* (2023) "Omecamtiv mecarbil and Mavacamten target the same myosin pocket despite antagonistic effects in heart contraction," *bioRxiv.org: the preprint server for biology* [Preprint]. Available at: https://doi.org/10.1101/2023.11.15.567213.

Auguin, D. *et al.* (2024) "Omecamtiv mecarbil and Mavacamten target the same myosin pocket despite opposite effects in heart contraction," *Nature communications*, 15(1), p. 4885.

Bähler, M. and Rhoads, A. (2002) "Calmodulin signaling via the IQ motif," *FEBS letters*, 513(1), pp. 107–113.

Bang, M.L. *et al.* (2001) "The complete gene sequence of titin, expression of an unusual approximately 700-kDa titin isoform, and its interaction with obscurin identify a novel Z-line to I-band linking system," *Circulation research*, 89(11), pp. 1065–1072.

Barefield, D.Y. *et al.* (2023) "Myosin-binding protein H-like regulates myosin-binding protein distribution and function in atrial cardiomyocytes," *Proceedings of the National Academy of Sciences of the United States of America*, 120(51), p. e2314920120.

Barnett, J.T. and Kad, N.M. (2019) "Understanding the coupling between DNA damage detection and UvrA's ATPase using bulk and single molecule kinetics," *The FASEB Journal*, 33(1). Available at: https://doi.org/10.1096/fj.201800899R>).

Basit, H. *et al.* (2025) "Hypertrophic cardiomyopathy," in *StatPearls*. Treasure Island (FL): StatPearls Publishing.

Bauman, A.L. and Scott, J.D. (2002) "Kinase- and phosphatase-anchoring proteins: harnessing the dynamic duo," *Nature cell biology*, 4(8), pp. E203-6.

Bayram, Y. *et al.* (2016) "Molecular etiology of arthrogryposis in multiple families of mostly Turkish origin," *The journal of clinical investigation*, 126(2), pp. 762–778.

Behrens-Gawlik, V. *et al.* (2014) "MYBPC3 in hypertrophic cardiomyopathy: From mutation identification to RNA-based correction," *Pflugers Archiv European Journal of Physiology*. Pflugers Arch, pp. 215–223. Available at: https://doi.org/10.1007/s00424-013-1409-7.

Behrmann, E. *et al.* (2012) "Structure of the rigor actin-tropomyosin-myosin complex," *Cell*, 150(2), pp. 327–338.

Belknap, B., Harris, S.P. and White, H.D. (2014) "Modulation of thin filament activation of myosin ATP hydrolysis by N-terminal domains of cardiac myosin binding protein-C," *Biochemistry*, 53(42), pp. 6717–6724.

Bello, J. and Pellegrini, M.V. (2023) "Mavacamten," in *StatPearls [Internet]*. StatPearls Publishing.

Bennett, P. *et al.* (1986) “The ultrastructural location of C-protein, X-protein and H-protein in rabbit muscle,” *Journal of muscle research and cell motility*, 7(6), pp. 550–567.

Bennett, P., Rees, M. and Gautel, M. (2020) “The Axial Alignment of Titin on the Muscle Thick Filament Supports Its Role as a Molecular Ruler,” *Journal of molecular biology*, 432(17), pp. 4815–4829.

Bennett, P.M. and Gautel, M. (1996) “Titin domain patterns correlate with the axial disposition of myosin at the end of the thick filament,” *Journal of molecular biology*, 259(5), pp. 896–903.

Berg, J.S., Powell, B.C. and Cheney, R.E. (2001) “A millennial myosin census,” *Molecular biology of the cell*, 12(4), pp. 780–794.

Bloemink, M.J. and Geeves, M.A. (2011) “Shaking the myosin family tree: biochemical kinetics defines four types of myosin motor,” *Seminars in cell & developmental biology*, 22(9), pp. 961–967.

Blumenthal, D.K. and Stull, J.T. (1980) “Activation of skeletal muscle myosin light chain kinase by calcium(2+) and calmodulin,” *Biochemistry*, 19(24), pp. 5608–5614.

Bonne, G. *et al.* (1995) “Cardiac myosin binding protein-C gene splice acceptor site mutation is associated with familial hypertrophic cardiomyopathy,” *Nature genetics*, 11(4), pp. 438–440.

Bootman, M.D. (2012) “Calcium signaling,” *Cold Spring Harbor perspectives in biology*, 4(7), p. a011171.

Brito, R. *et al.* (2011) “A molecular model of phosphorylation-based activation and potentiation of tarantula muscle thick filaments,” *Journal of molecular biology*, 414(1), pp. 44–61.

Brunello, E. *et al.* (2023) “Activation of skeletal muscle is controlled by a dual-filament mechano-sensing mechanism,” *Proceedings of the National Academy of Sciences of the United States of America*, 120(22), p. e2302837120.

Burgess, S.A. *et al.* (2007) “Structures of Smooth Muscle Myosin and Heavy Meromyosin in the Folded, Shutdown State,” *Journal of molecular biology*, 372(5), pp. 1165–1178.

Cabral-Lilly, D. *et al.* (1997) “Molecular polarity in tropomyosin-troponin T co-crystals,” *Biophysical journal*, 73(4), pp. 1763–1770.

Calore, C. *et al.* (2015) “A founder MYBPC3 mutation results in HCM with a high risk of sudden death after the fourth decade of life,” *Journal of medical genetics*, 52(5), pp. 338–347.

Cao, M. *et al.* (2023) “An actin filament branching surveillance system regulates cell cycle progression, cytokinesis and primary ciliogenesis,” *Nature communications*, 14(1), p. 1687.

Caremani, M. *et al.* (2019) “Low temperature traps myosin motors of mammalian muscle in a refractory state that prevents activation,” *The Journal of general physiology*, 151(11), pp. 1272–1286.

Caremani, M. *et al.* (2022) “The force of the myosin motor sets cooperativity in thin filament activation of skeletal muscles,” *Communications biology*, 5(1), p. 1266.

Carlsson, L. *et al.* (1977) “Actin polymerizability is influenced by profilin, a low molecular weight protein in non-muscle cells,” *Journal of molecular biology*, 115(3), pp. 465–483.

Carrier, L. *et al.* (2015) “Cardiac myosin-binding protein C (MYBPC3) in cardiac pathophysiology,” *Gene*, 573(2), pp. 188–197.

Carrington, G., Tomlinson, D. and Peckham, M. (2019) “Exploiting nanobodies and Affimers for superresolution imaging in light microscopy,” *Molecular biology of the cell*, 30(22), pp. 2737–2740.

Chan, J.Y. *et al.* (2008) “Identification of cardiac-specific myosin light chain kinase,” *Circulation research*, 102(5), pp. 571–580.

Chang, A.N. *et al.* (2015) “Constitutive phosphorylation of cardiac myosin regulatory light chain in vivo,” *The Journal of biological chemistry*, 290(17), pp. 10703–10716.

Chang, A.N. *et al.* (2016) “Cardiac myosin light chain is phosphorylated by Ca2+/calmodulin-dependent and -independent kinase activities,” *Proceedings of the National Academy of Sciences of the United States of America*, 113(27), pp. E3824-33.

Christiaans, I. *et al.* (2010) “Founder mutations in hypertrophic cardiomyopathy patients in the Netherlands,” *Netherlands Heart Journal*. Bohn Stafleu van Loghum, pp. 248–254. Available at: https://doi.org/10.1007/BF03091771.

Chuang, C. *et al.* (2021) “Discovery of aficamten (CK-274), a next-generation cardiac myosin inhibitor for the treatment of hypertrophic cardiomyopathy,” *Journal of medicinal chemistry*, 64(19), pp. 14142–14152.

Cirino, A.L. and Ho, C. (2021) “Hypertrophic Cardiomyopathy Overview,” *GeneReviews®*, pp. 1–16.

Clinch, N.F. (1968) “On the increase in rate of heat production caused by stretch in frog’s skeletal muscle,” *The journal of physiology*, 196(2), pp. 397–414.

Coats, C.J. *et al.* (2024) “Dosing and safety profile of aficamten in symptomatic obstructive hypertrophic cardiomyopathy: Results from SEQUOIA-HCM,” *Journal of the American Heart Association*, 13(15), p. e035993.

Colegrave, M. and Peckham, M. (2014) “Structural implications of β-cardiac myosin heavy chain mutations in human disease,” *The Anatomical record*, 297(9), pp. 1670–1680.

Colson, B.A. *et al.* (2008) “Protein kinase a-mediated phosphorylation of cmybp-c increases proximity of myosin heads to actin in resting myocardium,” *Circulation research*, 103(3), pp. 244–251.

Colson, B.A. *et al.* (2010) “Differential roles of regulatory light chain and myosin binding protein-C phosphorylations in the modulation of cardiac force development,” *The Journal of physiology*, 588(Pt 6), pp. 981–993.

Colson, B.A. *et al.* (2012) “Cardiac myosin binding protein-C restricts intrafilament torsional dynamics of actin in a phosphorylation-dependent manner,” *Proceedings of the National Academy of Sciences of the United States of America*, 109(50), pp. 20437–20442.

Comuzzi, C. *et al.* (2003) “SOLVERSTAT: a new utility for multipurpose analysis. An application to the investigation of dioxygenated Co(II) complex formation in dimethylsulfoxide solution,” *Talanta*, 59(1), pp. 67–80.

Cooke, R. (2011) “The role of the myosin ATPase activity in adaptive thermogenesis by skeletal muscle,” *Biophysical Reviews*, pp. 33–45. Available at: https://doi.org/10.1007/s12551-011-0044-9.

Cooke, R. and Pate, E. (1985) “The effects of ADP and phosphate on the contraction of muscle fibers,” *Biophysical journal*, 48(5), pp. 789–798.

Craig, R. *et al.* (2014) “Structure, sarcomeric organization, and thin filament binding of cardiac myosin-binding protein-C,” *Pflugers Archiv: European journal of physiology*, 466(3), pp. 425–431.

Craig, R. and Offer, G. (1976) “The location of C protein in rabbit skeletal muscle,” *Proceedings of the Royal Society of London - Biological Sciences*, 192(1109), pp. 451–461.

Daneshparvar, N. *et al.* (2020) “CryoEM structure of*Drosophila*flight muscle thick filaments at 7 Å resolution,” *Life science alliance*, 3(8), p. e202000823.

Daubert, C. *et al.* (2018) “Pacing for hypertrophic obstructive cardiomyopathy: an update and future directions,” *Europace: European pacing, arrhythmias, and cardiac electrophysiology: journal of the working groups on cardiac pacing, arrhythmias, and cardiac cellular electrophysiology of the European Society of Cardiology*, 20(6), pp. 908–920.

Davis, J.S. *et al.* (2001) “The overall pattern of cardiac contraction depends on a spatial gradient of myosin regulatory light chain phosphorylation,” *Cell*, 107(5), pp. 631–641.

Davis, J.S., Satorius, C.L. and Epstein, N.D. (2002) “Kinetic effects of myosin regulatory light chain phosphorylation on skeletal muscle contraction,” *Biophysical journal*, 83(1), pp. 359–370.

Desai, R., Geeves, M.A. and Kad, N.M. (2015) “Using fluorescent myosin to directly visualize cooperative activation of thin filaments,” *The Journal of biological chemistry*, 290(4), pp. 1915–1925.

Dhoot, G.K. *et al.* (1985) “The isoforms of C protein and their distribution in mammalian skeletal muscle,” *Journal of muscle research and cell motility*, 6(4), pp. 487–505.

Dhoot, G.K. and Perry, S.V. (2005) “Expression of slow skeletal myosin binding C-protein in normal adult mammalian heart,” *Journal of muscle research and cell motility*, 26(2–3), pp. 143–148.

Diffee, G.M. *et al.* (1996) “Altered kinetics of contraction in skeletal muscle fibers containing a mutant myosin regulatory light chain with reduced divalent cation binding,” *Biophysical journal*, 71(1), pp. 341–350.

Ding, P. *et al.* (2010) “Cardiac Myosin Light Chain Kinase Is Necessary for Myosin Regulatory Light Chain Phosphorylation and Cardiac Performance in Vivo*,” *The Journal of biological chemistry*, 285(52), pp. 40819–40829.

Doh, C.Y. *et al.* (2022) “Identification of Phosphorylation and Other Post-Translational Modifications in the Central C4C5 Domains of Murine Cardiac Myosin Binding Protein C,” *ACS omega*, 7(16), pp. 14189–14202.

Dominguez, R. *et al.* (1998) “Crystal structure of a vertebrate smooth muscle myosin motor domain and its complex with the essential light chain: visualization of the pre-power stroke state,” *Cell*, 94(5), pp. 559–571.

Dominguez, R. and Holmes, K.C. (2011) “Actin structure and function,” *Annual review of biophysics*, 40(1), pp. 169–186.

Dong, W.J. *et al.* (2007) “Effects of PKA phosphorylation of cardiac troponin I and strong crossbridge on conformational transitions of the N-domain of cardiac troponin C in regulated thin filaments,” *Biochemistry*, 46(34), pp. 9752–9761.

Dutta, D. *et al.* (2024) “Pathogenic cardiac thick filament variants: A structural perspective,” *Biophysical journal*, 123(3), p. 403a.

Eastwood, A.B. *et al.* (1979) “Chemically skinned mammalian skeletal muscle. I. The structure of skinned rabbit psoas,” *Tissue & cell*, 11(3), pp. 553–566.

Ebashi, S. and Ebashi, F. (1964) “A new protein factor promoting contraction of actomyosin,” *Nature*, 203(4945), pp. 645–646.

von der Ecken, J. *et al.* (2016) “Cryo-EM structure of a human cytoplasmic actomyosin complex at near-atomic resolution,” *Nature*, 534(7609), pp. 724–728.

Elliott, P.M. *et al.* (2014) “2014 ESC Guidelines on diagnosis and management of hypertrophic cardiomyopathy: the Task Force for the Diagnosis and Management of Hypertrophic Cardiomyopathy of the European Society of Cardiology (ESC): The Task Force for the Diagnosis and Management of Hypertrophic Cardiomyopathy of the European Society of Cardiology (ESC),” *European heart journal*, 35(39), pp. 2733–2779.

Elzinga, M. *et al.* (1973) “Complete amino acid sequence of actin of rabbit skeletal muscle,” *Proceedings of the National Academy of Sciences of the United States of America*, 70(9), pp. 2687–2691.

Elzinga, M. and Collins, J.H. (1975) “The Primary Structure of Actin from Rabbit Skeletal Muscle,” *The Journal of biological chemistry*, 250(15), pp. 5897–5905.

Espinoza-Fonseca, L.M. *et al.* (2015) “Sequential myosin phosphorylation activates tarantula thick filament via a disorder-order transition,” *Molecular bioSystems*, 11(8), pp. 2167–2179.

Farzam, K. and Jan, A. (2025) “Beta blockers,” in *StatPearls*. Treasure Island (FL): StatPearls Publishing.

Ferenczi, M.A. *et al.* (1978) “Reaction mechanism of the magnesium ion-dependent adenosine triphosphatase of frog muscle myosin and subfragment 1,” *The Biochemical journal*, 171(1), pp. 165–175.

Flashman, E. *et al.* (2004) “Cardiac myosin binding protein C: its role in physiology and disease,” *Circulation research*, 94(10), pp. 1279–1289.

Fukutani, A. *et al.* (2024) “Ca2+ and force during dynamic contractions in mouse intact skeletal muscle fibers,” *Scientific reports*, 14(1), p. 689.

Garfinkel, A.C., Seidman, J.G. and Seidman, C.E. (2018) “Genetic pathogenesis of hypertrophic and dilated cardiomyopathy,” *Heart failure clinics*, 14(2), pp. 139–146.

Gautel, M. *et al.* (1995) “Phosphorylation switches specific for the cardiac isoform of myosin binding protein-C: A modulator of cardiac contraction?,” *The EMBO journal*, 14(9), pp. 1952–1960.

Gebhardt, J.C.M. *et al.* (2013) “Single-molecule imaging of transcription factor binding to DNA in live mammalian cells,” *Nature methods*, 10(5), pp. 421–426.

Geeves, M.A., Fedorov, R. and Manstein, D.J. (2005) “Molecular mechanism of actomyosin-based motility,” *Cellular and molecular life sciences: CMLS*, 62(13), pp. 1462–1477.

Geeves, M.A. and Holmes, K.C. (2005) “The molecular mechanism of muscle contraction,” *Advances in protein chemistry*, 71(04), pp. 161–193.

Gelles, J., Schnapp, B.J. and Sheetz, M.P. (1988) “Tracking kinesin-driven movements with nanometre-scale precision,” *Nature*, 331(6155), pp. 450–453.

Gersh, B.J. *et al.* (2011) “2011 ACCF/AHA guideline for the diagnosis and treatment of hypertrophic cardiomyopathy: executive summary: a report of the American College of Cardiology Foundation/American Heart Association Task Force on Practice Guidelines: A report of the American college of cardiology foundation/American heart association task force on practice guidelines,” *Circulation*, 124(24), pp. 2761–2796.

Giganti, D. *et al.* (2018) “Disulfide isomerization reactions in titin immunoglobulin domains enable a mode of protein elasticity,” *Nature communications*, 9(1), pp. 1–11.

Gollapudi, S.K., Yu, M., *et al.* (2021) “Synthetic thick filaments: A new avenue for better understanding the myosin super-relaxed state in healthy, diseased, and mavacamten-treated cardiac systems,” *The journal of biological chemistry*, 296(100114), p. 100114.

Gollapudi, S.K., Ma, W., *et al.* (2021) “Two Classes of Myosin Inhibitors, Para-nitroblebbistatin and Mavacamten, Stabilize β-Cardiac Myosin in Different Structural and Functional States,” *Journal of molecular biology*, 433(23), p. 167295.

Gomes, A.V., Potter, J.D. and Szczesna-Cordary, D. (2002) “The role of troponins in muscle contraction,” *IUBMB life*, 54(6), pp. 323–333.

Graham, R.M. (1990) “Adrenergic receptors: structure and function,” *Cleveland Clinic journal of medicine*, 57(5), pp. 481–491.

Green, E.M. *et al.* (2016) “A small-molecule inhibitor of sarcomere contractility suppresses hypertrophic cardiomyopathy in mice,” *Science*, 351(6273), pp. 617–621.

Grillo, M.P. *et al.* (2019) “In vitro and in vivo pharmacokinetic characterization of mavacamten, a first-in-class small molecule allosteric modulator of beta cardiac myosin,” *Xenobiotica; the fate of foreign compounds in biological systems*, 49(6), pp. 718–733.

Grinzato, A. *et al.* (2023) “Cryo-EM structure of the folded-back state of human β-cardiac myosin,” *Nature communications*, 14(1), p. 3166.

Gross, S.M. and Lehman, S.L. (2016) “Functional phosphorylation sites in cardiac myofilament proteins are evolutionarily conserved in skeletal myofilament proteins,” *Physiological genomics*, 48(6), pp. 377–387.

Gruen, M. and Gautel, M. (1999) “Mutations in beta-myosin S2 that cause familial hypertrophic cardiomyopathy (FHC) abolish the interaction with the regulatory domain of myosin-binding protein-C,” *Journal of molecular biology*, 286(3), pp. 933–949.

Gruen, M., Prinz, H. and Gautel, M. (1999) “cAPK-phosphorylation controls the interaction of the regulatory domain of cardiac myosin binding protein C with myosin-S2 in an on-off fashion,” *FEBS letters*, 453(3), pp. 254–259.

Gurnett, C.A. *et al.* (2010) “Myosin binding protein C1: a novel gene for autosomal dominant distal arthrogryposis type 1,” *Human molecular genetics*, 19(7), pp. 1165–1173.

Hamdani, N., Herwig, M. and Linke, W.A. (2017) “Tampering with springs: phosphorylation of titin affecting the mechanical function of cardiomyocytes,” *Biophysical reviews*, 9(3), pp. 225–237.

Harris, K.M. *et al.* (2006) “Prevalence, clinical profile, and significance of left ventricular remodeling in the end-stage phase of hypertrophic cardiomyopathy,” *Circulation*, 114(3), pp. 216–225.

Harris, S.P. *et al.* (2002) “Hypertrophic cardiomyopathy in cardiac myosin binding protein-C knockout mice,” *Circulation research*, 90(5), pp. 594–601.

Harris, S.P. *et al.* (2004) “Binding of myosin binding protein-C to myosin subfragment S2 affects contractility independent of a tether mechanism,” *Circulation research*, 95(9), pp. 930–936.

Harris, S.P. (2021) “Making waves: A proposed new role for myosin-binding protein C in regulating oscillatory contractions in vertebrate striated muscle,” *The journal of general physiology*, 153(3), p. e202012729.

Harris, S.P., Lyons, R.G. and Bezold, K.L. (2011) “In the thick of it: HCM-causing mutations in myosin binding proteins of the thick filament,” *Circulation research*, 108(6), pp. 751–764.

Hartman, J.J. *et al.* (2024) “Aficamten is a small-molecule cardiac myosin inhibitor designed to treat hypertrophic cardiomyopathy,” *Nature cardiovascular research*, pp. 1–14.

Hartman, M.A. and Spudich, J.A. (2012) “The myosin superfamily at a glance,” *Journal of cell science*, 125(Pt 7), pp. 1627–1632.

Hartzell, H.C. and Sale, W.S. (1985) “Structure of C protein purified from cardiac muscle,” *The Journal of cell biology*, 100(1), pp. 208–215.

Hartzell, H.C. and Titus, L. (1982) “Effects of cholinergic and adrenergic agonists on phosphorylation of a 165,000-dalton myofibrillar protein in intact cardiac muscle,” *The journal of biological chemistry*, 257(4), pp. 2111–2120.

Heling, L.W.H.J., Geeves, M.A. and Kad, N.M. (2020) “MyBP-C: one protein to govern them all,” *Journal of muscle research and cell motility*, 41(1), pp. 91–101.

Herrmann, C. *et al.* (1993) “A structural and kinetic study on myofibrils prevented from shortening by chemical cross-linking,” *Biochemistry*, 32(28), pp. 7255–7263.

Herron, T.J. *et al.* (2006) “Activation of myocardial contraction by the N-terminal domains of myosin binding protein-C,” *Circulation research*, 98(10), pp. 1290–1298.

Hershberger, R.E. and Jordan, E. (2022) “Dilated cardiomyopathy overview.” Available at: https://www.ncbi.nlm.nih.gov/books/NBK1309/ (Accessed: August 5, 2024).

Hessel, A.L. *et al.* (2022) “Titin force in muscle cells alters lattice order, thick and thin filament protein formation,” *Proceedings of the National Academy of Sciences of the United States of America*, 119(48), p. e2209441119.

Hessel, A.L. *et al.* (2024) “Myosin-binding protein C regulates the sarcomere lattice and stabilizes the OFF states of myosin heads,” *Nature communications*, 15(1), p. 2628.

Hitchcock-DeGregori, S.E., Song, Y. and Greenfield, N.J. (2002) “Functions of tropomyosin’s periodic repeats,” *Biochemistry*, 41(50), pp. 15036–15044.

Ho, C.Y. *et al.* (2018) “Genotype and lifetime burden of disease in hypertrophic cardiomyopathy: Insights from the Sarcomeric Human Cardiomyopathy Registry (SHaRe),” *Circulation*, 138(14), pp. 1387–1398.

Ho, C.Y. *et al.* (2020) “Study design and rationale of EXPLORER-HCM: Evaluation of mavacamten in adults with symptomatic obstructive hypertrophic cardiomyopathy,” *Circulation. Heart failure*, 13(6), p. e006853.

Hofmann, P.A., Greaser, M.L. and Moss, R.L. (1991) “C-protein limits shortening velocity of rabbit skeletal muscle fibres at low levels of Ca2+ activation,” *The journal of physiology*, 439(1), pp. 701–715.

Hooijman, P., Stewart, M.A. and Cooke, R. (2011) “A new state of cardiac myosin with very slow ATP turnover: A potential cardioprotective mechanism in the heart,” *Biophysical journal*, 100(8), pp. 1969–1976.

Hornbeck, P.V. *et al.* (2015) “PhosphoSitePlus, 2014: mutations, PTMs and recalibrations,” *Nucleic acids research*, 43(Database issue), pp. D512-20.

Houdusse, A. *et al.* (1999) “Atomic structure of scallop myosin subfragment S1 complexed with MgADP: a novel conformation of the myosin head,” *Cell*, 97(4), pp. 459–470.

Houdusse, A., Szent-Gyorgyi, A.G. and Cohen, C. (2000) “Three conformational states of scallop myosin S1,” *Proceedings of the National Academy of Sciences of the United States of America*, 97(21), pp. 11238–11243.

Hu, Z. *et al.* (2016) “Structure of myosin filaments from relaxed Lethocerus flight muscle by cryo-EM at 6 Å resolution,” *Science advances*, 2(9), p. e1600058.

Huang, X. *et al.* (2023) “Cryo-electron tomography of intact cardiac muscle reveals myosin binding protein-C linking myosin and actin filaments,” *Journal of muscle research and cell motility*, 44(3), pp. 165–178.

Husberg, C. *et al.* (2012) “Dephosphorylation of cardiac proteins in vitro - a matter of phosphatase specificity,” *Proteomics*, 12(7), pp. 973–978.

Huxley, A.F. and Niedergerke, R. (1954) “Structural changes in muscle during contraction,” *Nature*, 4412(4412), pp. 971–973.

Huxley, H.E. (1969) “The mechanism of muscular contraction: Recent structural studies suggest a revealing model for cross-bridge action at variable filament spacing,” *Science (New York, N.Y.)*, 164(3886), pp. 1356–1365.

Huxley, H.E. and Hanson, J. (1954) “Changes in the Cross-Striations of Muscle during Contraction and Stretch and their Structural Interpretation,” *Nature* [Preprint].

Hyun, S.J. *et al.* (2008) “Head-head and head-tail interaction: A general mechanism for switching off myosin II activity in cells,” *Molecular biology of the cell*, 19(8), pp. 3234–3242.

Inchingolo, A.V. *et al.* (2019) “Revealing the mechanism of how cardiac myosin-binding protein C N-terminal fragments sensitize thin filaments for myosin binding,” *Proceedings of the National Academy of Sciences of the United States of America*, 116(14), pp. 6828–6835.

Irving, M. (2017) “Regulation of Contraction by the Thick Filaments in Skeletal Muscle,” *Biophysical journal*, 113(12), pp. 2579–2594.

Irving, T.C. and Craig, R. (2019) “Getting into the thick (and thin) of it,” *Journal of General Physiology*. Rockefeller University Press, pp. 610–613. Available at: https://doi.org/10.1085/jgp.201812307.

Ito, M. *et al.* (2022) “Regulation of myosin light-chain phosphorylation and its roles in cardiovascular physiology and pathophysiology,” *Hypertension research: official journal of the Japanese Society of Hypertension*, 45(1), pp. 40–52.

Jackson, A.P. and Bagshaw, C.R. (1988) “Kinetic trapping of intermediates of the scallop heavy meromyosin adenosine triphosphatase reaction revealed by formycin nucleotides,” *The Biochemical journal*, 251(2), pp. 527–540.

Jia, W. *et al.* (2010) “Identification of novel protein kinase A phosphorylation sites in the M-domain of human and murine cardiac myosin binding protein-C using mass spectrometry analysis,” *Journal of proteome research*, 9(4), pp. 1843–1853.

Johnson, M. (2022) “Detergents: Triton X-100, Tween-20, and More,” *Materials and Methods* [Preprint]. Available at: https://www.labome.com/method/Detergents-Triton-X-100-Tween-20-and-More.html (Accessed: April 11, 2022).

J.R.Sellers (2006) “CONTRACTILE PROTEINS,” in *Encyclopedia of Respiratory Medicine*, pp. 561–567.

Jung, H.S. *et al.* (2011) “Role of the tail in the regulated state of myosin 2,” *Journal of molecular biology*, 408(5), pp. 863–878.

Kad, N.M. *et al.* (2005) “Single-myosin crossbridge interactions with actin filaments regulated by troponin-tropomyosin,” *Proceedings of the National Academy of Sciences of the United States of America*, 102(47), pp. 16990–16995.

Kad, N.M. *et al.* (2010) “Collaborative dynamic DNA scanning by nucleotide excision repair proteins investigated by single- molecule imaging of quantum-dot-labeled proteins,” *Molecular cell*, 37(5), pp. 702–713.

Kamin-Belsky, N. *et al.* (1996) “Degradation of myosin by enzymes of the digestive system: Comparison between native and oxidatively cross-linked protein,” *Journal of agricultural and food chemistry*, 44(7), pp. 1641–1646.

Kampourakis, T. *et al.* (2018) “Omecamtiv mercabil and blebbistatin modulate cardiac contractility by perturbing the regulatory state of the myosin filament,” *The Journal of physiology*, 596(1), pp. 31–46.

Kampourakis, T. and Irving, M. (2015) “Phosphorylation of myosin regulatory light chain controls myosin head conformation in cardiac muscle,” *Journal of molecular and cellular cardiology*, 85, pp. 199–206.

Kawas, R.F. *et al.* (2017) “A small-molecule modulator of cardiac myosin acts on multiple stages of the myosin chemomechanical cycle,” *The Journal of biological chemistry*, 292(40), pp. 16571–16577.

Keam, S.J. (2022) “Mavacamten: First approval,” *Drugs*, 82(10), pp. 1127–1135.

Khapchaev, A.Y. and Shirinsky, V.P. (2016) “Myosin light chain kinase MYLK1: Anatomy, interactions, functions, and regulation,” *Biochemistry. Biokhimiia*, 81(13), pp. 1676–1697.

Kinoshita, E. *et al.* (2006) “Phosphate-binding tag, a new tool to visualize phosphorylated proteins,” *Molecular & cellular proteomics: MCP*, 5(4), pp. 749–757.

Knight, P.J. and Trinick, J.A. (1982) “[2] Preparation of myofibrils,” in *Methods in Enzymology*. Academic Press, pp. 9–12.

Kobayashi, T., Patrick, S.E. and Kobayashi, M. (2009) “Ala scanning of the inhibitory region of cardiac troponin I,” *The journal of biological chemistry*, 284(30), pp. 20052–20060.

Kominz, D.R. *et al.* (1965) “The papain digestion of skeletal myosin A*,” *Biochemistry*, 4(11), pp. 2373–2382.

Kooij, V. *et al.* (2013) “Characterization of the cardiac myosin binding protein-C phosphoproteome in healthy and failing human hearts,” *Journal of molecular and cellular cardiology*, 60, pp. 116–120.

Koretz, J.F. (1979) “Effects of C-protein on synthetic myosin filament structure,” *Biophysical journal*, 27(3), pp. 433–446.

Korte, F.S. *et al.* (2011) “Upregulation of cardiomyocyte ribonucleotide reductase increases intracellular 2 deoxy-ATP, contractility, and relaxation,” *Journal of molecular and cellular cardiology*, 51(6), pp. 894–901.

Kozaili, J.M., Leek, D. and Tobacman, L.S. (2010) “Dual regulatory functions of the thin filament revealed by replacement of the troponin I inhibitory peptide with a linker,” *The journal of biological chemistry*, 285(49), pp. 38034–38041.

Kretsinger, R.H. and Nockolds, C.E. (1973) “Carp muscle calcium-binding protein. II. Structure determination and general description,” *The journal of biological chemistry*, 248(9), pp. 3313–3326.

Krüger, M. and Linke, W.A. (2006) “Protein kinase-A phosphorylates titin in human heart muscle and reduces myofibrillar passive tension,” *Journal of muscle research and cell motility*, 27(5–7), pp. 435–444.

Kubo, T. *et al.* (2005) “Lifelong left ventricular remodeling of hypertrophic cardiomyopathy caused by a founder frameshift deletion mutation in the cardiac myosin-binding protein C gene among Japanese,” *Journal of the American College of Cardiology*, 46(9), pp. 1737–1743.

Kühne, W. (1864) *Untersuchungen über das Protoplasma und die Contractilität*. Leipzig: W. Engelmann.

Kumar, M. *et al.* (2015) “Cardiac myosin-binding protein C and troponin-I phosphorylation independently modulate myofilament length-dependent activation,” *The Journal of biological chemistry*, 290(49), pp. 29241–29249.

Kunst, G. *et al.* (2000) “Myosin binding protein C, a phosphorylation-dependent force regulator in muscle that controls the attachment of myosin heads by its interaction with myosin S2,” *Circulation research*, 86(1), pp. 51–58.

Kushmerick, M.J. and Paul, R.J. (1976) “Aerobic recovery metabolism following a single isometric tetanus in frog sartorius muscle at 0 degrees C,” *The Journal of physiology*, 254(3), pp. 693–709.

Labeit, S. and Kolmerer, B. (1995) “Titins: Giant proteins in charge of muscle ultrastructure and elasticity,” *Science*, 270(5234), pp. 293–296.

Landis, C. *et al.* (1999) “Effects of tropomyosin internal deletions on thin filament function,” *The journal of biological chemistry*, 274(44), pp. 31279–31285.

Lehman, W., Craig, R. and Vibert, P. (1994) “Ca2+-induced tropomyosin movement in Limulus thin filaments revealed by three-dimensional reconstruction,” *Nature*, 368(6466), pp. 65–67.

Levine, R.J.C. *et al.* (1996) “Myosin light chain phosphorylation affects the structure of rabbit skeletal muscle thick filaments,” *Biophysical journal*, 71(2), pp. 898–907.

Lewalle, A. *et al.* (2022) “Functional and structural differences between skinned and intact muscle preparations,” *The Journal of general physiology*, 154(2). Available at: https://doi.org/10.1085/jgp.202112990.

Li, A. *et al.* (2019) “Skeletal MyBP-C isoforms tune the molecular contractility of divergent skeletal muscle systems,” *Proceedings of the National Academy of Sciences of the United States of America*, 116(43), pp. 21882–21892.

Li, M. *et al.* (2016) “Knockdown of fast skeletal myosin-binding protein C in zebrafish results in a severe skeletal myopathy,” *The journal of general physiology*, 147(4), pp. 309–322.

Li, M.X. and Hwang, P.M. (2015) “Structure and function of cardiac troponin C (TNNC1): Implications for heart failure, cardiomyopathies, and troponin modulating drugs,” *Gene*, 571(2), pp. 153–166.

Lim, M.S. and Walsh, M.P. (1986) “Phosphorylation of skeletal and cardiac muscle C-proteins by the catalytic subunit of cAMP-dependent protein kinase,” *Biochemistry and cell biology = Biochimie et biologie cellulaire*, 64(7), pp. 622–630.

Lin, B. *et al.* (2013) “Cardiac myosin binding protein-C plays no regulatory role in skeletal muscle structure and function,” *PloS one*, 8(7), p. e69671.

Lin, B.L. *et al.* (2018) “Skeletal myosin binding protein-C isoforms regulate thin filament activity in a Ca2+-dependent manner,” *Scientific reports*, 8(1), p. 2604.

Linari, M. *et al.* (2015) “Force generation by skeletal muscle is controlled by mechanosensing in myosin filaments,” *Nature*, 528(7581), pp. 276–279.

Lodish, H. *et al.* (2016) *Molecular-Cell-Biology-8th-Edition*.

Lu, T.-W. *et al.* (2019) “Two PKA RIα holoenzyme states define ATP as an isoform-specific orthosteric inhibitor that competes with the allosteric activator, cAMP,” *Proceedings of the National Academy of Sciences of the United States of America*, 116(33), pp. 16347–16356.

Lu, X., Tobacman, L.S. and Kawai, M. (2003) “Effects of tropomyosin internal deletion Delta23Tm on isometric tension and the cross-bridge kinetics in bovine myocardium,” *The journal of physiology*, 553(Pt 2), pp. 457–471.

Luther, P.K. (2009) “The vertebrate muscle Z-disc: Sarcomere anchor for structure and signalling,” *Journal of muscle research and cell motility*, 30(5–6), pp. 171–185.

Lymn, R.W. and Taylor, E.W. (1971) “Mechanism of Adenosine Triphosphate Hydrolysis by Actomyosin,” *Biochemistry*, 10(25), pp. 4617–4624.

Lynne M. Coluccio (2008) *Myosins A Superfamily of Molecular Motors*.

Lyon, A.R. *et al.* (2009) “Loss of T-tubules and other changes to surface topography in ventricular myocytes from failing human and rat heart,” *Proceedings of the National Academy of Sciences of the United States of America*, 106(16), pp. 6854–6859.

Ma, W. *et al.* (2020) “Myosin dynamics during relaxation in mouse soleus muscle and modulation by 2’-deoxy-ATP,” *The Journal of physiology*, 598(22), pp. 5165–5182.

Ma, W. *et al.* (2021) “The super-relaxed state and length dependent activation in porcine myocardium,” *Circulation research*, 129(6), pp. 617–630.

Ma, W. *et al.* (2023) “Structural OFF/ON transitions of myosin in relaxed porcine myocardium predict calcium-activated force,” *Proceedings of the National Academy of Sciences of the United States of America*, 120(5), p. e2207615120.

Maciver, S.K. and Hussey, P.J. (2002) “The ADF/cofilin family: actin-remodeling proteins,” *Genome biology*, 3(5), p. reviews3007.

Malik, F.I. *et al.* (2022) “A phase 1 dose-escalation study of the cardiac myosin inhibitor aficamten in healthy participants,” *JACC. Basic to translational science*, 7(8), pp. 763–775.

Mamidi, R. *et al.* (2017) “Cardiac myosin binding protein-C Ser302 phosphorylation regulates cardiac β-adrenergic reserve,” *Science advances*, 3(3), p. e1602445.

Manning, E.P., Tardiff, J.C. and Schwartz, S.D. (2012) “Molecular effects of familial hypertrophic cardiomyopathy-related mutations in the TNT1 domain of cTnT,” *Journal of molecular biology*, 421(1), pp. 54–66.

Margossian, S.S., Stafford, W.F., 3rd and Lowey, S. (1981) “Homogeneity of myosin subfragments by equilibrium centrifugation,” *Biochemistry*, 20(8), pp. 2151–2155.

Mariano, A.C. *et al.* (2001) “Dimethyl sulphoxide enhances the effects of Pi in myofibrils and inhibits the activity of rabbit skeletal muscle contractile proteins,” *Biochemical Journal*, 358(3), pp. 627–636.

Markus, B. *et al.* (2012) “Autosomal recessive lethal congenital contractural syndrome type 4 (LCCS4) caused by a mutation in MYBPC1,” *Human mutation*, 33(10), pp. 1435–1438.

Maron, M.S. *et al.* (2023) “Phase 2 study of aficamten in patients with obstructive hypertrophic cardiomyopathy,” *Journal of the American College of Cardiology*, 81(1), pp. 34–45.

Maron, M.S. *et al.* (2024) “Impact of aficamten on disease and symptom burden in obstructive hypertrophic cardiomyopathy: Results from SEQUOIA-HCM,” *Journal of the American College of Cardiology*, 84(19), pp. 1821–1831.

Marrakchi, S. *et al.* (2020) “Risk stratification in hypertrophic cardiomyopathy,” *Herz*, 45(1), pp. 50–64.

Marston, S. and Zamora, J.E. (2020) “Troponin structure and function: a view of recent progress,” *Journal of muscle research and cell motility*, 41(1), pp. 71–89.

Maruyama, K. *et al.* (1977) “Connectin, an elastic protein of muscle. Characterization and Function,” *The journal of biochemistry*, 82(2), pp. 317–337.

McClellan, G., Kulikovskaya, I. and Winegrad, S. (2001) “Changes in cardiac contractility related to calcium-mediated changes in phosphorylation of myosin-binding protein C,” *Biophysical journal*, 81(2), pp. 1083–1092.

McKeever, R.G., Patel, P. and Hamilton, R.J. (2025) “Calcium channel blockers,” in *StatPearls*. Treasure Island (FL): StatPearls Publishing.

McKillop, D.F. and Geeves, M.A. (1993) “Regulation of the interaction between actin and myosin subfragment 1: evidence for three states of the thin filament,” *Biophysical journal*, 65(2), pp. 693–701.

McNamara, J.W. *et al.* (2014) “The role of super-relaxed myosin in skeletal and cardiac muscle,” *Biophysical reviews*, 7(1), pp. 5–14.

McNamara, J.W. *et al.* (2016) “Ablation of cardiac myosin binding protein-C disrupts the super-relaxed state of myosin in murine cardiomyocytes,” *Journal of molecular and cellular cardiology*, 94, pp. 65–71.

McNamara, J.W. and Sadayappan, S. (2018) “Skeletal myosin binding protein-C: An increasingly important regulator of striated muscle physiology,” *Archives of biochemistry and biophysics*, 660, pp. 121–128.

McNamara, J.W., Singh, R.R. and Sadayappan, S. (2019) “Cardiac myosin binding protein-C phosphorylation regulates the super-relaxed state of myosin,” *Proceedings of the National Academy of Sciences of the United States of America*, 116(24), pp. 11731–11736.

Mohran, S. *et al.* (2024) “The biochemically defined super relaxed state of myosin-A paradox,” *The Journal of biological chemistry*, 300(1), p. 105565.

Moos, C. *et al.* (1978) “The binding of skeletal muscle C-protein to F-actin, and its relation to the interaction of actin with myosin subfragment-1,” *Journal of molecular biology*, 124(4), pp. 571–586.

Morano, I. *et al.* (1985) “The influence of P-light chain phosphorylation by myosin light chain kinase on the calcium sensitivity of chemically skinned heart fibres,” *FEBS letters*, 189(2), pp. 221–224.

Morrison, J.F. (1969) “Kinetics of the reversible inhibition of enzyme-catalysed reactions by tight-binding inhibitors,” *Biochimica et biophysica acta*, 185(2), pp. 269–286.

Moss, R.L., Giulian, G.G. and Greaser, M.L. (1985) “The effects of partial extraction of TnC upon the tension-pCa relationship in rabbit skinned skeletal muscle fibers,” *The Journal of general physiology*, 86(4), pp. 585–600.

Mueller, H. and Perry, S.V. (1962) “The degradation of heavy meromyosin by trypsin,” *The Biochemical journal*, 85(3), pp. 431–439.

Mun, J.Y. *et al.* (2014) “Myosin-binding protein C displaces tropomyosin to activate cardiac thin filaments and governs their speed by an independent mechanism,” *Proceedings of the National Academy of Sciences of the United States of America*, 111(6), pp. 2170–2175.

Murakami, K. *et al.* (2008) “Structural basis for tropomyosin overlap in thin (actin) filaments and the generation of a molecular swivel by troponin-T,” *Proceedings of the National Academy of Sciences of the United States of America*, 105(20), pp. 7200–7205.

Muscles (2023) *Cleveland Clinic*. Available at: https://my.clevelandclinic.org/health/body/21887-muscle (Accessed: May 9, 2025).

Myburgh, K.H., Franks-Skiba, K. and Cooke, R. (1995) “Nucleotide turnover rate measured in fully relaxed rabbit skeletal muscle myofibrils,” *The Journal of general physiology*, 106(5), pp. 957–973.

Natori, R. (1986) *Skinned Fibres of Skeletal Muscle and the Mechanism of Muscle Contraction: A Chronological Account of the Author’s Investigations Into Muscle Physiology*. Jikei University School of Medicine.

Nelson, S. *et al.* (2023) “Myosin-binding protein C stabilizes, but is not the sole determinant of SRX myosin in cardiac muscle,” *The Journal of general physiology*, 155(4). Available at: https://doi.org/10.1085/jgp.202213276.

Nelson, S.R. *et al.* (2020) “Imaging ATP Consumption in Resting Skeletal Muscle: One Molecule at a Time,” *Biophysical journal*, 119(6), pp. 1050–1055.

Niimura, H. *et al.* (1998) “Mutations in the Gene for Cardiac Myosin-Binding Protein C and Late-Onset Familial Hypertrophic Cardiomyopathy,” *The New England journal of medicine*, 338(18), pp. 1248–1257.

Nogara, L. *et al.* (2016) “Piperine’s mitigation of obesity and diabetes can be explained by its up-regulation of the metabolic rate of resting muscle,” *Proceedings of the National Academy of Sciences of the United States of America*, 113(46), pp. 13009–13014.

Nyitrai, M. *et al.* (2003) “Ionic interactions play a role in the regulatory mechanism of scallop heavy meromyosin,” *Biophysical journal*, 85(2), pp. 1053–1062.

Nyitrai, M., Szent-Györgyi, A.G. and Geeves, M.A. (2003) “Interactions of the two heads of scallop (Argopecten irradians) heavy meromyosin with actin: influence of calcium and nucleotides,” *The Biochemical journal*, 370(Pt 3), pp. 839–848.

Oda, T., Yanagisawa, H. and Wakabayashi, T. (2020) “Cryo-EM structures of cardiac thin filaments reveal the 3D architecture of troponin,” *Journal of structural biology*, 209(3), p. 107450.

Olivotto, I. *et al.* (2020) “Mavacamten for treatment of symptomatic obstructive hypertrophic cardiomyopathy (EXPLORER-HCM): a randomised, double-blind, placebo-controlled, phase 3 trial,” *Lancet*, 396(10253), pp. 759–769.

Olsson, M.C. *et al.* (2004) “Basal myosin light chain phosphorylation is a determinant of Ca2+ sensitivity of force and activation dependence of the kinetics of myocardial force development,” *American journal of physiology. Heart and circulatory physiology*, 287(6), pp. H2712-8.

O’Mahony, C., Elliott, P. and McKenna, W. (2013) “Sudden cardiac death in hypertrophic cardiomyopathy,” *Circulation. Arrhythmia and electrophysiology*, 6(2), pp. 443–451.

Ommen, S.R. *et al.* (2020) “2020 AHA/ACC guideline for the diagnosis and treatment of patients with hypertrophic cardiomyopathy: Executive summary: A report of the American college of cardiology/American heart association joint committee on clinical practice guidelines,” *Circulation*, 142(25), pp. e533–e557.

Onishi, H., Mikhailenko, S.V. and Morales, M.F. (2006) “Toward understanding actin activation of myosin ATPase: the role of myosin surface loops,” *Proceedings of the National Academy of Sciences of the United States of America*, 103(16), pp. 6136–6141.

Palm, T. *et al.* (2001) “Disease-causing mutations in cardiac troponin T: Identification of a critical tropomyosin-binding region,” *Biophysical journal*, 81(5), pp. 2827–2837.

Park-Holohan, S.-J. *et al.* (2021) “Stress-dependent activation of myosin in the heart requires thin filament activation and thick filament mechanosensing,” *Proceedings of the National Academy of Sciences of the United States of America*, 118(16). Available at: https://doi.org/10.1073/pnas.2023706118.

Pavadai, E. *et al.* (2020) “Docking troponin T onto the tropomyosin overlapping domain of thin filaments,” *Biophysical journal*, 118(2), pp. 325–336.

Perrin, B.J. and Ervasti, J.M. (2010) “The actin gene family: function follows isoform,” *Cytoskeleton (Hoboken, N.J.)*, 67(10), pp. 630–634.

Petzhold, D. *et al.* (2010) “Auto-inhibitory effects of an IQ motif on protein structure and function,” *Biochemical and biophysical research communications*, 396(4), pp. 939–943.

Pilagov, M. *et al.* (2023) “Single-molecule imaging reveals how mavacamten and PKA modulate ATP turnover in skeletal muscle myofibrils,” *The journal of general physiology*, 155(1). Available at: https://doi.org/10.1085/jgp.202213087.

Pilagov, M. *et al.* (2024) “Spatially resolving how phosphorylation affects ß-cardiac myosin activity in porcine myofibril sarcomeres with single molecule resolution,” *bioRxiv*. Available at: https://doi.org/10.1101/2024.06.27.600847.

Pilagov, M. *et al.* (2025) “Spatially resolving how cMyBP-C phosphorylation and haploinsufficiency in porcine and human myofibrils affect β-cardiac myosin activity,” *The journal of general physiology*, 157(5), p. e202413628.

Ponnam, S. *et al.* (2019) “Site-specific phosphorylation of myosin binding protein-C coordinates thin and thick filament activation in cardiac muscle,” *Proceedings of the National Academy of Sciences of the United States of America*, 116(31), pp. 15485–15494.

Powers, J.D. *et al.* (2019) “Cardiac myosin activation with 2-deoxy-ATP via increased electrostatic interactions with actin,” *Proceedings of the National Academy of Sciences of the United States of America*, 116(23), pp. 11502–11507.

Preibisch, S. *et al.* (2010) “Software for bead-based registration of selective plane illumination microscopy data,” *Nature methods*, 7(6), pp. 418–419.

Previs, M.J. *et al.* (2012) “Molecular mechanics of cardiac myosin-binding protein C in native thick filaments,” *Science (New York, N.Y.)*, 337(6099), pp. 1215–1218.

Previs, M.J. *et al.* (2015) “Myosin-binding protein C corrects an intrinsic inhomogeneity in cardiac excitation-contraction coupling,” *Science advances*, 1(1), p. e1400205.

Previs, M.J. *et al.* (2016) “Phosphorylation and calcium antagonistically tune myosin-binding protein C’s structure and function,” *Proceedings of the National Academy of Sciences of the United States of America*, 113(12), pp. 3239–3244.

Pulcastro, H.C. *et al.* (2016) “Effects of myosin light chain phosphorylation on length-dependent myosin kinetics in skinned rat myocardium,” *Archives of biochemistry and biophysics*, 601, pp. 56–68.

Radnai, L. *et al.* (2019) “A Semi-High-Throughput Adaptation of the NADH-Coupled ATPase Assay for Screening Small Molecule Inhibitors,” *Journal of visualized experiments: JoVE* [Preprint], (150). Available at: https://doi.org/10.3791/60017.

Ratti, J. *et al.* (2011) “Structure and interactions of myosin-binding protein C domain C0: Cardiac-specific regulation of myosin at its neck?,” *The Journal of biological chemistry*, 286(14), pp. 12650–12658.

Rayment, I. *et al.* (1993) “Three-dimensional structure of myosin subfragment-1: A molecular motor,” *Science*, 261(5117), pp. 50–58.

Razumova, M.V. *et al.* (2006) “Effects of the N-terminal domains of myosin binding protein-C in an in vitro motility assay: Evidence for long-lived cross-bridges,” *The journal of biological chemistry*, 281(47), pp. 35846–35854.

Reinach, F.C., Masaki, T. and Fischman, D.A. (1983) “Characterization of the C-protein from posterior latissimus dorsi muscle of the adult chicken: heterogeneity within a single sarcomere,” *The journal of cell biology*, 96(1), pp. 297–300.

dos Remedios, C.G. *et al.* (2003) “Actin binding proteins: regulation of cytoskeletal microfilaments,” *Physiological reviews*, 83(2), pp. 433–473.

Risi, C.M. *et al.* (2021) “The structure of the native cardiac thin filament at systolic Ca 2+ levels,” *Proceedings of the National Academy of Sciences*, 118(13), p. e2024288118.

Risi, C.M. *et al.* (2022) “Cryo-electron microscopy reveals cardiac myosin binding protein-C M-domain interactions with the thin filament,” *Journal of molecular biology*, 434(24), p. 167879.

Robinett, J.C. *et al.* (2019) “Regulation of myofilament force and loaded shortening by skeletal myosin binding protein C,” *The journal of general physiology*, 151(5), pp. 645–659.

Robinson-White, A. and Stratakis, C.A. (2002) “Protein kinase A signaling: ‘cross-talk’ with other pathways in endocrine cells,” *Annals of the New York Academy of Sciences*, 968, pp. 256–270.

Rohde, J.A. *et al.* (2018) “Mavacamten stabilizes an autoinhibited state of two-headed cardiac myosin,” *Proceedings of the National Academy of Sciences of the United States of America*, 115(32), pp. E7486–E7494.

Roy, A., Kucukural, A. and Zhang, Y. (2010) “I-TASSER: a unified platform for automated protein structure and function prediction,” *Nature protocols*, 5(4), pp. 725–738.

Saber, W. *et al.* (2008) “Cardiac myosin binding protein-C modulates actomyosin binding and kinetics in the in vitro motility assay,” *Journal of molecular and cellular cardiology*, 44(6), pp. 1053–1061.

Sancho Solis, R., Ge, Y. and Walker, J.W. (2011) “A preferred AMPK phosphorylation site adjacent to the inhibitory loop of cardiac and skeletal troponin I: AMPK Phosphorylation Sites on Troponin I,” *Protein science: a publication of the Protein Society*, 20(5), pp. 894–907.

Scellini, B. *et al.* (2021) “Mavacamten has a differential impact on force generation in myofibrils from rabbit psoas and human cardiac muscle,” *The journal of general physiology*, 153(7). Available at: https://doi.org/10.1085/jgp.202012789.

Scruggs, S.B. *et al.* (2009) “Ablation of ventricular myosin regulatory light chain phosphorylation in mice causes cardiac dysfunction in situ and affects neighboring myofilament protein phosphorylation,” *The Journal of biological chemistry*, 284(8), pp. 5097–5106.

Scruggs, S.B. *et al.* (2010) “A Novel, in-solution separation of endogenous cardiac sarcomeric proteins and identification of distinct charged variants of regulatory light chain,” *Molecular & cellular proteomics: MCP*, 9(9), pp. 1804–1818.

Sebastian, S.A. *et al.* (2023) “Aficamten: A breakthrough therapy for symptomatic obstructive hypertrophic cardiomyopathy,” *American journal of cardiovascular drugs: drugs, devices, and other interventions*, 23(5), pp. 519–532.

Sevrieva, I.R. *et al.* (2020) “Cardiac myosin regulatory light chain kinase modulates cardiac contractility by phosphorylating both myosin regulatory light chain and troponin I,” *The Journal of biological chemistry*, 295(14), pp. 4398–4410.

Shaffer, J.F., Kensler, R.W. and Harris, S.P. (2009) “The myosin-binding protein C motif binds to F-actin in a phosphorylation-sensitive manner,” *The Journal of biological chemistry*, 284(18), pp. 12318–12327.

Sheikh, F. *et al.* (2012) “Mouse and computational models link Mlc2v dephosphorylation to altered myosin kinetics in early cardiac disease,” *The Journal of clinical investigation*, 122(4), pp. 1209–1221.

Sherwood, J.J. *et al.* (2004) “A point mutation in the regulatory light chain reduces the step size of skeletal muscle myosin,” *Proceedings of the National Academy of Sciences of the United States of America*, 101(30), pp. 10973–10978.

Smith, C.A. and Rayment, I. (1995) “X-ray structure of the magnesium(II)-pyrophosphate complex of the truncated head of Dictyostelium discoideum myosin to 2.7 A resolution,” *Biochemistry*, 34(28), pp. 8973–8981.

Song, T. *et al.* (2021) “Fast skeletal myosin-binding protein-C regulates fast skeletal muscle contraction,” *Proceedings of the National Academy of Sciences of the United States of America*, 118(17). Available at: https://doi.org/10.1073/pnas.2003596118.

Song, T. *et al.* (2023) “Etiology of genetic muscle disorders induced by mutations in fast and slow skeletal MyBP-C paralogs,” *Experimental & molecular medicine*, 55(3), pp. 502–509.

Spudich, J.A. (2001) “The myosin swinging cross-bridge model,” *Nature reviews. Molecular cell biology*, 2(5), pp. 387–392.

Starr, R. and Offer, G. (1971) “Polypeptide chains of intermediate molecular weight in myosin preparations,” *FEBS letters*, 15(1), pp. 40–44.

Steczina, S. *et al.* (2024) “MYBPC3-c.772G>A mutation results in haploinsufficiency and altered myosin cycling kinetics in a patient induced stem cell derived cardiomyocyte model of hypertrophic cardiomyopathy,” *Journal of molecular and cellular cardiology*, 191, pp. 27–39.

Stelzer, J.E., Dunning, S.B. and Moss, R.L. (2006) “Ablation of cardiac myosin-binding protein-C accelerates stretch activation in murine skinned myocardium,” *Circulation research*, 98(9), pp. 1212–1218.

Stelzer, J.E., Patel, J.R. and Moss, R.L. (2006a) “Acceleration of stretch activation in murine myocardium due to phosphorylation of myosin regulatory light chain,” *The Journal of general physiology*, 128(3), pp. 261–272.

Stelzer, J.E., Patel, J.R. and Moss, R.L. (2006b) “Protein kinase A-mediated acceleration of the stretch activation response in murine skinned myocardium is eliminated by ablation of cMyBP-C,” *Circulation research*, 99(8), pp. 884–890.

Stewart, M.A. *et al.* (2010) “Myosin ATP turnover rate is a mechanism involved in thermogenesis in resting skeletal muscle fibers,” *Proceedings of the National Academy of Sciences of the United States of America*, 107(1), pp. 430–435.

Sulbarán, G. *et al.* (2013) “Different head environments in tarantula thick filaments support a cooperative activation process,” *Biophysical journal*, 105(9), pp. 2114–2122.

Suraneni, P. *et al.* (2015) “A mechanism of leading-edge protrusion in the absence of Arp2/3 complex,” *Molecular biology of the cell*, 26(5), pp. 901–912.

Sweeney, H.L. and Hammers, D.W. (2018) “Muscle contraction,” *Cold Spring Harbor perspectives in biology*, 10(2), p. a023200.

Sweeney, H.L. and Stull, J.T. (1986) “Phosphorylation of myosin in permeabilized mammalian cardiac and skeletal muscle cells,” *The American journal of physiology*, 250(4 Pt 1), pp. C657-60.

Szent-Györgyi, A.G. (2004) “The early history of the biochemistry of muscle contraction,” *The journal of general physiology*, 123(6), pp. 631–641.

Takeda, S. *et al.* (2003) “Structure of the core domain of human cardiac troponin in the Ca2+-saturated form,” *Nature*, 424(6944), pp. 35–41.

Talbot, J.A. and Hodges, R.S. (1981) “Synthetic studies on the inhibitory region of rabbit skeletal troponin I. Relationship of amino acid sequence to biological activity,” *The journal of biological chemistry*, 256(6), pp. 2798–2802.

Tamborrini, D. *et al.* (2023) “Structure of the native myosin filament in the relaxed cardiac sarcomere,” *Nature*, 623(7988), pp. 863–871.

Tangen, C. and Wood, B. (2007) *Human muscle system*, *Encyclopedia Britannica*. Available at: https://www.britannica.com/science/human-muscle-system (Accessed: July 15, 2024).

Taylor, S.S. *et al.* (2021) “From structure to the dynamic regulation of a molecular switch: A journey over 3 decades,” *The journal of biological chemistry*, 296(100746), p. 100746.

Thomas, L.S.V. and Gehrig, J. (2020) “Multi-template matching: a versatile tool for object-localization in microscopy images,” *BMC bioinformatics*, 21(1), p. 44.

Tinevez, J.-Y. *et al.* (2017) “TrackMate: An open and extensible platform for single-particle tracking,” *Methods* , 115, pp. 80–90.

Tobacman, L.S. (2021) “Troponin revealed: Uncovering the structure of the thin filament on-off switch in striated muscle,” *Biophysical journal*, 120(1), pp. 1–9.

Toepfer, C.N., West, T.G. and Ferenczi, M.A. (2016) “Revisiting Frank-Starling: regulatory light chain phosphorylation alters the rate of force redevelopment (ktr) in a length-dependent fashion,” *The Journal of physiology*, 594(18), pp. 5237–5254.

Tong, C.W. *et al.* (2008) “Acceleration of crossbridge kinetics by protein kinase A phosphorylation of cardiac myosin binding protein C modulates cardiac function,” *Circulation research*, 103(9), pp. 974–982.

Tonino, P. *et al.* (2019) “Fine mapping titin’s C-zone: Matching cardiac myosin-binding protein C stripes with titin’s super-repeats,” *Journal of molecular and cellular cardiology*, 133, pp. 47–56.

Toseland, C.P. and Webb, M.R. (2011) “Fluorescent nucleoside triphosphates for single-molecule enzymology,” *Methods in molecular biology (Clifton, N.J.)*, 778, pp. 161–174.

Turner, K.L. *et al.* (2023) “RLC phosphorylation amplifies Ca2+ sensitivity of force in myocardium from cMyBP-C knockout mice,” *The Journal of general physiology*, 155(4). Available at: https://doi.org/10.1085/jgp.202213250.

Ušaj, M. *et al.* (2021) “Single molecule turnover of fluorescent ATP by myosin and actomyosin unveil elusive enzymatic mechanisms,” *Communications biology*, 4(1), p. 64.

Uyeda, T.Q., Ruppel, K.M. and Spudich, J.A. (1994) “Enzymatic activities correlate with chimaeric substitutions at the actin-binding face of myosin,” *Nature*, 368(6471), pp. 567–569.

Uyeda, T.Q. and Spudich, J.A. (1993) “A functional recombinant myosin II lacking a regulatory light chain-binding site,” *Science (New York, N.Y.)*, 262(5141), pp. 1867–1870.

Vinogradova, M.V. *et al.* (2005) “Ca(2+)-regulated structural changes in troponin,” *Proceedings of the National Academy of Sciences of the United States of America*, 102(14), pp. 5038–5043.

Von Der Ecken, J. *et al.* (2015) “Structure of the F-actin-tropomyosin complex,” *Nature*, 519(7541), pp. 114–117.

Walcott, S., Docken, S. and Harris, S.P. (2015) “Effects of cardiac Myosin binding protein-C on actin motility are explained with a drag-activation-competition model,” *Biophysical journal*, 108(1), pp. 10–13.

Walklate, J. *et al.* (2019) “A micro-volume adaptation of a stopped-flow system; use with µg quantities of muscle proteins,” *Analytical biochemistry*, 581, p. 113338.

Walklate, J. *et al.* (2021) “Alpha and beta myosin isoforms and human atrial and ventricular contraction,” *Cellular and molecular life sciences: CMLS*, 78(23), pp. 7309–7337.

Walklate, J. *et al.* (2022) “Exploring the super-relaxed state of myosin in myofibrils from fast-twitch, slow-twitch, and cardiac muscle,” *The Journal of biological chemistry*, 298(3), p. 101640.

Wang, K. *et al.* (1991) “Regulation of skeletal muscle stiffness and elasticity by titin isoforms: A test of the segmental extension model of resting tension,” *Proceedings of the National Academy of Sciences of the United States of America*, 88(16), pp. 7101–7105.

Wang, L. *et al.* (2018) “Thick filament protein network, functions, and disease association,” *Comprehensive Physiology*, 8(2), pp. 631–709.

Warren, S.A. *et al.* (2012) “Myosin light chain phosphorylation is critical for adaptation to cardiac stress,” *Circulation*, 126(22), pp. 2575–2588.

Watkins, H. *et al.* (1995) “Mutations in the cardiac myosin binding protein–C gene on chromosome 11 cause familial hypertrophic cardiomyopathy,” *Nature genetics*, 11(4), pp. 434–437.

Weber, F.E. *et al.* (1993) “Complete sequence of human fast-type and slow-type muscle myosin-binding-protein C (MyBP-C). Differential expression, conserved domain structure and chromosome assignment,” *European journal of biochemistry / FEBS*, 216(2), pp. 661–669.

Wegner, A. (1976) “Head to tail polymerization of actin,” *Journal of molecular biology*, 108(1), pp. 139–150.

Wendt, T. *et al.* (1999) “Visualization of head-head interactions in the inhibited state of smooth muscle myosin,” *The Journal of cell biology*, 147(7), pp. 1385–1389.

Wendt, T. *et al.* (2001) “Three-dimensional image reconstruction of dephosphorylated smooth muscle heavy meromyosin reveals asymmetry in the interaction between myosin heads and placement of subfragment 2,” *Proceedings of the National Academy of Sciences of the United States of America*, 98(8), pp. 4361–4366.

Wilson, C. *et al.* (2014) “The myosin inhibitor blebbistatin stabilizes the super-relaxed state in skeletal muscle,” *Biophysical journal*, 107(7), pp. 1637–1646.

Wilson, C., Naber, N. and Cooke, R. (2020) “The Role of the Super-Relaxed State of Myosin in Human Metabolism,” *Metabolism Open*, p. 100068.

Woodhead, J.L. *et al.* (2005) “Atomic model of a myosin filament in the relaxed state,” *Nature*, 436(7054), pp. 1195–1199.

Xu, C. *et al.* (1999) “Tropomyosin positions in regulated thin filaments revealed by cryoelectron microscopy,” *Biophysical journal*, 77(2), pp. 985–992.

Xue, B. *et al.* (2014) “Structural basis of thymosin-β4/profilin exchange leading to actin filament polymerization,” *Proceedings of the National Academy of Sciences of the United States of America*, 111(43), pp. E4596-605.

Yamada, Y., Namba, K. and Fujii, T. (2020) “Cardiac muscle thin filament structures reveal calcium regulatory mechanism,” *Nature communications*, 11(1), pp. 1–3.

Yamamoto, K. and Moos, C. (1983) “The C-proteins of rabbit red, white, and cardiac muscles,” *The journal of biological chemistry*, 258(13), pp. 8395–8401.

Yamasaki, R. *et al.* (2002) “Protein kinase A phosphorylates titin’s cardiac-specific N2B domain and reduces passive tension in rat cardiac myocytes,” *Circulation research*, 90(11), pp. 1181–1188.

Yasuda, M. *et al.* (1995) “Complete primary structure of chicken cardiac C-protein (MyBP-C) and its expression in developing striated muscles,” *Journal of molecular and cellular cardiology*, 27(10), pp. 2275–2286.

Yu, H. *et al.* (2016) “Phosphorylation of the regulatory light chain of myosin in striated muscle: methodological perspectives,” *European biophysics journal: EBJ*, 45(8), pp. 779–805.

Zoghbi, M.E. *et al.* (2008) “Three-dimensional structure of vertebrate cardiac muscle myosin filaments,” *Proceedings of the National Academy of Sciences of the United States of America*, 105(7), pp. 2386–2390.